MAGNETOSPHERE-IONOSPHERE-ATMOSPHERE COUPLING

Kaliningrag
2016

IMMANUEL KANT BALTIC FEDERAL UNIVERSITY
PUSHKOV INSTITUTE OF TERRESTRIAL MAGNETISM, IONOSPHERE
AND RADIO WAVE PROPAGATION, RAS
RUSSIAN FOUNDATION FOR BASIC RESEARCH

MAGNETOSPHERE-IONOSPHERE-ATMOSPHERE COUPLING

Proceedings
Of First Baltic School

Kaliningrad
2016

UDK 550.51
BBK 552.44
A92

The First Baltic School "MIAC" was supported by Russian Foundation for Basic Researches (Grant No. 16-35-1015216).

A92 **Magnetosphere-Ionosphere-Atmosphere Coupling** / ed. M.V. Klimenko. — Kaliningrad, 2016. —284 p.

Proceedings of first Baltic young scientists' international school on "Magnetosphere-Ionosphere-Atmosphere Coupling" (First Baltic School "MIAC") include materials reports on response analysis of the atmosphere — ionosphere to natural and manmade processes, various causes related geophysical phenomena and evaluate possible consequences of their effects on the human system and process. Content of the reports is of interest for researchers and students specializing in physics and chemistry of the atmosphere-ionosphere-magnetosphere system.

UDK 550.51
BBK 552.44

PLENARY SESSIONS (PL)

Long-Term Trends in the Ionosphere and Upper Atmosphere— different trend drivers

Jan Laštovička

Institute of Atmospheric Physics ASCR, Bocni II, 14131 Prague 4, Czech Republic

1. Introduction. The anthropogenic emissions of greenhouse gases influence the troposphere, weather, and climate. They appear to be the primary driver of a significant increase of surface temperature in recent decades, thus affecting directly our life. However, these polluting substances affect not only the troposphere and stratosphere, their effect is observed to penetrate throughout the upper atmosphere, including the mesosphere (~50—90 km), the thermosphere (~90—1000 km), and the ionosphere, which is embedded in the upper atmosphere. The thermosphere is the operating environment of many satellites**,** including the International Space Station, and thousands of pieces of space debris dangerous for satellites, the orbital lifetime of which depends on long-term changes of thermospheric density. Propagation of Global Positioning System (GPS) signals and radio communications are affected by the ionosphere.Thus anthropogenic changes of high-altitude regions can affect also satellite-based technologies, which are increasingly important to modern life.

The greenhouse gas increase has an opposite, cooling effect in the upper atmosphere. Greenhouse gases in the troposphere are optically thick to outgoing longwave (infrared) radiation, which they both absorb and reemit back to the surface to produce the heating effect. In contrast, greenhouse gases in the much lower density upper atmosphere are optically thin to outgoing infrared radiation. In-situ collisional excitation results in atmospheric thermal energy readily lost to space via outgoing infrared radiation (CO_2 and NO are the two main "coolers" of the thermosphere), while the absorption of radiation emanating from the lower atmosphere plays only a secondary role in the energy balance. The net result is that the radiatively active greenhouse gases act as cooling agents, and their increasing concentrations enhance the cooling effect in the upper atmosphere [1].

In the early period of long-term trend studies in the upper atmosphere, results of individual studies were often inconsistent and sometimes controversial. However, with the increasing amount of observational and model results and findings, a global pattern of trend behavior began to emerge, and, in 2006, the first global scenario of trends in the upper atmosphere and ionosphere was constructed [2, 3]. However, at that time results concerning some variables were not consistent with the global scenario. Moreover, in recent years it became increasingly clear that other drivers play an important role in long-term trends in the upper atmosphere and

ionosphere, in addition to the increasing atmospheric concentration of greenhouse gases, which is the dominant driver of upper atmosphere trends. In this paper we shall focus on the role of different drivers in trends in the thermosphere and ionosphere, and to some extent also in the mesosphere.

2. Global scenario of long-term trends. The first global scenario of trends shown in Fig. 1 is created by trends in mesospheric temperature (mesospheric cooling and no trend in mesopause region), electron concentration in the lower ionosphere below 100 km (increase at fixed heights), maximum electron concentration (slight increase) and height of this maximum (statistically rather insignificant decrease due to coarse resolution of height measurements by ionosondes) in the E region, electron concentration in the F1-region maximum (slight increase), thermospheric neutral density (moderate decrease) and F2-region ion temperature (evident decrease). All these trends are qualitatively mutually consistent and qualitatively agree with model simulations of consequences of the enhanced greenhouse effect, and with the hypothesis of global cooling and contracting of the upper atmosphere. Changes in temperature influenced chemistry of minor constituents, which is probably the main reason of observed changes in the E and F1 region ionosphere. The global trend scenario has been improved continuously and it has been broaden to include more parameters but still various controversies and gaps remain.

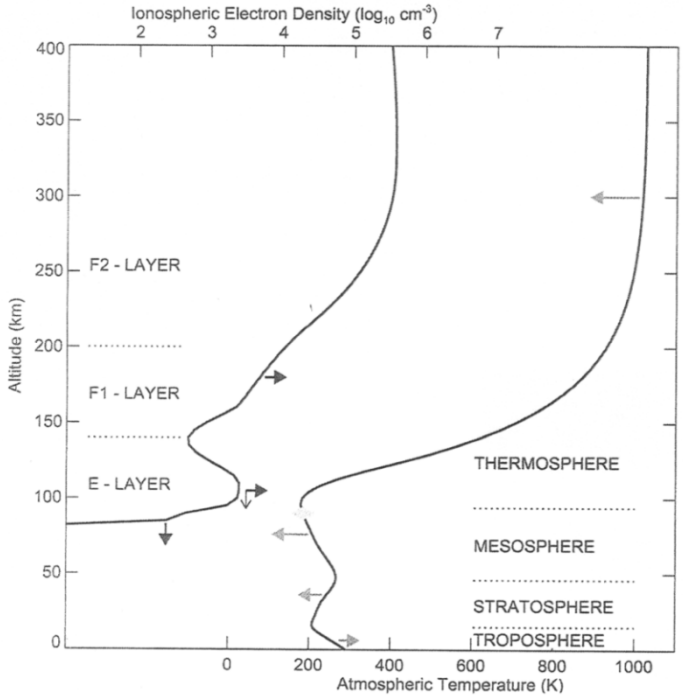

FIGURE 1. The first scenario of global change in the atmosphere and ionosphere.Adopted from [3].Arrows indicate the direction of change. Temperature profile — left cooling, right heating, no change of temperature in the mesopause; electron density profile — changes in electron density (horizontal) and heights of ionospheric layers (vertical).

3. Different trend drivers. The main reason for the observed long-term trends is considered to be the increasing concentration of greenhouse gases (predominantly CO_2) in the atmosphere, which affects the whole atmosphere from the surface up to heights of several hundred kilometers, both in the neutral and ionized component. However, there are also other drivers of long-term changes and trends in the upper atmosphere, which cannot be neglected. In the ionosphere and thermosphere they are as it follows: Long-term changes of solar and geomagnetic activities, secular change of the Earth's magnetic field, atmospheric wave activity, and evolution of stratospheric ozone concentration.

Let us start with solar activity. Solar activity appears to have decreased during the second half of the 20th century, and particularly in the beginning of the 21st century, which is a tendency opposite to what is required to explain the observed positive ionospheric trends in the E and F1 regions. Moreover, the effect of solar activity, on solar cycle time scales, has to be removed when long-term trends are computed both in the ionosphere and thermosphere. Different corrections to solar activity are one of the sources of differences between different trend results in F2-region parameters, foF2 and hmF2. On the long time-scales like more than four solar cycles (1959—2005), when the effect of solar activity was not removed, it explained 5—40 % of total trends in hmF2 and 20—80 % in foF2 for various ionospheric stations [4]. In this context it should be mentioned that foF2 is not a good parameter for studying trends of anthropogenic origin, because hmF2 is close to the boundary where a positive anthropogenic trend in electron density below changes to a negative trend above according to model calculations [5].

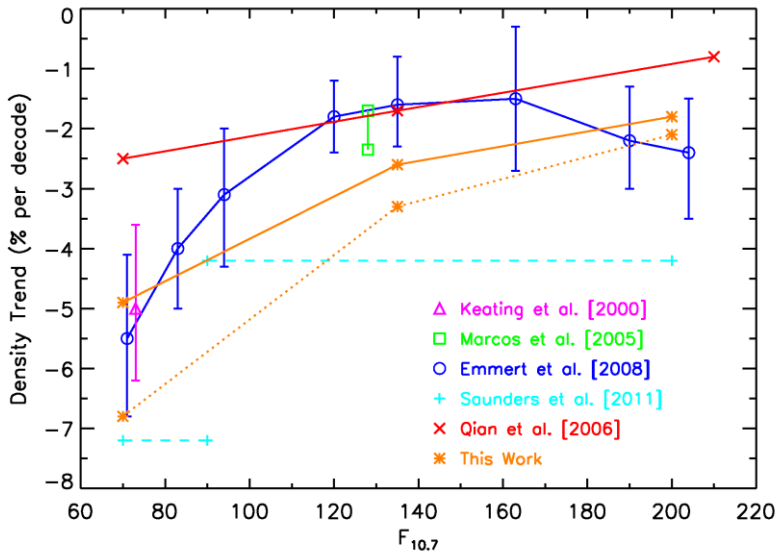

FIGURE 2. Neutral density trends at 400 km. Crosses — model calculations, middle curve are new calculations with model WACCM and new realistic profile of CO_2 concentration. Other symbols — observational trends from satellite drag measurements. Adopted from [7].

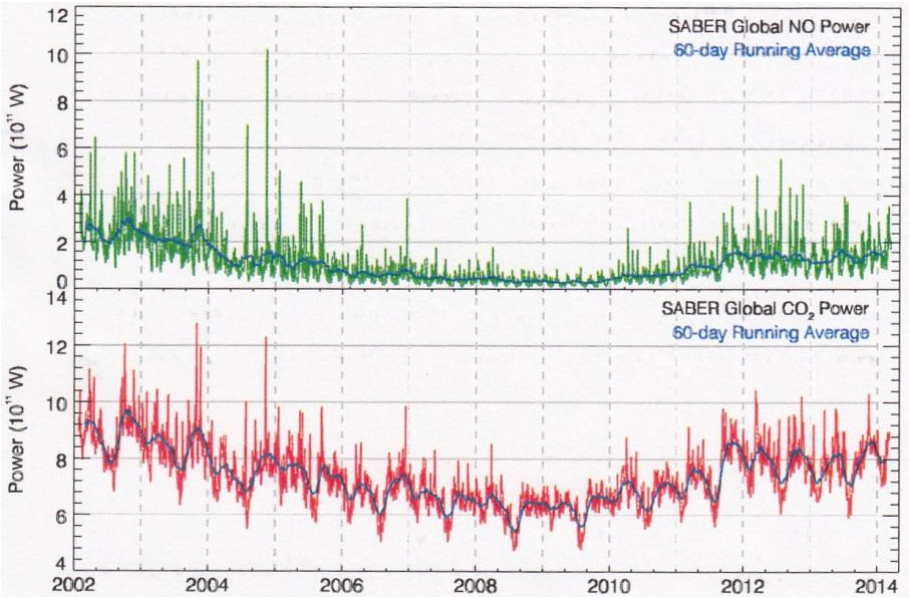

FIGURE 3.SABER/TIMED NO (top panel) and CO_2 (bottom panel) radiative power evolution over 2002—2014.Adopted from [8].

It is necessary to mention that trends may be quantitatively different under solar activity maximum and minimum conditions, as it was shown for thermospheric density [6]. Figure 2 shows this for both observational and model-derived trends of thermospheric density [7]. The reason is much larger relative role of the CO_2 radiative cooling compared to the NO radiative cooling under solar minimum conditions as shown in Fig. 3. The NO radiative power decreased by almost an order of magnitude from 2002 to 2009, whereas the CO_2 radiative power decreased only by $\sim 35\%$ according to SABER/TIMED measurements [8]. However, Emmert [9] quite recently created a puzzle, as his newest results provide no statistically significant dependence of thermospheric density trends on solar activity. This puzzle needs to be solved.

Long-term change of geomagnetic activity means its increase almost throughout the 20th century followed by a deep drop in the 21th century. In the 20th century the role of geomagnetic activity in the observed long-term trends/changes in the atmosphere-ionosphere system was decreasing from its beginning towards its end [10]. Mikhailov and de la Morena [11] found thattrends in foE were controlled by geomagnetic activity before about 1970, but not in morerecent years. Bremer et al. [12] summarized various European studies and reported that the change of dependence of trendson long-term change of geomagnetic activity occurred in mid-1990s in the F1 region and around 2000 in the F2 region (in hmF2 substantially earlier). More recent data confirm this finding.

Effects of the secular change of the main magnetic field of the Earth were modeled and summarized by Cnossen [13]. As Fig. 4 shows for ion temperature T_i, this effect is very regional. For foF2 and hmF2 it is very important in a few regions, particularly around the equatorial Southern America and adjacent part of Atlantic Ocean, whereas it is negligible in most of other regions. For T_i these model calculations (which probably underestimate the effect of CO_2) provide globally comparable effect of secular change of magnetic field and CO_2 (Fig. 4). Some effect of secular magnetic field change was found even in neutral temperature trends [13].

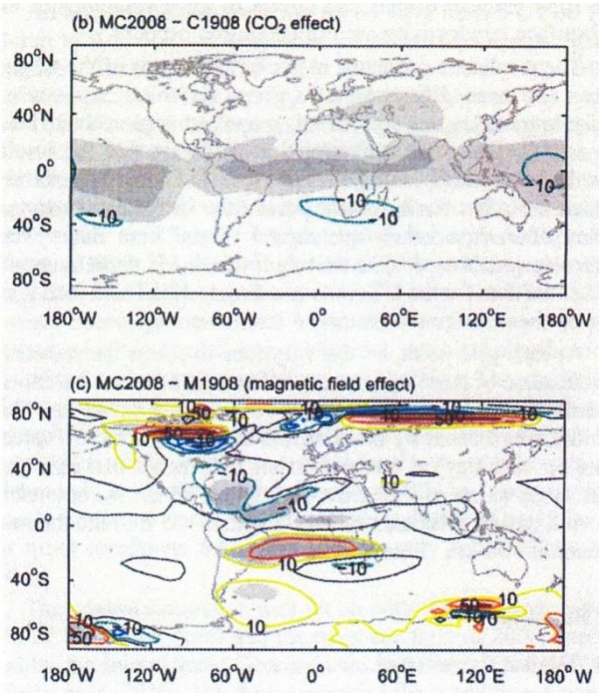

FIGURE 4.Trend in ion temperature $T_i$at ~300 km, 12 LT, 1908—2008, model TIE-GCM [13]. Top panel — control run, upper middle panel — effect of CO_2, lower middle panel —effect of magnetic field.

Another important factor is long-term trends in atmospheric dynamics and atmospheric wave (gravity, tidal and planetary waves) activity. They are only poorly known. However, it became clear that these trends are regionally significantly different and changing with time, at least in the mesosphere and lower thermosphere (we have very little observational information from the middle and upper thermosphere), as it was summarized in [14]. Trends in atmospheric wave activity are of key importance as they couple trends in the lower and upper atmosphere.

The evolution of the stratospheric ozone concentration appears to be important trend driver in the mesosphere and lower thermosphere. The stratospheric ozone at northern middle latitudes changed trend from negative to none or positive in the

mid-1990s (~1995—1997) and later also at southern middle latitudes. Its changes at low and equatorial latitudes are small but they are large in high latitudes, particularly in the region of the Antarctic ozone hole.

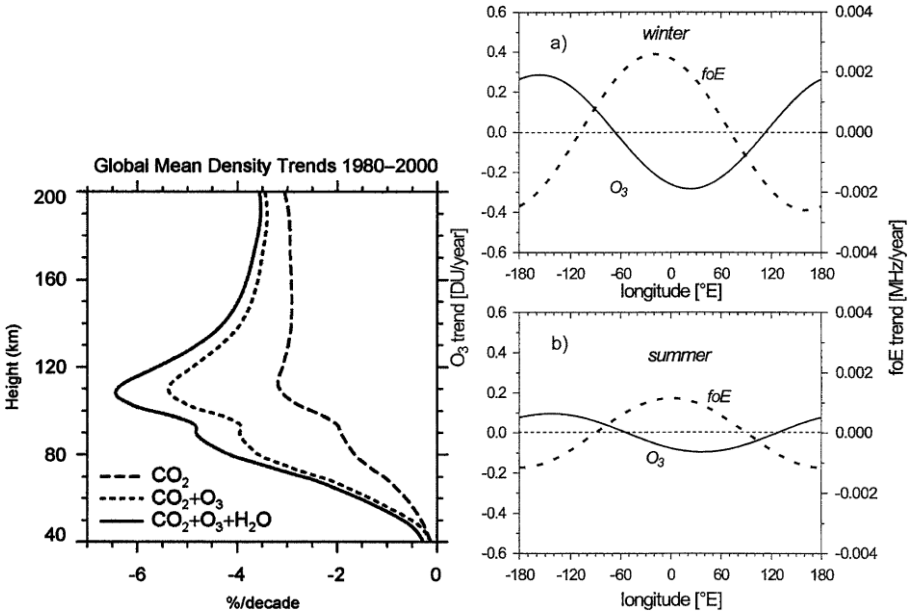

FIGURE 5. Impact of ozone on trends. Left panel — trends in global-mean atmospheric density at 40—200 km caused by changes of CO_2, ozone and water vapor concentrations over 1980—2000 according to model calculations [15]. Right panel — longitudinal variation of deviations of foE trends from the average trend in foE (ionosondes between 30—75°N) and of deviations of total ozone trends from the average trend (ERA40, 30—75 °N); top panel — winter, bottom panel — summer [16].

Figure 5, left panel, shows an evident impact of stratospheric ozone on trends in density in the lower thermosphere (even though these model calculations probably somewhat overestimate the effect of ozone), which peaks at 110 km [15]. Figure 5, right panel, reveals an out-of-phase correlation between deviations of foE and total ozone trends from zonal mean trends as another evidence of the stratospheric ozone influence on trends at lower thermosphere heights [16]. However, effect of ozone on trends was not found in the F1 region ionosphere (foF1) [17].

Mesopause temperature trends changed from no trend before ozone trend reversal in the mid-1990s (Fig. 1) to negative trends after the ozone trend reversal, and mesospheric temperature trends changed from negative (Fig. 1) to essentially no trends [18]. There is also other evidence supporting impact of the stratospheric ozone trends on trends at mesospheric and lower thermospheric heights [1, 14].

Walsh and Oliver [19] based on historical Saint Santin incoherent scatter radar data on T_i claimed that ozone, not CO_2, is the main trend driver in the upper ther-

mosphere. However, no response of ion temperature measured by the Millstone Hill incoherent scatter radar to change of ozone trend in the mid-1990s shows that ozone has little, if any, impact on trends in the upper thermosphere [20].

Oliver et al. [21, 22] claimed that the increasing activity of gravity waves, which cools the thermosphere, in combination with the decreasing height of the turbopause by 4 km and related increase of n(O) at 120 km explain trends in ion temperature above Millstone Hill over 1966—2012, not increasing concentration of greenhouse gases. However, Laštovička [23] showed that explanation via changes in gravity wave activity is very uncertain and that via turbopause height and n(O) is incorrect.

4. Conclusions. Carbon dioxide CO_2 is the main driver of long-term trends in the ionosphere-thermosphere system, particularly over long time intervals, but its effect is modified by other trend drivers. Effects of some other trend drivers are spatially very variable, like effects of the secular change of the Earth's magnetic field or of atmospheric wave activity; others are principally changing with time like effects of stratospheric ozone or geomagnetic activity. Consequently we can hardly expect trends in various ionospheric and thermospheric parameters to be temporally and spatially uniform and stable.

Acknowledgements:*Support by the Czech Scientific Fund via grant 15-03909S is acknowledged.*

1.J. Laštovička, S. C. Solomon, and L. Qian, Trends in the neutral and ionized upper atmosphere, *Space Sci. Revs.*, 2012, 168, pp. 113—145, doi: 10.1007/s11214-011-9799-3.

2. J. Laštovička, R.A. Akmaev, G. Beig et al., Global change in the upper atmosphere,*Science*,2006, 314(5803), pp. 1253—1254.

3. J. Laštovička, R. A. Akmaev, G. Beig et al., Emerging pattern of global change in the upper atmosphere and ionosphere, *Ann. Geophysicae*, 2008, 26(5), pp. 1255—1268.

4. I. Cnossen and C. Franzke, The role of the Sun in long term change in the F2 peak ionosphere: New insights from EEMD and numerical modeling, *J. Geophys. Res. Space Phys.*, 2014, 119(10), doi: 10.1002/2014JA020048.

5. L. Qian, S. C. Solomon, R. G. Roble, and T. J. Kane, Model simulations of global change in the ionosphere, *Geophys. Res. Lett*., 2008, 35, L07811.

6. J. T. Emmert, J. M. Picone, and R. R.Meier, Thermospheric global average density trends 1967—2007, derived from orbits of 5000 near-Earth objects,*Geophys. Res. Lett.*, 2008, 35, L05101, doi:10.1029/2007GL032809.

7. S. C. Solomon,L. Qian, and R. G. Roble, New 3-D simulations of climate change in the thermosphere, *J. Geophys. Res. Space Phys.*, 2015, 20(3), pp. 2183—2193, doi: 10.1002/2014JA020886.

8. M.G. Mlynczak, L. A. Hunt, C. J. Mertens et al., Influence of solar variability on the infrared radiative cooling of the thermosphere from 2002 to 2014, *Geophys. Res. Lett.*, 2014, 41, pp. 2508—2513, doi: 10.1002/2014GL059556.

9. J. T. Emmert, Altitude and solar activity dependence of 1967—2005 thermospheric density trends derived from orbital drag, *J. Geophys. Res. Space Phys.*, 2015, 120(4), pp. 2940—2950, doi: 10.1002/2015JA021047.

10. J. Laštovička, On the role of solar and geomagnetic activity in long-term trends in the atmosphere-ionosphere system, *J. Atmos. Sol.-Terr. Phys*., 2005, 67(1—2), pp. 83—92.

11. A. V. Mikhailov and B. A. de la Morena, Long-term trends of *foE* and geomagnetic activity variations. *Ann. Geophysicae*, 2003,21, pp. 751—760.

12. J. Bremer, J. Laštovička, A. V. Mikhailov et al., Climate of the upper atmosphere, *Annals Geophys*., 2009, 52(3/4), pp. 273—299.

13. I. Cnossen, The importance of geomagnetic field changes versus rising CO_2 levels for long-term change in the upper atmosphere,*J. Space Wea. Space Clim*.,2014, 4, A18.

14. J. Laštovička, Trends in the upper atmosphere and ionosphere: Recent progress, *J. Geophys. Res. Space Phys*., 2013, 118, pp. 3924—3935, doi:10.1002/jgra.50341.

15. R. A. Akmaev, V.I. Fomichev, and X. Zhu, Impact of middle-atmospheric composition changes on greenhouse cooling in the upper atmosphere. *J. Atmos. Sol.-Terr. Phys*., 2006, 68, pp. 1879—1889, doi:10.1016/j.jastp.2006.03.008.

16. J. Bremer and D. Peters, Influence of stratospheric ozone changes on long-term trends in the meso- and lower thermosphere.*J. Atmos. Sol.-Terr. Phys*., 2008, 70(11—12), pp. 1473—1481, doi:10.1016/j.jastp.2008.03.024.

17. J. Bremer, Long-term trends in the ionospheric E and F1 regions, *Ann. Geophysicae*,2008, 26, pp. 1189—1197, doi: 10.5194/angeo-26-1189-2008.

18. G. Beig, Long-term trends in the temperature of the mesosphere/lower thermosphere region: 1. Anthropogenic influences, *J. Geophys. Res*., 2011, 116, A00H11.

19. P. L. Walsh and W. L. Oliver, Is thermospheric long-term cooling due to CO2 or O3?*Ann. Geophysicae*, 2011, 29, pp. 1779—1782, doi: 10.5194/angeo-29-1779-2011.

20. J. Laštovička, On the role of ozone in long-term trends in the upper atmosphere-ionosphere system, *Ann. Geophysicae*, 2012, 30, pp. 811—816.

21. W. L. Oliver, S.-R. Zhang, and L. P. Goncharenko, Is thermospheric global cooling caused by gravity waves?*J. Geophys. Res. Space Phys*., 2013, 118, pp. 3898—3908.

22. W. L. Oliver, J. M. Holt, S.-R. Zhang and L. P. Goncharenko, Long-term trends in thermospheric neutral temperatures and density above Millstone Hill, *J. Geophys. Res. Space Physics*, 2014, 119, pp. 7940—7946, doi: 10.1002/2014JA020311.

23. J. Laštovička, Comment on "Long-term trends in thermospheric neutral temperatures and density above Millstone Hill" by W. L. Oliver et al., *J. Geophys. Res. Space Physics*, 2015, 120, pp. 2347—2349, doi: 10.1002/2014JA020864.

Generation of Nonmigrating Tides and Ionospheric Disturbances during SSW Events

Alexander I. Pogoreltsev

Department of Meteorological Forecasting, Russian State Hydrometeorological University, St.Petersburg, 195196, Russia

The coupling of atmospheric layers is one of the most interesting and important problems of atmospheric dynamics [1]. Results of the numerical simulations performed with the Middle and Upper Atmosphere Model (MUAM) show that the direct propagation of longer-period and stationary planetary waves (PW) from the

lower atmosphere into the thermosphere up to the ionospheric F2-layer is not possible [2]. However, the shorter-period PW such as the ultra-fast Kelvin waves, Rossby-gravity waves, and atmospheric tides are capable of propagating into the thermosphere. One of the possible ways to transfer the effects of the long-period variability in the middle atmosphere up to the thermospheric heights is the generation and/or modulation of these waves by the nonlinear interaction with quasi-stationary PW in the stratosphere. The results of calculation of nonmigrating tides forced by the interaction of migrating tides with stationary m = 1 PW during sudden stratospheric warming (SSW) strongly support this possibility and show that modulation of the fast waves by stratospheric processes is one of the most promising mechanisms in the explaining the coupling the lower and upper atmosphere [2]. In recent years many efforts have been spent to arrange a new parameterization of gravity wave (GW) effects in the upper atmosphere [3] (see also reviews [1, 4] and references therein). A modified version of this parameterization is inserted into the MUAM. Unfortunately, this parameterization does not take into account the reflection of the large-scale GW form the dissipative region in the thermosphere that first was noted in classical paper [5] and later was supported by the numerical simulation [6]. In result of this the GW effects in the upper atmosphere are overestimated. Another possible mechanism that can be responsible for the observed longer-period PW-like perturbations observed in the ionospheric parameters [7] is the generation of the electromagnetic field disturbances due to an interaction of global scale neutral motions with the ionospheric plasma in the dynamo-region [8, 9]. The discussion of this problem is out the scope of the paper. The main purpose of the present paper is to consider the behavior of the tidal oscillations in the neutral wind and ionospheric characteristics during development of the SSW events in the stratosphere.

Figure 1 shows the main characteristics of the SSW events observed in the 1997—98 winter obtained on the basis of the MERRA data [10]. This year was selected due to the fact that there were a strong El-Nino conditions that are favorable for development the SSW.

Figure 2 demonstrates the results of simulation with the MUAM (a set of the ensemble runs for El-Nino conditions have been performed and the results obtained in one of the runs that are more closely to observations is presented). One can see in these figures that in the both cases there exists a strong heating of the polar region at the beginning of February and the reversal of the zonal mean wind at the middle latitudes of Northern Hemisphere in the upper stratosphere, i. e., the major SSW event is observed.

To demonstrate SSW effects in the upper thermosphere, in Fig. 3 the results of simulation up to the 200 km during the time interval when the SSW event was developed are presented. It is clear that during SSW the heating of the lower thermosphere is observed and the cooling of the upper thermosphere followings with some delay (lower panel in Fig. 3). There is also some changes of the tidal oscillations at the upper levels (upper and middle panels in Fig. 3).

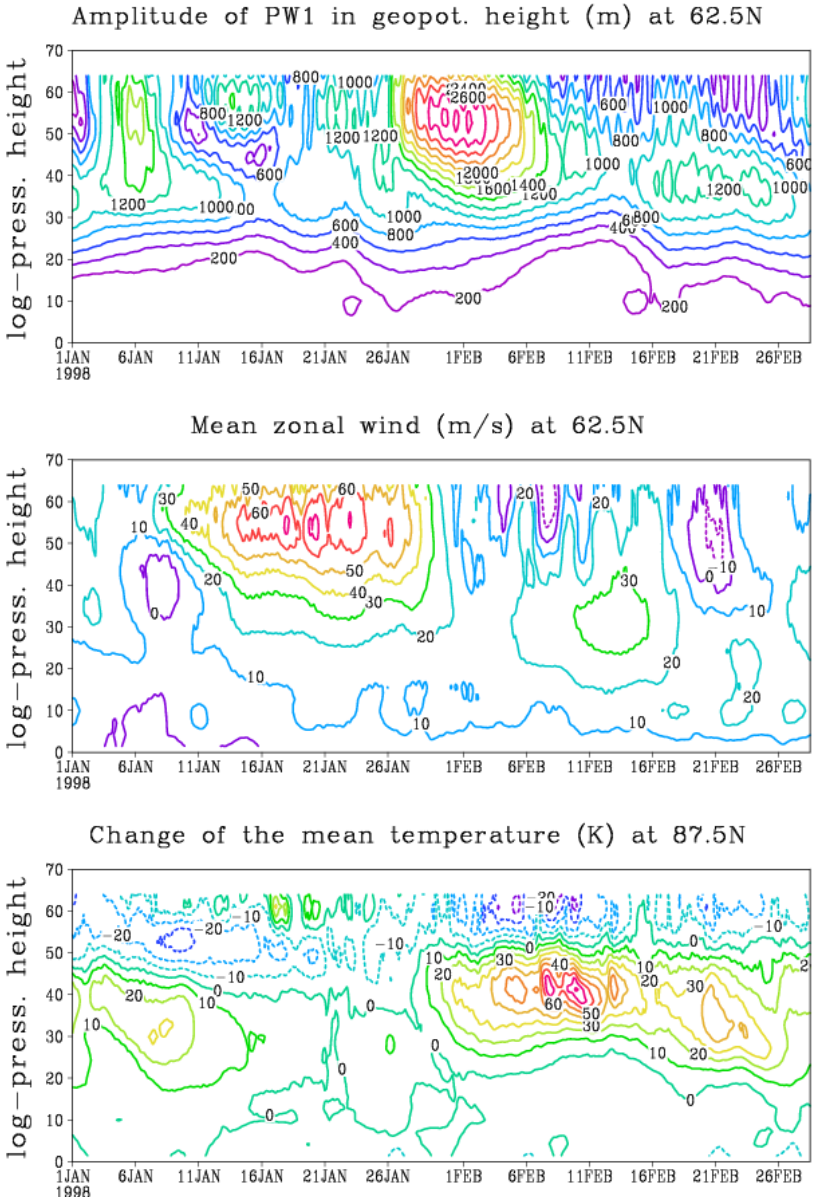

FIGURE 1. The time-altitude cross-sections of the amplitude of zonal harmonic with m = 1 in the geopotential height and the mean zonal wind at latitude 62.5N (upper and middle panels) observed in January-February 1998. The changes of the zonal mean temperature during these months at 87.5N are shown in the lower panel. MERRA data.

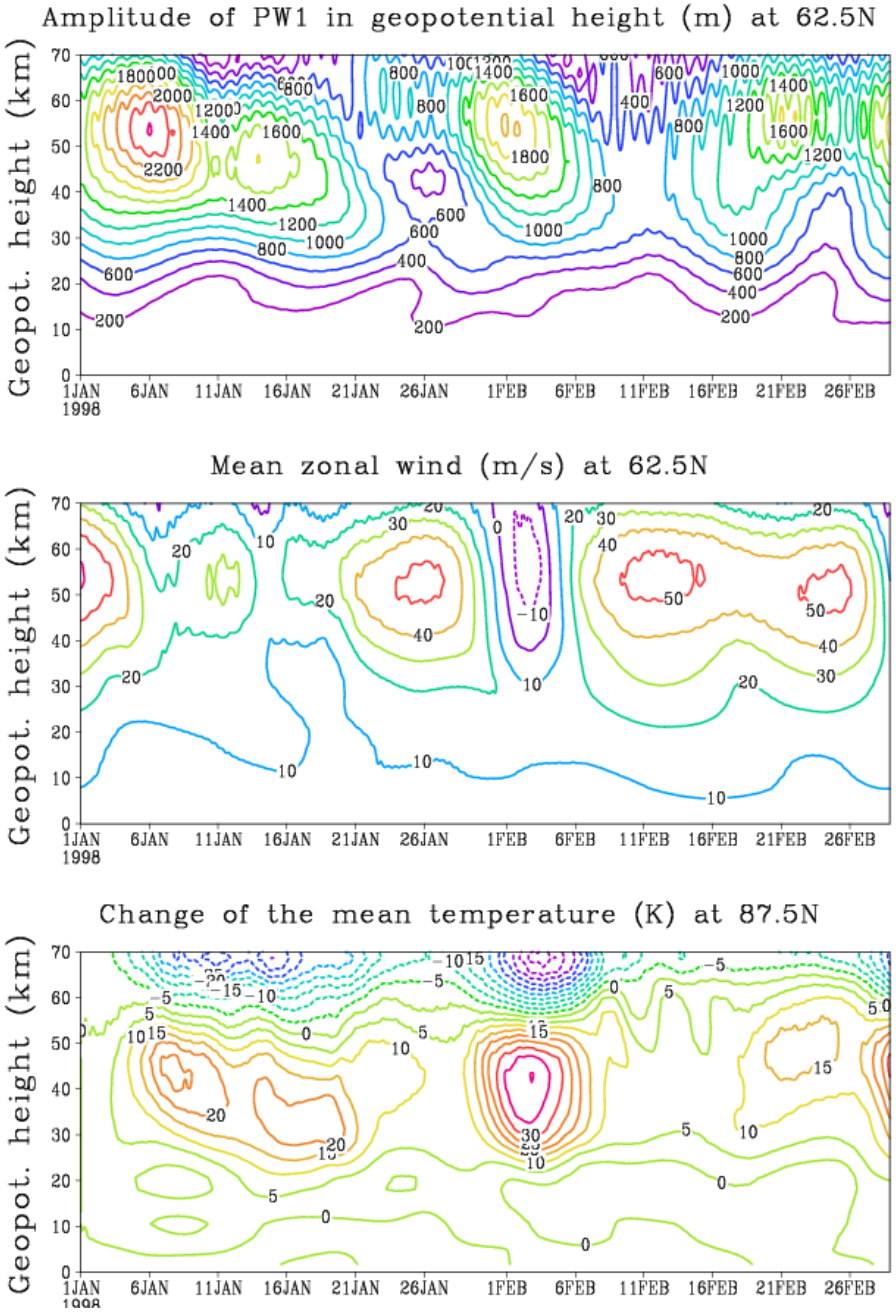

FIGURE 2.The time-altitude cross-sections of the amplitude of zonal harmonic with m = 1 in the geopotential height and the mean zonal wind at latitude 62.5N (upper and middle panels). Change of the mean temperature at 87.5N is shown in the lower panel. In all panels the height is up to 70 km. MUAM simulation.

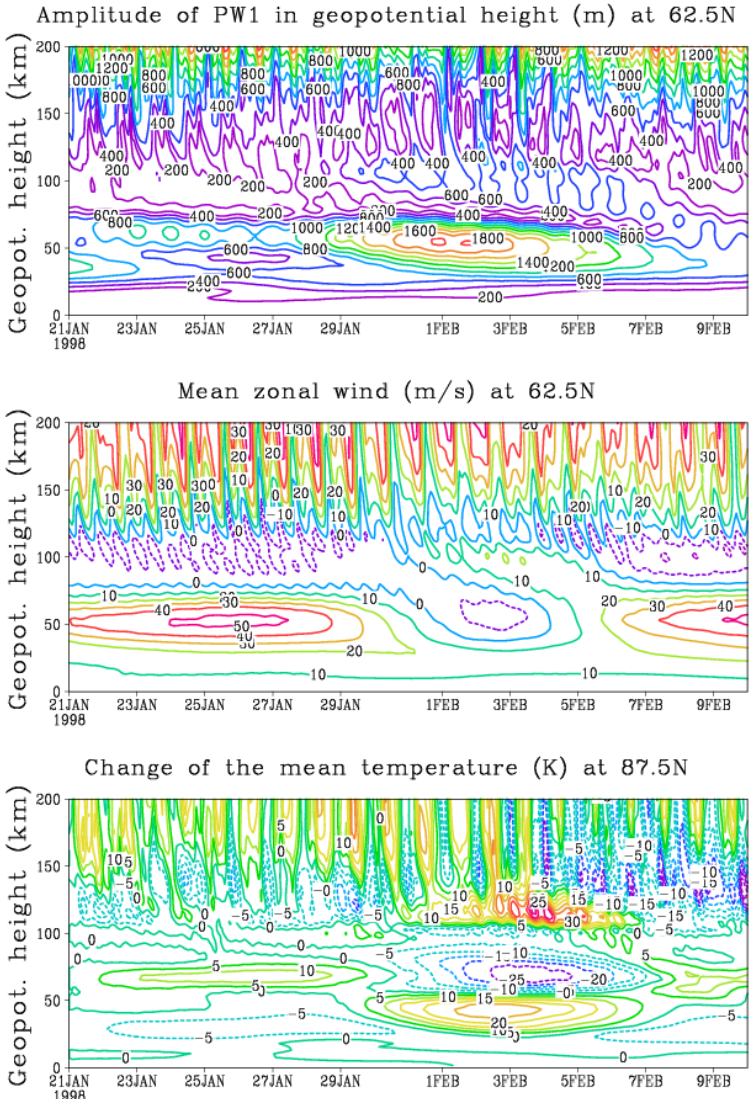

FIGURE 3.The time-altitude cross-sections of the amplitude of zonal harmonic with m = 1 in the geopotential height and the mean zonal wind at latitude 62.5N (upper and middle panels) during the SSW event. Change of the mean temperature during this time interval at 87.5N is shown in lower panel. In all panels the height is up to 200 km. MUAM simulation.

There exists a strong increase in the amplitude of the PW with m=1 during the SSW (upper panels in Figs. 1 and 2). Therefore, during this time we can expect an increase in the nonlinear interaction between the primary migrating tides with this wave and generation of the secondary nonmigrating tides. Fig. 4 shows the amplitude wavelet spectra for westward propagating waves with m = 1—3 in meridional wind at low latitudes in the lower thermosphere where this oscillation can be ob-

served, for instance, by meteor radar systems. This figure shows that just before SSW there is a decrease and then an increase in the amplitude of migrating diurnal tide and the semidiurnal tide is enforced during the development the SSW event.

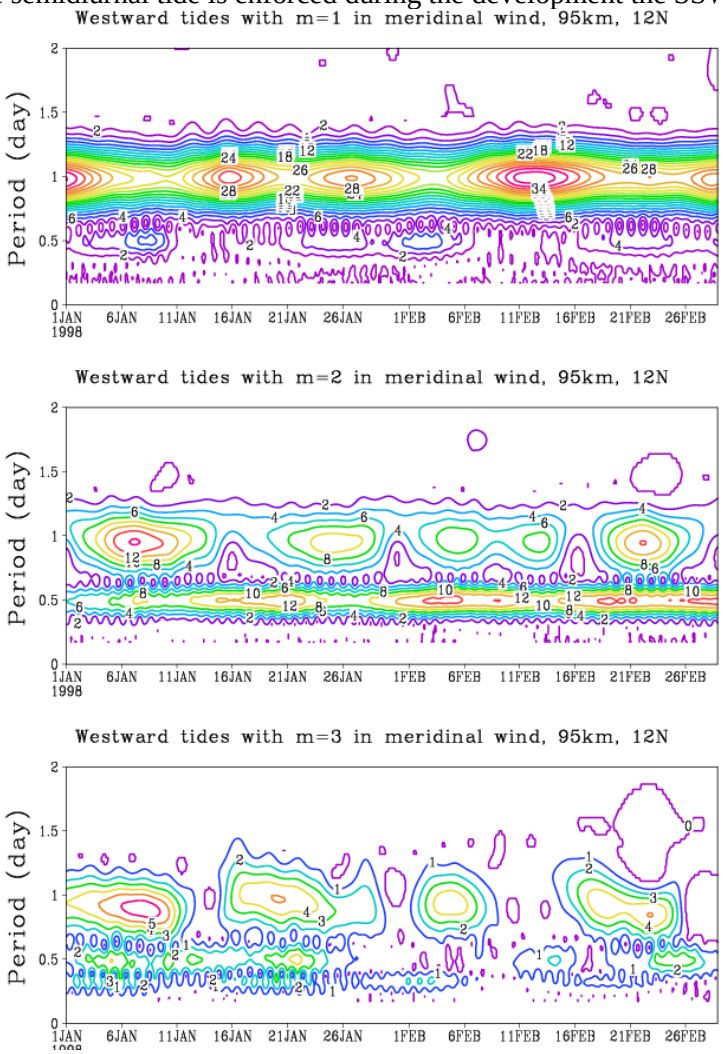

FIGURE 4. Amplitude wavelet spectra for westward propagating waves with m = 1 (upper panel), m = 2 (middle panel), and m = 3 (lower panel) in the meridional wind at latitude 12.5N at the altitude of the lower thermosphere (z = 95km). MUAM simulation.

To consider possible effects of the SSW in the ionospheric plasma the total electron content (TEC) data have been used. These data are available at the site of the Center for Orbit Determination in Europe (CODE) http://www.aiub.unibe.ch/download. Figure 5 demonstrates that during SSW a substantial increase of the diurnal and semidiurnal tidal components in the TEC oscillations is observed. Unfortunately, at the moment the MERRA data for February 2016

are not yet available and the UK Met Office data [11] have been used to plot the upper panel in Fig. 5.

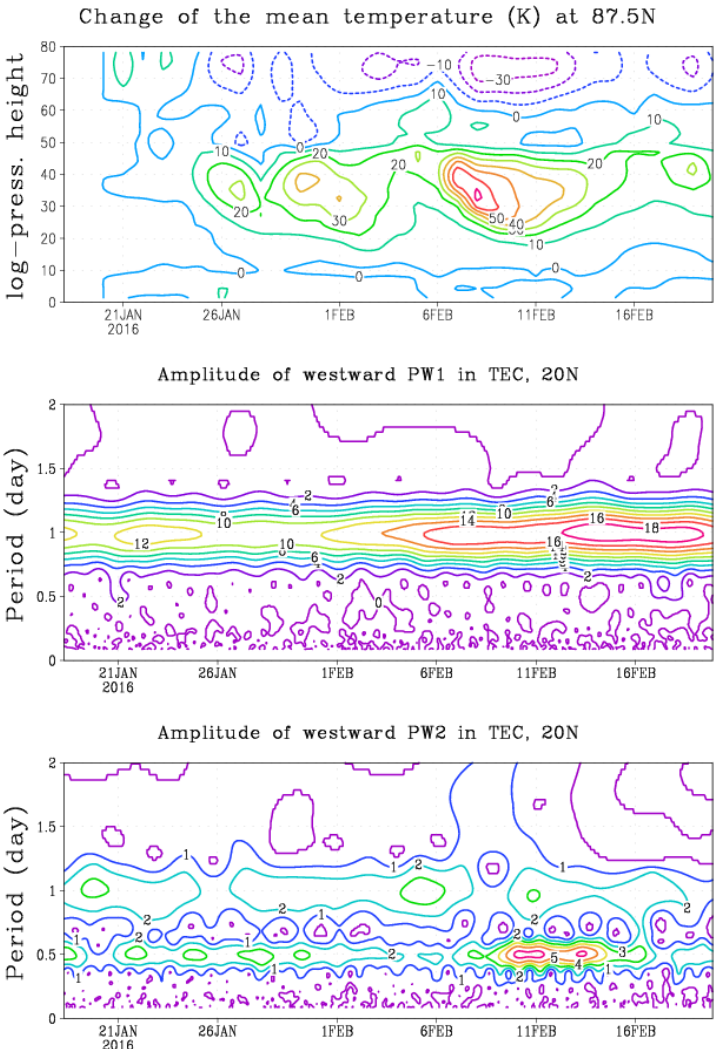

FIGURE 5. The time-altitude cross-section of the mean temperature change at latitude 87.5N (upper panel) during the SSW event in January-February 2016.Amplitude wavelet spectra for westward propagating waves with m = 1 and 2 in TEC at latitude 20N are shown in the middle and lower panels, respectively.

Conclusion. The results of the data analysis and simulation with the MUAM show that there is a signature of the SSW event in the upper thermosphere as well as in the ionospheric characteristics. The main suggested mechanism of transferring the “information” from the stratosphere into the upper atmosphere is the modulation of the migrating tides and/or generation of the propagating nonmigrating tides aris-

ing from a nonlinear interaction between the primary migrating tides with the quasi-stationary PW at the stratospheric heights.

Acknowledgements: *This research was supported by the Russian Science Foundation under Grant 14-17-00685.*

1. E. Yiğit, P. K.Knížová, K. Georgieva, and W. Ward, *J. Atmos. Solar-Terr. Phys.*, 2016, 141, pp. 1—12.

2. A. I. Pogoreltsev, A. A. Vlasov. K. Fröhlich, and Ch. Jacobi, *J. Atmos. Solar-Terr. Phys*., 2007, 69, pp. 2083—2101.

3. E. Yiğit, A. D. Aylward, and A. S. Medvedev, *J. Geophys. Res*., 2008, 11355.

4. E. Yiğit and A. S. Medvedev, *Adv. Space Res*., 2015, 55, pp. 983—1003.

5. M. Yanowitch, *J. Fluid Mech*., 1967, 29(2), pp. 209—231.

6. E. R. Bidlingmayer, A. I. Ivanovsky, and A. I. Pogoreltsev,*Izv. USSR Acad. Sci., Atmos. Oceanic Phys*., 1990, 26, pp. 682—692.

7. C. Borries, N. Jakowski, Ch. Jacobi et al., *J. Atmos. Solar-Terr. Phys.*, 2007, 69, pp. 2442—2451.

8. M. L. Glushakov, V. N. Dulkin, and A. I. Ivanovsky, *Geom. and Aeron.*, 1981, 21, pp. 629—631.

9. A. D. Richmond, *Geophys. Monogr.Ser.*, 1995, 87.AGU, Washington, DC, pp. 49—65.

10. M. M. Rienecker et al., *J. Climate*, 2011, 24, pp. 3624—3648.

11. R. Swinbank and A. O'Neil, *Mon. Weather Rev.*, 1994, 122, pp. 686—702.

Morphology and Mechanisms of the Ionospheric *F* Region Electron Density Disturbances during Geomagnetic Storm and Sudden Stratospheric Warming

Maxim V. Klimenko[1,2], Vladimir V. Klimenko[1], Fedor S. Bessarab[1], Yury N. Korenkov[1], Konstantin G. Ratovsky[3], Nina A. Korenkova[1], and Irina E. Zakharenkova[1]

[1]West Department of Pushkov IZMIRAN, RAS, 236017, Kaliningrad, 41 Pobeda Av., Russia
[2]Immanuel Kant Baltic Federal University, 236041, Kaliningrad,14 A. Nevsky Str., Russia
[3]Institute of Solar-Terrestrial Physics, SB RAS, 664033, Irkutsk P/O Box 291, 126a Lermontov Str., Russia

Ionosphere's *F* region disturbances during geomagnetic storm and sudden stratospheric warming (SSW) are the most essential and unexpected issues on the topic of the ionosphere modeling. These issues are broadly discussed during recent years [1—6]. These problems are very important in terms of understanding of the interrelated processes in the upper atmosphere and the key in the background values selection to study the ionospheric disturbances effects of different origin. Therefore it is necessary to carry out a research on the formation mechanisms of the ionospheric disturbances and to clarify the effects of the neutral composition changes and ionosphere-plasmasphere connections on the formation of the iono-

spheric effects during geomagnetic storm and SSW. This study summarizes the general features and interpretations of the observed ionospheric disturbances during geomagnetic storms on September 26—30, 2011 and March 17—23, 2015 and SSW on January 2009.

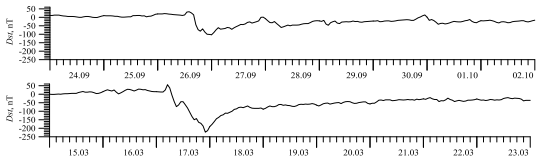

FIGURE 1. Behavior of the *Dst* index of geomagnetic activity during disturbed periods from September 24, 2011 to October 02, 2011 and from March 15, 2015 to March 23, 2015.

The geomagnetic storm occurred on 17—19 March 2015 was the record in strength over the past ten years. It was the strongest storm in the 24th solar cycle. The maximum values of the geomagnetic activity *Kp* index reached the value of 8 during this period. Last time the disturbances of such intensity in Kp index were observed during the geomagnetic storm on September 26, 2011, which was one of the strongest storms in the period 2007—2011. Figure 1 shows the behavior of the *Dst* index on March 15—23, 2015 and from September 24 to October 2, 2011, respectively. Both storms occurred in the equinox conditions at the moderate level of solar activity. Beginning the greatest changes of the geomagnetic field in both cases occurred at ~ 12:00 UT. Ionospheric effects of these storms are being studied intensively [6—8].

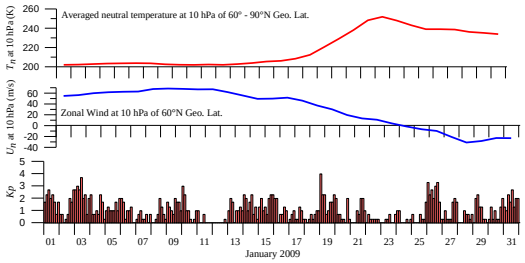

FIGURE 2. Averaged stratospheric (10 hPa) neutral temperature in January 2009 obtained at 60° — 90° N (a), zonal wind velocity at 60° N (b), and Kp (c) index of geomagnetic activity.

The January 2009 presents a unique major SSW event that was very strong and long-lasting. Due to unique conditions during 2009 SSW event there were many observational and theoretical studies that attempted to consider different aspects of the upper atmosphere response to this SSW event [1, 2, 5, 9—13]. Figure 2 summarizes stratospheric and geophysical conditions during the period on January 1—31, 2009 with the episode of the major SSW event that is used for this study. The top two panels of Fig. 2 show stratospheric data from the National Center for Environmental Predictions (NCEP) of conditions at 10 hPa (~ 32 km) for January 2009. During the single record-breaking 2009 sudden stratospheric warming event, stratospheric temperatures at 90°N sharply increased by more than 70 K, while the zonal mean zonal wind at 60°N reversed from westerly (wintertime) to easterly (summertime). The peak warming at the 10 hPa level is reached on 23—24 January 2009.

As a database for the given research we use the *F*2 peak critical frequency (*foF*2) and the total electron content values (*TEC*)from the Irkutsk (52.3°N,

104.3°E) and Kaliningrad (54.6°N, 20.0°E) ionosondes and nearest GPS receivers. Here we extract *TEC* data from GIMs and generate the daily files of *TEC* latitudinal profiles for two specific longitudes (105°Eand 15°E) that represent the closest longitudes to Irkutsk and Kaliningrad.

The Global Self-consistent Model of the Thermosphere, Ionosphere, and Protonosphere (GSM TIP) [14] was developed in WD IZMIRAN. The calculation of electric fields recently was modified in [15]. A modified GSM TIP model has already been used to study the ionospheric behavior during geomagnetic storms [6, 16], and the global thermospheric and ionospheric response to 2008 and 2009 SSW events [1, 5, 17]. In the present paper we used the same statements of the problem and summarize all interpretation of the observed ionospheric disturbances during the geomagnetic storms on September 26—30, 2011 and March 17—23, 2015 and 2009 SSW event.

Figure 3 shows the *foF*2 behavior over Irkutsk and Kaliningrad stations from 26 to 30 September 2011 according to the vertical sounding data and the calculation results obtained using the GSM TIP model. Over Kaliningrad only negative disturbances in *foF*2 are formed in the period under consideration both in the calculation results, and in the observation data. Over Irkutsk during the main phase of the geomagnetic storm on September 26, 2011 the positive *foF*2 disturbances are formed in the evening sector, which are replaced by the negative disturbances at night. The negative disturbances occurred on the recovery phase, on September 28, whereas on September 29—30 they are replaced by daytime positive and nighttime negative disturbances in *foF*2. Based on the satisfactory qualitative agreement of the calculation results with the observed data, we are able to explore the formation mechanisms of the ionospheric disturbances on the recovery phase. Figures 4 presents the temporal variations of the latitudinal profiles of the *TEC* disturbances obtained according to GPS observations and disturbances in *TEC*, *foF*2, meridional velocity of the thermospheric wind, $n(O)/n(N_2)$ and $n(N_2)$, calculated in the GSM TIP model during geomagnetic storms on September 26—30, 2011 at the longitude of 105°E.

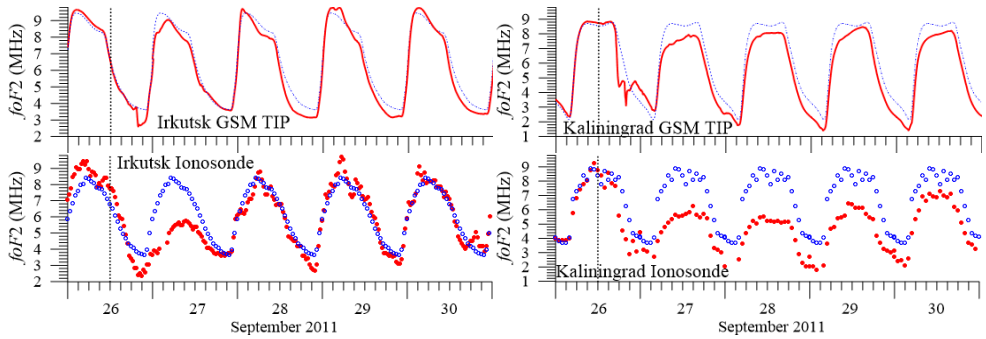

FIGURE 3. Behavior of the *foF*2 above Irkutsk and Kaliningrad during the geomagnetic storm on September 26—30, 2011 (red lines and circles) and in the quiet geomagnetic conditions (blue dotted lines and circles) obtained in the GSM TIP model (top panel) and derived from the ionosonde data (bottom panel).

It can be seen that the disturbances in *TEC* and *foF*2 are similar, but they do not correlate with each other (over the same latitude the disturbances in *TEC* and *foF*2 may have the different signs at the same time). At that the model-calculated *TEC* disturbances are consistent with the observed data. Variations of the meridional thermospheric wind velocity are responsible for the positive disturbances in the middle and subauroral latitudes at the main phase of a geomagnetic storm. The negative disturbances at high and middle latitudes on September 27 and 28 are related to the reduction in the $n(O)/n(N_2)$ ratio in the daytime and with the growth in $n(N_2)$ at night. It should be emphasized the positive disturbances formation in *foF*2 during a recovery phase of the geomagnetic storms at heights of the ionospheric *F* region in the daytime mid-latitude ionosphere by an increase in $n(O)/n(N_2)$.

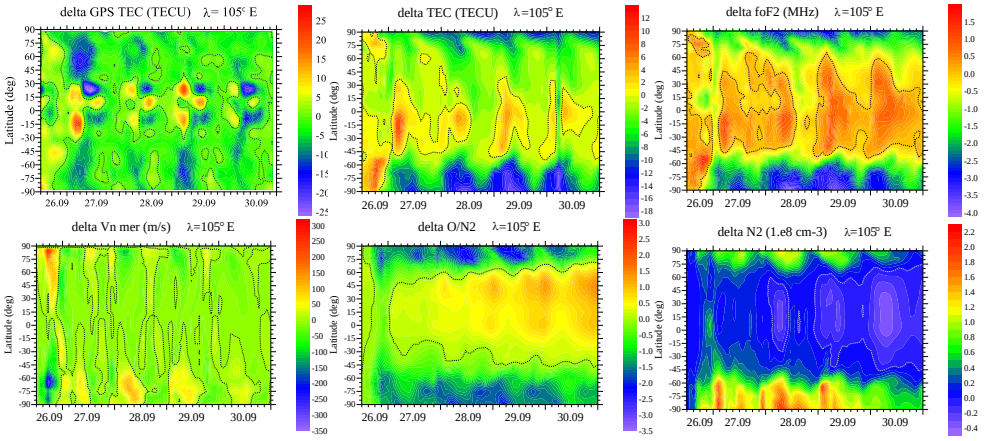

FIGURE 4. Behavior of the GPS *TEC* disturbances, and the GSM TIP model-derived disturbances in *TEC*, *foF*2, meridional velocity of the thermospheric wind, $n(O)/n(N_2)$ and $n(N_2)$ at the height of 300 km during geomagnetic storms on September 26—30, 2011 at the longitude of 105°E.

Figure 5 shows the behavior of the critical frequency of the ionosphere *F*2 layer peak, *foF*2, and total electron content, *TEC*, above the ionospheric stations Irkutsk and Kaliningrad during March 17—23, 2015, according to the GSM TIP model calculation results, digital ionosonde data and data of the GPS receivers. As a reference values of the ionospheric parameters we chose the daily variations for March 15, 2015, when the geomagnetic activity was low. At the initial stage of storm development it led to the formation of the positive ionospheric disturbances over Kaliningrad in the afternoon and in the evening over Irkutsk. An important feature of the ionosphere behavior above Irkutsk and Kaliningrad stations during the recovery phase of a geomagnetic storm on March 21—23, 2015 is the appearance of the positive daytime disturbances in the *foF*2 and *TEC*.

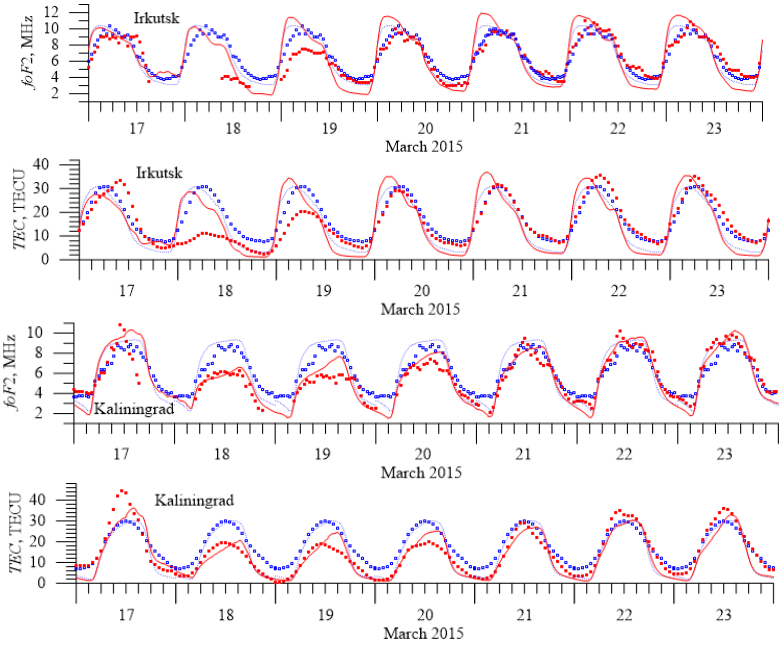

FIGURE 5. Variations of *foF*2 and *TEC* over Kaliningrad and Irkutsk stations according to the ionosonde data and GPS receivers (circles) and model-derived results (lines) during March 17—23, 2015 (red color) comparing with the quiet geomagnetic conditions on March 15, 2015 (blue color).

The calculation results obtained using different atmospheric model output as the lower boundary conditions for GSM TIP model qualitatively reproduce the observed strengthening in the morning upward and occurrence of afternoon downward ***E*×*B*** plasma drift velocity at low-latitudes [5]. However, the magnitude and appearance time of vertical ***E*×*B*** plasma drift disturbances in the model calculations significantly differ from observational data.

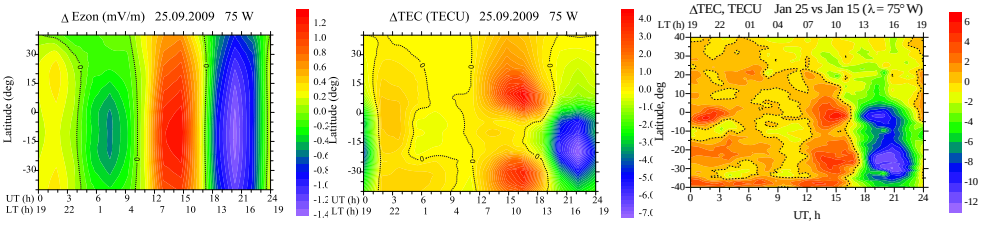

FIGURE 6. Diurnal variations in zonal electric field (left), GSM TIP modeled (middle) and GPS observed (right) -40º-to-40º *TEC* disturbances on 25 January 2009 in American longitudinal sector (75ºW). GSM TIP model results were obtained using TIME GCM model output with additional electric potential which has peak at the equator.

At present we can not exactly specify the underlying cause of discrepancies between low latitude electric fields obtained in GSM TIP model results and observed during 2009 SSW event. However, as an additional step in the present study we have tried to answer the following question: Is it possible to reproduce the *TEC* disturbances observed during SSW 2009 by applying additional electric field in GSM TIP? For this purpose we have set the additional electric potential in its equation in the GSM TIP model at all geomagnetic latitudes in the Magnetic Local Time (MLT) interval

$$6 \le MLT \le 18 \text{ as } \Delta\Phi = \Phi_0 \cdot (1 + \sin(3 \cdot \pi / 2 \cdot (\cdot MLT / 9 - 1))) \cdot \sin^2 \Theta,$$

where $\Phi_0 = -5\,\text{kV}$, Θ is geomagnetic co-latitude. Figure 6 presents the additional (25 vs 15 January 2009) zonal electric field that we obtained using this procedure. The obtained maxima of additional eastward (~1.3 mV/m) and westward (~1.4 mV/m) electric field should produce additional upward and downward electromagnetic drift velocities of the order of ~30 m/s that is very close to Jicamarca observations [2]. Figure 6 shows change in *TEC* that results from the additional electric field, indicating that the model can qualitatively and quantitatively reproduce the observed pre-noon positive and daytime negative *TEC* disturbances in the equatorial ionization anomaly region on 25 January associated with 2009 SSW event (compare to observation).

Results of this study are consistent with conclusions of other researchers that the primary mechanism for the formation of *TEC* disturbances at low latitudes during 2009 SSW event is the perturbation of the zonal electric field (the vertical $\boldsymbol{E}\times\boldsymbol{B}$ plasma drift) [20, 32]. In recent years, several scientific groups using different models and various additional techniques (assimilation, nudges, etc.) attempted to reproduce the observed equatorial electromagnetic drift disturbances, with different level of success [15, 20, 32]. However, it remains an open question: what is the generation mechanism of such zonal electric field disturbances during SSW event and what steps are needed in the development of first-principles models of the atmosphere-ionosphere system that will allow reproducing such electric fields at decision of model equations without any additional artificial sources, nudging and assimilation?

Acknowledgments. *The geomagnetic indices were obtained from http://wdc.kugi.kyoto-u.ac.jp/. These investigations were performed with financial support of the Russian Foundation for Basic Research Grants No. 14-05-00578 and 15-35-20364 and within the project "Physical mechanisms of the reaction of the upper atmosphere and ionosphere on the processes in the lower atmosphere and on the Earth surface" (State task Education and Science Ministry of the Russian Federation, the competitive part of the task No. 3.1127.2014/K).*

1. F. S. Bessarab, Yu. N. Korenkov, M. V. Klimenko et al., Modeling the effect of Sudden Stratospheric Warming within the thermosphere-ionosphere system, *J. Atmos. Solar-Terr. Phys.*, 2012, 90—91, pp. 77—85.

2. J. L. Chau, L. P. Goncharenko, B. G. Fejer et al., Equatorial and Low Latitude Ionospheric Effects During Sudden Stratospheric Warming Events Ionospheric Effects During SSW Events, *Space Sci. Rev.*, 2012, doi: 10.1007/s11214-011-9797-5.

3. N. Balan, Y. Otsuka, M. Nishioka et al., Physical mechanisms of the ionospheric storms at equatorial and higher latitudes during the recovery phase of geomagnetic storms, *J. Geophys. Res.*, 2013, 118, pp. 2660—2669, doi:10.1002/jgra.50275.

4. A. V. Suvorova, A. V. Dmitriev, L.-C. Tsai et al., TEC evidence for near-equatorial energy deposition by 30 keV electrons in the topside ionosphere, *J. Geophys. Res.*, 2013, 118, pp. 4672—4695, doi: 10.1002/jgra.50439.

5. M. V. Klimenko, V. V. Klimenko, F. S. Bessarab et al., Study of the thermospheric and ionospheric response to the 2009 sudden stratospheric warming using TIME-GCM and GSM TIP models: First results, *J. Geophys. Res.*, 2015, 120, doi:10.1002/2014JA020861.

6. M. V. Klimenko, V. V. Klimenko, F. S. Bessarab et al., Influence of geomagnetic storms of September 26—30, 2011, on the ionosphere and HF radiowave propagation. I. Ionospheric effects, *Geomagn. Aeron.*, 2015, 55(6), pp. 744—762.

7. I. Cherniak, I. Zakharenkova, and R. J. Redmon, Dynamics of the high-latitude ionospheric irregularities during the March 17, 2015 St. Patrick's Day storm: Ground-based GPS measurements, *Space Weather*, 2015, 13, doi:10.1002/2015SW001237.

8. D. S. Kotova, M. V. Klimenko, V. V. Klimenko et al., Using IRI and GSM TIP model results as environment for HF radio wave propagation model during the geomagnetic storm occurred on September 26—29, 2011, *Adv. Space Res.*, 2015, 56(9), pp. 2012—2029.

9. L. P. Goncharenko, J. L. Chau, H.-L. Liu et al., Unexpected connections between the stratosphere and ionosphere, *Geophys. Res. Lett.*, 2010, 37, L10101.

10. T. Fuller-Rowell, H. Wang, R. Akmaev et al., Forecasting the dynamic and electrodynamic response to the January 2009 sudden stratospheric warming, *Geophys. Res. Lett.*, 2011, 38, L13102, doi:10.1029/2011GL047732.

11. D. Pancheva and P. Mukhtarov, Stratospheric warmings: The atmosphere—ionosphere coupling paradigm, *J. Atmos. Solar-Terr. Phys.*, 2011, 73(13), pp. 1697—1702.

12. T.-W. Fang, T. Fuller-Rowell, R. Akmaev et al., Longitudinal variation of ionospheric vertical drifts during the 2009 sudden stratospheric warming, *J. Geophys. Res.*, 2012, 117, A03324, doi:10.1029/2011JA017348.

13. H. Jin, Y. Miyoshi, D. Pancheva et al., Response of migrating tides to the stratospheric sudden warming in 2009 and their effects on the ionosphere studied by a whole atmosphere-ionosphere model GAIA with COSMIC and TIMED/SABER observations, *J. Geophys. Res.*, 2012, 117, A10323, doi:10.1029/2012JA017650.

14. Yu. N. Korenkov, V. V. Klimenko, M. Förster et al., Calculated and observed ionospheric parameters for a Magion-2 passage and EISCAT data on July 31, 1990, *J. Geophys. Res.*, 1998, 103(A7), pp. 14697—14710.

15. M. V. Klimenko, V. V., Klimenko, and V. V. Bryukhanov, Numerical modeling of the equatorial electrojet UT-variation on the basis of the model GSM TIP, *Adv. Radio Sci.*, 2007, 5, pp. 385—392.

16. M. V. Klimenko, V. V. Klimenko, K. G. Ratovsky et al., Numerical modeling of ionospheric effects in the middle- and low-latitude F region during geomagnetic storm sequence of 9—14 September 2005, *Radio Sci.*, 2011, 46(3), RS0D03, doi:10.1029/2010RS004590.

17. Yu. N. Korenkov, V. V. Klimenko, M. V. Klimenko et al., The global thermospheric and ionospheric response to the 2008 minor sudden stratospheric warming event, *J. Geophys. Res.*, 2012, 117, A10309, doi:10.1029/2012JA018018.

18. N. M. Pedatella, H.-L. Liu, F. Sassi et al., Ionosphere variability during the 2009 SSW: Influence of the lunar semidiurnal tide and mechanisms producing electron density variability, *J. Geophys. Res.*, 2014, 119, pp. 3828—3843, doi:10.1002/2014JA019849.

The Physical Bases for the Short-Term EarthQuake Precursors Generation

Sergey A. Pulinets

Space Research Institute, Russian Academy of Sciences 117997, Moscow Russia

We can consider this year as a moment of enlightenment: no doubts left in understanding the physical nature of the short-term earthquake precursors (at least at atmosphere and ionosphere domains). All pieces of the puzzle fit one another to compose the complete picture of the Lithosphere-Atmosphere-Ionosphere Coupling (LAIC). We will try to follow how the information and energy are transported from underground to the near-Earth space passing through several interfaces, first of which is Lithosphere-Atmosphere.

Lithosphere-Atmosphere interface. If one will try to imagine how the lithosphere can interact with atmosphere, the natural answer will be — with something of which atmosphere is consisting, i. e. with gases. But how the gases released from the earth's crust know that earthquake is approaching if they are released all the time? It is well known that at the latest stage of the earthquake cycle the deformation is not elastic but brittle what leads to asperities formation opening the new ways of gases migration in the crust. The character of seismic activity described by Gutenberg-Richter relation also called *Frequency-Magnitude Relation* (FMR)

$$log\ N(M) = a - b \cdot M \qquad (1)$$

at the latest stage is characterized by *b*-value drop. Schorlemmer et al. [1] claim that "lower than average *b*-values characterize locked patches of faults (asperities), from which future mainshocks are more likely to be generated". This is the direct indication on the physical interpretation of the FMR. In [2] FMR is interpreted as a power law (fractal) scaling between the number of earthquakes with rupture areas greater than a given value and the rupture area itself, which has a spatial fractal dimension $D \sim 2b$. In [3] the authors interpret the low *b*-values as a probable strong and homogeneous stress field near an asperity. It means that decrease of *b*-value is equivalent to decrease of fractal dimension what can be interpreted as consolidation and clustering of seismic activity (observed experimentally) and increase of cracks formation what leads to higher level of radon emanation before earthquakes. One can compare in the Fig. 1 the *b*-value and fractal dimension D_2 drop before the Kobe M6.9 earthquake on 17 January 1995 in Japan [4] with radon variations [5]. One can see also that the period of increased seismic activity before the Kobe earthquakes starts after the period of seismic quiescence (SQ) when the fractal dimension growth. So we can expect that during periods of decreased *b*-value magnitude the increased release of radon will be observed as it happened before the Kobe earthquake. Unfortunately, there are very few reliable measurements of radon on earthquake prone areas in recent years.

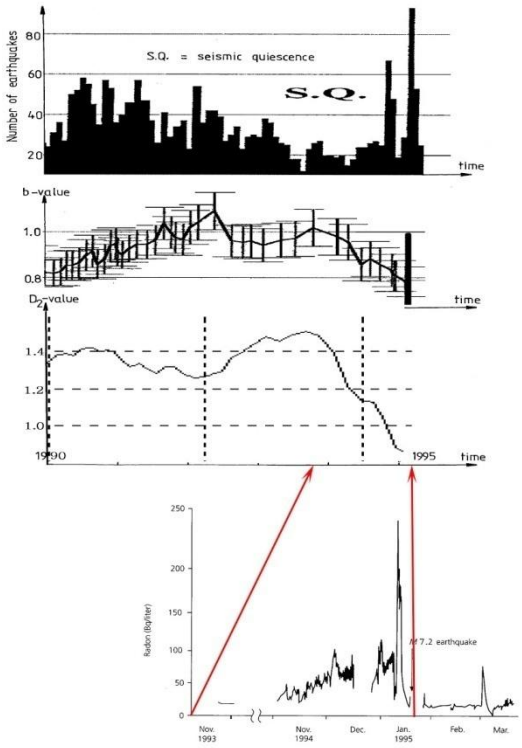

FIGURE 1. From top to bottom: seismic activity in Kobe area for the period 1990—1995; *b*-value variations for the same period of time; fractal dimension D_2 for seismic activity in Kobe area; radon activity (in water) for the period from November 1993, the time correspondence is indicated by arrows.

According to [6] radon is the main source of the boundary layer modification through the ionization. Similarly to the effects of galactic cosmic rays on the condensation nucleus formation [7] radon produces the large hydrated ion clusters leading to formation of thermal anomalies before earthquake and local modifying the electric properties of the Global Electric Circuit (GEC). This we can call the Geochemical interface which transforms the geochemical emanation of radon into the heat generation machine (Geochemical/thermal interface) and background to electromagnetic coupling of atmosphere and ionosphere (Geochemical/electromagnetic interface).

Geochemical/thermal interface. Figure 2 demonstrates schematically the geochemical interface which transforms the radioactive gaseous flux into exothermic reactor. It is shown in [6] that effectiveness of this reactor reaches the value of order of 10^{10}. The source of energy is the water vapor in atmosphere. The energy release depends on the ion production rate and the final size of the hydrated particles. The mentioned above effectiveness is achieved when the particles reach the size of order 1—3 μm.

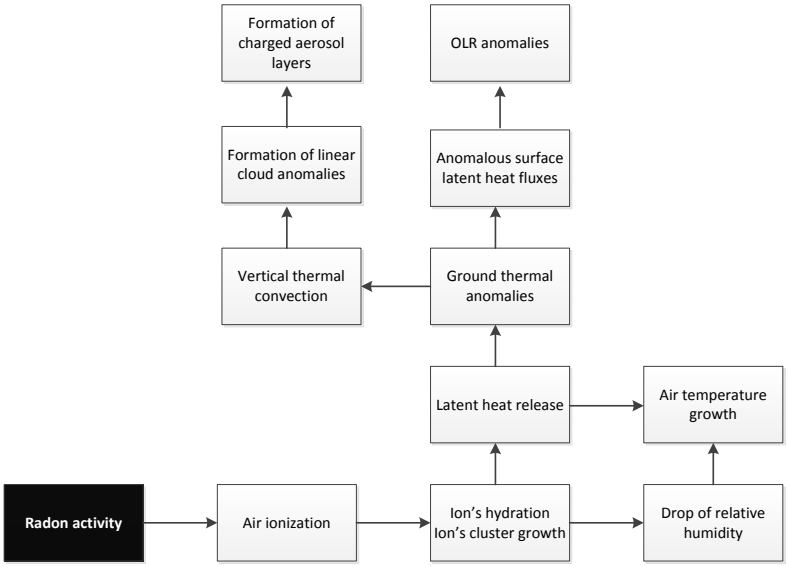

FIGURE 2. Schematic presentation of the geochemical/thermal interface.

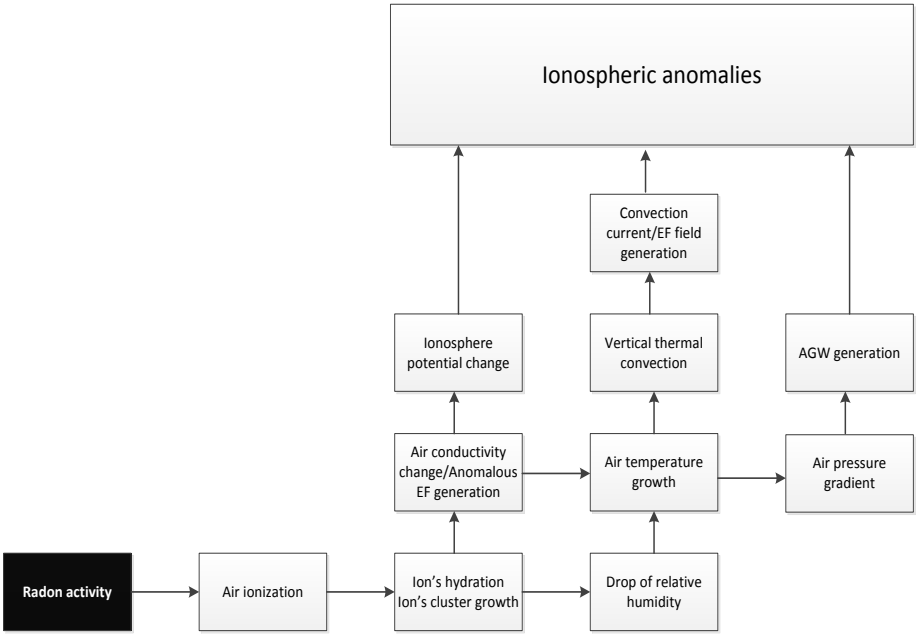

FIGURE 3. Schematic presentation of the geochemical/electromagnetic interface.

Geochemical/electromagnetic interface. The formed large cluster ions reaching the concentration superior than the small ions concentration (sometimes completely removing the light ions) essential change of the boundary layer conductivity what modifies all parameters of the GEC over the earthquake preparation zone leading to the change of ionospheric potential as a final stage of atmosphere-ionosphere coupling and creating the ionospheric anomalies. Two other possible mechanisms could be considered — the direct effect of the anomalous electric field penetration from the ground surface under special conditions of temperature inversion during the night-time and effects of convective currents/fields due to uprising of the charged clusters by thermal convection in the upper layers of atmosphere, their separation due to different mobilities of the positive and negative ions. We leave also the possibility of acoustic gravity waves generation over the large-scale ground surface thermal anomalies but the modern experimental results do not demonstrate any wave activity in ionosphere before earthquake. The schematic presentation of the geochemical/electromagnetic interface is demonstrated in the Fig. 2.

The majority of existing models of the seismo-ionospheric coupling (see their review in [7]) to reproduce the observed experimentally ionospheric anomalies before earthquake introduce manually the zonal electric field or current but cannot say anything on these external fields origin. The proposed geochemical/electromagnetic interface which is the part of the LAIC model [6] provides such opportunity and this mechanism is presented in the Fig.4. where is shown the equatorial ionosphere longitudinal (zonel) cross-section. Geomagnetic field is directed perpendicular to the figure plane.

On initial stages of ionization, and also under weak ionization levels the light ions will prevail in the boundary layer of atmosphere what will lead to the general increase of the bulk conductivity of atmosphere and consecutive decrease of the ionospheric potential relative to the ground (left panel of the Fig. 4). Let it happens during afternoon hours when the east directed electric field is present (white arrows in the figure). The ionosphere is a high conductive media and it will not tolerate the local decrease of potential, it will try to maintain its equipotentiality by creating the field directed to the center of anomaly (grey arrows). In these conditions the “grey field” (artificial) will be added to the “white field” (natural) at the west side from conductivity anomaly, and subtracted to the east side of conductivity anomaly. It means that the level of equatorial anomaly development (ratio of electron concentration in the crests of anomaly to the concentration in the trough of anomaly) will increase to the west from conductivity anomaly, and to the east from conductivity anomaly the equatorial anomaly will be inhibited.

The other opportunity rises if the ionization rate is very high, relative humidity is enough to create the large ion clusters, and calm weather conditions let to form the large clouds of aerosol size heavy ion clusters. In this case we will observe the amplification of equatorial anomaly at the east side from ionization sources, and equatorial anomaly inhibition to the west. The vertical drift velocity is demonstrated by vertical white arrow in ovals, and one can see the difference on both sides of conductivity anomaly.

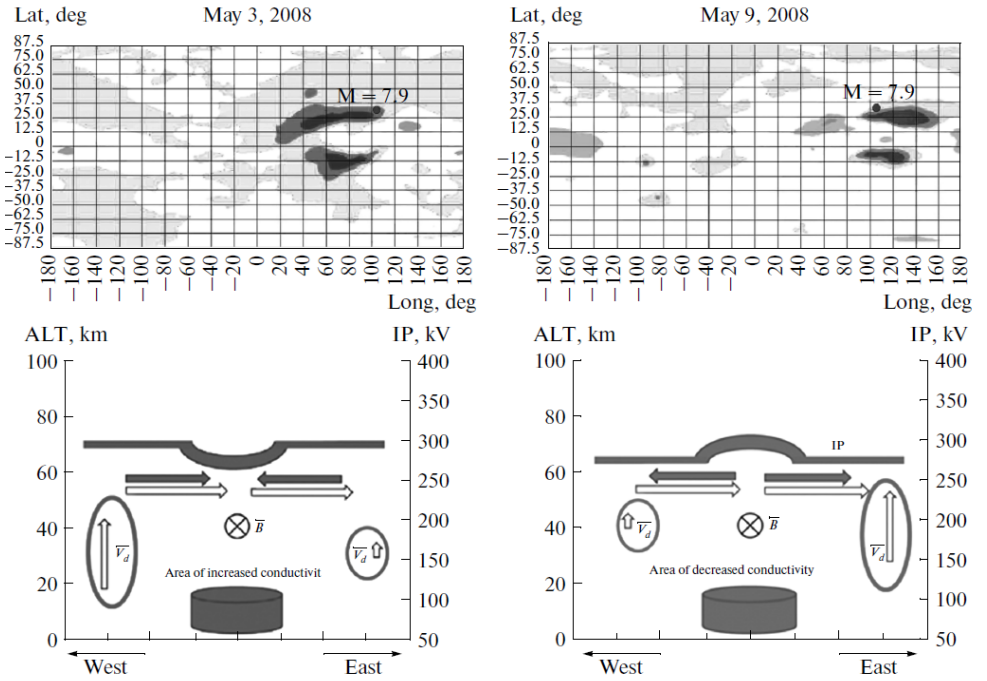

FIGURE 4. Bottom panel — schematic conception of atmosphere-ionosphere coupling through the global electric circuit: left panel — for condition of increased air conductivity, right panel — for condition of decreased air conductivity. Upper panel — the differential maps obtained from the GIM GPS TEC data for the period before the Wenchuan earthquake on 12 May 2009. Left panel — 2D distribution obtained on 3 of May 2009, right panel — 2D distribution obtained on 9 of May 2009.

The most important factor which should be taken into account is that all physical precursors (at least considered within the framework of the LAIC model) are not independent, they are elements of the open complex nonlinear dissipative system. They should be considered from the point of view of synergetics and their comprehensive analysis should reveal the directivity of the process of earthquake preparation, so called “arrow of time” showing approaching of the system to the critical point. Sometimes such directivity could be detected when multiparameter analysis shows the time delays of one parameter uprising in reaction to other showing the temporal chain of the processes. Such chain is demonstrated in the Fig. 5 presenting temporal/altitude development of several precursors before the L’Aquila M6.3 earthquake on 6 April 2009 in Italy. The oblique dashed line in the figure can be interpreted as the arrow of time.

The proposed physical bases give opportunity to realize the multiparameter monitoring consciously and purposefully.

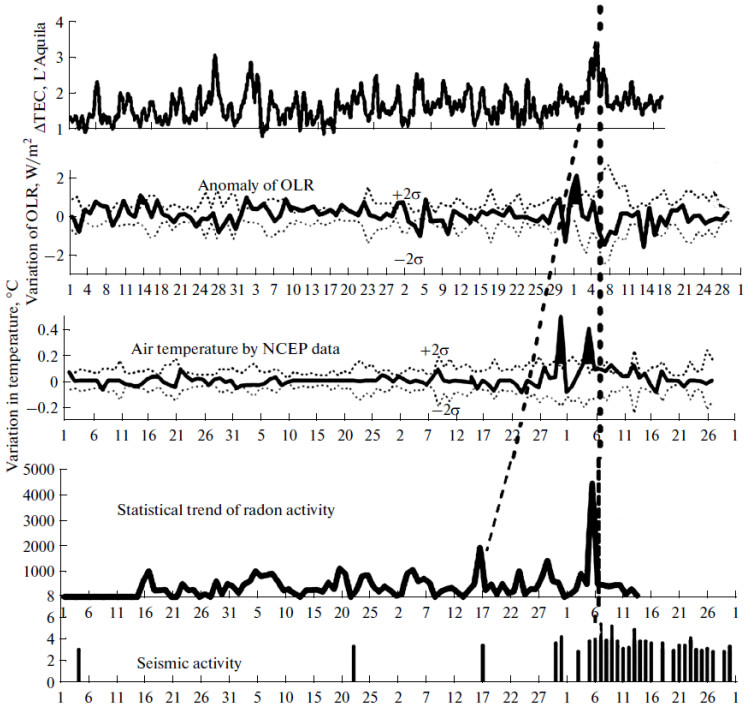

FIGURE 5. Temporal dynamics of radon release and variations of atmospheric and ionospheric parameters before the L'Aquila earthquake.

1. D. Schorlemmer, S. Wiemer, and M. Wyss, Earthquake statistics at Parkfield: 1. Stationarity of b-values, *J. Geophys. Res.*, 109, B12307, doi:10.1029/2004JB003234.

2. D. L. Turcotte, Fractals and Chaos in Geology and Geophysics, Cambridge University Press, Cambridge, 1997, 414 p.

3. D. L. Turcotte and B. D. Malamud, Earthquakes as a complex system, *International Handbook of Earthquake and Engineering Seismology Part A*, Edited by Lee W.H.K., Kanamori H., Jennings P., Kisslinger C., Academic Press, New York, London, 2002, 14, pp. 209—227.

4. B. Enescu and K. Itu, Values of b and p: their Variations and Relation to Physical Processes for Earthquakes in Japan, *Annuals of Disas. Prev. Res. Inst*., Kyoto Univ., 2003, No. 46 B.

5. G. Igarashi et al., Ground-water radon anomaly before the Kobe earthquake in Japan, *Science*, 1995, 269(5220), pp. 60—61.

6. S. A. Pulinets, D. P. Ouzounov, A. V. Karelin, and D. V. Davidenko, Physical Bases of the Generation of Short-Term Earthquake Precursors: A Complex Model of Ionization-Induced Geophysical Processes in the Lithosphere—Atmosphere—Ionosphere—Magnetosphere System, *Geomagn. Aeron.*, 2015, 55(4), pp. 540—558.

7. H. Svensmark et al.,Experimental evidence for the role of ions in particle nucleation under atmospheric conditions, *Proc. Royal Soc. A.*, 2007, 463, pp. 385—396.

8. V. V. Denisenko, Estimate for the strength of the electric field penetrating from the Earth's surface to the ionosphere, *Russ. J. Phys. Chem. B*, 2015, 9, pp. 789—795.

Influence of Precipitating Energetic Particles on Ozone Layer and Climate

Eugene V. Rozanov[1,2]

[1]Institute for Atmospheric and Climate Science, Swiss Federal Institute of Technology (IAC ETHZ), Universittstrasse 16, 8092, Zurich, Switzerland.
[2]Physikalisch-Meteorologishes Observatorium, Davos, World Radiation Center (PMOD/WRC), Dorfstrasse 33, 7260 Davos Dorf, Switzerland

The Earth's atmosphere is continuously bombarded by different energetic precipitating particles (EPP). Their impacts on the atmosphere have been studied for many years, however only recently it was recognized that EPP are able to substantially affect ozone layer and surface climate [1, 2].

The energetic particles can be differentiated according to their origin, energy spectrum, location of the direct impact and connection to solar activity cycle. The properties of main types of precipitating energetic particles are presented in Table 1. More detailed description of different precipitating particles can be found in the extensive review by Mironova et al. [3].

Precipitating energetic particles loss their energy ionizing neutral molecules (mostly N_2 and O_2) in the middle atmosphere. The ionization by all particle types is followed by chemical transformation of neutral constituents leading to additional production of reactive hydrogen ($HO_x = H + OH + HO_2$) and nitrogen ($NO_x = N + + NO + NO_2$) oxides. These species can play a role in several catalytic ozone destruction cycles. For example, ozone destruction by hydrogen oxides is important in the mesosphere while nitrogen oxides play important role in the stratosphere

$$OH + O_3 \rightarrow HO_2 + O_2NO + O_3 \rightarrow NO_2 + O_2$$

$$HO_2 + O \rightarrow OH + O_2NO_2 + O \rightarrow NO + O_2$$

==========

Total: $O_3 + O \rightarrow 2O_2$Total: $O_3 + O \rightarrow 2O_2$

The fate of the additional nitrogen and hydrogen containing radicals produced by energetic particles depends on their lifetime. The effects of short-lived HO_x are very local and observable only right after the event and in the region where the particles deposit the energy, while more stable NO_x could be transported by air motions and their effects are observable out of the production area and with some time shift. This chain of processes has been coined as indirect EPP effect [4]. These effects are the most visible after strong explosive solar proton event (SPE). Figure 1 illustrates the ozone changes after October 2003 SPE measured by MIPAS instrument onboard ENVISAT [5]. The pronounced (up to 80 %) short-term ozone depletion in the mesosphere during the two main ionization events are caused by the additional hydrogen radicals produced by solar protons.

TABLE 1. Characteristics of the different types of energetic precipitating particles.

Type	Auroral electrons	Middle range energy electrons	Relativistic electrons	Solar Protons	Galactic cosmic rays
Origin, source	Solar wind, magnetosphere	Solar wind, radiation belt	Solar wind, radiation belt	Coronal mass ejections	Galaxy, Supernova explosions
Energy range	<30 keV	30—300 keV	300 keV— 2 MeV	1—200 MeV	1—$5x10^{13}$ MeV
Vertical location of the maximum impact	110 km	80 km	60 km	40 km	15 km
Geographic location of the maximum impact	Auroral oval, around 70^o geomagnetic latitude	Subauroral zone, 55^o—75^o geomagnetic latitude	Subauroral zone, 55^o—75^o geomagnetic latitude	Magnetic poles	Magnetic poles
Duration of the events	Almost continuous	Several days	Up to several hours	Several days	Continuous
Connection to the solar activity phase	2—3 years time lag	2—3 years time lag	2—3 years timelag	In phase	In anti phase
Maximal ionization rates(ions/cm^3/s)	30000	5000	10000	30000	500

The depleted ozone area in the upper stratosphere is visible until the end of November 2003 and is caused by NO_x produced by SPE during the main events [5]. The large magnitude of the ozone depletion after strong SPE has weak implications for the long-term mean of the stratospheric ozone or surface climate because the really strong SPE are very rear. During last 15 years there were only about 10 events. Similar effects are observable also after the precipitation of the middle range energy and relativistic electrons from the outer radiation belt. These events are much more frequent and can potentially affect ozone layer and surface climate. However lower signal to nose ratio and pure knowledge of the particle energy spectrum does not always allow clear characterization and attribution of the ozone depletion [6]. The influence of auroral electrons and galactic cosmic rays (GCR) on the ozone layer differs from the SPE and highly energetic electrons. The lower thermosphere where the auroral electrons deposit their energy has virtually no water vapor, therefore the HO_x production does not play a role and the ozone layer is affected only via the downward transport of NO_x [4]. The influence of GCR mostly confine to polar lower atmosphere where their effect on ionization rates is the most pronounced. In this region an additional production of NO_x could lead either to ozone decrease or increase caused by so-called photo-smog reactions (Jackman et al., 2015), which masks the signal from GCR. Therefore, these processes are better visible in the model results because of the possibility to detect relatively weak ozone depletion by comparing experiment (e. g., with aural electrons) against the results of reference model run. Jackman et al. [7] recently discussed the effects of GCR on ozone.

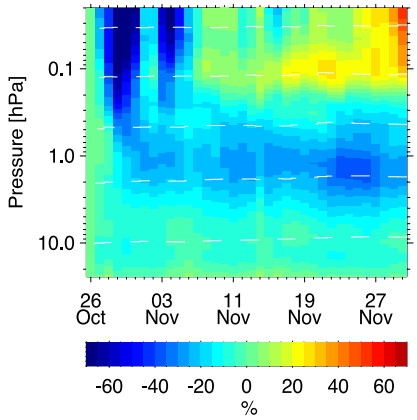

FIGURE 1. Temporal evolution of relative O3 changes with respect to 26 October 2003 in MIPAS observations averaged over 70°—90° N. Figure is reproduced from Funke et al. (2011).

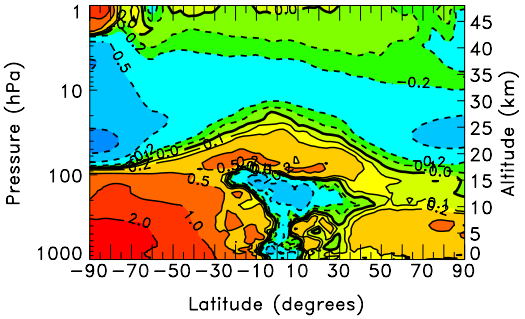

FIGURE 2. Annual average percentage change for year 2009 in zonal mean ozone due to GCR simulated with SD-WACCM. The contour intervals are: 0.1, 0.2, 0.5, 1 and 2 %. Figure is reproduced from Jackman et al. (2015).

Figure 2 illustrates that the GCR tend to destroy ozone in the stratosphere, but increase its amount in the troposphere. The latter is more pronounced in the relatively clean southern hemisphere, where additional NO_x produced by GCR are more efficient ozone precursor, however even in this case the ozone response does not exceed 4 %. Rozanov et al. [8] evaluated combined influence of auroral electrons, SPE and GCR on the ozone using the chemistry-climate model (CCM) SOCOL. Figure 3 illustrates the response of zonal mean ozone (%) to GCR, SPE, and auroral electrons. The most pronounced (up to 10 %) ozone decrease in visible in the polar middle atmosphere above 10 hPa during the cold seasons, however some ozone depletion (up to 4 %) remains even until the warm season. The effects of GCR similar in magnitude and location to the results of Jackman et al. (2015) are also visible and statistically significant.

The ozone depletion can in turn lead to the changes in cooling and heating rates caused by absorption and emission of solar and infrared radiation. During the polar night the infrared component is more important though. The calculations with reference line-by-line codes show that 10 % ozone decrease in the upper stratosphere is enough to provide additional 0.25 K/day cooling inside the vortex area. This cooling increases the temperature gradient between polar and tropical areas leading to the acceleration of the polar night jet, warming of the tropical lower stratosphere, shift of the Hadley sell and appearance of the positive phase of the North Atlantic oscillation [9, 10]. The representative for this case pattern of the surface temperature changes is characterized by a pronounced warming of the Scandinavia,

central par of Russia and North America. This pattern depicted in Fig. 4 has been identified by Seppälä et al. [2] in the reanalysis data comparing surface temperature distribution during boreal winter between years with high and low geomagnetic activity. Similar distribution of the surface temperature changes has been obtained from the CCM experiments described by [1, 8] and attributed to the influence of NO_x produced by EPP.

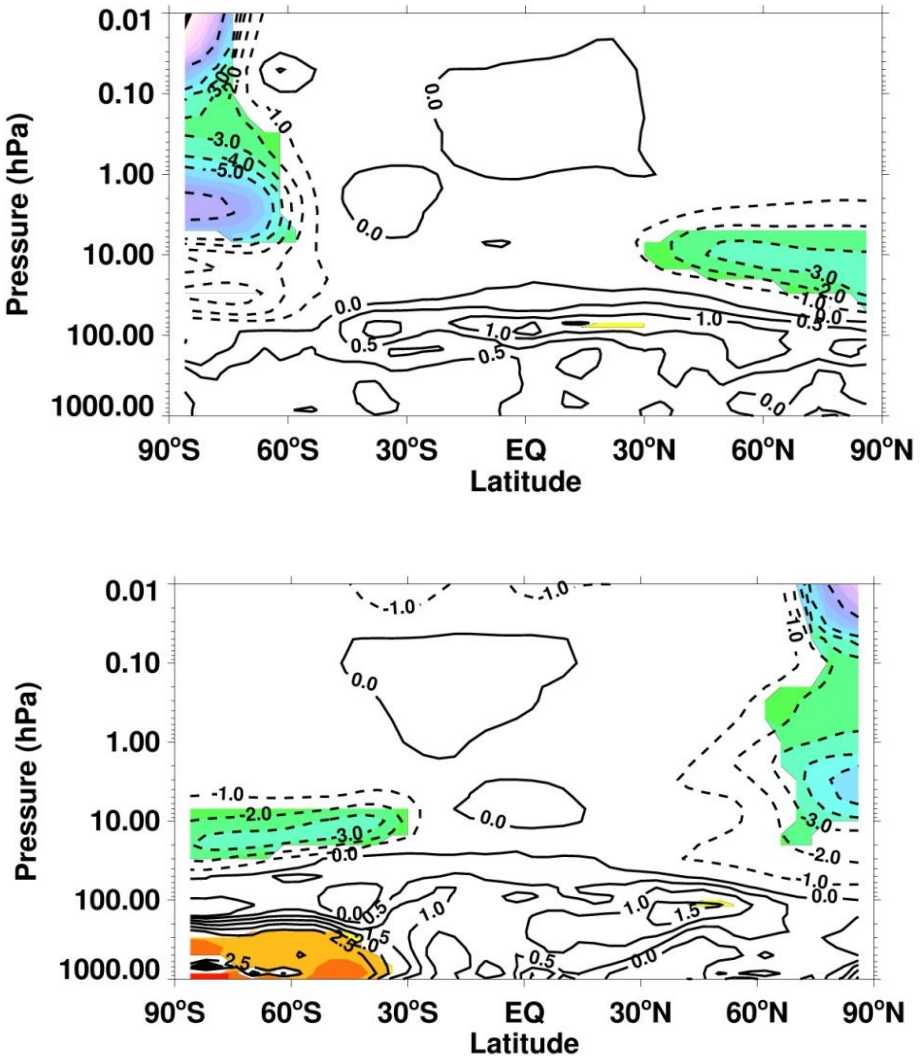

FIGURE 3. DJF (upper panel) and JJA (lower panel) mean response of zonal mean ozone (%) to GCR, SPE, and EEP. Results are averaged from 1960 to 2005. Solid contours indicate positive, dotted contours negative changes. Color pattern indicates the regions where the changes are judged statistically significant at or better than 10 % level.

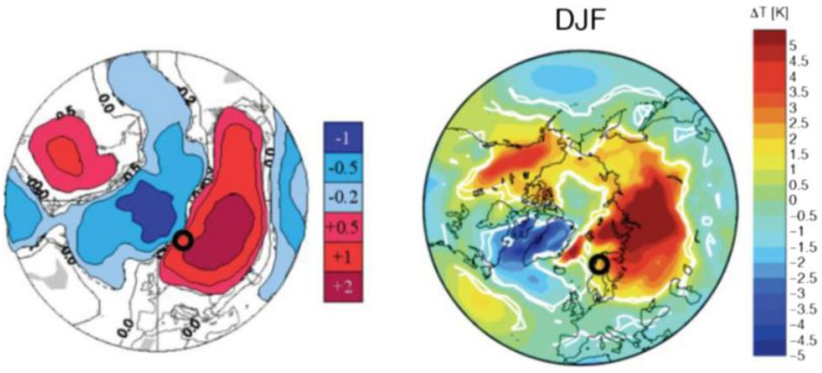

FIGURE 4. Left: Surface air temperature changes in the northern winter hemisphere from model calculation including energetic electron precipitation [1]. Right: Difference between surface air temperatures for the high Ap (geomagnetic activity index) minus low Ap years from 1957 to 2006 [2]. Figure adapted from [11].

The presented results suggest that energetic particles can significantly affect ozone layer and climate during the cold season and should be considered in the models aimed at the study of climate change. A proper treatment of the energetic particles is especially important for the simulation of the future ozone layer and climate in case if widely discussed decline of the solar activity is real [12]. This decrease of the solar magnetic activity is able to weaken the frequency and intensity of the electron precipitation events leading to ozone increase in the polar middle stratosphere and cooling of the northern land masses during cold season. This effect can partly compensate global warming caused by greenhouse gases and the assessment of its magnitude is important for the understanding of future climate.

1. E. Rozanov et al., Atmospheric response to NOy source due to energetic electron precipitation, *Geophys. Res. Lett*., 2005, 32, L14811.

2. A. Seppälä et al., Geomagnetic activity and polar surface air temperature variability, *J. Geophys. Res*., 2009, 114, A10312.

3. I. Mironova et al., Energetic Particle Influence on the Earth's Atmosphere, *Space Science Reviews*, 2015, 194(1), pp. 1—96.

4. C. Randall et al., Energetic particle precipitation effects on the Southern Hemisphere stratosphere in 1992—2005, *J. Geophys. Res*., 2007, 112, D8308.

5. B. Funke et al., Composition changes after the "Halloween" solar proton event: the High-Energy Particle Precipitation in the Atmosphere (HEPPA) model versus MIPAS data intercomparison study, *Atmos. Chem. Phys.*, 2011, 11, pp. 9089—9139.

6. M. Andersson et al., Missing driver in the Sun-Earth connection from energetic electron precipitation impact mesospheric ozone, *Nature communications*, 2014, 5, 5197.

7. C. Jackman et al., Atmospheric changes caused by galactic cosmic rays over the period 1960—2010, *Atmos. Chem. Phys. Disc*., 2015, 15, pp. 33931—33966.

8. E. Rozanov et al., Influence of the Precipitating Energetic Particles on Atmospheric Chemistry and Climate, *Surveys in Geophysics*, 2012, 33(3), pp. 483—501.

9. K. Kodera and Y. Kuroda, Dynamical response to the solar cycle, *J. Geophys. Res.*, 2002, 107, D24, 4749.

10. J. Kidstone et al., Stratospheric influence on tropospheric jet streams, storm tracks and surface weather, *Nature Geoscience*, 2015, 8, pp. 433—440.

11. I. McCrea et al., The science case for the EISCAT_3D radar, *Progress in Earth and Planetary Science*, 2015, 2:21.

12. J. Anet et al., Impact of a potential 21st century "grand solar minimum" on surface temperatures and stratospheric ozone, *Geophys. Res. Lett.*, 2013, 40, pp. 4420—4425.

Ground-Based, Satellite and Rocket Studies of the Polar Cap Patches, Auroral Blobs, and Flow Shears

Wojciech J. Miloch, Andres Spicher, Yaqi Jin, Lasse B. N. Clausen, and Jøran I. Moen

Department of Physics, University of Oslo,Postboks 1048 Blindern 0316 Oslo, Norway

Dynamic phenomena in outer space, i. e., the solar wind, influence the Earth's ionosphere and magnetosphere by momentum and energy transfer, and thereby act on the Earth's near space environment. This is predominantly visible at high (polar) latitudes: increased solar activity can lead to particle precipitation and auroras, geomagnetic storms, and associated phenomena [1]. All these phenomena are a part of space weather and are becoming increasingly important for our technology-based society [2]. Space weather can have a severe impact on man-made infrastructure, with examples being failures of the electric grid, disruption of HF radio communication, or the influence of plasma irregularities on reliability of Global Navigation Satellite Systems (GNSS), such as GPS, GLONASS, or Galileo [2, 3]. Plasma dynamics in the ionosphere are often highly nonlinear and turbulent, where the scales for crucial processes span over orders of magnitude in space and time. This, together with the complexity of the high-latitude ionosphere, makes a thorough and complete description of plasma in the polar ionosphere a challenging task.

GNSS is of increasing importance for operations in the Arctic, but the positioning accuracy is largely dependent on the state of the ionosphere. Irregularities in the ionospheric density modify transionospheric radio waves and lead to signal scintillations [3], which can degrade the quality of signal and degrade communication. Ionospheric scintillations are most severe at high latitudes and in the equatorial region [2—4]. With increasing human activity in the Arctic, space weather effects at high latitudes are of growing importance for shipping, offshore industry, security, and safety.

Most of the processes in the Polar ionosphere involve nonlinear phenomena at kinetic scales, including instabilities and turbulence, and these kinetic scales should be resolved in the measurements. Recently, the technological progress has allowed for insitu experimental studies of the polar ionosphere at the smallest scales with sounding rockets or multi-spacecraft missions. Kinetic scales can now be studied in the context of large-scale, global ionospheric phenomena with concurrent measurements with optical instruments, GPS receivers, and radars at large scales [4—6].

Within the 4DSpace Strategic Research Initiative at the University of Oslo we focus on insitu studies of the ionosphere at high latitudes with sounding rockets, optical measurements and radars. In this work we present some recent results from investigations into the particular phenomena at high latitudes in the Scandinavian sector: polar cap patches, auroral blobs, and reversed flow events.

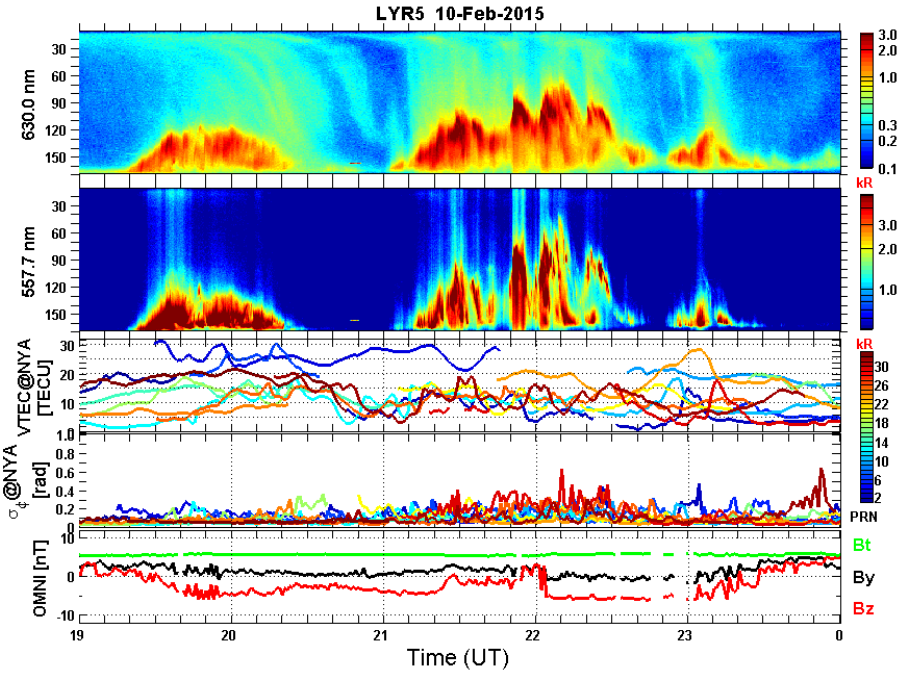

FIGURE 1. (top) The keogram data derived from all-sky imager in Longyearbyen at 630.0 nm and 557.7 nm as a function of the scan angle from 15° North to 165° South. The intensity is given in kR. (middle) The GPS vertical TEC and phase scintillation indices, σ_ϕ from all tracked GPS satellites, which are color coded on the right by their PRN code. (bottom) IMF strength (Bt), By, and Bz from the OMNI dataset.

Polar cap patches are islands of high-density plasma (with a factor of 2 increase with respect to the background plasma density) that are created in the dayside cusp region, in the F layer in the ionosphere, by a combination of particle precipitation

and pulsed intake of high-density solar ionized plasma [1]. They then follow the magnetospheric convection pattern, usually drifting across the polar cap.Most polar cap patches eventually reach the nightside auroral boundary before recombination destroys the elevated plasma density associated with the patch. Polar cap patches are subject to plasma instabilities (most likely the gradient-drift instability) and the resulting irregularities can give rise to scintillations of the GNSS signals. These irregularities are the main scintillations sources poleward of the auroral oval.

Polar cap patches can be studied by optical means using All-Sky-Imagers (ASI) on Svalbard, which are collocated with the receivers of GNSS scintillations [4, 7]. During the polar night, in the dark polar cap winter condition, the polar cap patches can be tracked by using all-sky imagers and meridian scanning photometers (MSP). The monitoring emission line comes from atomic oxygen at the wavelength of 630.0 nm during the recombination process of the dominant O^+ ions. Recent case and statistical studies pin the increased scintillation rate to the polar cap patches in the polar cap [4]. Some of the patches exhibit internal structuring, and hence their whole area, and not only the trailing edge, is subject to the scintillations [7].

When a patch enters into the auroral oval it becomes an auroral blob. Blobs are in general referred to localized enhancement in plasma density. Studies of scintillation sources with ASI and collocated GNSS receivers have shown that blobs due to polar cap patches merging into aurora are the most intense scintillation sources in the Scandinavian sector [7]. This situation is exemplified in Fig. 1, which shows the optical emission from 630,0 nm and 557,7 nm lines as measured by ASI in the keogram format; vertical total electric content (VTEC) and the phase scintillation σ_ϕ for the observed GPS satellites, as well as background conditions of the Interplanetary Magnetic Field (IMF).

Polar cap patches are represented in Fig. 1 as inverted integral signatures poleward from the auroral activity, and are clearly observed in data for 630,0 nm emission line. They propagate southward (and hence the inverted integral sign), and eventually merge with the auroral oval between 21 and 23 UT. This region, when the auroral blobs are formed, is also characterized by the strongest scintillation level σ_ϕ, reaching up to 0.6 rad. Note that the aurora alone does not produce such large scintillations, as it can also be inferred from data around 20 UT in Fig. 1 where σ_ϕ~0.3 rad despite rather strong values for VTEC. In the Scandinavian Arctic sector the following are the most important scintillation sources: auroral ovals, polar cap patches, and then auroral blobs, which are the combination of the two previous phenomena [7].

Ionospheric scintillations are due to decameter size structures and irregularities [2, 3]. In order to investigate the internal structures of the polar cap patches, which are often at small, kinetic scales, insitu measurements at high spatiotemporal resolution are required. Such studies can be carried out with satellites, such as Swarm [8], or with sounding rockets [5, 6, 9]. Sounding rockets give unique possibility to carry out experiment in a targeted manner, and at the same time offer high spatio-

temporal resolution. The ICI-2 sounding rocket, of the Investigation of Cusp Irregularities rocket series, was launched from Ny -Ålesund, Svalbard on 5 December 2008, at 1035 UT in a southwest direction almost parallel to the magnetic field with the goal to study the early evolution of polar cap patches [6]. It reached the apogee after t = 302 s of flight at an altitude h = 328.8 km, thus flying through the ionospheric F-layer. The rocket intersected a polar cap patch as well as several density enhancements, as also shown in Fig. 2(a), and provided high-resolution measurements.

The trailing edges of these density enhancements exhibit strong fluctuations in the density, which are likely to result from gradient drift instabilities. The spectrum of these strong fluctuations is given by a double slope and enhanced power at the regions corresponding to strong density gradients (Figs. 2b-c). For those regions the slope of the spectrum at low frequencies is approximately $p = -1.8$, being rather close to the well-known Kolmogorov spectrum $p = -1.66$. At higher frequencies the slope of the spectrum is given by $p = -3.8$, and the spectral break can be related to the gyro-frequency of O^+ and the onset of kinetic processes [9]. These results agree well with the previous sounding rocket and satellite experiments that were carried out at low latitudes. However, previously the double-slope spectra in the high-latitude ionosphere were not directly observed, presumably due to insufficient resolution. The new instrument, multi-needle Langmuir probe (mNLP) [10] that was flown on ICI-2 rocket allowed for measurements of plasma density with unprecedented resolution, down to kinetic scales. Thus the rocket confirmed that the double-slope spectra of ionospheric plasma irregularities are common also in the high-latitude ionosphere. The results also indicate the role of auroral particle precipitation in creating more turbulent plasma in contrast to the predominant nonlinear wave interaction in the purely gradient drift instability case [5].

Another rocket from the series, ICI-3 sounding rocket, was launched into the dayside region from Ny-Ålesund, Svalbard at 07:21:31 UT on 03 December 2011. While the geomagnetic condition was relatively quiet, the rocket intersected the reversed flow event (RFE) [11, 12], which gave the opportunity to study instabilities related to flow shears. The RFE has been defined by studying plasma with incoherent scatter radars, and as a relatively large structure of 100—200 km width channel where the line-of-sight velocity is greater than 250 m/s in the direction opposite to the background flow. Indeed, the EISCAT radar that was measuring during the rocket campaign, confirmed the occurrence of the RFE and that the rocket intersected it. The data from the radar is shown together with the rocket trajectory in Fig. 3. The data from ICI-3 rocket are characterized by little density gradients, but intense flow shear events and auroral particle precipitation, and show that the previously quasi-static picture of RFE needs to be revised, as the flow channels can be very structured.

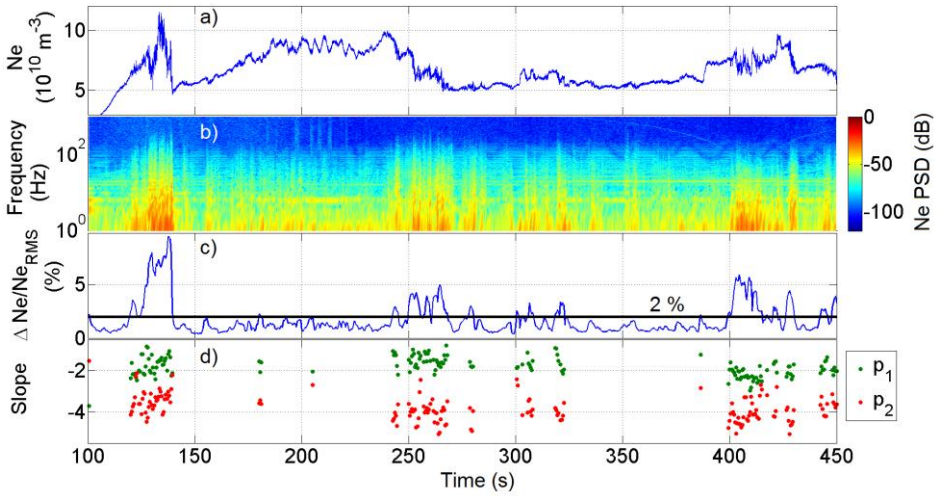

FIGURE 2. (a) The electron density and (b) the corresponding power spectrogram of density fluctuations for the whole flight of the ICI-2 rocket. (c) Relative fluctuations of the plasma density fluctuations, and (c) the corresponding spectral indices indicating regions where double slope spectra were observed.

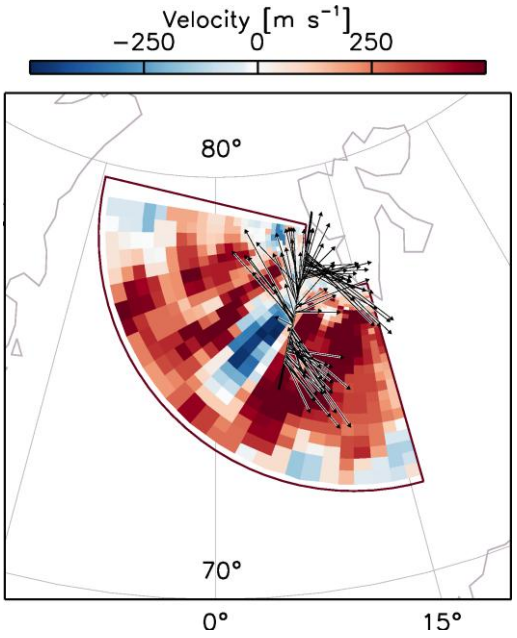

FIGURE 3. The EISCAT Svalbard radar data showing the reversed flow event on 03 December 2011, and the rocket trajectory (black solid line) with arrows indicating the insitu measurements of the velocity. The colors are referring to the ion flow velocity in the line-of-sight of the radar: red show the plasma moving away from the radar, while blue the plasma moving towards the radar. The plot is in geographical coordinate system.

Integrated studies of the ionospheric processes in high-latitude ionosphere with sounding rockets, satellites, and ground-based measurements provide unique possibility of addressing complex geophysical problems in a comprehensive way by addressing multiscale physics with a set of complementary measurements. Multiscale study can be achieved with large scale, ground based measurements and high-resolution studies at medium and kinetic scales by sounding rockets and satellites.

However, plasma turbulence and processes in the ionosphere are three-dimensional problems, and to properly understand them, multi-point studies, and volumetric studies are required. These would be achieved in the future by constellations of satellites, initiatives such as EISCAT3D, and sounding rockets with subpayloads. The latter approach will be tested in summer 2016 during a launch of a rocket with the 4DSpace section, which will eject six subpayloads during the flight. These miniaturized payloads of size ca. 10x6 cm will provide independent, spatially distributed measurements of ionospheric plasma parameters to better understand the physical processes behind the space weather phenomena.

1. M. C. Kelley, The Earth Ionosphere, Amsterdam, 2009.

2. V. Bothmer and I. A. Daglis, Space Weather — Physics and Effects, New York, 2007.

3. P. M. Kintner, B. M. Ledvina, and E. R. de Paula, GPS and ionospheric scintillations, *Space Weather*, 2007, 5(9), 09003; doi:10.1029/2006SW000260.

4. Y. Jin, J.I. Moen, and W.J. Miloch, On the collocation of the cusp aurora and the GPS phase scintillation: A statistical study, *J. Geophys. Res*., 2015,120, pp. 9176—9191.

5. A. Spicher, W.J. Miloch, L.B.N. Clausen, and J.I. Moen, Plasma turbulence and coherent structures in the polar cap observed by the ICI-2 sounding rocket, *J. Geophys. Res. Space Physics*, 2015, 120, doi:10.1002/2015JA021634.

6. A. Spicher, T. Cameron, E. M. Grono et al., Observation of Polar Cap Patches and Calculation of Gradient Drift Instability Growth Times: A Swarm Case Study, *Geophys. Res. Letters*, 2015, 42(2) pp. 201—206, doi:10.1002/2014GL062590.

7. J. I. Moen, K. Oksavik, T. Abe et al., First in-situ measurements of HF radar echoing targets, *Geophys. Res. Lett.*, 2012, 39, L07104, doi:10.1029/2012GL051407.

8. A. Spicher, W. J. Miloch, and J. I. Moen, Direct evidence of double slope power spectra in the high latitude ionospheric plasma, *Geophys. Res. Letters*., 2014,41, pp. 1406—1412.

9. Y. Jin, J. I. Moen, and W. J. Miloch, GPS scintillation effects associated with polar cap patches and substorm auroral activity: Direct comparison, *J. Space Weather Space Clim.*, 2014,4, A23, doi: 10.1051/swsc/2014019.

10. T. A. Bekkeng, K. S. Jacobsen, J. K. Bekkend et al. Design of a multi-needle Langmuir probe system, *Meas. Sci. Technol.*, 2010, 21, 085903.

11. Y. Rinne, J. I. Moen, K. Oksavik, and H. C. Carlson, On the occurrence of reversed flow events in the cusp ionosphere observed by European Incoherent Scatter (EISCAT) Svalbard radar, *J. Geophys. Res.*, 2007, 112, A10313, doi:10.1029/2007JA012366.

12. J. I. Moen, Y. Rinne, H. C. Carlson et al., On the relationship between thin Birkeland current arcs and reversed flow channels in the winter cusp/cleft ionosphere, *J. Geophys. Res*., 2008, 113, A09220, doi:10.1029/2008 JA013061.

Particle Precipitation from Magnetosphere to Atmosphere in High-to-Low Latitudes

Alexander G. Yahnin

Polar Geophysical Institute, Apatity, Murmansk region, Russia, 184209

The magnetosphere consists of different domains, which are connected with atmosphere by the magnetic field lines. The plasma and magnetic properties of these domains significantly differ. Consequently, precipitation in each domain has own mechanism(s). Here, the precipitation producing the ionization of the atmospheric constitutes in different latitudes (from the polar cap to the equator) and altitudes as well as they source domains and assumed mechanisms will be briefly outlined.

Polar rain is "homogeneous" precipitation covering most of the polar cap region. This is the suprathermal component of the solar wind electron population, which can penetrate into magnetotail lobes and reach the polar cap atmosphere propagating along the magnetic field lines. The average energy of these electrons is n*100 eV, and the energy flux varies from 10^{-4} to 10^{-2} mW/m^2. The intensity of the polar rain typically decreases from dayside to night side across the polar cap. The total power carried by this kind of precipitation is of the order of 0.1 GW [1].

Auroral particle precipitation forming the auroral oval originates from the magnetospheric plasma sheet. Simultaneously measured plasma sheet particle spectra show clear differences in protons and electrons. Main electron population has energies 0.1—1 keV, while the energy of the main proton population is 0.1—30 keV. The flux of the main population of electrons is significantly higher than that of the proton population, but at energies >30 keV the proton flux is much higher [2]. The motion of 5—30 keV protons in the equatorial plasma sheet is nonadiabatic (these particles are nonmagnetized in the vicinity of the current sheet, that is, in the weak magnetic field region). Thus, they are scattered into the loss cone and precipitate. In contrast, plasma sheet electrons (0.1—10 keV) are magnetized and fill the loss cone due to the wave-particle interactions. Within the auroral oval the precipitation has energy flux of 1—5 mW/m^2. Overall, electrons are a dominant particle energy source. Protons contribution is ~15 %, but in some regions (equatorward boundary of the evening-side oval, cusp) the proton input is significant in comparison with electrons [3, 4]. The Hall and Pedersen conductance of ionosphere are calculated using the parameters of precipitation. Further, the Joule heating is deduced from the electric field, the Pedersen conductance, and the neutral wind. The diurnal variation observed in the Joule heating is due to the offset between the geographic pole and the geomagnetic pole. The maximum in Joule heating occurs when the area of the auroral oval illuminated by the sun is the largest, that is, when the magnetic pole is located at 12 local time. The average total power

due to plasma sheet electron precipitation is about 20 GW and some 60 % is due to diffuse electron precipitation [5]. During extreme events (substorms) the total power is 60—90 GW. Energy dissipation during substorms is some 300 TJ [6].

Medium energy particle precipitation (E>30 keV) arises from plasma sheet (protons), ring current (protons) and outer radiation belt (electrons). In the ring current and radiation belt, the particle motion is adiabatic, so the loss cone can be filled due to wave-particle interactions. Energetic electron precipitation is mainly due to interaction with whistler mode chorus [7]. Sub-oval precipitation of protons correlates with geomagnetic pulsations in the Pc1 range, which are an indicator of electromagnetic ion-cyclotron (EMIC) waves. Thus, such proton precipitation is the result of interaction of ring current protons with EMIC waves (e. g., [8]). Statistically, maximal fluxes of protons and electrons are at dusk and dawn, respectively. Power of >30 keV particle precipitation is several times less than auroral power, and varies from 0.05—6 GW for electrons and 0.2—2.3 GW for protons.

Relativistic electron precipitation (REP) from the outer radiation belt is typically observed at corrected geomagnetic latitudes 58—68°. There are two major types of REP — microbursts with duration of <1 s and so-called precipitation bands. The latter are spatial structures rather than temporal ones because low-orbiting satellites often observe them at consequent orbits. The latitudinal size of precipitation bands is 0.1—3°. Microbursts are mostly observed in the late morning sector in relation to whistler mode chorus waves [9]. There are several categories of precipitation band events (e. g., [10]). On the night side the precipitation are often produced by scattering of electrons due to violation of the particle motion in the stretched magnetic field [11]. Sometimes, especially in the evening sector, REP correlates with bursts of precipitating protons. This correlation evidences the possibility for relativistic electrons to be scattered by EMIC waves (e. g., [12]). Other REP events can be related to upper hybrid resonance (UHR) waves or plasmaspheric hiss depending on their location outside or inside plasmasphere (e. g., [10] and references therein). Measurements of ~1 MeV precipitating electrons onboard low-orbiting satellites give the energy flux as large as $\sim 5 \cdot 10^{-2}$ mW/m^2.

Energetic neutral atoms (ENA) are an agent depositing energy into atmosphere at more equatorial latitudes. Hot ions of the ring current come into collision with cold exospheric atoms and can become neutral due to charge exchange. Energetic neutrals become non-magnetized and move along straight lines. Some part of such energetic atoms will impact the thermosphere. Before most of kinetic energy is dissipated, the energetic particles can go through many cycles of being neutralized and ionized by charge exchange being trapped and untrapped [13]. If equatorial particles have a 90º distribution, one may expect maximum of ENA precipitation at equator. Isotropic distribution of hot electrons (say, during the main phase of a storm) gives maximum outside equator [13]. Then, due to faster loses of particles with small pitch angles, precipitation will concentrate around equator and decay. This scenario was confirmed using low-orbiting satellite observations [14]. During geomagnetic storms ENA reproduce the dynamics of the ring current and demon-

strate distinct asymmetry during the main phase and becomes symmetric during the recovery phase [15]. The energy flux of ENA was estimated as large as 0.01—0.1 mW/m^2. Keeping in mind the large area of the ENA precipitation during a great storm [15, 16] one can estimate the total power of precipitating ENA as ~0.5 GW.

Since the electrons and protons from different magnetospheric domains have different energies, they produce the ionization and energy deposition at different altitudes (e. g., [17]). The Table below summarizes the main characteristics of different precipitation types.

TABLE 1

	Energy Flux	Total Power	Latitudinal location/ Altitude of the energy deposition	Precipitation mechanism
Polar Rain	(10^{-4}—10^{-2})mW/m^2	0.1 GW	Polar Cap / ~150 km	Penetration of supra-thermal solar wind electrons into the tail lobes
Auroral electrons (Substorm)	(1—5) mW/m^2 (>10 mW/m^2)	(10—35) GW (>100 GW)	Auroral oval / 90—120 km	Scattering by electrostatic waves
Auroral protons	(0.1—0.5) mW/m^2	(2—5) GW	Auroral oval / 110—130 km	Scattering in a weak magnetic field
Electrons >30 keV	(0.01—0.2) mW/m^2	(0.05—6) GW	Sub-oval zone/ 75—100 km	Whistler mode waves
Protons >30 keV	0.05 mW/m^2	(0.2—2) GW	Sub-oval zone/ ~100—110 km	Scattering in a weak magnetic field, EMIC waves
Relativistic electrons	$5\cdot(10^{-3}$—$10^{-2})$ mW/m^2	(0.01—0.1) GW	L=3—6 55—70 km	Scattering in a weak magnetic field, UHR, Whistler mode, EMIC waves
ENA	(0.01—0.1) mW/m^2	(0.1—1) GW	Low latitudes ~100—120 km	Charge exchange with exospheric neutrals

It is worth to note, that estimates of the energy flux and total power presented in the Table are rather crude. They significantly vary depending on many factors including geomagnetic activity, solar wind condition, precipitation area, etc. Some entries in the Table correspond to extreme values.

Particle precipitation provides an important link between magnetospheric plasma domains and atmosphere through the transfer of energy, momentum, influence on the conductivity, Joule heating, etc. The precipitation patterns from different domains differ in the intensity, location, duration, and altitude of the energy

deposition. It seems, however, that no single precipitation type can be neglected to give a full account of the interlink between the Earth atmosphere and its plasma environment.

Acknowledgements. *The work of the author is supported by the Russian Science Foundation grant № 15-12-20005.*

1. P. T. Newell, K. Liou, and G. R. Wilson, Polar cap particle precipitation and aurora: Review and commentary, *J. Atmos. Solar-Terr. Phys.*, 2009, 71, pp. 199—215.

2. S. P. Christon, D. J. Williams, D. G. Mitchell et al., Spectral characteristics of plasma sheet ion and electron populations during disturbed geomagnetic conditions, *J. Geophys. Res.*, 1991, 96(A1), pp. 1—22, doi:10.1029/90JA01633.

3. M. Galand, T. J. Fuller-Rowell, and M. V. Codrescu, Response of the upper atmosphere to auroral protons, *J. Geophys. Res.*, 2001, 106(A1), pp. 127—139, doi:10.1029/2000JA002009.

4. V. G. Vorobjev and O. I. Yagodkina, Comparative characteristics of ion and electron precipitation in the dawn and dusk sectors, *Geomagn. Aeron.*, 2014, 54, pp. 50—58.

5. P. T. Newell, T. Sotirelis, and S. Wing, Diffuse, monoenergetic, and broadband aurora: The global precipitation budget, *J. Geophys. Res.*, 2009, 114, A09207, doi:10.1029/2009JA014326.

6. V. G. Vorobjev and O. I. Yagodkina, Empirical model of auroral precipitation power during substorms, *J. Atmos. Solar-Terr. Phys.*, 2008, 70, pp. 654—662

7. M. M. Lam, R. B. Horne, N. P. Meredith et al., Origin of energetic electron precipitation >30 keV into the atmosphere, *J. Geophys. Res.*, 2010, 115, A00F08, doi:10.1029/2009JA014619.

8. A. G. Yahnin and T. A. Yahnina, Energetic Proton Precipitation Related to Ion-Cyclotron Waves, *J. Atmos. Solar-Terr. Phys*., 2007, 69(14), pp. 1690—1706.

9. K. R. Lorentzen, J. B. Blake, U. S. Inan, and J. Bortnik, Observations of relativistic electron microbursts in association with VLF chorus, *J. Geophys. Res*., 2001, 106(A4), pp. 6017—6027, doi:10.1029/2000JA003018.

10. A. G. Yahnin, T. A. Yahnina, N. V. Semenova, and A. B. Pashin, Morphology of Relativistic Electron Precipitation (this issue).

11. W. L. Imhof, H. D. Voss, J. Mobilia et al., The precipitation of relativistic electrons near the trapping boundary. *J. Geophys. Res.*, 1991, 96, pp. 5619—5629.

12. B. R. Carson, C. J. Rodger, and M. A. Clilverd, POES satellite observations of EMIC-wave driven relativistic electron precipitation during 1998—2010, *J. Geophys. Res. Space Physics*, 2012, 118, pp. 232—243, doi:10.1029/2012JA017998.

13. B. A. Tinsley, Neutral atom precipitation — a review, *J. Atmos. Terr. Phys.*, 1981, 43(5/6), pp. 617—632.

14. M. Sørbø, F. Søraas, K. Aarsnes et al., Latitude distribution of vertically precipitating energetic neutral atoms observed at low altitudes, *Geophys. Res. Lett.*, 2006, 33, L06108, doi:10.1029/2005GL025240.

15. F. Søraas, K. Oksavik, K. Aarsnes et al., Storm time equatorial belt — an ''image'' of RC behavior, *Geophys. Res. Lett.*, 2003, 30(2), 1052, doi:10.1029/2002GL015636.

16. Y. Zhang, L. J. Paxton, J. U. Kozyra et al., Nightside thermospheric FUV emissions due to energetic neutral atom precipitation during magnetic superstorms, *J. Geophys. Res*., 2006, 111, A09307, doi:10.1029/2005JA011152.

17. V. E. Ivanov and B. V. Kozelov, Transport of electron and proton-hydrogen atom fluxes in the Earth atmosphere — Apatity, Published by KSC RAS, 2001.

Ionospheric Effects of Forbidden Energetic Electron Enhancements at Low Latitudes

Alexei V. Dmitriev[1,2], Alla V. Suvorova[1,2]

[1]*Institute of Space Science National Central University, Chung-Li, Taiwan*
[2]*Institute of Nuclear Physics Moscow State University, Moscow, Russia*

Abstract: Strong long-lasting enhancements of energetic particles in the equatorial and low-latitude ionosphere over Pacific were discovered recently. Being forbidden in the theory of radiation belts, the phenomenon of enhancements is still very poorly investigated and not understood. We have found that the energetic particles are injected to the ionosphere from the inner radiation belt. We revealed a significant ionizing effect of the enhancements in positive ionospheric storms. An influence of particle enhancements to low-mid latitude ionospheric scintillations was also found.

Radiation trapped in the innermost magnetosphere at radial distances from the peak of inner radiation belt (RB) to the forbidden zone below RB is believed to have almost stable intensity. The current paradigm of the near-Earth radiation also asserts particle fluxes in the forbidden zone of low latitudes are always of low intensity due to permanent effective scattering and losing the energy in collisions with atmospheric neutrals [1, 2]. The concept is illustrated in Fig. 1 (left), which shows a global distribution of the energetic electrons of >30 keV energy observed by NOAA/POES satellites at heights of ~850 km during a quiet period. At low and equatorial latitudes, the fluxes of electrons are very weak ($<10^2$ (cm^2 s $sr)^{-1}$), excepting a region of South Atlantic Anomaly (SAA), where the inner RB approaches the Earth very closely and, thus, can be observed at low altitudes.

The fluxes of energetic particles with energies of a few tens of keV have been observed at the ionospheric heights in numerous experiments in the past [1]. The phenomenon of energetic electron enhancements in the forbidden zone of low latitudes was known from 1960s and the problem was widely discussed at that time [3—7]. However, information about fluxes and spectra provided by early space experiments was scarce and controversial. From the second spaceship experiment, *Savenko et al.* [5] found sporadic events with unusually large fluxes of ~10 keV electrons within the equatorial ionospheric F-region at ~320 km height outside of SAA, over the Western Pacific region. Later, *Leiu et al*. [8] found flux increases and the appearance of an energy spectrum peak at ~10 keV for precipitating low-energy electrons at ~240 km height during the disturbed period over the Indochina and Pacific regions. However, sparse observations of sporadic events by a single satellite caused strong argument due to a doubt about validity of measured high intensity [1]. As a result of this, further investigation of the phenomenon was not carried out.

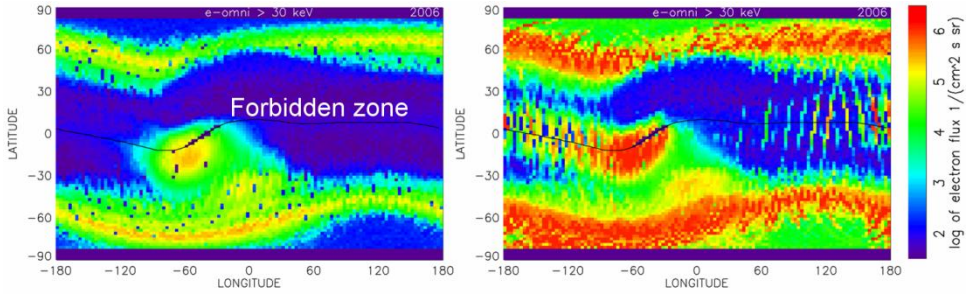

FIGURE 1. Geographic maps of >30 keV electron fluxes during (left) quiet days on 2—4 Dec. 2006 and (right) storm days on 14—16 Dec. 2006. The maps are composed from data retrieved from two orthogonally directed detectors over multiple orbits of the NOAA/POES satellites at 850 km altitude during three days. The solid curve indicates the dip equator. The forbidden zone is indicated near the equator and outside the SAA area (adopted from [9]).

Since the 2000th, when low Earth orbit multi-satellite measurements of radiation have begun, it became possible comprehensive investigations of the energetic particles. We have found a strong dynamics of the energetic electrons in the forbidden zone, or so-called forbidden energetic electrons (FEE) of energy 10—300 keV [9—13]. Namely, FEE fluxes unexpectedly and extremely increase and even achieve a typical RB intensity of ~ 10^6—10^7 electron/(cm^2 s sr) during magnetic storms. Figure 1 (right) shows >30 keV electron fluxes during the 14—16 Dec 2006 storm. The storm-time FEE fluxes increase by 4—5 orders of magnitude that refute completely the previously accepted concept.

Energy flux of enhanced FEE was calculated from the data on electron spectra in energy ranges >30 keV, >100 keV and >300 keV measured by the fleets of the NOAA/POES and DMSP satellites [11]. Also, this allows deriving the energy deposition of FEE in the topside ionosphere. Usually, integral fluxes of the quasi-trapped electrons have steep spectrum, which is softer than within the SAA area (or the inner RB edge). Using approximations by power and exponential laws, we fit the observation and estimate the integral energy fluxes of FEE in the 30—100 keV range from 0.5 to 10 mW/m^2. These values can be even larger if a contribution of lower energy electrons measured by DMSP satellites is accounted for. Equivalent values of produced ionization vary from several to tens of total electron content units (TECU) [11]. Evidently, the energy fluxes brought by enhanced FEE in ionizing process are comparable with the solar EUV irradiance, solar X-flares, and exceed plasmaspheric source effects [14, 15]. For example, the energy flux of solar EUV and X-ray emission during an X17 class solar flare on 28 October 2003 can be estimated of ~9 mW/m^2 [16] and produced an ionospheric enhancement of ~25 TECU at noon [14].

A trajectory of particles in the forbidden zone is shown in Fig. 1. The distinct feature of these "quasi-trapped" particles is that their mirror points are located at heights of a few hundred km and they can make thousands of bounces before they lost their energy in the upper atmosphere (from ~200 to 600 km), i. e. they are lost

during the asimuthal drift around the Earth [2]. Apparently, the quasi-trapped particles of high intensity in the forbidden zone are able to produce ionospheric effects at low and middle latitudes.

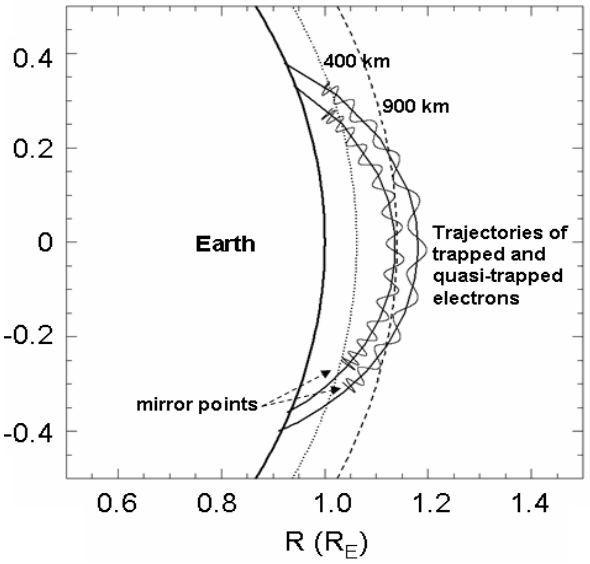

FIGURE 2. Trajectory of quas-trapped particles in the geomagnetic trap.

In general, energetic particles of tens of keV affect the ionosphere through ionization and excitation of atmospheric neutrals as auroral particles do [17], generate the X-ray bremsstrahlung radiation [18—19] and cause different kind of spacecraft malfunctions as radiation belt do [20]. Hence, FEE should produce additional ionisation in the topside ionosphere.

Figure 3 represents a meridional cut of electron content (EC) derived at 04 to 06 UT from COSMIC/FS3 3-D ionospheric tomography in longitudinal range of ~130° to 135°E (~14 LT) where FEE were observed at the same time. Six satellites of COSMIC/FS3 experiment produce a sounding of the ionosphere on the base of radio occultation technique, which makes use of radio signals transmitted by the GPS satellites [21]. Usually over 2500 soundings per day provide ionospheric electron content (EC) height profiles over ocean and land. A 3-D EC distribution is deduced through relaxation using red-black smoothing on numerous EC height profiles around whole globe with a time step of 2 hours and spatial grid of 5° in longitude, 1° in latitude, and 5 km in height [22].

At low latitudes, the EC increased significantly in the topside ionosphere (up to ~700 km). Similar pattern is revealed at other longitudes above Pacific during whole of the main phase and maximum of the geomagnetic storm from 00 to 06 UT, when enhanced fluxes of FEE persisted.

The spatial extension of enhanced ionization at 00 to 06 UT on 15 Dec 2006 is shown in Fig. 4. Global ionospheric maps (GIM) of vertical total EC (VTEC) are provided every 2 hours by a worldwide network of ground-based GPS receivers.

The residual VTEC (dVTEC) was calculated as a difference between the storm and quiet day on 3 Dec 2016.

In Fig. 4, one can distinguish two branches of the VTEC enhancements: at low (~10° to 20° deg) and middle (~30° to 40°) latitudes. The low-latitude positive storm is oriented strictly along the geomagnetic equator at dip latitudes of ~15°. This storm can be explained in the frame of a continuous complex effect of daytime eastward PPEF and equatorward neutral wind [23]. The positive storm at middle latitudes persisted within first 6 hours and then diminished fast after ~06 UT right at the same time as FEE enhancement diminished. The amplitude of mid-latitude ionospheric storm achieved ~20 TECU in the maximum. That is in good agreement with our estimations of the ionizing effect produced by FEE.

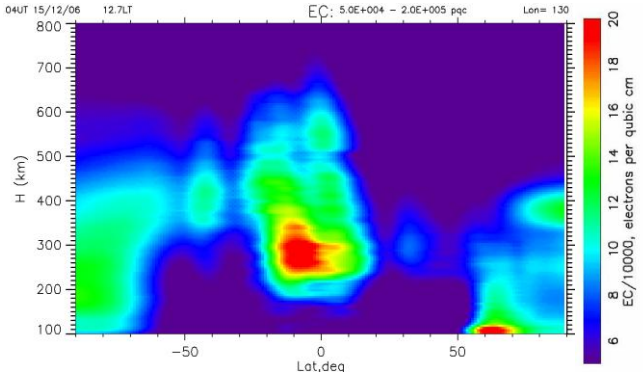

FIGURE 3. Meridional cut of electron content derived from COSMIC/FS3 3-D tomography at 130°—135° longitudes at 04—06 UT on 15 Dec 2006 (from [10]).

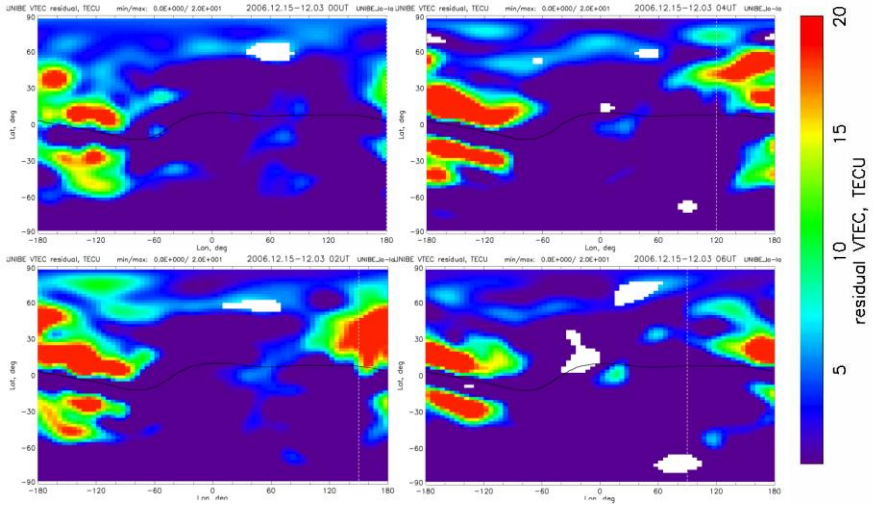

FIGURE 4. Global ionospheric maps of residual VTEC between the quiet day on 3 Dec and storm on 15 Dec 2006 at 00—06 UT. Geomagnetic equator is indicated by black curve. Local noon is depicted by vertical white dashed line (from [10]).

Figure 5 demonstrates temporal variation of the FEE fluxes and residual ionization. One can clearly see that the intense fluxes of quasi-trapped electrons coexist and correlate with the positive ionospheric storm observed at middle latitudes. The low-latitude storm has much longer duration and its maximum occurs later. Hence, the positive ionospheric storm at middle latitudes above Pacific can be produced by intense fluxes of quasi-trapped electrons in the forbidden zone.

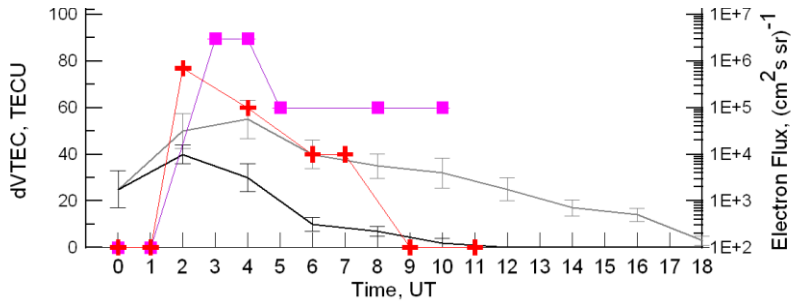

FIGURE 5. Variation of fluxes of >30 keV magnetospheric electrons and ionospheric residual VTEC (dVTEC) during magnetic storm from 00 to 18 UT on 15 December: electron fluxes at ~120° longitude (red), at ~180° (violet), maximum values of dVTEC at middle (black) and low (gray) latitudes (from [10]).

1. G. A. Paulikas, Precipitation of particles at low and middle latitudes, *Rev. Geophys. Space Phys.*, 1975, 13(5), pp. 709—734.

2. L. R. Lyons and D. J. Williams, Quantitative Aspects of Magnetospheric Physics, D. Reidel Pub. Co., Dordrecht Boston, 1984.

3. V. I. Krasovskii et al., The observation of corpuscles by means of the third artificial earth satellite (in Russian), *Iskusstvennye Sputniki Zemli*, 1958, 2, pp. 59—60, (English translation: *Planet. Space Sci.*, 1961, 5, pp. 248—249)

4. V. I. Krasovskii et al., The detection of electrons with energies of approximately l0 keV in the upper atmosphere (in Russian), *Iskusstvennye Sputniki Zemli*, 1961, 6, pp. 113—126, (English translation: *Planet. Space Sci.*, 1962, 9, pp. 27—40).

5. I. A. Savenko et al., Soft particle radiation at an altitude of 320 km in the latitudes near the equator (in Russian), *Iskusstvennye Sputniki Zemli*, 1962, 13, pp. 75—80, (English translation: *Planet. Space Sci.*, 1963, 11, pp. 431—436).

6. W. J. Heikkila, Soft particle fluxes near the equator, *J. Geophys. Res.*, 1971, 76, pp. 1076—1078.

7. S. Hayakawa et al., Existence of geomagnetically trapped electrons at altitudes below the inner radiation belt, *J. Geophys. Res.*, 1973, 78, pp. 2341—2343.

8. R. Lieu et al., Observations of low-latitude electron precipitation, *J. Geophys. Res.*, 1988, 93, pp. 4131—4133.

9. A. V. Suvorova,C.-M. Huang, L.-C. Tsai, A. V. Dmitriev, and K. G. Ratovsky, Long-duration positive ionospheric storm during the December 2006 geomagnetic storm: Ionizing effect of forbidden electrons, *Adv. Space Res.*, 2015, 56(9), pp. 2001—2011, doi:10.1016/j.asr.2015.06.001.

10. A. V. Suvorova, L.-C. Tsai, A. V. Dmitriev, On relation between mid-latitude ionospheric ionization and quasi-trapped energetic electrons during 15 December 2006 magnetic storm, *Planet. Space Sci.*, 2012, 60, pp. 363—369, doi:10.1016/j.pss.2011.11.001.

11. A. V. Suvorova, A. V. Dmitriev, L.-C. Tsai et al., TEC evidence for near-equatorial energy deposition by 30-keV electrons in the topside ionosphere, *J. Geophys. Res. Space Physics*,2013,118, pp. 4672—4695, doi:10.1002/jgra.50439.

12. A. V. Suvorova, C.-M. Huang, H. Matsumoto et al., Low-latitude ionospheric effects of energetic electrons during a recurrent magnetic storm, *J. Geophys. Res. Space Physics*, 2014, doi: 10.1002/2014JA020349.

13. A. V. Suvorova and A. V. Dmitriev, Radiation aspects of geomagnetic storm impact below the radiation belt, *Cyclonic and Geomagnetic Storms: Predicting Factors, Formation and Environmental Impacts*, 2015, Ed. Victoria P. Banks, NOVA Science Publishers, Inc., New York, pp.19—76.

14. B. T. Tsurutani et al., The October 28, 2003 extreme EUV solar flare and resultant extreme ionospheric effects: Comparison to other Halloween events and the Bastille Day event, *Geophys. Res. Lett.*, 2005, 32, L03S09, doi:10.1029/ 2004GL021475.

15. E. Yizengaw et al., The global plasmaspheric TEC and its contribution to the GPS TEC, *J. Atmos. Solar-Terr. Phys.*, 2008, 70, 1541—1548, doi:10.1016/j.jastp.2008.04.022.

16. D. J. Strickland et al., Constraining and validating the Oct/Nov 2003 X-class EUV flare enhancements with observations of FUV dayglow and E-region electron densities, *J. Geophys. Res.*, 2007, 112, A06313, doi:10.1029/2006JA012074.

17. M. H. Rees, Auroral ionization and excitation by incident energetic electrons, *Planet. Space Sci.*, 1963, 11, pp. 1209—1218, doi:10.1016/0032-0633 (63)90252-6.

18. R. A. Goldberg, Rocket observation of soft energetic particles at the magnetic equator, *J. Geophys. Res.*, 1974, 79, pp. 5299—5303.

19. A. Gusev, I. Martin, and G. Pugacheva, The soft X-ray emission of nocturnal atmosphere during the descending phase of the 23rd solar cycle, *Sun and Geosphere*, 2012, 7(2), pp. 127—131.

20. D. N. Baker, Satellite Anomalies due to Space Storms, *Space Storms and Space Weather Hazards, NATO ASI Ser.*, 2001, 38, pp. 79—102.

21. G. A. Hajj, L. C. Lee, X. Pi et al., COSMIC GPS ionospheric sensing and space weather, *Terr. Atmos. Oceanic Sci.*, 2000, 11(1), pp. 235—272.

22. L.-C. Tsai, W. H. Tsai, J. Y. Chou, and C. H. Liu, Ionospheric tomography of the reference GPS/MET experiment through the IRI model, *Terr. Atmos. Oceanic Sci.*, 2006, 17, pp. 263—276.

23. N. Balan et al., A physical mechanism of positive ionospheric storms at low latitudes and midlatitudes, *J. Geophys. Res.*, 2010, 115, A02304, doi:10.1029/2009JA014515.

Linear Temperature Profile in the Mesosphere and Lower Thermosphere and Internal Gravity Waves

Nataliya V. Bakhmetieva, Gennady I. Grigoriev, Ariadna V. Tolmacheva, and Elena E. Kalinina

Radiophysical Research Institute, 25/12a, Bol'shaya Pecherskya St., Nizhniy Novgorod, 603950, Russia

In order to determine of the temperature and density of the neutral component of the lower ionosphere by method based on the creation artificial periodic irregularities in the lower ionosphere [1, 2], we considered the problem of propagation of internal gravity waves in the atmosphere with the linear profile of the equilibrium temperature. We found the original solution of the linearized system of equations for small perturbations of the thermosphere parameters such as pressure, density, temperature and velocity of the medium. We selected sessions from a large array of experimental data in which some profiles of the neutral temperature depending on the height were well approximated by a linear function. The resulting characteristics of internal gravity waves for the temperature profile were compared with the results of measurements of atmosphere parameters. We found a satisfactory agreement of theoretical and experimental values of the obtained quantities that confirms the correctness of the chosen model.

We propose that internal gravity waves (IGWs) of small amplitudes propagate in the atmosphere, and the equilibrium temperature varies with altitude z in accordance to the linear law:

$$T_0(z)=T_s(1+\alpha z), \tag{1}$$

where $dT_0/dz=\alpha T_s$ is the temperature gradient.

The polarization relations for the relative changes in pressure p/p_0, density ρ/ρ_0, temperature T/T_0 and electron density N/N_0 were obtained in the paper [3]. Index "0" denotes unperturbed values of all parameters. These relations are expressed through the vertical component of the velocity $w(z)$ and for disturbances ~ $\exp(-i\,\omega t+ikx)$ can be written as

$$\frac{\rho}{\rho_0}=\frac{i(1+\alpha H_s)w(z)}{\omega H_s(1+\alpha z)},\frac{p}{p_0}=\frac{\omega\rho_s\sqrt{\varepsilon(z)}w(z)}{k^2p_s(1+\alpha z)}, \tag{2}$$

$$\frac{T}{T_0}=\frac{p}{p_0}-\frac{\rho}{\rho_0},u=\sqrt{\frac{\beta}{1+\alpha z}}\cdot w, \tag{3}$$

$$\varepsilon(z) = k^2\left(\frac{\beta}{1+\alpha z} - 1\right), \beta = g(1 + \alpha H_s)/H_s\omega^2. \quad (4)$$

Here ω is the frequency of the wave, k is its wave number, u is the horizontal velocity of the medium under the action of the propagating wave. Index "s" denotes values at the level z=0, H_s is the scale height of the atmosphere.

The vertical wavelength is determined by the formula:

$$\lambda_z = \frac{2\pi}{k}\left(\frac{\beta}{1+\alpha z} - 1\right)^{-1/2}, \quad (5)$$

The formula is essentially the dispersion equation for IGWs in the atmosphere with a linear temperature profile.

The values obtained according to relations (2) and (3) were compared with observed variations of the neutral temperature and the density. For the lower ionosphere studies we used the method based on the resonance scattering of radio waves on the artificial periodic irregularities (APIs), created in the field of the standing wave by heating the ionosphere with powerful HF radio waves [1, 2]. This method of diagnostics of the ionosphere includes the measurement of parameters of the neutral and plasma components of the ionosphere at the mesosphere and lower thermosphere heights. Powerful heating facility SURA creates APIs and then they are probed with short pulses. After the heater switch off APIs destroy. Amplitude and phase of the API scattered signal are measured with high spatial and temporal resolutions at their relaxation stage. It allows us to identify a large number of parameters of the ionosphere and neutral atmosphere in the altitude of 60—120 km with the high accuracy [1, 2]. In the lower thermosphere the API relaxation occurs as a result of the ambipolar diffusion and time decay of the irregularities is determined by the formula $= (K^2D)^{-1}$, where K is the wave number of the powerful standing radio wave and D is the ambipolar diffusion coefficient.

For temperature dependence (1) the API time decay may be written as

$$\frac{\tau_0}{\tau_s} = (1 + \alpha z)^{-2-1/\alpha H}. \quad (6)$$

Note that if the neutral temperature is depend on the height parabolically as $T_0=T_s(1-z^2/L^2)$, we obtain the following formula for τ_0(z):

$$\tau_0 = \frac{\tau_s(1-z/L)^\delta}{(1-z^2/L^2)^2(1+z/L)^\delta}, \delta = L/2H \quad (7)$$

API decay time changes under IGW effect due to variations of the neutral density and the temperature. If the relaxation process of irregularities is determined according to (6, 7), variations of the time decay are given by the formula:

$$\frac{\tau}{\tau_s} = 2\frac{\rho}{\rho_0} - \frac{p}{p_0} \quad (8)$$

For the analysis formula (8), we used data of API experiments carried out 24 September, 2007 when the neutral temperature, the density, the vertical component of neutral velocity and the electron density were determined simultaneously. The altitude profiles and temporal variations of ionosphere and the neutral atmosphere parameters were obtained in the range of height 60—120 km. We selected sessions

of observations in which the undisturbed temperature profiles were close to linear. Wave disturbances with the most typical periods of 20 and 30 minutes were usually observed in temporal variations of the measured parameters. Figure 1 shows the calculated IGW polarization relations for the density (left panel) and the pressure (right panel) perturbations in units $B = \frac{w(1+\alpha H_s)}{\omega H_s}$ and $C = \frac{w\omega}{kV_s^2}$ (V_s is the sound velocity) for two values of β=50 and β=200.

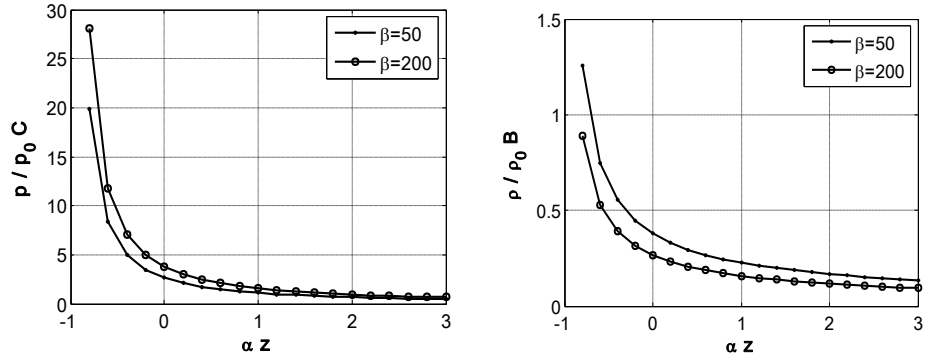

FIGURE 1. Dependences of the density ρ/ρ_0 (left panel) and the pressure p/p_0(right panel) perturbations, calculated according to IGW polarization relations in units B and C.

Table 1summarizes data on variations of measured characteristics relative to their average values using a typical value of the vertical velocity w=1,5 m/s. We used experimental data on the electron density profile measured by the two-frequency API technique [4, 5]. The formula linking the variations of the electron density with the vertical plasma velocity w can be easily obtained and has a form

$$\frac{N}{N_0} = \frac{w}{\omega}\frac{1}{N_0}\frac{dN_0}{dz} \quad (9)$$

Table 1. Variation of the measured and calculated parameters.

Environmental parameters	T, K	ρ, kg·m^{-3}	N, cm^{-3}
Average values	225	1,6·10—^{7}	10^5
Variations relative to average values	0,158	0,150	0,150
The measured relative variations of the parameters	0,110	0,190	0,130

Analyzing table 1, we note the satisfactory agreement of the measured and calculated values based on the adopted model of propagation of internal gravity waves in the lower thermosphere with a linear temperature profile. The velocity u of the horizontal motion and the horizontal component of the phase velocity of the wave were equal to u=21 m/s and V=140 m/s respectively at λ_z=10 km.

For example in the Fig. 2 we show some profiles of the atmosphere neutral temperature. Each of the temperature profiles contains a linear section. Figure 3

shows temporal variations of the neutral temperature and density measured by API technique.

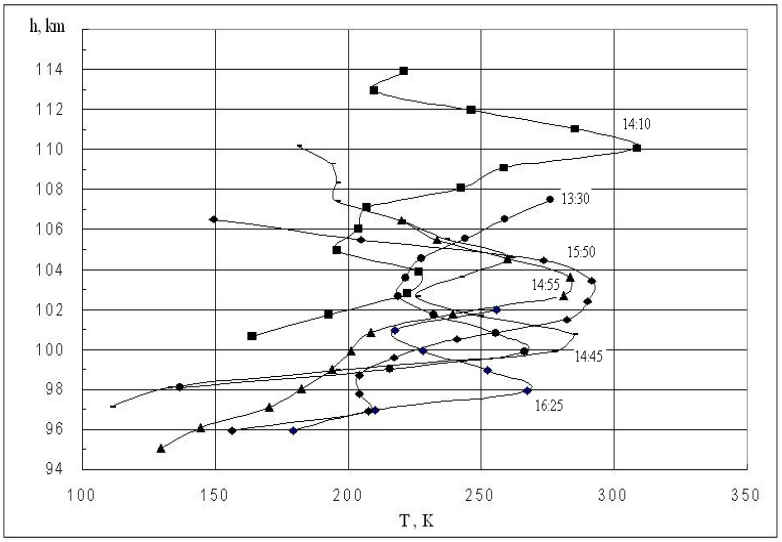

FIGURE 2. There are some profiles of the neutral temperature atmosphere for 24 September, 2007. Note that each profile contains a quasi-linear section.

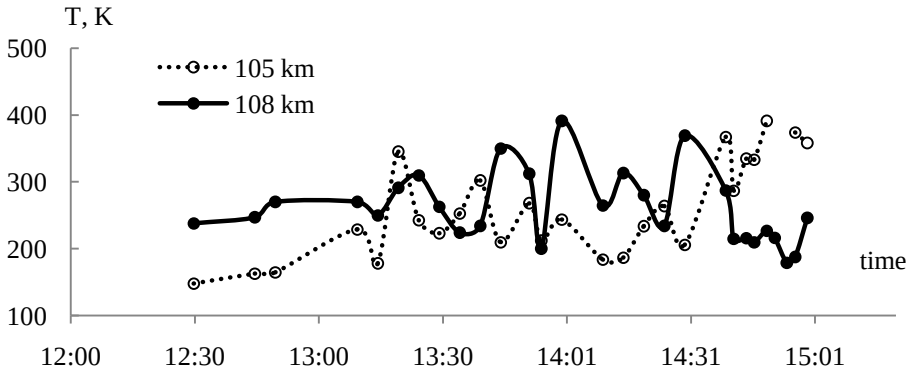

FIGURE 3. Temporal variations of the neutral temperature and density measured by API technique 27.09.2007. One can see wave-like variations of the neutral frequency and density with periods of 20—25 and 60—90 minutes.

In conclusion, we can state the propagation of internal gravity waves in the Earth's atmosphere at altitudes of the lower thermosphere with a linear profile of equilibrium temperature was studied. Experiments to determine the temperature of the neutral components have shown that the temperature gradient can be both positive and negative and its magnitude may vary within wide limits. From a compari-

son of theoretically calculated and experimentally measured values of density, temperature, the relaxation time and the concentration of electrons in terms of wave propagation with a period of about 20 minutes we can conclude about satisfactory compliance of above quantities in the case when the equilibrium temperature depending on the height was close to linear function.

Acknowledgments. *The work was founded in part by Russian Foundation for Basic Research under grants No 14-05-00565. The results of the simulation obtained with the support of the Russian Science Foundation under grant 14-12-00556.*

1. N. V. Bakhmet'eva, V. V. Belikovich, E. A. Benediktov, et al., *Radio Sci.*, 1998, 33(3), pp. 583—595.

2. V. V. Belikovich, E. A. Benediktov, A. V. Tolmacheva, and N. V. Bakhmetieva, Ionospheric Research by Means of Artificial Periodic Irregularities, Copernicus GmbH, Katlenburg-Lindau, 2002, 160 p.

3. N. V. Bakhmetieva, G. I. Grigoriev, A. V. Tolmacheva et al., Gravity waves in the lower thermosphere with linear temperature profile — theory and experiment, *Radiophysics and Quantum electronics*, 2016 (in press)

4. A. V. Tolmacheva, G. I. Grigoriev, and N. V. Bakhmetieva, *Russ.J. Phys. Chem. B*, 2013, 7(5), pp. 663—669.

5. A. V. Tolmacheva, N. V. Bakhmetieva, G. I. Grigoriev, and E. E. Kalinina,*Adv. Space Res.*, 2015, 56(6), pp. 1185—1193.

TEC Dynamics during Sudden Stratospheric Warmings in Arctic Region

Anna S. Polyakova, Anna A. Mylnikova

Institute of Solar-Terrestrial Physics of Siberian Branch of the Russian Academy of Sciences, Irkutsk, Russia

1. Sudden stratospheric warmings in 2006—2013.A sudden stratospheric warming (SSW) is a significant unexpected increase in temperature (up to 50° or more) in the winter polar and subpolar stratosphere. It lasts for several days or weeks and covers most of the hemisphere. Major (strong) warmings are characterized by the reversal of the meridional temperature gradient sign over the hemisphere; besides, the western direction of the stratospheric zonal circulation changes to the eastern one. Weakening or destruction of the circumpolar vortex, determining the dynamics of the polar and subpolar middle atmosphere in winter, is also observed.

It is believed that the SSW development is connected with intensification and penetration of planetary waves to the stratosphere from the troposphere and with their interaction with the western stratospheric flow. This interaction results in the

dissipation of waves and in the release of large amounts of wave energy, which leads to an increase in the stratospheric temperature [1]. In turn, wave activity intensification and significant changes in the atmospheric circulation during SSW periods may have an impact on ionospheric plasma. Various ionospheric effects of SSWs are identified and analyzed in the equatorial [2—4] and mid-latitude [4] regions. According to [5], remarkable abnormality of regular dynamics of the total electron content (TEC) is observed during SSWs in the mid-latitude ionosphere.

Since the state of the unlit winter polar ionosphere under quiet geomagnetic conditions is determined mainly by the dynamics of the neutral atmosphere, it is natural to expect that such large-scale phenomena as SSWs have to influence its behavior. Therefore, the purpose of this work was to study ionospheric disturbances in Arctic region during stratospheric warmings.

In 2006—2013, six major stratospheric warmings occurred in the Northern hemisphere. The peaks (maximums) of these events (day of the zonal wind reverse at a level of 10 hPa) were registered on the following dates:

on January 21, 2006;
on February 24, 2007;
on February 22, 2008;
on January 24, 2009;
on February 9, 2010;
on January 6, 2013.

All SSW events, are usually accompanied by an increase in intensity of stationary planetary waves with zonal number 1 (SPW1) and 2 (SPW2) [6]. The amplitude of SPW1 characterizes the degree of the polar circulation displacement. During stratospheric warmings, prevailed by SPW1, the polar cyclone moves to lower latitudes and the polar anticyclone is formed. The SPW2 amplitude determines the polar vortex splitting. During the events with great SPW2 intensity the circumpolar vortex divides into two alternating pairs of cyclones and anticyclones.

The centers (the region of the most significant increase in the stratospheric temperature) of all the SSWs, except for the warming of 2008/09, were located in the Asian region of Russia. The center of the 2008/09 warming was located over the Northern part of the Atlantic Ocean. Minor SSWs were registered almost every winter.

It should also be noted that the years chosen for the study were characterized by a relatively low solar and geomagnetic activity; geomagnetic disturbances were not recorded during the periods of the maximum development of the SSWs under consideration.

2. TEC variations. Analysis of the total electron content variations was carried out using data from the phase dual-frequency GPS/GLONASS receivers [7] located in the area under study. The series of vertical TEC were calculated from the initial data with the method described in [8].

The method uses the model of TEC measurements, which is, in essence, a classical second-order Taylor series expansion of vertical TEC ($I_V(\varphi, l, t)$) at station coordinates in space (φ_0, l_0) and time:

$$I_m = S_j^i \left[I_V(\varphi_0, l_0, t_0) + G_\varphi \Delta\varphi_j^i + G_{q_\varphi} \left(\Delta\varphi_j^i\right)^2 + G_l \Delta l_j^i + G_{q_l} \left(\Delta l_j^i\right)^2 + G_t \Delta t_j^i + G_{q\_t} (\Delta t_j^i)^2 \right] + I_{DCB,j},$$

where $G_\varphi = \partial I_V / \partial \varphi$, $Gl = \partial I_V / \partial l$, $G_{q\_\varphi} = \partial^2 I_V / \partial \varphi^2$, $G_{q\_l} = \partial^2 I_V / \partial l^2$ are linear and quadratic spatial TEC gradients; $G_t = \partial I_V / \partial t$ and $G_{q\_t} = \partial^2 I_V / \partial t^2$ are the first and second time derivatives. Here, mixed spatial and time derivatives are neglected. I_{DCB} is a contribution of differential code biases, S^i_j is the oblique factor.

Figures 2 and 3 present the examples of the TEC distributions obtained at high-latitude stations NRIL (88.36°E, 69.36°N) and TIXI (128.86°E, 71.63°N), correspondingly, in January-February of 2006, 2010, 2012 and 2013 years. Variations of geomagnetic AE index are depicted on each panel by white line. On each panel of the Fig. 2 and 3 the local time (LT) is scaled vertically, while days from January to February are scaled horizontally.

Figures 2 and 3 indicate, that a decrease in the TEC daily maximum and a slight increase in the nighttime TEC is observed during the warming development. After the SSW peak, TEC is increasing considerably during 5—6 days: daytime *Iv* values are almost twice as high as TEC magnitudes registered before the warming peak. The TEC behavior is the same during the periods of other major SSWs, except for the events that took place in late winter. The dynamics of TEC during the periods of SSWs is similar for both considered stations.

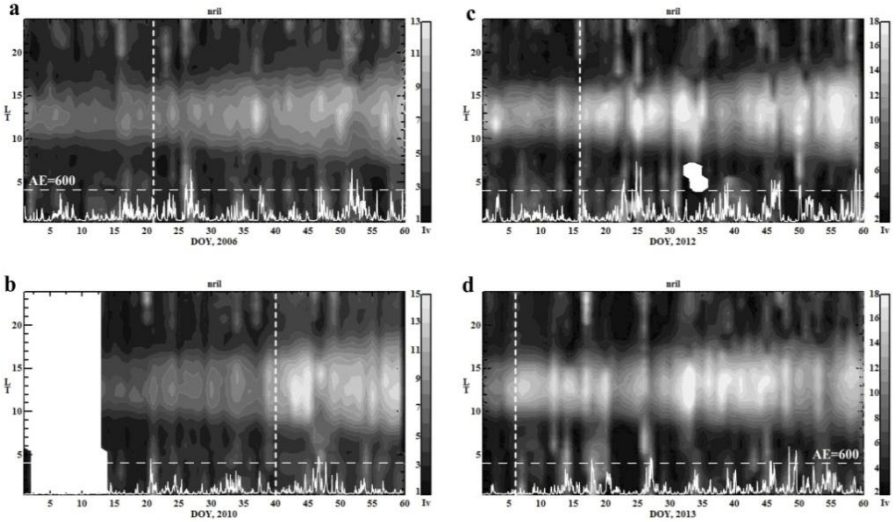

FIGURE 1.TEC dynamics at NRIL station in January-February 2006, 2010, 2012 and 2013. The vertical dotted lines show the SSW peaks. Variations of AE index are depicted on each panel by white line.

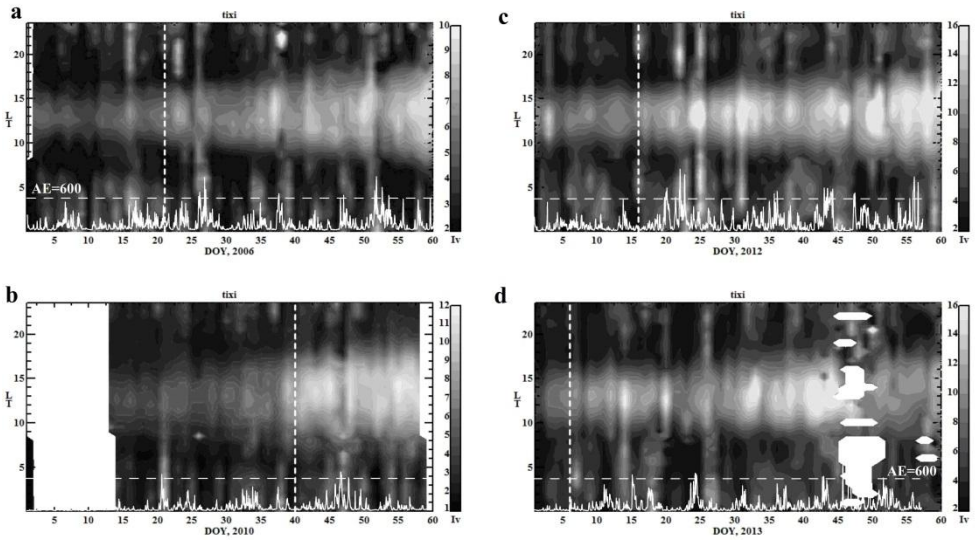

FIGURE 2. The same for Fig. 1 except for the TIXI station.

3. The amplitude of diurnal TEC variations. Due to the low density of GPS/GLONASS receivers in Russia's Asian region, it is difficult to obtain the TEC spatial pattern using only its direct measurements. Therefore, global ionospheric maps (GIM, ftp://cddisa. gsfc. nasa. gov/pub/gps/products/ionex) were used to evaluate the spatial structure of ionospheric disturbances during the periods of SSWs. These maps contain vertical TEC data around the world with a step of 2.5° in latitude and 5° in longitude. Based on these data, distributions of amplitude of diurnal TEC variations were calculated at different longitudes in the latitudinal belt 50—80°N. The amplitude of diurnal TEC variations was calculated as the difference between the daily TEC maximum and minimum. The obtained distributions of the amplitude of diurnal TEC variations at longitude of Norilsk in January-February 2006 and in December-January 2012/13 are shown in Fig. 3.

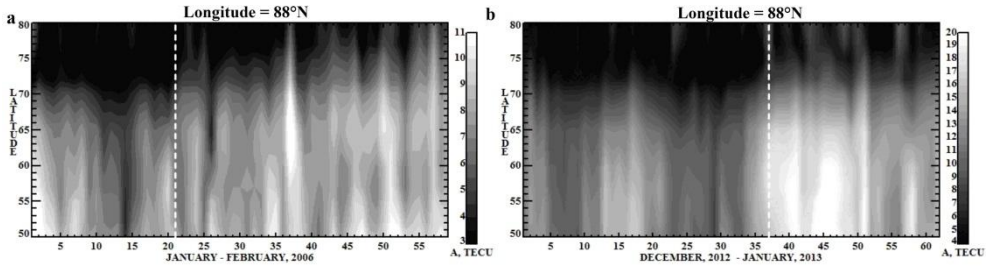

FIGURE 3. The amplitude of diurnal TEC variations at longitude of Norilsk in the latitudinal belt 50—80°N. The vertical dashed lines mark peaks of major SSWs in 2006 (a) and 2012/2013 (b).

The development of warmings is accompanied by a decrease in amplitude of TEC diurnal variations, whereas a considerable increase in amplitude is recorded after the SSW maximum. The difference between the amplitude values before and after the SSW peaks is more than 2 times. Increased values of the amplitude of diurnal TEC variations are observed during 10—15 days. It should also be noted that the changes in the amplitude of diurnal TEC variations are more pronounced at lower latitudes; however, they are clearly observed up to latitudes 75°N.

4. Conclusion. Analysis of the behavior of the high-latitude ionosphere in winters 2006—2013 showed that, despite quiet geomagnetic conditions, significant changes in the ionospheric dynamics are observed during the periods of sudden stratospheric warmings. During the warming development phase, a decrease in diurnal TEC values is observed. On the contrary, the TEC nighttime values slightly increase. This leads to the decrease in the amplitude of diurnal TEC variations. After the SSW peak, a significant growth of the parameters under study is registered for all events. The increase in the amplitude of diurnal TEC variations after the SSW maximum is shown to be observed up to 70—75°N.

Ionospheric effects of SSW may be due to the changes of the vertical transport of molecular gas from the underlying atmosphere to the lower thermosphere, occurring near the SSW center. Besides, they can be due to the alteration of the neutral atmosphere composition, which can affect the electron concentration. Modeling results in[9]showed, that neutral temperature changes in the MLT region lead to a decrease in [$n(O)/n(N_2)$] within the thermosphere that causes electron density changes (similarly to the process during geomagnetic storms). This mechanism explains well the revealed negative TEC response to SSWs at the middle and high latitudes. However, probably mechanisms of the observed TEC increase after the warming peaks require further researches. Dynamics of the ionosphere can also be influenced by the stationary planetary waves, an increase in intensity of which usually accompanies the SSW events.

The work is performed under support of the Russian Foundation for Basic Research grant No.16-35-60018.

1. T. Matsuno, A dynamical model of the Stratospheric Sudden Warming,*J. Atm. Sci.*, 1971, 28, pp. 1479—1494.

2. L. P. Goncharenko, J. L. Chau, H. L. Liu, and A. J. Coster, Unexpected connections between the stratosphere and ionosphere.*Geophys. Res. Lett*., 2010, 37, L10101.

3. S. G. Sumod, T. K. Pant, Jose Lijo et al., Signatures of Sudden Stratospheric Warming on the Equatorial Ionosphere-Thermosphere System, *Planet. Space Sci.*, 2012, 63—64, pp. 49—55.

4. D. Pancheva and P. Mukhtarov,Stratospheric warmings: The atmosphere—ionosphere coupling paradigm, *J. Atm. Solar-Terr. Phys.*, 2011, 73, pp. 1697—1702.

5. A. S. Polyakova, M. A. Chernigovskaya, and N. P. Perevalova, Ionospheric Effects of Sudden Stratospheric Warmings in Eastern Siberia Region, *J. Atm. Solar-Terr. Phys.*, 2014, 120, pp. 15—23, doi: 10.1016/j. jastp.2014.08.011.

6. J. Kuttippurath and G. Nikulin, A comparative study of the major sudden stratospheric warmings in the Arctic winters 2003/2004—2009/2010, *Atmos. Chem. Phys.*, 2012, 12, pp. 8115—8129, doi:10.5194/acp-12-8115-2012.

7.J. M. Dow, R. E. Neilan, and C. Rizos, The International GNSS Service in a changing landscape of Global Navigation Satellite Systems, *J. Geodesy*, 2009, 83(3—4), pp. 191—198.

8. Yu. V. Yasyukevich, A. A. Mylnikova, and A. S. Polyakova, Estimating the total electron content absolute value from the GPS/GLONASS data, *Res. in Phys.*, 2015, 5, pp. 32—33, doi: 10.1016/j. rinp.2014.12.006.

9. M. V. Klimenko, V. V. Klimenko, F. S. Bessarab et al., Study of the thermospheric and ionospheric response to the 2009 sudden stratospheric warming using TIME-GCM and GSM TIP models: First results, *J. Geophys. Res. Space Physics*, 2015, 120.

Modelling of the Influence of Internal Gravity Waves Excited in the Stratosphere during Sudden Stratospheric Warming Periods on the Upper Atmosphere

Pavel A. Vasiliev[1], Ivan V. Karpov[1,2], and Sergey P. Kshevetskii[1]

[1]Immanuel Kant Baltic Federal University, 236004, Nevskogo 14, Kaliningrad, Russia
[2]West Department of Pushkov IZMIRAN, RAS, 236017, Pobedy 41, Kaliningrad, Russia

Abstract. The results of modeling of the influence of internal gravity waves (IGW) excited in the stratosphere during the sudden stratospheric warming (SSW) on the upper atmosphere are presented. A two-dimensional model of propagation of atmospheric waves, taking into account nonlinear and dissipative processes accompanying waves propagation is applied for numerical experiments. The perturbations of the stratosphere temperature and density in the SSW periods are taken as a source of waves. The amplitude and frequency characteristics of the source are taken from the observation results and IGW theory. The results of the fulfilled numerical simulations revealed that the waves arisen at stratospheric heights during the SSW periods can generate temperature perturbations in the upper atmosphere at the altitudes of 100—200 km. The perturbations of the upper atmosphere parameters have influence on dynamics of charged components in the ionosphere and can input an additional contribution to the observed ionospheric effects of SSW.

1 Introduction. Internal gravity waves (IGWs) can be an important mechanism of communication of the lower and upper atmosphere. The propagation of IGW from the lower layers of the atmosphere significantly influences many phenomena in the upper atmosphere and ionosphere [1]. The ionospheric disturbances during periods of sudden stratospheric warming (SSW) are one of examples of realization of such connection of the dynamics of the lower and upper atmospheric layers.

The SSW is a phenomenon of abrupt, up to eighty degrees for a few days, raises the stratosphere temperature at high latitudes. The heated area extends along the latitude and can be up to four thousand kilometers in length, and up to two thousand in width. The SSWs are observed in winter, mostly in the north hemisphere [2]. Up to present, there is large quantity of data about the SSW. At the same time, a complete theoretical description of the origin and evolution of the SSW mechanism isn't created yet. The hypothesis of interaction between zonal wind and planetary waves in the stratosphere is the most common now [3].

Impact on atmospheric processes outside the field of warming is an important feature of SSWs. In particular, the impact of SSW on various ionospheric parameters, such as critical frequency of the F2-layer (of foF2), maximum height (hmF2) and total electron content (TEC) was noted in the studies [4—6]. Data on changes of ionospheric parameters in the lower latitudes, far from the SSW for thousands kilometers are of particular interest [7]. The observations show that the time delay in the appearance of disturbances in the lower atmosphere and ionosphere is negligible compared with the duration of existence of SSW and the periods of planetary waves.

Once can assume that the IGWs excited in the field of emergence of SSW may be a physical process that ensures rapid realization of links of dynamics of the lower and upper atmosphere. In experimental studies, really the data of observations being evidence of intensification of IGW activity during the SSWs are given [8].

The aim of this work is to study the possibility of excitation of IGWs that can propagate into the upper atmosphere and that are generated by stratospheric sources stipulated by perturbation of stratosphere parameters during SSW.

2 Description of the numerical experiment. The numerical experiment was carried out with using of the two-dimensional non-hydrostatic model of the neutral atmosphere. The model was based on solving of full hydrodynamic equations for atmosphere taking into account nonlinear and dissipative processes during wave propagation, as well as interaction between them [9]. Numerical solution of equations for basic parameters of the neutral atmosphere was performed in the area with scales 2,000 kilometers horizontally and 500 km vertically from the Earth's surface. The time-step of simulation was equal 0.3 seconds.

The perturbations of temperature and density corresponding to the observational data of the warming of 2009 were put as a source of wave disturbances. This SSW taken place under the conditions of low solar activity and quiet geomagnetic conditions is well examined. In particular, there are data of lidar sensing of the atmosphere, which allow restoring the temperature profile of the SSW and its deviation from the unperturbed state [10]. On the basis of this information, as well on the basis of data of temporal temperature variations at different altitudes [11], and on the IGW theory [12] we described an appropriate temperature source.

Based on the analysis of observational data [6], two components were picked up in the temperature source. The long-period component corresponds to a SSW, and has a period of 20 days and the amplitude of 80^0K. The short-period component has the amplitude of 70^0 K, the period equals to 30 minutes and a vertical scale of 10 kilometers. The short-period component has the amplitude of 70 K, the period equals to 30 min and the vertical wavelength equals to 10 km.

The source was placed in the simulation domain near the left boundary of the domain in order to track propagation of the wave disturbance in a horizontal direction. It corresponds to modeling of longitude cut of the southern half of the warming. Thus, the temperature source is described by superposition of two oscillatory processes:

$$\Delta T = \exp\left(\frac{x^2}{x_0^2}\right)\left[\sin(\omega_1 t)+\sin(\omega_2 t)\sin(\omega_z z)\right]\exp\left(\frac{(z-z_0)^2}{z_s^2}\right) \qquad (1)$$

where: x_0=500 km; z_0=35 km; z_s=7 km; $\omega_1=3{,}63\cdot10^{-6}$ s^{-1}; $\omega_2=3{,}48\cdot10^{-3}$ s^{-1}; $\omega_z=6{,}28\cdot10^{-4}$ m^{-1}.

In accordance with the IGW theory, a polarization ratio can determine the density perturbation associated with IGW:

$$\frac{\Delta T}{T} = -\frac{\Delta \rho}{\rho} \tag{2}$$

This given perturbation source was running continuously in our numerical experiment, beginning from the simulation start and up to 12 hours.

3. Results of the experiment. This work presents information about the evolution of the temperature and the wave addition thereto.

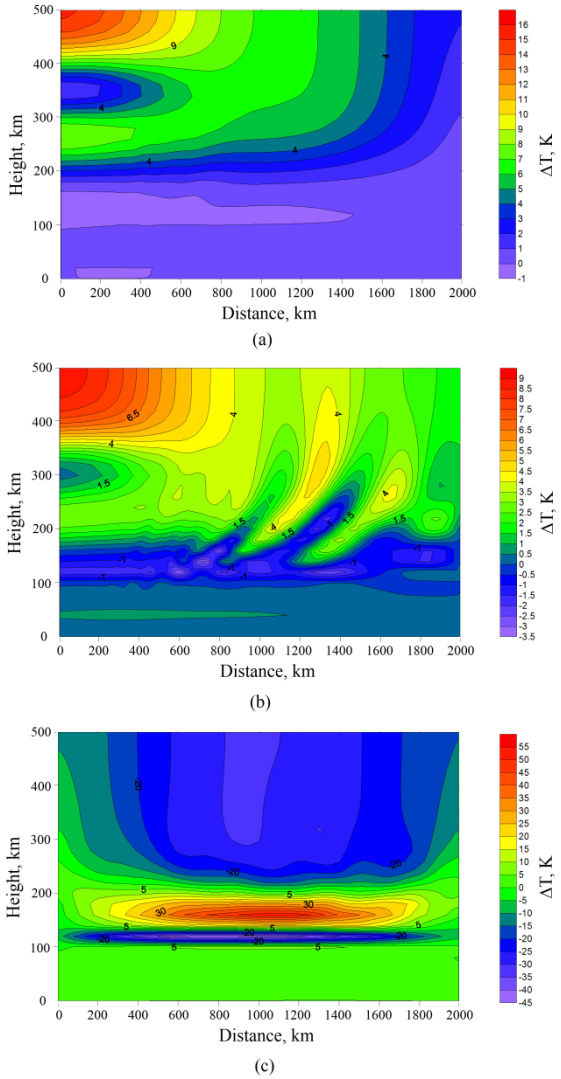

FIGURE 1. Distribution of the wave addition to the temperature in one hour (a), two and a half hours (b) and twelve hours (c) after the beginning of simulation.

In the first stage of simulation, during the first hour of the simulation, there was a transition process. It was heating of the area directly above the source maximum, near the left border of the simulated area (Fig. 1a). Then, in 2.5 h after starting of the simulation, at the altitude higher one hundred kilometers, at the right side of the area, with the horizontal source abroad, some periodic structure begins to form (Fig. 1b), which propagates in time almost into the entire simulation area.

While the simulation progresses, an amplitude of the perturbation is increasing in the range of heights between 100 and 200 kilometers; at the same time the disturbance maximum lies in the area above the source abroad. After ten hours of modeling, the difference between the maximum and minimum of wave additions exceed one hundred degrees, and the disturbance changes its sign with periodicity of a few hours (Fig. 1c).

A periodic process of heating and cooling of the upper atmosphere temperature is observed, which also has a maximum above the area of the source (Fig. 2). Its period is about 3 hours, and the disturbance amplitude is about 40^0—60^0 K.

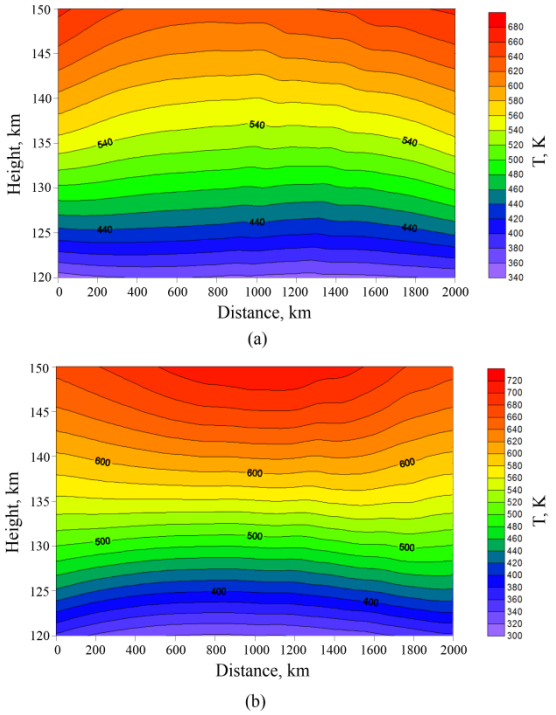

FIGURE 2.Distribution of the background temperature in ten (a) and twelve (b) hours after beginning the calculation.

Thus, as the result of the fulfilled numerical experiment, it is shown that the wave disturbance in the temperature and density arisen at stratospheric heights during SSW periods may cause some changes in the upper atmosphere temperature. These changes take place in the interval of heights of 100—200 km and have maximum lying above the horizontal border of the source.

Such perturbations of the upper atmosphere, in turn, have influence on the dynamics of charged components of the ionosphere E-region and can make additional impact on the observed ionospheric SSW effects. It should be noted that the numerical experiment was fulfilled with a two-dimensional model. Therefore, the results can't fully describe real dynamics of the atmosphere, because taking into account of the Coriolis force is necessary for such a long time of existence of large-scale inhomogeneity. That is, a three-dimensional consideration has to be involved. At the same time, the influence of the stratospheric IGW source on the state and wave activity of the upper atmosphere is beyond doubt and takes place in reality.

This work was supported by the Ministry of Education and Science of Russian Federation (contract 3.1127.2014/K) and RFBR grant 15-05-01665.

1. I. V. Karpov and S. P. Kshevetskii, Formation of large-scale disturbances in the upper atmosphere caused by acousdtic gravity wave sources on the Earth's surface, *Geomagn. Aeron.*, 2014, 54(4), pp. 553—562.

2. Y. Harada, A. Goto, H. Hasegawa et al., A major stratospheric sudden warming event in January 2009, *J. Atmos. Sci.*, 2010, 67, pp. 2052—2069, doi: 10.1175 / 2009JAS3320.1.

3. K. Labitzke and M. Kunze, On the remarkable Arctic winter 2008/2009, *J. Geophys. Res*., 2009, 114, D00I02, doi: 10.1029 / 2009JD012273.

4. D. Pancheva and P. Mukhtarov, Stratospheric warmings: The atmosphere-ionosphere coupling paradigm, *J. Atmos. Sol.—Terr. Phys.*, 2011, 73, pp. 1697—1702.

5. A. S. Polyakova, M. A. Chernigovskaya, and N. P. Perevalova, Ionospheric effects of sudden stratospheric warmings in eastern Siberia region, *J. Atmos. Sol.—Terr. Phys*., 2014, 120, pp. 15—23.

6. B. G. Shpynev, D. Pancheva, P. Muchtarov et al., Ionosphere response over eastern Siberia during the 2009 sudden stratospheric warming derived from data of ground based and satellite radio sounding, *Current problems in remote sensing of the earth from space*, 2013, 10(1), pp. 153—163.

7. S. G. Sumod, T. K. Pant, Jose Lijo et al., Signatures of Sudden Stratospheric Warming on the Equatorial Ionosphere-Thermosphere System, *Planetary and Space Sci.*, 2012, 63—64, pp. 49—55.

8. L. Wang and M. J. Alexander, Gravity wave activity during stratospheric sudden warmings in the 2007—2008 Northern Hemisphere winter, *J. Geophys. Res.*, 2009, 114, D18108.

9. S. P. Kshevetskii, Modeling of Propagation of internal Gravity Waves in Gases, *Computational Mathematics and Mathematical Physics*, 2001, 41(2), pp. 273—288.

10. N. S. Erokhin, N. N. Zolnikova, and L. A. Mikhailovskaya, Features of interaction of gravitational waves with wind-temperature structure of the atmosphere during the propagation in the ionosphere, *Current problems in remote sensing of the earth from space*, 2007, 4(2), pp. 84—89.

11. H. Jin et al., Response of migrating tides to the stratospheric sudden warming in 2009 and their effects on the ionosphere studied by a whole atmosphere-ionosphere model GAIA with COSMIC and TIMED / SABER observations. *J. Geophys. Res.*, 2012, 117, A10323, doi: 10.1029 / 2012JA017650.

12. G. I. Grigoriev, Acoustic-gravity waves in the Earth's atmosphere (review), *Radiophysics and Quantum Electronics*, 1999, 42(1), pp. 3—25.

The Ionospheric Response on Gravity Waves generated by Stratospheric Jet Stream

Denis S. Khabituev, Marina A. Chernigovskaya, Boris G. Shpynev, and Konstantin G. Ratovsky

Institute of Solar-Terrestrial Physics SB RAS, Irkutsk, Russia

Numerous experimental and theoretical studies point to the fact that disturbances in the lower and middle atmosphere can be sources of atmospheric waves which penetrate into the heights of the ionosphere under certain conditions and manifest themselves as traveling ionospheric disturbances (TID) [1, 2]. There were many papers showing a close correlation between wave disturbances in the atmosphere and ionosphere and severe weather phenomena (thunderstorms, tornados, tropical cyclones, cold fronts, etc). Stratospheric jet stream (JS) can be source of atmospheric waves too [3, 4]. It is generally accepted that the winter stratospheric JS is formed as a result of the temperature gradient at the boundary of the polar night. At a boundary between gas flows with different velocities and/or directions (such as, for example, a stratospheric circumpolar vortex (CPV) with high velocities and ambient atmosphere with relatively weak winds), instabilities are formed with atmospheric waves of various scales, including Kelvin waves and IGWs at certain critical wind velocities in the JS [5].

According to the study [6] the gravity potential of descending and cooling stratospheric air is the energy source of circulation in the winter polar stratosphere. This potential transforms into CPV kinetic energy. Inside CPV there exist conditions for generation of baroclinic instability that produces atmospheric waves including internal gravity waves (IGW). These waves can propagate upward to mesosphere, low thermosphere and to ionosphere in some cases. IGWs transfer energy upward and play an important role in instability development and heating of upper atmosphere. However, until now studies dealing with analysis of the ionospheric disturbances caused by the processes in underlying layers of the lower and middle atmosphere are not so numerous compared to the intensive research of heliogeomagnetic effects.

In the present paper, we study the stratospheric JS effects in variations of ionospheric parameters measured in years 2008—2010 with two DPS-4 digisondes: Norilsk (69°N, 88°E; 60°N GLat, 166°E GLon) and Irkutsk (52°N, 104°E; 42°N GLat, 177°E GLon). The Earth ionosphere can be divided into three latitude zones that have rather different properties according to their geomagnetic latitude: low-latitude zone (Glat < 30º), mid-latitude zone (30º < Glat < 60º) and high-latitude zone (Glat > 60º) [7]. From this classification, Irkutsk is a typical mid-latitude station, whereas Norilsk being near a boundary between the mid- and high-latitude

zones combine the properties of both mid- and high-latitude ionosphere. 2008—2010 time interval is featured by long solar activity minimum with low intensity of active events on the Sun and geomagnetic disturbances accompanying them. This essentially facilitated the efficiency in studying the ionospheric disturbances associated with the effect of internal atmospheric processes.

To study the thermo-dynamical structure of the strato-mesosphere we used the ECMWF ERA-Interim reanalysis data (http://www. ecmwf. int/en/research/ climate-reanalysis/era-interim) and Aura MLS satellite data (http://disc.sci.gsfc. nasa. gov/Aura/data-holdings/MLS). Based on the ECMWF ERA-Interim data, we identified periods of strong middle-scale wave-like motions at the heights of the strato-mesosphere between Novembers and Februaries 2008—2010. These wave-like motions were associated with stratospheric JS.

To investigate parameters of middle-scale wave disturbances appeared in winter JS we calculated and analyzed spatial spectrum of vertical velocity of atmospheric gas along all latitudes in Northern Hemisphere. Such spectrum describes zonal wavelength of IGW. The spectral characteristics of the waves generated by winter CPV at the strato-mesospheric heights show two types of wave disturbances.

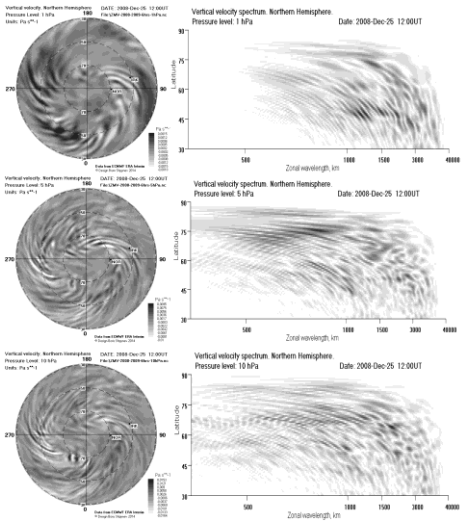

FIGURE 1. Vertical velocity variations and zonal wavelength spectrum in the stratosphere and low mesosphere 25.12.2008.

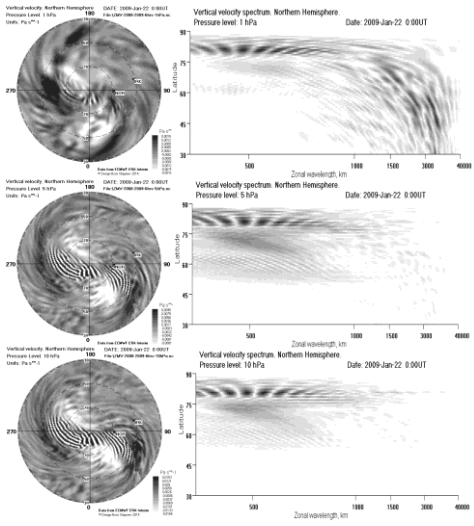

FIGURE 2. Vertical velocity variations and zonal wavelength spectrum in the stratosphere and low mesosphere 22.01.2009.

First type is observed during quiet CPV and is caused by shear-layer instability at JS boundary. Figure 1 (left column) shows the example of zonal wavelength spectrum at three pressure levels 1 hPA (50 km) (top plots), 5 hPA (46 km) (middle plots) and 10 hPA (30 km) (bottom plots) for December 25, 2008. Left maps in

column show IGW structures in latitudinal range 30°-90°N, and right plots show IGW spectral density distributions. We can see that IGWs have wide spatial spectrum and with increasing of height waves with 700—1500 km wavelengths become dominant. In the stratopause-low mesosphere area at altitudes of ~50 km (1 hPa) (top plots) spectrum is shifted to lower frequencies (larger wavelength). This means that IGW with high wavelengths more efficiently penetrate into the upper atmosphere layers, transferring energy from the lower layers. However, we can see also that IGW wavelength is restricted from above by value of ~3500 km, that shows frequency cutoff due to achieving of critical ratio between wave frequency and Brunt-Väisälä frequency which is equal to ~5. Depending on the propagation angle and zonal wind velocity in the stratosphere and mesosphere IGWs can penetrate from the mesosphere into the thermosphere, or reflect from the turbopause at altitudes 85—90 km, or scatter by turbopause due to cascading destruction [8, 9]. Such distribution of the spectral density IGW observed constantly in winter stratosphere, starting from the second decade of November for all years analyzed.

Second type of IGW spectral characteristics reveals during sudden stratospheric warmings (SSW), when the structure of winter CPV is changing dramatically. Figure 2 shows in the same manner as on Fig. 1 the structure of stratosphere during SSW event on January 22, 2009. We can see that along with regular IGWs there appear specific small-scale structures of nonlinear waves ("vortex sheet" or rolls) [6]. Rolls are formed by IGW overturning and manifest themselves as acoustic waves. The energy of these waves is transferred to stratosphere heating and it appears as high temperature regions in polar stratosphere. Zonal wavelengths of vortex sheet are 200—300 km and these structures localize near heating area and do not propagate upward.

Analytical description of waves observed in winter strato-mesosphere can be done on the base of well known dispersion equation for upper atmosphere [10]:

$$k_h^2 + k_z^2 = \frac{k_h^2 \Omega_B^2}{\omega^2} + \frac{\omega^2 - \omega_A^2}{C_0^2} \tag{1}$$

Here Ω_B is Brunt-Väisälä frequency; k_z, k_h are vertical and horizontal component of wave vector; $\omega_A = \sqrt{g\gamma / 4H}$ is acoustic cutoff frequency; γ is the adiabatic factor; H is the scale height; C_0 is sound speed. Second term described acoustic waves corresponded to high frequency vortex sheets showed on Fig. 2 that exist propagate only near the jet-stream active zone. First term corresponds to IGWs and frequency for this type of waves can be estimated as

$$\omega^2 = \frac{\Omega_B^2}{1 + k_z^2 / k_h^2} = \frac{\Omega_B^2}{1 + \lambda_h^2 / \lambda_z^2} \cong \Omega_B^2 \lambda_z^2 / \lambda_h^2 = \Omega_B^2 \cos^2 \theta \tag{2}$$

Actual wave lengths which are observed in ECMWF ERA-Interim data have values λ_h = 1500÷3000 km and λ_z = 5÷10 km, so typical periods of IGWs may be estimated as T = 70÷135 min.

To analyze the influence of the middle atmosphere processes on the ionosphere, we used the coefficient of daytime variations in the *F2* peak electron density (VrN_mF2):

$$VrN_mF2 = 100\% \cdot \sqrt{\left\langle (N_mF2 - \langle N_mF2 \rangle)^2 \right\rangle} / \langle N_mF2 \rangle \quad (3)$$

Here we used the averaging over the period T centered near the local noon. A disturbance of an ionospheric parameter is considered as deviation of the observed value from a regular behavior. The coefficient VrN_mF2 is proportional to N_mF2 variations in the range of periods that do not exceed the averaging period T. If T is of the order of several hours, the VrN_mF2 variation coefficient describes the high-frequency part of the *F2* peak density variability. The high-frequency part of the ionosphere variability (in the range of periods from 0.5 to hours) is mainly caused by the TIDs associated with propagation of IGW. Consequently, the coefficient reflects the IGW activity at heights of the *F2* layer for same IGW periods that we estimate from Era Interim reanalysis data. For the mid-latitude Irkutsk ionosphere data, we used the averaging over the period 09—15 LT. A 6-hour interval corresponds to the daytime duration at the *F2* peak height over Irkutsk in winter. Compared to Irkutsk, the ionosphere above high-latitude Norilsk is partially lighted only for ~4 hours during the daytime at the *F2* peak height in winter. So the Norilsk VrN_mF2 coefficient was calculated for a 4-hour interval (10—14 LT), as well as for a 6-hour interval (09—15 LT) similar to Irkutsk.

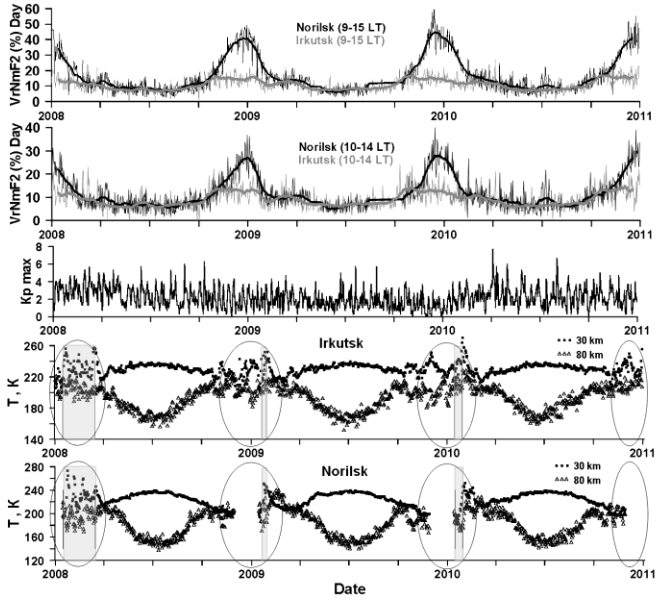

FIGURE 3. Time changes in VrN_mF2 variation coefficient (thin curves) and smoothed VrN_mF2 values (bold curves) by running mean for 27 day interval over Irkutsk and Norilsk for different averaging periods in (1) (top plots); the daily maximum geomagnetic index K_p (middle plot) and Aura MLS temperature data in the daytime at the heights of 30 and 80 km over Irkutsk and Norilsk in 2008—2010.

The upper plots of Fig. 3 present the time changes in VrN_mF2 coefficient over Norilsk and Irkutsk for the years under study. A noticeable increase in the IGW activity was observed at the heights of the *F2* layer during the periods of the increased stratospheric wave activity associated with stratospheric JSs (marked by ovals on the bottom plots of Fig. 3). For both stations, there is a clear seasonal dependence of the high-frequency part (periods from 0.5 to hours) of the N_mF2 variability. The relative TID variability in the summer months for all years analyzed was about the same for both stations. Averaged values of VrN_mF2 are more than doubled in winter compared to the undisturbed summer period. In spite of arising of very intense, long-time, major SSW events covering large part of the Northern Hemisphere in January-February 2008, January 2009 and January 2010 (shown as grey rectangles on the bottom plots of Fig. 3), no significant differences in the VrN_mF2 were observed comparing to the regular winter values (upper plots of Fig. 3). This argues that IGW generation was not a feature of SSW-initiated changing in circulation and it was more likely the own property of JSs.

Ionospheric disturbances can be also due to temperature variations in the middle atmosphere. We analyzed time variations of temperature in the stratosphere (~30 km) and mesosphere (~80 km), using Aura MLS satellite measurement data which provide daytime and nighttime vertical profiles of temperature in the stratosphere and upper mesosphere. During the periods of increased stratospheric wave activity accompanied by a noticeable increase in the IGW activity at the heights of the *F2* layer, significant variations in satellite temperature were observed at heights of the stratosphere and mesosphere.

The VrN_mF2 variability over Irkutsk was much smaller than that over Norilsk during winter regardless of the averaging period.The reasons why the variability coefficients over Norilsk and Irkutsk were different in winter could be associated with the fact that these stations were located under different circulation zones of the winter stratospheric CPVs in the Northern Hemisphere. Besides when discussing the peculiarities in ionosphere response to atmospheric disturbances traveling from below, it is necessary to take into account regular regional features of the ionospheric characteristics from digisonde measurements over the analyzed stations [11, 12].

The CPVs had individual structure every winter and transformed significantly, especially during SSW events. The characteristics of the middle-scale wave motions generated above the CPVs were determined by the stratospheric JS peculiarities. Under certain conditions, these gravity waves could travel upward to the mesosphere, thermosphere, and ionosphere. When GWs reached the thermosphere, they uplifted or lowered molecular species through outflow or inflow of molecular gas from/into the ionosphere. The changes in the composition couldlead to modification of the $[O^+]/[N_2]$ balance, and to variations in ionospheric parameters [13—15].

As a result of the analysis aimed at determining JS effects in variations of ionospheric parameters from vertical sounding at Norilsk and Irkutsk in years 2008—

2010, we made the following conclusions. (1) Based on the ECMWF ERA-Interim reanalysis data, we identified periods of middle-scale wave-like motions in the autumn-winter period (between November and February) for all years under analysis. These wave-like motions were associated with jet streams at the stratosphere/lower mesosphere heights and could be sources of atmospheric gravity waves. (2) The height variations of the vertical velocity spectra showed that these waves propagated as IGWs above the some critical stratosphere height near the stratopause. Below this height the waves decayed as a result of the turbulent cascade process. Region of the generation of the wave-like motions coincided with the zone of interaction of the JSs, located at the different stratosphere heights. (3) Aura MLS temperature measurements confirmed the existence of variations in parameters of the stratosphere and upper mesosphere, which were accompanied by increases in the *F2* layer wave disturbance activity. (4) During the periods of stratospheric wave activity, we observed a significantly increased IGW activity at the ionosphere *F2*-layer above the East Siberia region of Russia according to vertical sounding at Norilsk and Irkutsk for all the years analyzed. (5) A clear seasonal dependence of the high-frequency part of the *F2* peak density variability was observed for all the stations. The largest variability in the ionosphere *F2*-layer was observed in winter and the smallest one in summer. The summer-winter difference was more pronounced in the case of Norilsk.

This study was supported by the RAS Basic Research Program II.16.1.2 and by the RFBR projects No. 15-05-05227 and No. 16-05-01087.

1. K. Hocke and K. Schlegel, A review of atmospheric gravity waves and travelling ionospheric disturbances: 1982—1995, *Ann. Geophys.*, 1996, 14, pp. 917—940.

2. E. Yiğit and A. S. Medvedev, Internal wave coupling processes in Earth's atmosphere, *Adv. Space Res.*, 2015, 55, pp. 983—1003.

3. P. A. Newman and M. R. Schoeberl, Middle atmosphere: Polar vortex, *Encyclopedia of Atmospheric Sciences*, San Diego, Calif.: Academic, 2003, pp. 1321—1328.

4. D. W. Waugh and L. M. Polvani, Stratospheric Polar Vortices, in: *The Stratosphere: Dynamics, Transport, and Chemistry*, Geophys. Monogr.Ser., 2010, Vol. 190.

5. J. T. Abatzoglou and G. Magnusdottir, Wave breaking along the stratospheric polar vortex as seen in ERA-40 data, *Geophys. Res. Lett.*, 2007, 34, L08812.

6. B. G. Shpynev, S. M. Churilov, and M. A. Chernigovskaya, Generation of waves by jet-stream instabilities in winter polar stratosphere/mesosphere, *J. Atmos. Sol. Terr. Phys.*, 2015, 136, pp. 201—215.

7. R. D. Hunsucker and J. K. Hargreaves, The High-Latitude Ionosphere and Its Effects on Radio Propagation, Cambridge University Press, New York, 2003.

8. B. Kaifler, F.-J. Lübken, J. Höffner et al., Lidar observations of gravity wave activity in the middle atmosphere over Davis (69°S, 78°E), Antarctica, *J. Geophys. Res. Atmos*., 2015, 120(10), pp. 4506—4521, doi:10.1002/2014JD022879.

9. K. D. Bossert, C. Fritts, P.-D. Pautet et al., Momentum flux estimates accompanying multiscale gravity waves over Mount Cook, New Zealand, on 13 July 2014 during the DEEPWAVE campaign, *J. Geophys. Res. Atmos.*, 2015, 120(18), pp. 9323—9337.

10. C. O. Hines, Internal gravity waves at ionospheric heights, *Can. J. Phys.*, 1960, 38, pp. 1441—1481.
11. K. G. Ratovsky and A. V. Oinats, Local empirical model of ionospheric plasma density derived from Digisonde measurements at Irkutsk, *Earth, Planets and Space*, 2011, 63(4), pp. 351—357.
12. K. G. Ratovsky, A. V. Oinats, and A. V. Medvedev, Regular features of the polar ionosphere characteristics from Digisonde measurements over Norilsk, *Adv. Space Res.*, 2013, 51(4), pp. 545—553.
13. G. W. Prölss and S. Werner, Vibrationally excited nitrogen and oxygen and the origin of negative ionospheric storms, *J. Geophys. Res*., 2002, 107(A2), pp. 1016.
14. K. Liou, P. T. Newell, B. J. Anderson et al., Neutral composition effects on ionospheric storms at middle and low latitudes, J. *Geophys. Res*., 2005, 110, A05309.
15. F. S. Bessarab, Yu. N. Korenkov, M. V. Klimenko et al., Modeling the effect of Sudden Stratospheric Warming within the thermosphere-ionosphere system, *J. Atmos. Sol. Terr. Phys.*, 2012, 90—91, pp. 77—85.

Influence of Strong Meteorological Processes on the Ionospheric Parameters

Olga P. Borchevkina[1], Ivan V. Karpov[1,2], Ruslan Z. Dadashev[1], and Alexandra V. Ilminskaya[1]

[1]Immanuel Kant Baltic Federal University, Kaliningrad, Russia
[2]WD IZMIRAN, Kaliningrad, Russia

Numerous experimental and theoretical results show that a variety of dynamic processes in the lower atmosphere, associated with meteorological and seismological phenomena, as well as orographic features of the Earth's surface, have a significant impact on the state of the ionosphere. Connections of dynamic processes in the Earth's lower atmosphere and ionosphere changes state were convincingly proven in experimental studies [1—4]. Theoretical studies due the dynamics of the upper and lower atmosphere is proved that acoustic-gravity waves (AGWs) perform the most important role in the implementation of dynamic connection of atmospheric layers allowing the transfer of energy from the lower to the upper atmosphere [5—7]. Meteorological processes are an important source of generation of AGWs in the atmosphere. The changes in the ionosphere that occur during periods of meteorological perturbations have been observed using different methods and described in numerous papers [2, 8—10].

Observations of gravity waves have great interest for understanding the physical processes of implementing connections atmospheric layers. At the same time it is also important to identify the morphological characteristics of ionospheric irregularities that arise during periods of meteorological perturbations.

The time periods that have been marked the strongest weather storms in the Kaliningrad region were selected for analysis of ionospheric dynamics in the conditions of meteorological perturbations. To identify morphological characters perturbations of ionospheric parameters, appearing in periods of weather storms, the studied time period began a few days before the date of the storm and ended in a few days after its passage.

The paper analyzed the variations of F2-layer critical frequency and the total electron content (TEC) derived from observations at the station. Kaliningrad. The data about the behavior of the total electron content TEC were obtained from the reception of navigational satellite signals and converted into the TEC by the procedures KF IZMIRAN [11].

Meteorological data for selected periods are derived from base data www. gismeteo.ru.

To eliminate the influence of geomagnetic factors on the variation of the ionosphere, were selected only such weather perturbations that occurred during quiet geomagnetic conditions.

In the work will be considering variations of ionospheric and atmospheric parameters in December 2010, for the meteorological storm, which was marked 9—10.12.2010.

Geomagnetic conditions for this period shown in Fig. 1, was relatively quiet, with the exception of the perturbation marked 5.12.2010 (Kp = 6, Fig. 1b). Since meteorological storm proceeded after 4 days, it can be assumed that the influence of the geomagnetic perturbation on ionospheric variations in the duration of the storm was the insignificant.

Figure 1 c-e shows diurnal variations of the TEC (Fig.1c) and critical frequency of F2 layer of the ionosphere (Fig. 1d) during the study period, as well as the atmospheric pressure variations (Fig. 1f) and wind speed (Fig. 1e). As can be seen directly in the period of meteorological storm 9—10.12.2010 decrease in the amplitude of the diurnal variations TEC reaches 50 % compared with the meteorologically quiet days. In variations of the critical frequency of the F-region of the ionosphere in a storm day there is a decrease of the amplitude of the diurnal variations of up to 15 %, as well as the appearance of the periods with the manifestations of F-scattering.

Meteorological conditions at this period is characterized by intensification of the wind in the daytime, in the maximum period of meteorological storm (Fig. 1d), and low atmospheric pressure (Fig. 1e).

As can be seen from the figure observed perturbations of ionospheric parameters correlate with changes of the meteorological parameters, in particular changes in the wind. Analysis of several meteorologically disturbed period 2008—2010 showed that these features of disturbances of the ionosphere parameters are observed quite regularly.

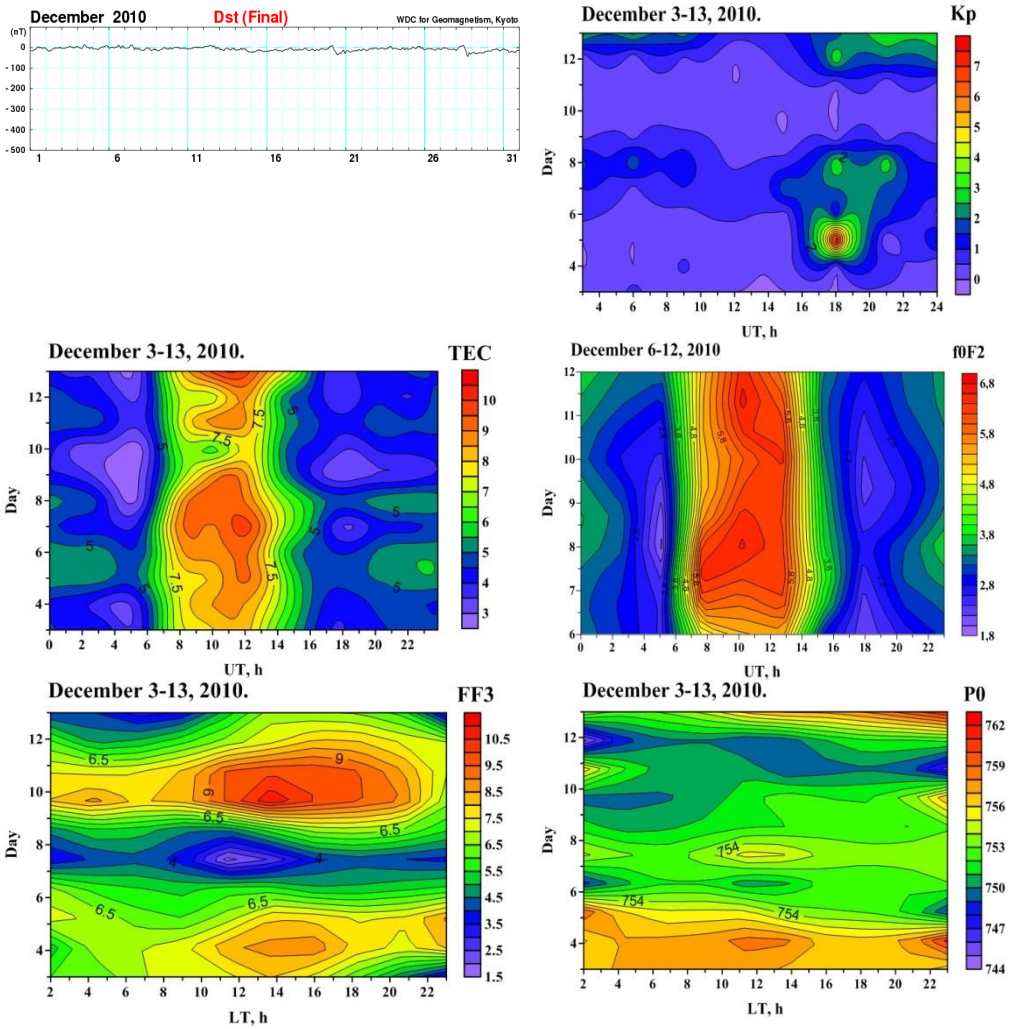

FIGURE 1.a — Ap index for 12.2010, b — Kp index for 3—13.12.2010, c — daily variations of TEC, d- daily variations of f0F2, e — daily variations of wind speed, f — daily variations of pressure in the period 3—13.12.2010 from observations Kaliningrad station.

As follows from the results, the characteristic response of the ionosphere during the meteorological storm seen in lowering the TEC values and f0F2 especially noticeable in the daytime. The reasons for lowering the concentration of charged particles in the ionosphere may be associated with perturbations of the thermosphere, initiated by meteorological storm. Thus ionospheric reaction occurs quickly, within a few hours. Of course, it is assumed that the most likely carrier of energy of meteorological perturbation to the upper atmosphere are the AGW. Experimental observation of the ionosphere wave variations in periods of strengthening of cyclonic activity detected in observations of TEC variations with periods of infrasound and gravity waves (2—20 min) [12].

Theoretical studies of the AGW's propagation from sources in the lower atmosphere show that the waves of this range are able to quickly reach the upper atmosphere and to form large-scale perturbations due to the dissipation, and in particular the local heating region. Significant perturbations of the upper atmosphere caused by the AGW's propagation from sources in the lower atmosphere, marked by 1—2 hours after the starting of source operation (Karpov, 2014). It is obvious that the appearance of the area of a local heating in the upper atmosphere should lead to decreasing of the electron concentration in the ionosphere due to the growing influence of recombination processes.

Observations of variations in the lower atmosphere and ionosphere parameters were carried in Kaliningrad (54 N, 20 E) in the period of meteorological storm February 03, 2015. The observations in the lower thermosphere were carried out by lidar sensing with the use of two-wavelength lidar LSA-2c produced by LLC «Obninsk photonics». These observations determined the time evolution of the intensity of lidar signal scattered in atmosphere.

For the analysis of the observed variations in the parameters the methods of harmonic analysis for determining the frequency characteristics of variations that are typical for atmospheric disturbances was used. The technique of data analysis, aimed at selection such disturbances is presented in the work [13]. It focuses on the study of the dynamics of AGWs and GWs with periods of 2—16 minutes. It is assumed that such AGWs may propagate to the heights of the upper atmosphere and ionosphere.

The Fig. 2 shows the change in spectra variations of the scattered lidar signal in the period of observations. As the figure shows, in the lower atmosphere variations the area of variations is clearly seen. Observations show that the variations with periods of about 2—3 minutes. have a small amplitude in comparison with the amplitude variations with smaller and larger periods. It is natural to assume that the upper boundary of this area corresponds to the period Brunt-Vaisala for internal gravity waves, and the lower boundary of the region corresponds to the period of the acoustic cutoff. Thus, lidar observations allow to highlight the acoustic (infrasound) and the gravitational branches of the variations in observations of the atmosphere. Note also that the decrease in the amplitude of ionospheric variations during periods of meteorological storms accompanied by increased infrasonic variations in the lower atmosphere. Meteorological storm is also observed a decrease in the amplitude infrasonic harmonics and gain harmonic amplitudes with periods of internal gravity waves.

An analysis of the meteorological situation shows that a storms arise, as a rule, against the background of the rapid decreasing of atmospheric pressure and they are accompanied by increased wind. It is assumed that the rapid changes of meteorological conditions create favorable conditions for the AGW's generation in a wide range of periods. Propagation of AGW's to the upper atmosphere and their dissipation in the upper atmosphere cause the corresponding ionospheric perturbations. Lidar observations during a strong meteorological storm held against the background of strong wind, without rain also showed the presence of variations with periods of acoustic gravity waves (Fig.2).

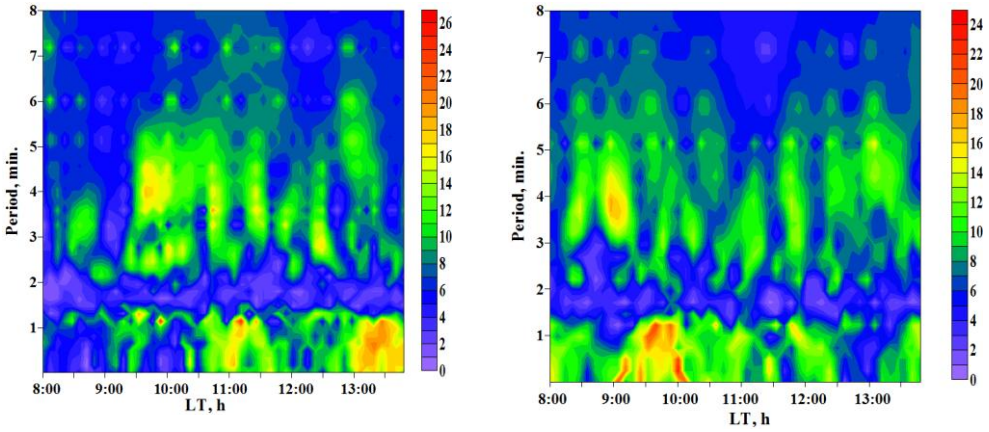

FIGURE 2. The change with time of the lidar signal spectrum during meteorological storm in 3 February 2015 at a wavelength of 532 mt (left) and 1024 nm (right).

Results of the analysis of ionospheric observations have shown that during periods of meteorological disturbances reduction of the TEC diurnal variations, reaching about 50 % in comparison with the meteorological quiet days, appears on the background of low atmospheric pressure. The decreasing of the amplitude of diurnal variations of the critical frequency of the F-region reaches ~ 15 %. F — scattering often observed during periods of meteorological disturbances.

Analysis of the ionospheric data suggests that changes of the ionosphere were determined by meteorological conditions. It is assumed that the most likely cause of ionospheric perturbations are the processes of formation of local area heating of the thermosphere due to AGW's dissipation coming into the upper atmosphere from the area of meteorological perturbations in the lower atmosphere.

Acknowledgments. *These investigations were performed with financial support of the Russian Foundation for Basic Research Grants No. 15-05-01665 and within the project "Physical mechanisms of the reaction of the upper atmosphere and ionosphere on the processes in the lower atmosphere and on the Earth surface" (State task Education and Science Ministry of the Russian Federation, the competitive part of the task No 3.1127.2014/K).*

1. D. Altadill, E. M. Apostolov, J. G. Solé, and Ch. Jacobi, Origin and development of vertical propagating oscillations with periods of planetary waves in the ionospheric F region, *Physics and Chemistry of the Earth, Part C: Solar, Terrestrial & Planetary Science*, 2001, 26(6), doi: 10.1016/S1464-1917(01)00019-8.

2. P. Sauli and J. Boska, Observations of Gravity Waves of Meteorological Origin in the F-Region Ionosphere.*Phys. Chem. Earth (C),* 2001, 26, doi: 10.1016/S1464-1917(01)00024-1.

3. J. Lastovicka and P. Sauli, Are planetary wave type oscillations in the F2 region caused by planetary wave modulation of upward propagating tides? *Adv. Space Res.*, 1999, 24, doi: 10.1016/S0273-1177(99)00708-5.

4. D. C. Fritts and M. J. Alexander, Gravity wave dynamics and effects in the middle atmosphere, *Rev. Geophys.*, 2003, 41, doi: 10.1029/2001RG000106.

5. V. E. Kunitsyn, S. N. Suraev, and R. R. Akhmedov, Modeling of atmospheric propagation of acoustic gravity waves generated by different surface sources, Moscow University Physics Bulletin, 2007, 62.

6. I. V. Karpov and S. P. Kshevetskii, Formation of Large Scale Disturbances in the Upper Atmosphere Caused by Acoustic Gravity wave Sources on the Earth's Surface, *Geomagn. Aeron.*, 2014, 54(4), doi: 10.1134/S0016793214040173.

7. N. M. Gavrilov and S. P. Kshevetskii, Dynamical and thermal effects of nonsteady nonlinear acoustic-gravity waves propagating from tropospheric sources to the upper atmosphere, *Adv. Space Res.*, 2015, doi:10.1016/j. asr.2015.01.033.

8. S. L. Vadas and H.-L. Liu, Generation of large-scale gravity waves and neutral winds in the thermosphere from the dissipation of convectively generated gravity waves, *J. Geophys. Res. Space Physics*, 2009, 114, doi: 10.1029/2009JA014108.

9. T. Sindelarova, D. Buresova, J. Chum, and F. Hruska, Doppler observations of infrasonic waves of meteorological origin at ionospheric heights, *Adv. Space Res.*, 2009, 43, doi:10.1016/j. asr.2008.08.022.

10. M. A. Chernigovskaya, B. G. Shpynev, and K. G. Ratovsky, Meteorological effects of ionospheric disturbances from vertical radio sounding data. *J. Atmos. Sol.—Terr. Phys.*, 2015, 136, doi:10.1016/j. jastp.2015.07.006.

11. L. W. Baran, I. I. Shagimuratov, and N. J. Tepenitzina, The Use of GPS for Ionospheric Studies, *Artificial Satellites*, 1997, 32(2), pp. 49—60.

12. A. S. Polyakova and N. P. Perevalova, Comparative analysis of TEC disturbances over tropical cyclone zones in the north-west Pacific ocean,*Adv. Space Res. (includes Cospar Information Bulletin)*, 2013, 52(8), doi:10.1016/j. asr.2013.07.029

13. O. P. Suslova, I. V. Karpov, and A. V. Radievskii, Frequency characteristics of the troposphere and ionosphere variations in periods of solar terminator passage, *Russ. J. Phys. Chem. B*, 2013, 7(5), pp. 652—655, doi: 10.1134/S1990793113050242.

Case Studies of IGW-Wind Interaction in Upper Atmosphere

Andrey V. Medvedev, Maxim V. Tolstikov, Konstantin G. Ratovsky, Sergey S. Alsatkin, and Dmitry S. Kushnarev

Institute of Solar-Terrestrial Physics, Siberian Branch, Russian Academy of Sciences (ISTP SB RAS), P. O. Box 4026, Irkutsk 664033, Russia

This paper was devoted to the study of the interaction of internal gravity waves (IGW) with a neutral wind, using data Irkutsk incoherent scatter radar(IISR) and ionosonde DPS-4. The DPS-4 ionosonde is located in Irkutsk. The incoherent scatter radar is 98 km northwestward of Irkutsk. In the mode of traveling ionospheric

disturbances(TID) characteristics measurements, the radar performs scanning with a time step of 40 ms, alternatively in two directions, which allows almost simultaneous measurements of scattered signals height profiles by means of two oblique beams with integration time from 1 to 10 minutes. The ionosonde measures electron density profiles with a time step of 15 minutes. Thus, the instruments give three electron density profiles estimated independently of each other at spaced points. All electron density profiles are interpolated to 15 — minute step on time. The relative positions of the instruments form a basis with a typical scale of ~ 100 km and provide measurements of the TID dynamic characteristics. Using lags between electron density disturbances, observed with two IISR beams and the ionosonde, at each height we obtain a system of linear equations for the full velocity vector of TID. Methods of determining TID propagation parameters are described in detail by Medvedev et al. [2009] and Ratovsky K. G. et al. [2008]. Processing long series of measurements requires automated ways of identifying ionospheric disturbances. The automatic method for identifying TIDs assumes that the energy of the TID spectrum is mainly concentrated in the dominant harmonic. The existence of local spectral maximum at the same frequency at three neighboring heights (at least) for each of the tools (the ionosonde and two IISR beams) is the criterion of the presence of a wave disturbance. The method is described in detail by Medvedev et al. [2013]. The developed method has been used to process long series of electron density profiles with determination of the full velocity vector for 1—6 hour ionospheric disturbances corresponding to IGW. Distribution of observed events is presented in Table 1.

TABLE 1.Distribution of observed events.

Observation period	Number of TIDs
Winter *from8.02.2010 to 14.02.2010* *from 24.02.2010 to 28.02.2010* *from 16.01.3011 to16.02.2011* *from 17.01.2012 to 9.02.2012* *from 25.12.2012 to 21.01.2013* *from 26.12.2013 to 12.01.2014*	**5677**
Spring *from 1.04.2009 to 12.04.2009* *from 12.04.2011 to 21.04.2011* *from 5.04.2012 to 22.04.2012*	**1246**
Summer *from 1.06.2007 to 24.06.2007* *from 22.06.2013 to 1.07.2013*	**1372**

Because the daily variations of the neutral wind are weakly dependent on years, according HWM2007 model (less than 10 %), it is possible to combine data from different years and compares with averaged model data. Figure1 illustrates the azimuth distributions. The azimuth is measured clockwise from north.

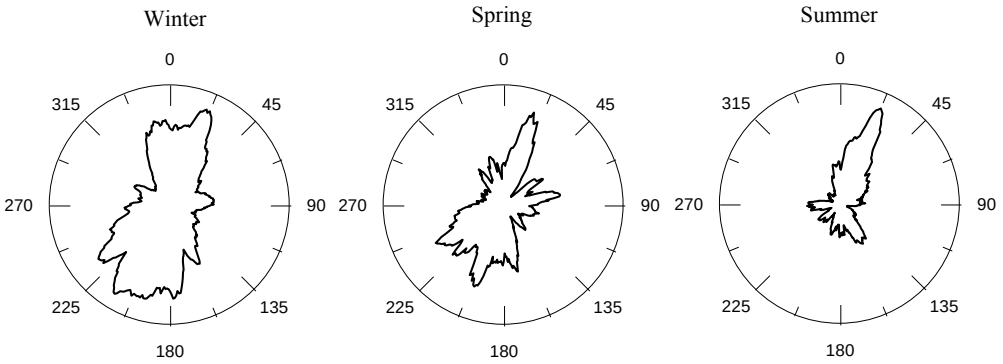

FIGURE 1.Distributions of TIDs azimuths.

The predominant directions of TIDs are from north to south and from south to north. As can be seen from figure 1 there are characteristic inclinations of azimuth distributions(~22.5º) for all seasons. The presence of the characteristic inclinations of azimuth distributions noted also by other reseachers [Oinats et al., 2015]. It has been suggested that such inclinations can be related to the interaction with the neutral wind. Wind amplifies IGWs propagating upwind and weakens IGWs propagating down the wind.

Figure 2 shows the distribution of TIDs azimuths on time for the winter season (~ 5677 TIDs). If the main sources of TIDs are IGWS, the distribution of azimuths TIDs on time should determine by neutral wind. Thus, the maximums in the distribution of azimuths TIDs must coincide with the directions opposite azimuths of strongest and frequent at this time winds. Light-gray lines in figure 2 shows rose of "antiwind" at heights where TIDs observed. We define the antiwind as wind opposite the wind according HWM2007 model and define the rose of antiwind as distributions of "antiwind" projections on TIDs propagation direction with considering wind velocity:

$$OpsWnd(t,\phi) = \sum_{day_{\min}}^{day_{\max}} \sum_{h_{\min}}^{h_{\max}} W((t,day,h))\cos(\phi - \phi^{aW}(t,day,h)) * P(t,day,h), \quad (1)$$

where t — local time, h —height, W(t,day,h) —wind magnitude velocity, φ^{aW} — azimuth opposite azimuth wind, P(t,day,h) — probability of TIDs observation.

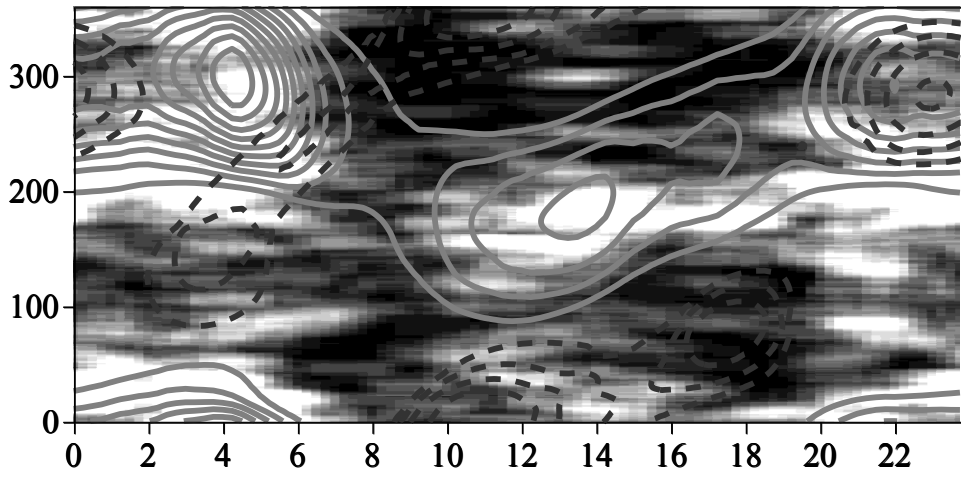

FIGURE 2. Distributions of TIDs azimuths on time for winter season.

As can be seen from figure 2, in most cases maximums of TIDs azimuth distribution coincide with maximums of antiwind rose, but there are cases, when minimum of TIDs azimuth distribution coincide with maximums of antiwind rose. Such situation can be caused by the fact that distribution of TIDs azimuths is defined not only the wind at observation height, but the winds at the heights through which TIDs passed before reach observation height. The strongest influence should be provided by winds at mesopause, where wind direction changes significantly with altitude. Dark gray dashed lines in figure 2 shows the "strong wind" rose at heights 90—200 km. We define "strong wind" rose as distributions of wind projections on TIDs propagation direction with velocity more then 50 m/s:

$$Wnd(t,\phi)=\sum_{day_{\min}}^{day_{\max}}\sum_{90km}^{200km}\begin{cases}W((t,day,h))\cos(\phi-\phi^{W}(t,day,h))\geq 50m/s,\\ W((t,day,h))\cos(\phi-\phi^{W}(t,day,h))*P(t,day)\\ W((t,day,h))\cos(\phi-\phi^{W}(t,day,h))<50m/s,0\end{cases} \quad (2)$$

where t — local time, h —height, W(t,day,h) — wind magnitude velocity, φ^{W} — wind azimuth, P(t,day) — probability of TIDs observation.

As can be seen from figure 2, the combination of amplifying winds and prohibiting winds is already fairly well describes the distribution of TIDs azimuths. Figure 3 depicts the elevation angles distribution. The elevation angle is measured from the horizon; the positive elevation angles corresponds to the upward phase velocity; the negative one to the downward phase velocity. Most of TIDs (79 %) have a downward phase velocity (negative elevation angle), which corresponds to IGW propagating from the source located under the region considered. Positive elevation angles, can be divided into two ranges: 0º—45º (reflected TIDs ~ 12 %) and 45º—90º (TIDs from sources above observation area ~ 9 %).

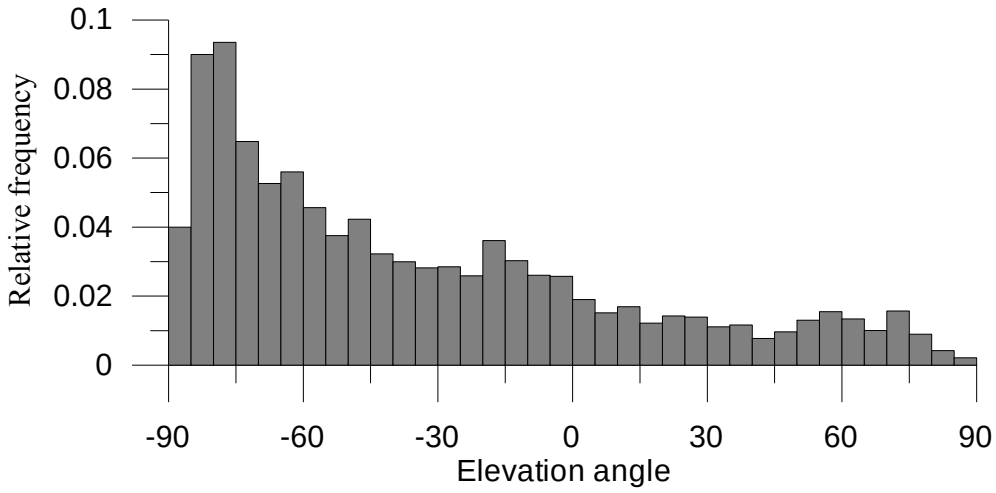

FIGURE 3.Distributions of TIDs elevation angles.

The distribution of reflected TIDs azimuths should repeated distribution of TIDs azimuths with negative elevation angle, but be more narrowly focused, because these TIDs have been a double filtering by neutral winds. TIDs from sources above observation area should have distribution of TIDs azimuths depending on winds at altitudes lying above observation area.

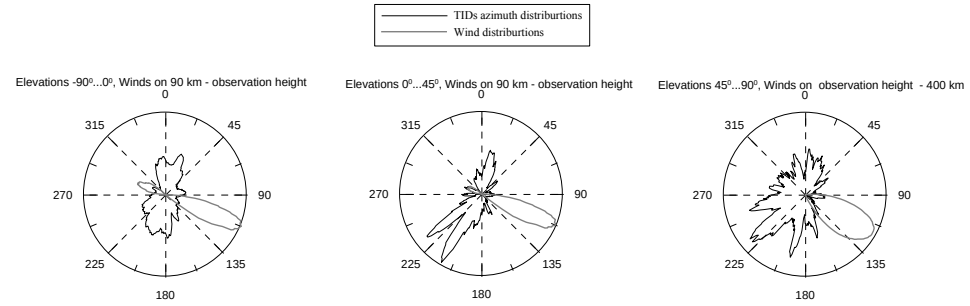

FIGURE 4. Distributions of TID azimuths.

As can be seen from figure 4, peculiarities of TIDs azimuths distributions for different elevation angles are well explained by the neutral wind.

Because the most of the observed TIDs agree with theoretical concepts of the IGW propagation in the presence of horizontal wind [Medvedev et al., 2015], we can formulate the inverse task. Interaction of IGW with horizontal wind in the linear approximation is given by:

$$\omega' = \omega_{obs} - k_h U \tag{3}$$

Using typical values of ionospheric parameters we can obtain wind along TID propagation direction. From equation (4) follow:

$$T^{`} = \frac{L_h T_{obs}}{L_h - U T_{obs}} \tag{4}$$

From equation (4):

$$U = \frac{L_h (T^{`} - T_{obs})}{T_{obs} T^{`}} \tag{5}$$

From Hines dispersion equation T' can be found by solving biquadratic equation:

$$\frac{\cos^2(\theta)}{T_b^2} T'^4 - (1 + \frac{L^2}{C_0^2 T_A^2}) T'^2 + \frac{L^2}{C_0^2} = 0 \tag{6}$$

Where T_{obs} is TID ground-observed period, T' is intrinsic TID period, L is wave length, $L_h$is horizontal wave length, T_b is Brunt-Vaisala period, T_A is acoustic cutoff period, θ is elevation angle, C_0 is sound velocity, U is wind velocity.

Representative TIDs statistic allow us to find average meridional and zonal winds as minimum of functional:

$$\sum (U_x \sin(\varphi_i) + U_y \cos(\varphi_i) - U_i)^2 \to \min \tag{7}$$

where summation is over all TIDs in four-hour time window, which $|U_i| <= 300$ m/s, $U_x$is zonal wind (positive — eastward), $U_y$is meridional wind (positive southward), $U_i$is wind along TID propagation direction, φ_i is azimuth (azimuth angle with respect to north, taking clockwise as a positive).

Minimizing the sum (7) gives the following linear equations system:

$$\begin{cases} U_x \sum \sin^2(\varphi_i) + U_y \sum \sin(\varphi_i)\cos(\varphi_i) = \sum U_i \sin(\varphi_i) \\ U_x \sum \sin(\varphi_i)\cos(\varphi_i) + U_y \sum \cos^2(\varphi_i) = \sum U_i \cos(\varphi_i) \end{cases} \tag{8}$$

Having carried out calculations by the above scheme, we obtain not single values of wind velocity but monthly average diurnal variations in zonal and meridional winds, which can already be compared to model values. Besides the HWM2007 model, we compared calculation results with the meridional neutral wind velocity measured by IISR. The wind velocity was determined using plasma drift velocity measured with IISR and ambipolar diffusion velocity. The plasma drift velocity was calculated using a method for analyzing phase of the autocorrelation function of incoherent scattering signal, which takes into account constructional features of the Irkutsk radar. The calibration of the obtained radial velocity was tested in the series of special experiments on estimation of low orbital spacecraft's velocity using IISR. The ambipolar diffusion velocity was computed using data on characteristics of the neutral atmosphere from the MSISE model. Figure 5 shows the calculation results in comparison to the IISR-measured meridional neutral wind velocity and the HWM2007 model. Figure 5 shows that the calculations of the meridional and zonal neutral wind velocity agree well both with the HWM2007 model and the IISR measurements.

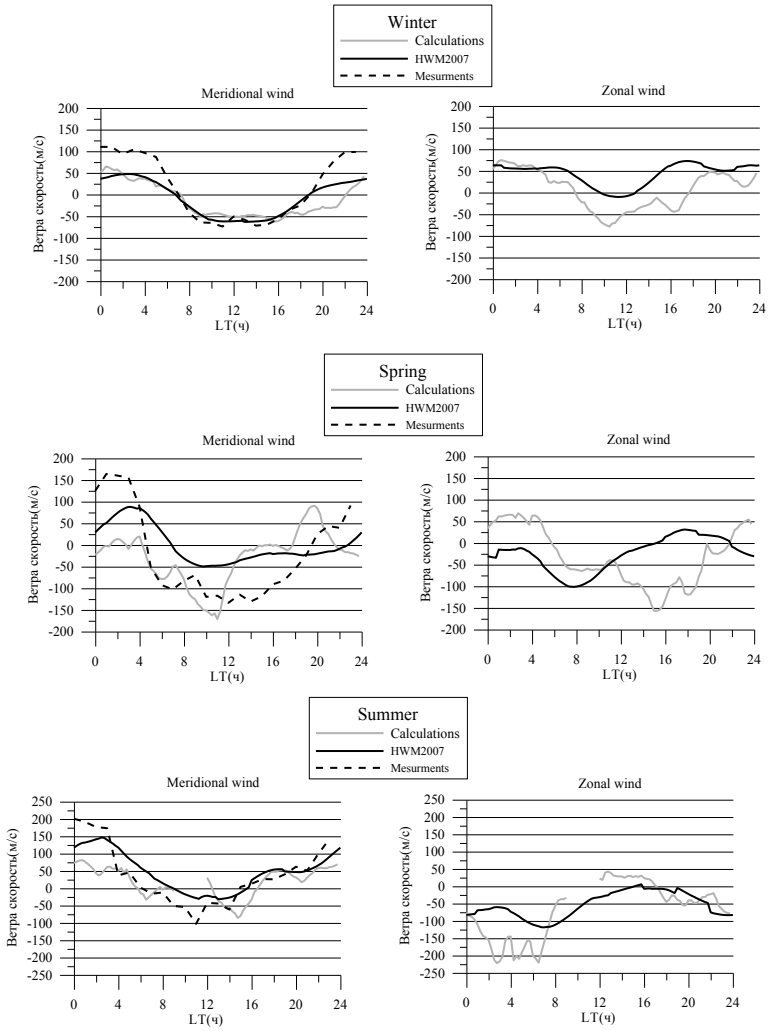

FIGURE 5. Monthly average diurnal variations in zonal and meridional wind velocities.

Conclusion. The main cause of the observed anisotropy of TIDs characteristics associated with filtration IGWs by neutral wind. IGWs, propagating against the neutral wind at observations heights, increase amplitudes, and azimuths, co-directional with a strong neutral wind (over 50 m / s) on any of the heights through which IGWs passed before reaching observation height, were prohibited. Peculiarities of TIDs azimuths distributions for different elevation angles were also well explained by the neutral wind. Assuming fulfillment of Hines dispersion equation, average diurnal variation of meridional and zonal wind for winter, spring and summer seasons were obtained.

Acknowledgments.*The present work was done under support of the Russian fund of basic research (grant № 15-05-02313).*

1. K. G. Ratovsky, A. V. Medvedev, M. V. Tolstikov, and D. S. Kushnarev, Case studies of height structure of TID propagation characteristics using cross-correlation analysis of incoherent scatter radar and DPS-4 ionosonde data, *Adv. Space Res.*, 2008, 41, pp. 1453—1457.

2. A. V. Medvedev, K. G. Ratovsky, M. V. Tolstikov, and D. S. Kushnarev, Method for Studying the Spatial—Temporal Structure of Wave-Like Disturbances in the Ionosphere. *Geomagn.Aeron.*, 2009, 49(6), pp. 775—785.

3. A. V. Medvedev, K. G. Ratovsky, M. V. Tolstikov et al., Studying of the spatial-temporal structure of wavelike ionospheric disturbances on the base of Irkutsk incoherent scatter radar and Digisonde data, *J. Atmos. Sol.—Terr. Phys.*, 2013, 105—106, pp. 350—357.

4. A. V. Medvedev, K. G. Ratovsky, M. V. Tolstikov et al., A statistical study of internal gravity wave characteristics using the combined Irkutsk Incoherent Scatter Radar and Digisonde data, *J. Atmos. Sol.—Terr. Phys.*, 2015, 132, pp.13—21.

Subauroral Trough Modeling for the Nighttime Winter Conditions

Alexander T. Karpachev[1], Maksim V. Klimenko[2,3], Vladimir V. Klimenko[2], Lubov V. Pustovalova[1], and Nikolay V. Chirik[3]

[1]Pushkov IZMIRAN, RAS, 142190, Moscow, Troitsk Region, Russia
[2]West Department of Pushkov IZMIRAN, RAS, 236017, Kaliningrad, 41 Pobeda Av., Russia
[3]Immanuel Kant Baltic Federal University, 236041, Kaliningrad,14 A. Nevsky Str., Russia

Introduction. The Main Ionospheric Trough (MIT) has been firstly detected from the Alouette I data by Muldrew [1]. MIT is the main structure of the winter subauroral ionosphere [2]. The repeated attempts to develop a MIT model have been made [3—5]. However, each of them was a local empirical model. For global model development we used topside sounding data (*foF*2) obtained onboard Interkosmos-19 (IK-19) and CHAMP *in situ* data (N_e). These data have been recorded for all levels of solar activity. So our task consisted of two stages of development: 1) the MIT position model; 2) the MIT shape model, i. e. the model of *foF*2 distribution in the trough region in Northern and Southern Hemispheres.

1. Observation data. The satellites data were collected for the periods from November to February in the Northern Hemisphere and from May to August in the Southern Hemisphere. The IK-19 satellite was operated from February 1979 until March 1982 during high solar activity ($F_{10.7}$ = 150—250). The IK-19 database consists of 3500 satellite passes in winter night-time ionosphere. Figure 1a shows the examples of the *foF*2 latitudinal cross-section, obtained by IK-19 topside sounding

on February 2, 1980 in the Northern Hemisphere (a) and on July 18, 1979 in the Southern Hemisphere (b). These both plots clearly present the general features of the main ionospheric trough (MIT) structure: its equatorial wall, polar wall and deep trough minimum. The CHAMP satellite operated from July 2000 to September 2010 when $F_{10.7}$ changed from 220 to 68. The CHAMP data for period of 2005—2010 were used for MIT model development for low solar activity and the CHAMP data for 2000—2002 together with the IK-19 data were used for MIT model development for high solar activity. The *in-situ* measurements ofN_e(plasma frequency, f_p) at a fixed CHAMP heights (300—450 km)were used to estimate the *foF*2 values by means of the IRI model. About 30 000 CHAMP satellite passes through the winter night-time ionosphere of both hemispheres were used for the model development. Figure 1 shows the f_p latitudinal distribution obtained on August 4, 2008 (c) and on July 24, 2007 (d) in the Southern Hemisphere. These examples illustrate a difficulty of the data processing in the trough region: (1) double troughs structure sometimes was observed (c); (2) MIT as a plateau in a broad latitudinal interval (d).

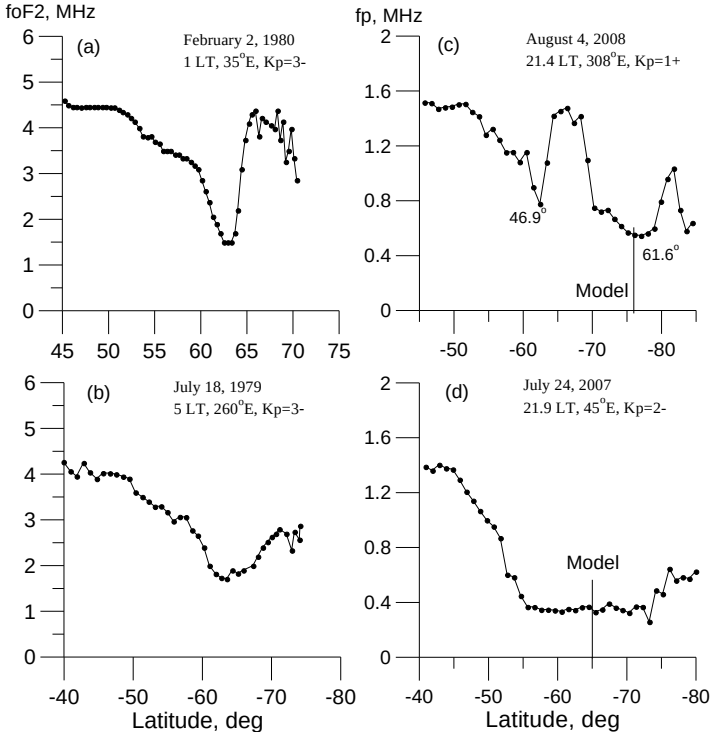

FIGURE 1. Examples of the latitudinal variation in *foF*2 according to the IK-19 satellite data (left panel) and in plasma frequency, f_p, at height of ~350 km according to CHAMP satellite measurements (right panel) at high latitudes of the Northern and Southern hemispheres. The vertical lines show the trough minimum model position.

2. Model of the trough position. The trough position strongly depends on the level of magnetic activity, local time and longitude [5—10]. We developed the empirical model of MIT position for quiet geomagnetic conditions (Kp = 2). Since the parameter of geomagnetic activity was fixed the dependence of MIT position only from local time and longitude will be considered below. Figure 2 shows the modeled longitudinal variations in the MIT position in the Northern Hemisphere from 18:00 LT to 06:00 LT. The features of such variations don't practically vary with solar activity changes, to a first approximation they are similar to the longitudinal variations in the geomagnetic latitude. At high solar activity the trough is located at somewhat lower latitudes than at low activity. This difference is maximal in the morning.

Figure 3 shows the model results of the trough position in the Southern Hemisphere. As in the Northern Hemisphere, the trough position in a first approximation follows up the geomagnetic latitude variations. Therefore the longitudes with minimum and maximum distance from the pole are practically interchanged the places in the Northern and Southern Hemispheres. Since the difference between magnetic and geographic poles in the Southern Hemisphere is much greater than in the Northern Hemisphere, the range of MIT position variations in Southern Hemisphere is also greater. And again the trough at high solar activity is located at lower latitudes in comparison to MIT position at low solar activity.

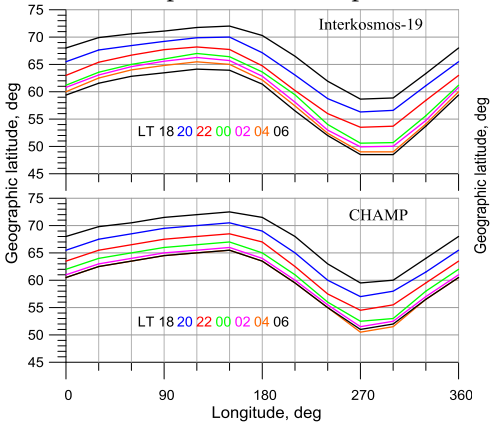

FIGURE 2. The modeled longitudinal variation of the trough minimum position for different local time in the Northern Hemisphere at high solar activity (top) and at low solar activity (bottom).

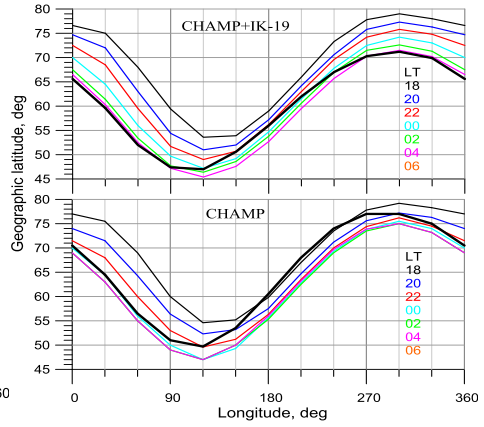

FIGURE 3. The same that in Figure 2 but for Southern Hemisphere.

3. Model of the trough shape. At the second stage of MIT model development we are created the *foF*2 model in the trough region: (1) the *foF*2 longitudinal variations have been carefully revealed and analyzed; (2) then latitudinal variations, which determine the shape of the trough, its depth and width were derived. The good knowledge of the main features of *foF*2 longitudinal variation (see e. g. [11—13])

allows controlling and correcting the *foF*2 longitudinal variations even when the quality of the dataset was insufficiently high. The *foF*2 latitudinal distribution were obtained by the superposed epoch method when all individual *foF*2 profiles for a given time and longitudinal sector were combined at the latitude of the trough minimum determined in a previous step of empirical model development.

Figure 4 shows the *foF*2 latitudinal distributions in the trough region in the characteristic longitudinal sectors of the Northern Hemisphere for different local time at high and low solar activity. These distributions present the results of the trough shape model. It is evident that with longitude not only the position, but also the trough shape (MIT depth and width) are varied. At low solar activity the trough is much better expressed than at high solar activity for any local time and longitude. In the Southern Hemisphere the peculiar longitudinal sectors are other, but again the trough is more pronounced during the low solar activity then during high activity.

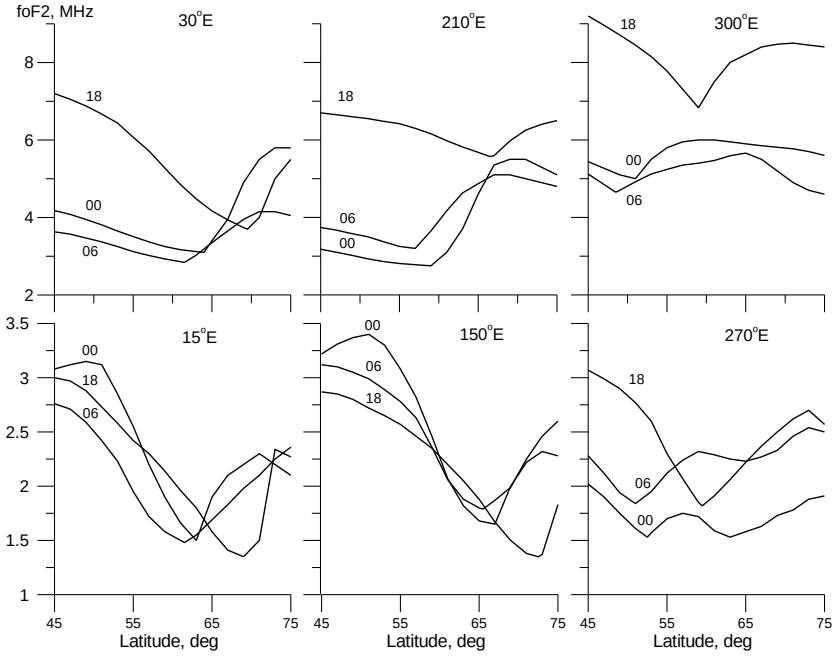

FIGURE 4. Latitudinal variations in *foF*2 in the most peculiar longitudinal sectors of the Northern Hemisphere for different local time at high (top panel) and low (bottom panel) solar activity.

We estimated the empirical model accuracy using the comparison of the *foF*2 latitudinal and longitudinal variations with empirical IRI model, first-principal GSM TIP model, ionosondes and radiooccultation data in the both hemispheres for different geophysical conditions. The observation data are in rather good accordance with model. The IRI model does not reproduce the subauroral trough structure.

Conclusion. The MIT model was developed for the most common conditions in a quiet ionosphere (*Kp*=2). For these conditions the accurate trough position model was developed in the term of geographic latitude for all longitudes and local time hours in the interval from 18:00 LT to 06:00 LT. The accuracy of the trough minimum position determination is about of 2°. The comparison with the observation data showed that the rather adequate model of the trough shape was also constructed. I. e. the model of the subauroral ionosphere in the Northern and Southern Hemispheres for night winter conditions was created. The error of *foF*2 description on the trough equatorial wall depending on the conditions under consideration is 0.2—0.4 MHz and increases up to 1.0 MHz on the polar wall.

The model can befound on the IZMIRAN website: http://www.izmiran.ru/ionosphere/sm-mit/ for free using. The modelallows to calculate the trough position for any level ofsolar activity$F_{10.7}$from 70 to200, *foF*2valueat one point, *foF*2 longitudinalandlatitudinal variations,as well as *foF*2 spatial distributionin the range of 45—75°Nlatitudesin the Northern Hemisphereand of 40—80°Sin the Southern Hemisphere. The new model much more adequate describes the subauroral ionosphere structure then IRI-2012.

Acknowledgements.*The authors would like to give thanks to sponsors and operators of the CHAMP mission; Deutsches GeoForschungsZentrum (GFZ) Potsdam and German Aerospace Center (DLR). The investigations were carried out at partial financial support of Russian Foundation for Basic Research (RFBR) — Grant No. 14-05-00788 and 15-35-20364.*

1. D. B. Muldrew, F-layer ionization troughs deduced from Alouette Data, *J. Geophys. Res.*, 1965, 70(11), pp. 2636—2650.

2. A. T. Karpachev and V. V. Afonin, Ionospheric troughs occurrence probability dependence on season, local time, longitude and magnetic activity, *Geomagn.Aeron*., 1998, 38(3), pp. 79—91.

3. B. W. Halcrow and J. S. Nisbet, A model of F2 peak electron densities in the main trough region of the ionosphere, *Radio Sci.*, 1977, 12(5), pp. 815—820.

4. E. Feichter and R. Leitinger, Properties of the main trough of the F region derived from Dynamic Explorer 2 data, *Ann. Geophys.*, 2002, 45(1), pp. 117—124.

5. S. E. Pryse, L. Kersley, D. Malan D. et al., Parameterization of the main ionospheric trough in the European sector, *Radio Sci.*, 2006, 41, doi:10.1029/2005RS003364.

6. W. Kohnlein and W. J. Raitt, Position of the mid-latitude trough in the topside ionosphere as dedused from ESRO 4 observations, *Planet. Space Sci.*, 1977, 25(5/6), pp. 600—602.

7. J. Oksman, Apparent diurnal movements of the trough it total electron content (TEC) of the ionosphere, *Geophysica*, 1982, 19(1), pp. 13—22.

8. S. Werner and G. W. Prolss, The position of the ionospheric trough as a function of local time and magnetic activity, *Adv. Space Res.*, 1997, 20(9), pp. 1717—1722.

9. A. T. Karpachev, The dependence of the main ionospheric trough shape on longitude, altitude, season, local time, and solar and magnetic activity, *Geomagn. Aeron.*, 2003, 43(2), pp. 256—269.

10. M. He, L. Liu, W. Wan et al., A study on the nighttime midlatitude ionospheric trough, *J. Geophys. Res.*, 2011, 116 (A05315), doi:10.1029/2010JA016252.

11. M. G. Deminov and A. T. Karpachev, Longitudinal effect in main ionospheric trough configuration. I. Trough position, *Geomagn. Aeron.*, 1986, 26(1), pp. 63—68.

12. M. G. Deminov and A. T. Karpachev, Longitudinal effect in the main ionospheric trough configuration. 2. The trough shape, *Geomagn. Aeron.*, 1986, 26(4), pp. 682—684.

13. A. T. Karpachev and N. A. Gasilov, Causes of longitude-latitudinal variations in the ionospheric F2-layer maximum in summer nighttime conditions, *IJGA*, 2006, 6, GI2006, doi:10.1029/2005GI000112.

Statistics of Daytime Ionospheric Disturbances in the Recovery Phase of Magnetic Storms from 2003—2016 Irkutsk Ionosonde Data

Konstantin G. Ratovsky[1], Maxim V. Klimenko[2,3], and Vladimir V. Klimenko[2]

[1]Institute of Solar-Terrestrial Physics SB RAS, Irkutsk 664033, Russia
[2]West Department of Pushkov Institute of Terrestrial Magnetism, Ionosphere and Radio Wave Propagation, RAS, Kaliningrad 236017, Russia
[3]Immanuel Kant Baltic Federal University, Department of Radiophysics and Information Safety, Kaliningrad 236000, Russia

In the paper [1] related to modeling of ionospheric effects of the September 26—30, 2011 geomagnetic storm, it was shown that the positive electron density disturbances were formed in the daytime at the 3d and 4th day of the geomagnetic storm recovery phase due to increasing density ratio of atomic oxygen to molecular nitrogen $n(O)/n(N_2)$. In this paper, we test how this conclusion can be generalized to other geomagnetic storms. For testing we used the 2003—2016 Irkutsk ionosonde (52.3N, 104.3E) data set.

Identification of the start time of geomagnetic storm recovery phase was performed using the following algorithm for processing the Dst index data. A moment was considered as the start time (hereinafter referred to as t_0) under the following conditions:

(1) $\mathrm{Dst}(t_0)$ is the globalminimum in theintervalt_0±12hours;

(2) $\mathrm{Dst}(t_0) \leq -50$nT.

The developed algorithm revealed 291 geomagnetic storms for the Jan 1, 2003 — Jan 31, 2016 period. An additional algorithm selected 98 cases of isolated geomagnetic storms using the following criteria: the time interval between each t_0 should be not less than 5 days.

Statistics of daytime ionospheric disturbances was made using the following method. As the F2 layer electron density disturbance ($\Delta NmF2$) we considered the

percentage differences between the observed peak density ($NmF2_{OBS}$) and the 27-day sliding median value ($NmF2_{MED}$):

$$\Delta NmF2(\%) = (NmF2_{OBS} - NmF2_{MED})/NmF2_{MED} \cdot 100\,\%.$$

For the analysis of daytime ionospheric disturbances we calculated daytime averaged value (ΔNmF2 averaged over the 10—14 LT interval), as well as the maximal and minimal ΔNmF2 values for this interval. Calculations were carried out for the day corresponding to t_0 (Day 0) and five consecutive days (Day 1,.., Day 5). Fig. 1 showsthe distributionof the daytime averaged ΔNmF2 for Day0 — Day5 daysfor all the geomagnetic storms, the digitsshow the mean (Mean)and root mean square (RMS) values.Fig. 2 showsa similardistributionobtained for the isolatedgeomagnetic storms. Fig. 1 shows thationosphericresponses togeomagnetic stormsare random processes. One may see both positiveand negative disturbances for all the considered days. Positive disturbance are seen even on the most negatively disturbed day (Day 1). Day 1 is characterized by the most negative mean value (-10 %) and the largest RMS (24 %). From Day 1 to Day 5 both the absolute mean value and RMS decreases. On the Day 5 ΔNmF2 distribution looks like a normal distribution with a near zero mean value and RMS of 19 %.

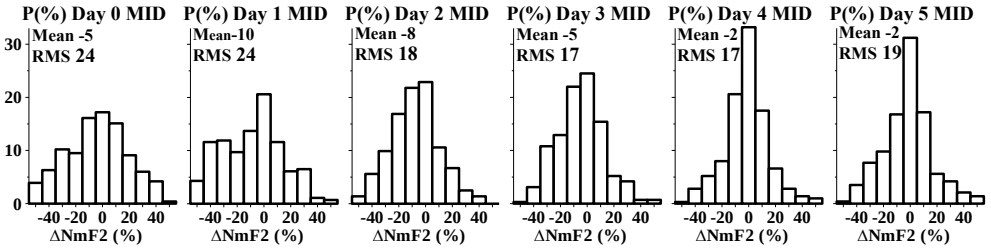

FIGURE 1. Distribution of the daytime averaged ΔNmF2 for Day 0 -Day 5 days for all the geomagnetic storms.

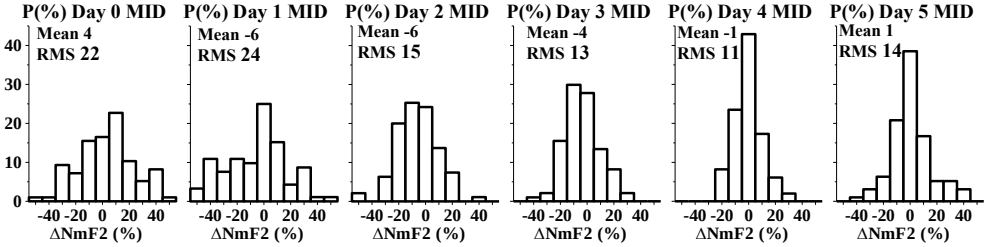

FIGURE 2. Distribution of the daytime averaged ΔNmF2 for Day 0 — Day 5 days for isolated geomagnetic storms.

The ΔNmF2 distributions in case of only isolated geomagnetic storms show the same tendencies as in case of all the storms. The difference lies in that: (1) the absolute mean value decreases (due to decrease in the number of strong distur-

bances); and (2) RMS reduces. Statistics of the maximal and minimal ΔNmF2 values are not presented here because they are mainly similar to the statistics of the daytime averaged ΔNmF2. The difference lies in that the maximal ΔNmF2 values are shifted positively by 14—16% and the minimal ΔNmF2 values are shifted negatively by 13—16% relative to the daytime averaged ΔNmF2.

Fig. 3 shows day to dayvariations in the median,upper and lowerquartiles of the ΔNmF2 distributionfor both all and isolatedstorms. Thelargest changesare observedin the lower quartile: its value varies from – 30%onDay1 to – 12%onDay5 for all the storms and from– 23% onDay1 to – 7% onDay5for isolatedstorms.This changeshows the decrease inthe number ofstrong negativedisturbancesfromDay1toDay5. Additionally,it is clearthat the lowerquartile in the case of all the stormsis lowerthan that in the case of isolated storms, which indicates a decrease inthe number ofstrong negativedisturbanceswhen we consider onlyisolatedstorms.

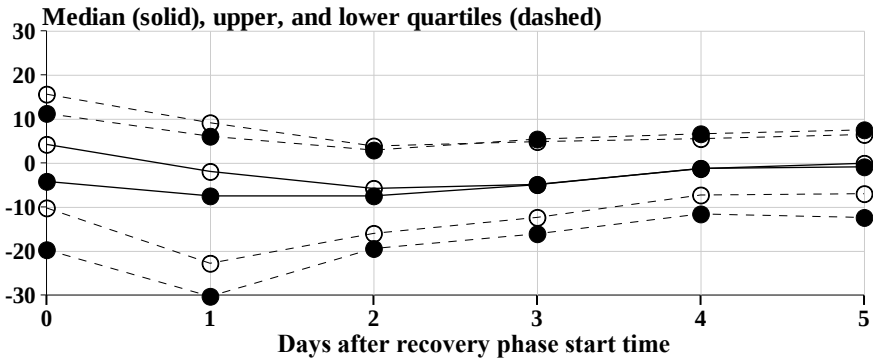

FIGURE 3. Day to day variations in median (solid), upper and lower quartiles (dashed), of ΔNmF2 distribution for both all (black circles) and isolated storms (white circles).

What is the cause of the spread in ionospheric responses to geomagnetic storms? Why are both positiveand negative disturbances seen throughout all the considered period?

In our view, the spread of ionospheric responses may be due to the following reasons.

(1) Ionospheric responses to geomagnetic storm are accompanied by disturbances of non-geomagnetic origin (so-called meteorological disturbances). These disturbances can superimpose additively on disturbances caused by a geomagnetic storm.

(2) An ionospheric storm scenario the may depend on meteorological disturbances. In this case, the scenario is a random process (due to randomicity of meteorological disturbances), and the final result is not a simple superimposition of geomagnetic and meteorological disturbances.

(3) Even without meteorological disturbances, an ionospheric response to geomagnetic storm may have various scenarios that depend on storm local time, season, storm strength, and the behavior of geomagnetic activity indices.

We did not obtain the expected effect, which is a signature of positive electron density disturbances in the daytime of some day of the recovery phase. The cause may be related to various scenarios of ionospheric responses. The transition from negative to positive ΔNmF2 can occur on different days (in the range from Day 2 to Day 5), so that positive and negative disturbances compensate each other in a statistical sense resulting in near zero mean value and median.

Further we plan to separate geomagnetic storms into different groups depending on season, storm local time, and storm strength. Such separation may reduce a number of various scenarios depending on the mentioned above factors.

Acknowledgments. *Authors express the huge gratitude to NASA's Space Physics Data Facility (SPDF) for use of the geomagnetic indices from the website http://omniweb. gsfc. nasa. gov/form/dx1.html. This investigations were performed with financial support of the Russian Foundation for Basic Research Grants No. 14-05-00578. This work was partially carried out with-in the project "Physical mechanisms of the reaction of the upper atmosphere and ionosphere on the processes in the lower atmosphere and on the Earth surface" (State task Education and Science Ministry of the Russian Federation, the competitive part of the task No 3.1127.2014/K).*

1. M. V. Klimenko, V. V. Klimenko, F. S. Bessarab et al., Influence of geomagnetic storms of September 26—30, 2011, on the ionosphere and HF radiowave propagation. I. Ionospheric Effects, *Geomagn. Aeron.*, 2015, 55(6), pp. 744—762.

GPS-Monitoring of the Ionospheric Reaction on Solar Eclipse using Single-Frequency Mode on the Example of Event 20 March 2015

Andrey A. Kholmogorov, Vsevolod B. Ivanov

Irkutsk State University, 664003, Irkutsk, Russia

This article is devoted to the influence of solar eclipse of 20 march 2015 on the total electron content (TEC) of the ionosphere with using data from satellite navigation system GPS. In considering addition of TEC variations, the main aim is to show the possibility of using the data of the single-frequency receivers for the diagnostics of the ionosphere. Data from the single-frequency receivers are compared with dual-frequency receivers GPS. As a result, the possibility of using of the low-

cost and mobile single-frequency devices for diagnostics of the ionosphere has been demonstrated. It should be noted that the data from the single-frequency receivers, as expected, showed a more noisy result, compared with the phase measurement on two-frequencies.

Introduction. Under the guidance of Professor E. L. Afraimovich was formed a new direction diagnosis of the condition the upper atmosphere of the Earth based on the signal processing of satellite navigation systems. Theoretical bases and various examples of this diagnostic presented in [1]. In this work, as well as a number of articles colleagues and students of Professor Afraimovich (in particular, in doctoral dissertation N. P. Perevalova [2]) were carried out investigations effects in the Earth's ionosphere, associated with solar eclipses, earthquakes, geomagnetic disturbances, powerful tropical cyclones by GPS — monitoring. For example, a detailed analysis of the solar eclipse effect was presented on 22.08.2009 in [3]. All these results have been obtained on the basis of studies of relative time variations the total electron content (TEC) of the ionosphere, by using two-frequency receiver equipment, registered the data the changes of the phase paths of satellite radio. In the present study is analyzed the impact on the TEC of the last total solar eclipse that occurred on 20 March 2015, most clearly observed in the northwestern part of Europe and over the Atlantic. At the same time, it demonstrate the ability to detect variations of TEC using single-frequency radio navigation GPS signals.

Methods and results of the experiment. When registering GPS signals on two frequencies L1 and L2 is possible to measure the time course of the phase of the received signal up to an unknown additive constant — phase ambiguity [4]. At the same time excluding the constant addition, the accuracy of phase measurement reaches millimeter values. The value of the total electron content along a beam from the antenna phase center of the satellite to the receiver antenna is determined by the well-known formula:

$$I = \frac{1}{40.308} \frac{f_1^2 f_2^2}{f_1^2 - f_2^2} [(L_1\lambda_1 - L_2\lambda_2) + const] , \quad (1)$$

where f_1 and f_2 — frequency radio waves, $L_1\lambda_1$ and $L_2\lambda_2$ — phase path at the corresponding frequencies. The presence of the unknown constants in the formula (1) is connected with the phase ambiguity. Thus, it is possible to measure not the absolute value of TEC, as it changes over time relative to the start time of registration.

Initial data for the calculation of TEC variations can be obtained from the RINEX-files, which contain values of daily moves of pseudorange and phases (up to an additive constant) for each of the tracked GPS navigation satellites, and in recent years for GLONASS. Station MORP of the international network of IGS with the coordinates 55.2˚ north latitude, 1.7˚ west longitude (UK) is the most suitable for the analysis of considered solar eclipse. For this station, there has been the greatest illumination of the Sun the moon disc — about 90 %. Start eclipse near MORP station corresponds to about 8 hours 40 minutes UTC. The total duration of the eclipse was about 2 hours.

Using the formula (1) was produced the calculation of the time changes of the inclined TEC for GPS satellites G6, G9, G10. Starting time of the analysis were 6 hours and 47 minutes UTC. Analysis time was 3 hours 50 minutes. In the next period there have been failures of the carrier phase tracking, which were not allowed to analyse the longer session. In accordance with the format of the RINEX files, the time step of the calculations is 30 seconds, so the data are presented for 460 time points. For comparison, calculations were made for the preceding and following days 19 and 21 March 2015. GPS satellite orbital period was 11 hour 58 minutes, so the geometry and configuration of the constellation of satellites in the two neighboring day was almost identical.

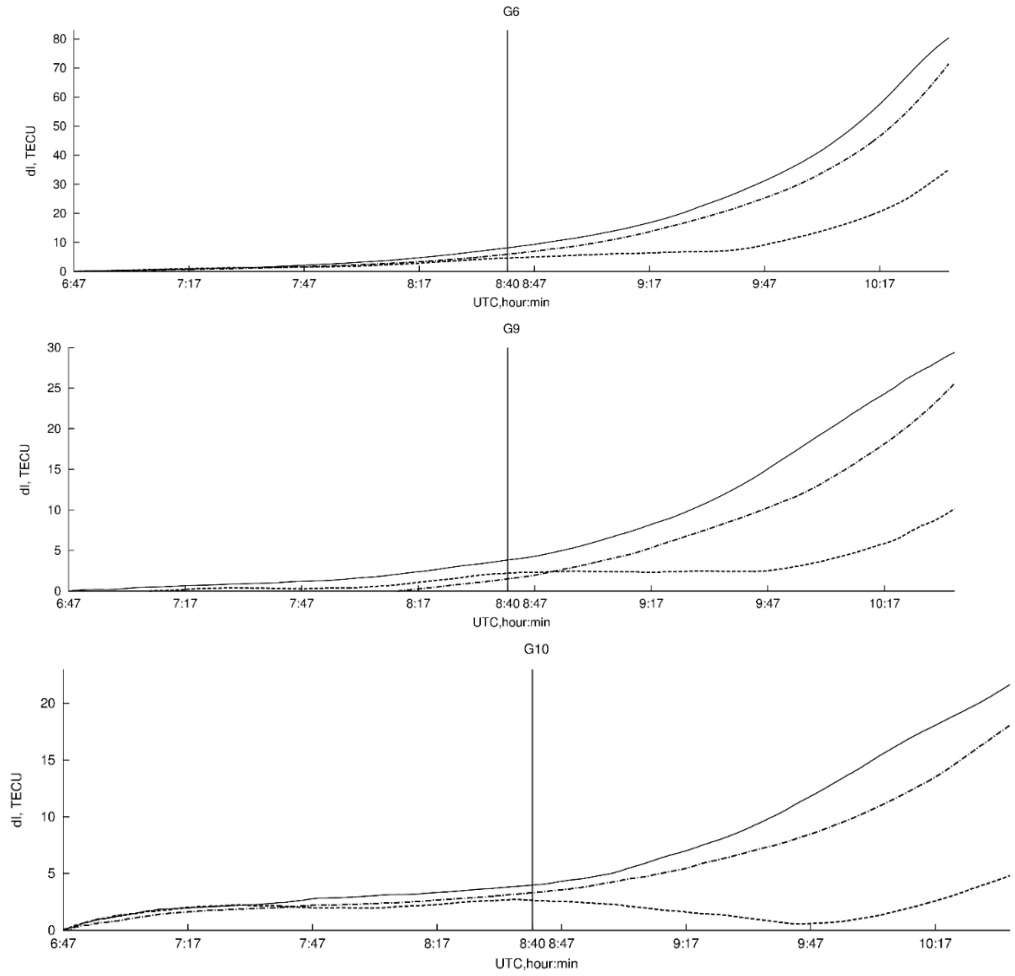

FIGURE 1. The relative of the time variation of the inclined TEC for the day of the solar eclipse 20 march — dashed line, the previous day on 19 march the solid line, and for the subsequent day on 21 march — dot-dash line for the three GPS satellites.

Graphical changes TEC inclined relative to the initial time for the satellites mentioned above, are shown on Fig. 1. Variations of TEC are given in TECU units, 10^{16} m^{-2}. The dashed lines show the course of TEC of the day of a solar eclipse, the solid lines — for the previous day 19 March 2015 and the dot-dash — for the next day 21 March 2015.

It can be seen that the degree of eclipse influence at TEC for different satellites differ, because under ionospheric points were values of different degrees of closing of the solar disk. Satellite G10 has the most significant effect. For this satellite the maximum deviation of TEC, related to the eclipse, is approximately 15 TECU relative to the control days. From graphs of TEC variation, it can be concluded that the reaction to the solar eclipse starts immediately with the beginning of closing of the solar disk for the corresponding ionospheric point. Start time closing of the solar disk above the station MORP in the graphs in Fig. 1 is shown at vertical line.

The next step was investigated the possibility of such detection with the use of a much simpler single-frequency equipment.

As is well known, pseudorange from the receiver to the transmitter of the satellite with the number i can be represented by the formula:

$$P_i = R_i + T + I_i + D_i + S\,, \tag{2}$$

where R_i — the geometric distance from the receiver to the satellite, T — the contribution from the shift of the receiver clock relative to the system time, I_i — the contribution from the additional delay during the propagation of radio waves in the ionosphere, D_i — contributions from other factors, including the shift of the satellite clock, the additional delay in the troposphere, multipath, S — noise.

For phase-way of radio signals is the following relation:

$$F_i = R_i + T - I_i + D_i + const\,. \tag{3}$$

The contribution of the ionosphere in the last formula is entered with the opposite sign. Accuracy of phase measurements is much smaller than the amplitude, so the noise missed in this formula. However, there is an additive constant associated with the ambiguity of the definition of phase. In the following stages, this constant is not taken into account, because the absolute variation of TEC is not considered. Taking into account the comments made above, by subtracting (2) — (3) the final value of the TEC is obtained as:

$$I = 3.08(C1 - L_1\lambda_1)\,. \tag{4}$$

In this formula, for uniformity with the formula (1) used the multiplication $L_1\lambda_1$. C1 should be understood as pseudorange obtained for the code signal.C/A is the value difference in the ratio in brackets (4) can be taken directly from RINEX-files.TEC calculated by the formula (4), presented in the TECU units.

According to the method provided for satellite signals of G10, simultaneously with the dual-frequency carrier phase measurements were carried out measurements of the difference between pseudorange and phase path on the frequency L1. Figure 2 is shown the changes of the TEC in a longer session (4 hours and 40 minutes) in a single frequency and dual frequency data — dashed and solid lines, respectively.

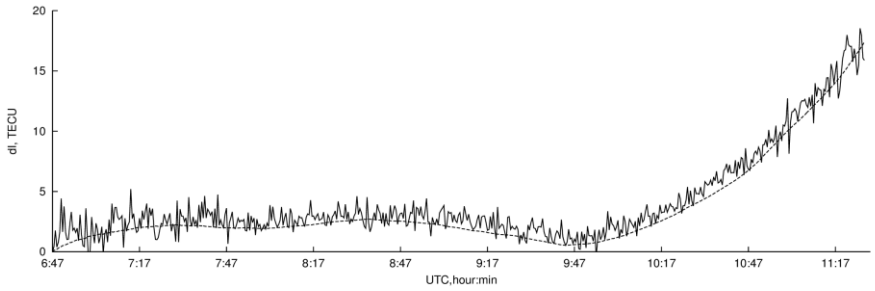

FIGURE 2. The time variation of the relative changes of inclined TEC at a solar eclipse. Dashed line — dual-frequency measurements, solid line — single-frequency measurements.

Single-frequency data, as expected, noisy greater than two-frequency data, however, can be seen that both plots are qualitatively the same. Some systematic displacement of one curve from another on the vertically is immaterial, such as presented variations with respect to start time.

Conclusion. In addition to the study of the time variations TEC in the specific conditions of the solar eclipse, the main result of this work is the conclusion of the possibility of using low-cost single frequency devices for diagnostics the ionosphere. Task of the further analysis is based on the possibility to research, with using single frequency devices, short-period perturbations, such as ionospheric response to earthquakes.

1. E. L. Afraimovich and N. P. Perevalova, GPS- monitoring verhney atmosferyi Zemli [GPS —monitoring of the Earth's upper atmosphere], Irkutsk, 2006, 480 p.

2. N. P. Perevalova, Issledovanie ionosfernyh vozmushhenij metodom transionosfernogo GPS-zondirovanija, Dokt. Diss. [The study of the ionospheric disturbances by the trans ionospheric GPS-sensing, Doct. Diss.], Irkutsk, 2014, 286 p.

3. E. L. Afraimovich, S. V. Voeykov and I. K. Edemskiy, Ionospheric effects of the total solar eclipse 22 July 2009 according to the data a dense network of GPS in Japan (GEONET), *Sovremennye problemy distancionnogo zondirovanija Zemli iz kosmosa [Modern problems of remote sensing of the Earth from space]*, 2010, vol. 7, iss. 3, pp. 94—98 (in Russian).

4. V. S. Shebshaevich, P. P. Dmitriev and N. V. Ivancevich, Setevye sputnikovye radionavigacionnye sistemy [Network satellite radio navigation systems], Moscow, 1993, 408 p.

N_mF2 Dependence from Solar and Geomagnetic Activity in the Middle Latitudes in January 2012—2015

Alexander V. Markov[1], Alisher R. Abdullaev[1], Maxim V. Klimenko[1,2], Konstantin G. Ratovsky[3], Nina A. Korenkova[2], Vladimir S. Leshchenko[2], and Artem M. Vesnin[3]

[1]Immanuel Kant Baltic Federal University, 236004, Nevskogo 14, Kaliningrad, Russia
[2]West Department of Pushkov IZMIRAN, RAS, Kaliningrad, Russia
[3]Institute of Solar-Terrestrial Physics, SB RAS, Irkutsk, Russia

1. Introduction. The $F2$ layer peak electron density (N_mF2) is larger for higher solar activity and is proportional to sunspots number and the $F_{10.7}$ index [1]. At the all latitudinal regions, the diurnal—seasonal variations of the ionospheric electron density are caused by the changes: in the ion-production rate which is proportional to the cosine of the solar zenith angle; in the neutral atmosphere composition controlled by global thermospheric circulation and neutral temperature; in the plasma transport associated with neutral winds [2]. Solar and geomagnetic activity dependence of diurnal and seasonal variations in ionospheric F region parameters in the East-Siberian region is investigated in details by Ratovsky et al. [3]. It was shown, that the higher solar activity leads to the growth rate of the N_mF2, which is greatest in the afternoon at winter solstice. Contrary, N_mF2 weakly depends on solar activity in the nighttime winter ionosphere which is caused by plasma flows from a plasmasphere. Lei et al. [4] concluded that N_mF2 above Millstone Hill at 12:00 LT in winter increases linearly with increasing in solar activity proxy $F_{10.7}$ index. Hence, linear function can be used to represent the N_mF2 and proxy $F_{10.7}$ correlation. In this paper we examined N_mF2 dependence on the solar and geomagnetic activity in January 2012—2015 at different locations.

2. Observation data. We analyzed the daily $F_{10.7}$ index data from the web-site http://lasp.colorado.edu/lisird/tss/noaa_radio_flux.html and geomagnetic activity index Ap from the web-site http://wdc.kugi.kyoto-u.ac.jp/kp/index. html for January-February 2012—2015. We obtained 27-day and 81-day averaged values of solar ($<F_{10.7}>_{27}$ and$<F_{10.7}>_{81}$) and geomagnetic ($<Ap>_{27}$ and $<Ap>_{81}$) activity indices for 19 January of each year (Table 1). $<Ap>_{27}$ and $<Ap>_{81}$ showed that the considered periods were geomagnetically quiet. We used $<F_{10.7}>_{27}$ (since it was similar to $<F_{10.7}>_{81}$ for the considered periods (see Table 1)) to examine N_mF2 dependence on the solar activity.

In order to estimate dependence on solar activity of N_mF2 diurnal variation in the middle latitudes we used the ionosonde data of seven stations from the Space Physics Interactive Data Resource (SPIDR) (http://spidr.ngdc.noaa.gov). We carried out the manual processing of SPIDR data due to various technical aspects of data recording. In addition we used the N_mF2 observation data from the Irkutsk and Kaliningrad ionosondes.

TABLE 1. 27- and 81-averaged values of the $F_{10.7}$ and *Ap* indexes for 19 January 2012—2015.

Year	$<F10.7>_{27}$	$<F10.7>_{81}$	$<Ap>_{27}$	$<Ap>_{81}$
2012	128	124	7.3	6.5
2013	122	110	5.4	4.7
2014	149	154	4.7	6.8
2015	132	139	9.3	10.2

TABLE 2. The list of stations.

Station	Latitude, degrees	Longitude, degrees
Port Stanley	-51.7	-57.8
Jeju	33.5	126.5
I-Cheon	37.1	127.5
Boulder	40.0	-105.3
Rome	41.8	12.5
Pruhonice	50.0	14.6
Irkutsk	52.5	104.0
Kaliningrad	54.0	20.0
Moscow	55.5	37.3

In order to estimate dependence on solar activity of N_mF2 diurnal variation in the middle latitudes we used the ionosonde data of seven stations from the Space Physics Interactive Data Resource (SPIDR) (http://spidr.ngdc.noaa.gov). We carried out the manual processing of SPIDR data due to various technical aspects of data recording. In addition we used the N_mF2 observation data from the Irkutsk and Kaliningrad ionosondes. These data were obtained from the manually scaled ionograms using interactive ionogram scaling software, SAO Explorer [5, 6] in the case of the Irkutsk ionosonde and PARUS software [7] in the case of the Kaliningrad ionosonde. The geographic coordinates of all considered stations are presented in the Table 2. We obtained 27-daily median N_mF2 values for diurnal variations over all 9 stations for 19 January 2012, 2013, 2014 and 2015. Diurnal variations in N_mF2 were obtained in terms of UT epoch and then transferred to local time (LT) diurnal variations.

3. Data analysis result. Figure 1 shows N_mF2 27-day median diurnal variations on 19 January for four years (2012—2015) over nine stations. It is evident that the solar activity has the greatest impact on the daytime N_mF2 values. Over all stations (exclude Port Stanley) the following paradox is revealed: the greatest daytime N_mF2 values observed in January of 2015 do not correspond to the maximum in $<F_{10.7}>_{27}$ index (that observed on January 2014). As the following step, we cal-

culated the 19 January daytime averaged (10:00—14:00 LT) N_mF2 values ($<N_mF2>$) for all the considered stations. On the basis of $<N_mF2>$ and $<F_{10.7}>_{27}$ values in a manner similar to [3, 8] we constructed the linear regressions $<N_mF2>_{27,daytime} = a_0 + a_1 \times (<F_{10.7}>_{81} - 70)$ for different data sets: (1) "without 2014"; (2) "without 2015"; and (3) "all years"; (4) dual linear regressions $<N_mF2>_{27,\ day} = = b_0 + b_1 \times (<F_{10.7}>_{81} - 70) + b_2 \times (<Ap>_{27} - 4)$ for 2012—2015 years. Linear and dual regression coefficients for all considered datasets are shown in the Table 3.

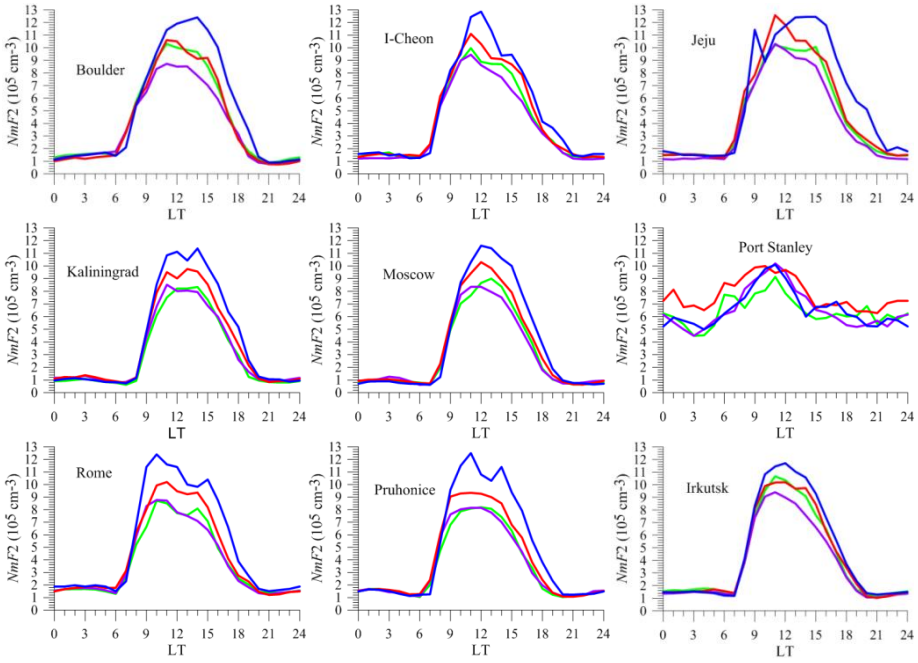

FIGURE 1.27-day median *NmF*2 diurnal variation on 19 January 2012 (green), 2013 (purple), 2014 (red), 2015 (blue) for all considered stations.

Figure 2 shows the solar activity dependences of daytime $<N_mF2>_{27}$ and results of all the obtained linear and dual linear regressions. It is seen that: (1) the cases of "without 2015" and "all years" are close to each other and differ significantly from the case "without of 2014"; and (2) $<N_mF2>_{27}$ in 2015 has the greatest deviations from the linear regression compared to $<N_mF2>_{27}$ in other years in the "all years" case. Additionally, the linear regression in the "without 2014" case leads to negative (confusion) $<N_mF2>_{27}$ values at $<F_{10.7}>_{27}=70$ that is nor seen in linear regressions for the cases of "without 2015" and "all years". All these results demonstrate that daytime $<N_mF2>_{27}$ on 19 January 2015 does not fit the solar activity dependence obtained for $<N_mF2>_{27}$ in other years, i. e. are anomalous from solar activity dependence view point. Also it is evident that the linear regression are the greatest deviations from baseline data in 2014 and 2015.

TABLE 3. Linear and Dual regression coefficients for different time intervals.

Station	Linear regression coefficients for 2012, 2013, 2015		Linear regression coefficients for 2012, 2013, 2014		Linear regression coefficients for 2012—2015		Dual linear regression coefficients for 2012—2015
	a_0	a_1	a_0	a_1	a_0	a_1	b_0 b_1 b_2
Boulder	-7.654	0.306	6.888	0.038	7.713	0.034	4.148 0.066 0.545
I-Cheon	-4.159	0.239	6.226	0.046	7.002	0.043	4.196 0.068 0.394
Irkutsk	-3.728	0.237	7.355	0.035	7.894	0.031	5.284 0.055 0.404
Jeju	0.329	0.172	6.282	0.062	6.679	0.059	5.236 0.072 0.192
Kaliningrad	-4.867	0.236	4.853	0.053	5.707	0.049	2.803 0.077 0.385
Moscow	-4.671	0.236	5.133	0.053	5.884	0.049	3.168 0.075 0.374
Port Stanley	11.682	-0.06	6.838	0.028	6.801	0.028	7.677 0.022 -0.182
Pruhonice	-9.441	0.322	5.219	0.049	6.326	0.043	2.086 0.083 0.591
Rome	-7.196	0.284	4.504	0.064	5.479	0.060	2.140 0.091 0.450

Analyzing Figure 3 and Table 1, we find that the January of 2015 is characterized by the greatest geomagnetic activity and the January of 2014 is characterized by the lowest geomagnetic activity compared to other years. Considering a positive deviation of $<N_mF2>_{27}$ in 2015 and a negative deviation of $<N_mF2>_{27}$ in 2014 from the linear regression in the "all years" case, we may assume a positive impact of geomagnetic activity on the January daytime N_mF2 values. So the positive correlation of geomagnetic activity and the daytime $<N_mF2>_{27}$ January values is revealed. We carried out verification of the version about a positive contribution of geomagnetic activity to в daytime $<N_mF2>_{27}$ on the basis of the dual linear regression. Comparison of dual linear regression with observation data and linear regressions (Fig. 2) has revealed smaller deviations of dual linear regression from basic data. This result confirms a conclusion about a positive contribution of geomagnetic activity to daytime January N_mF2 values.

4. Conclusions. In this paper we have analyzed the solar activity dependence of the 2012—2015 N_mF2 winter diurnal variations and daytime N_mF2 values for different locations. We have shown that usually the daytime N_mF2 depends linearly on solar activity. The following paradox was discovered: the daytime N_mF2 values in January of 2014 were less than those in January of 2015, although the solar activity index $<F_{10.7}>_{27}$ in January of 2014 was more than that in January of 2015. This paradox was seen for all the considered stations (excluding Port Stanley). Constructing linear and dual linear regressions for different data sets and analyzing the geomagnetic activity behavior we made a conclusion about a positive impact of geomagnetic activity on the January daytime N_mF2 values.

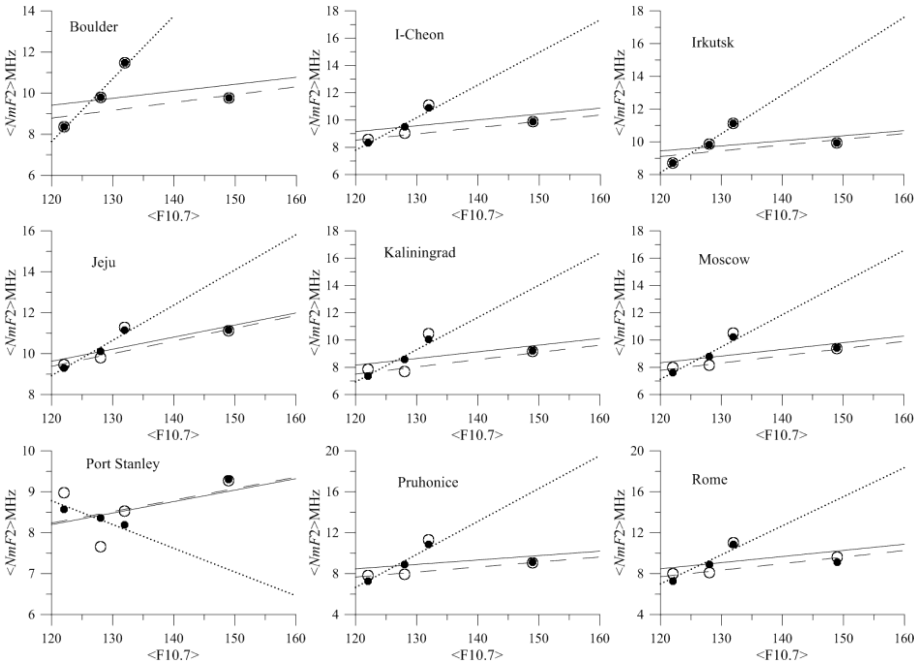

FIGURE 2. Daytime *NmF*2 dependence on the solar activity at different stations obtained by linear regression of data (presented by circles) for January 19 (1) 2012, 2013, 2015 (dotted line); (2) 2012, 2013, 2014 (dashed line); (3) all years in the consideration (solid lines) and dual linear regressions for 2012—2015(dark circles).

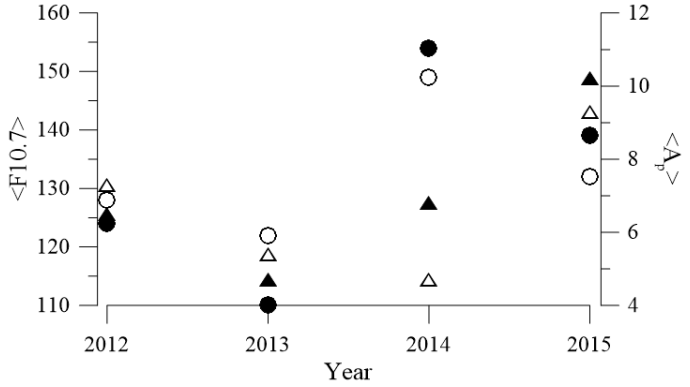

FIGURE 3.$<F10.7>_{27}$ (○), $<F10.7>_{81}$ (●), $<Ap>_{27}$ (Δ), $<Ap>_{81}$ (▲) for 19 January 2012—2015.

1. B. E. Bryunelli and A. A. Namgaladze, Physics of the ionosphere, M., Nauka, 1988, 526 p. (in Russian).

2. H. Rishbeth and I. C. F. Müller-Wodarg, Vertical circulation and thermospheric composition: a modeling study, *Ann. Geophys.*, 1999, 17, pp. 794—805.

3. K. G. Ratovsky and A. V. Oinats, Medvedev, Similitaries and differences between regular variations of F2-layer parameters of the polar and midlatitude ionosphere in east Siberian sector, *Sol.-Terr. Phys.*, 2015, 1(2), pp. 70—79.

4. J. Lei, L. Liu, W. Wan, and S.-R. Zhang, Variations of electron density based on long-term incoherent scatter radar and ionosonde measurements over Millstone Hill, *Radio Sci*., 2005, 40, RS 2008, doi: 10.1029/2004RS003106.

5. B. W. Reinisch, I. A. Galkin, G. Khmyrov et al., Automated collection and dissemination of ionospheric data from the digisonde network, *Adv. Radio Sci.*, 2004, 2, pp. 241—247.

6. G. M. Khmyrov, I. A. Galkin, A. V. Kozlov et al., Exploring digisonde ionogram data with SAO-X and DID Base, In: *Proc. AIP Conf. Radio Sounding and Plasma Physics*, 2008, 974, pp. 175—185.

7. A. L. Karpenko and N. I. Manaenkova, Nonlinear time series analysis of the ionospheric measurements, *Geologishe Rundshau*, 1996, 85(1), pp.124—129.

8. K. G. Ratovsky and A. V. Oinats, Local empirical model of ionospheric plasma density derived from digisonde measurements at Irkutsk, *Earth Planets Space*, 2011, 63(4), pp. 351—357.

Statistical Processing of Radio Occultation Data of the Ionospheric F2 Peak Parameters

Nicolai V. Chirik[1], Maxim V. Klimenko[1,2]

[1]Immanuel Kant Baltic Federal University, 236004, Nevskogo 14, Kaliningrad, Russia
[2]West Department of Pushkov IZMIRAN, RAS, Kaliningrad, Russia

Electron density distribution in the ionosphere play the main role in HF radio wave propagation, space radio communication, radiolocation, navigation and GPS positioning system quality. In order to resolve the problem of modeling of the ionospheric electron density and to test the ionosphere models we must know the typical spatial and temporal variations of electron density in different conditions. Despite the fact that the main morphological features, all large-scale ionospheric irregularities and their formation mechanisms are well known, there is not the empirical model which could reproduce all these features.

IRI (International Reference Ionosphere) model is widely used in the different applications and reproduced main climatological properties of the ionosphere in the last 40 years. IRI represents good results for ionospheric parameters in the middle latitudes for quiet geomagnetic conditions. URSI and CCIR options of the IRI model describe the *F*2 layer peak parameters obtained from ground-based and satellite observation data. The ionospheric parameters according to the CCIR option of IRI model for Southern Hemisphere were obtained by extrapolation along geomagnetic field lines [1]. In contrast the URSI option of IRI model uses the theoretical model results and observed *foF*2 values [2]. IRI model uses the international geomagnetic reference field model for correct geomagnetic field calculations. IRTAM model uses Non-linear Error Compensating Technique for Associative Res-

toration (NECTAR) to adjust the CCIR coefficients to match real-time digisonde measurements from the Global Ionosphere Radio Observatory (GIRO) [3].

Figure 1 summarizes the main aspects of radio occultation (RO) method for ionospheric parameters retrieval. The vertical profile of the physical parameters of the atmosphere and ionosphere are measured along the trajectory of tangent point *T* where radio waves propagate along atmospheric (ionospheric) layers. The main assumptions for RO technique are the following:(1) spherical symmetry of the atmosphere and ionosphere; (2) the existence only one tangent point on ray GTL which coincides with radio ray perigee *T*.

High-precision GPS radio signals at two frequencies f_1 = 1575.42 and f_2 = 1227.6 MHz emitted by a GPS satellite (point *G*) arrive at the receiver onboard of the LEO satellite (point *L*) along the ray GTL. In the case of spherical symmetry with center *O* the amplitude and phase variations of the RO signals are caused mainly owing to the medium influence at the tangent point *T*. At the tangent point *T* the RO ray is perpendicular to the vertical gradient of refractivity. The cornerstone assumption of the RO technique is: the tangent point coincides with the ray perigee *T*. Location of the center *O* is supposed to be known and the geographical coordinates of the ray perigee (point *T*) can be evaluated by use of orbital data of GPS and LEO satellites. Then the Doppler frequency and orbital data are used to find the impact parameter *p* and refraction angle *x*(*p*). Abel inversion technique allows one to obtain the vertical profile of the refractivity $N_e(h)$ in the atmosphere and/or in the ionosphere, where *h* is the height of the ray perigee [4].

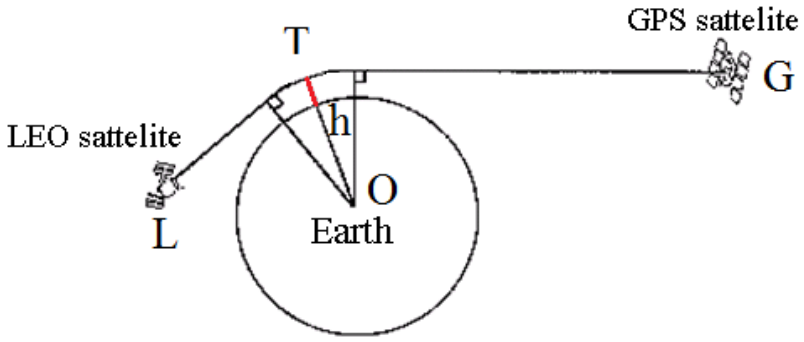

FIGURE 1. Scheme of radio occultation technique.

We code softwarefor statistical analysis of radio occultation data obtained by COSMIC, GRACE, and CHAMP satellites that allow to obtain ionospheric *F*2 layer peak parameters. Now we can process data set from 2001 to 2015 and use the different solar activity indices. The algorithm of data averaging allows to choose the day, hour and averaging interval for these parameters. For the rejection of non-physical data we can choose available altitudinal, latitudinal and longitudinal intervals of vertical profiles. Using the code results we can get the table with geographic coordinates, average arithmetic and median values of the h_mF2, $foF2$, and N_mF2 and count the rejected data for each criterion. Figure 2 presents the h_mF2 and

*foF*2 maps for 12:00 LT in solar activity minimum ($F_{10.7}$ ~ 60—100) obtained using our software.

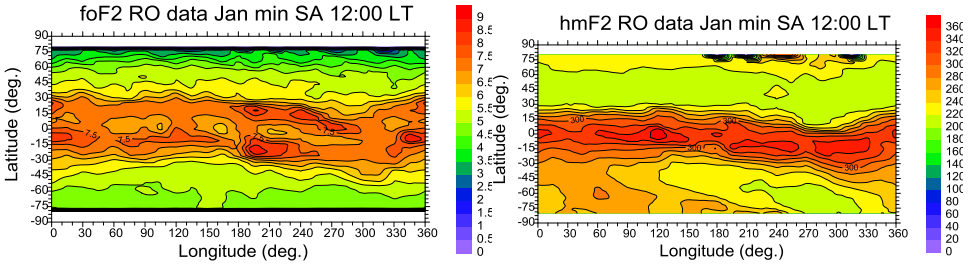

FIGURE 2. Maps of the foF2 and NmF2 values, constructed using the data obtained by radio occultation method.

As another example of our software application we study diurnal-seasonal variation of N_mF2 during 2009 using radio occultation data of COSMIC and GRACE satellites. We calculate the median N_mF2 values for the 22nd day of each month averaged in interval ± 30 days. Radio occultation measurements deviation of current coordinates does not exceed 5 degrees in latitude and 15 degrees in longitude. In addition we used the following radio occultation data restrictions:

1) the*F*2 peak height lies in altitudinal interval from 180 km up to 450 km;

2) the latitudinal and longitudinal intervals of RO vertical profiles don't exceed of 10° in latitude and of 20° in longitude;

3) the number of negative data does not exceed 100 values per file;

4) the vertical gradients between maximum and adjacent points don't exceed 20%.

Also we used the ionosonde data of N_mF2 values in interval ± 13 days about each day of 2009 and the results of GSM TIP and IRI modeling. Figure 3 presents the comparison of diurnal-seasonal variations of normalized N_mF2(LT)/ N_mF2(12:00 LT) over Kaliningrad. One more example of usage radio occultation measurements (Fig. 4) presents its possibility to reproduce climatological spatial features of sub-auroral ionospheric *foF*2 and in particular the main ionospheric thougth modeling. The similar results were presented in [5].

Acknowledgments. *These investigations were performed with financial support of the Russian Foundation for Basic Research Grants No. 14-05-00788 and 15-35-20364 and within the project "Physical mechanisms of the reaction of the upper atmosphere and ionosphere on the processes in the lower atmosphere and on the Earth surface" (State task Education and Science Ministry of the Russian Federation, the competitive part of the task No. 3.1127.2014/K).*

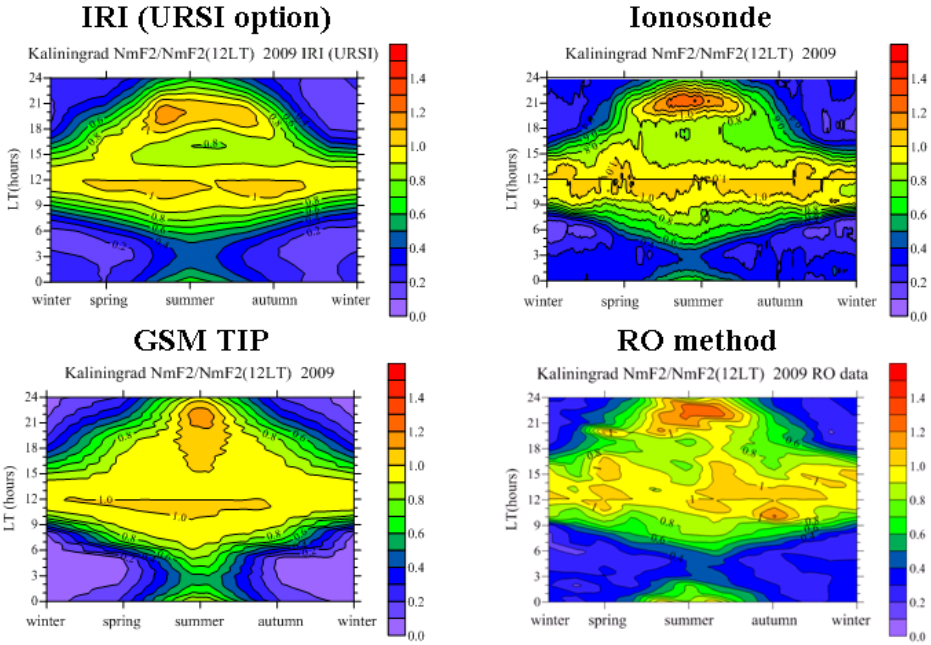

FIGURE 3. Seasonal dependence of diurnal variation in NmF2/NmF2(12 LT) in 2009 above Kaliningrad. On the left panel are shown the simulated results obtained in IRI (top) and GSM TIP model (bottom). On the right panel are shown the observation data of ground-based ionosonde (top) and radio occultation (bottom).

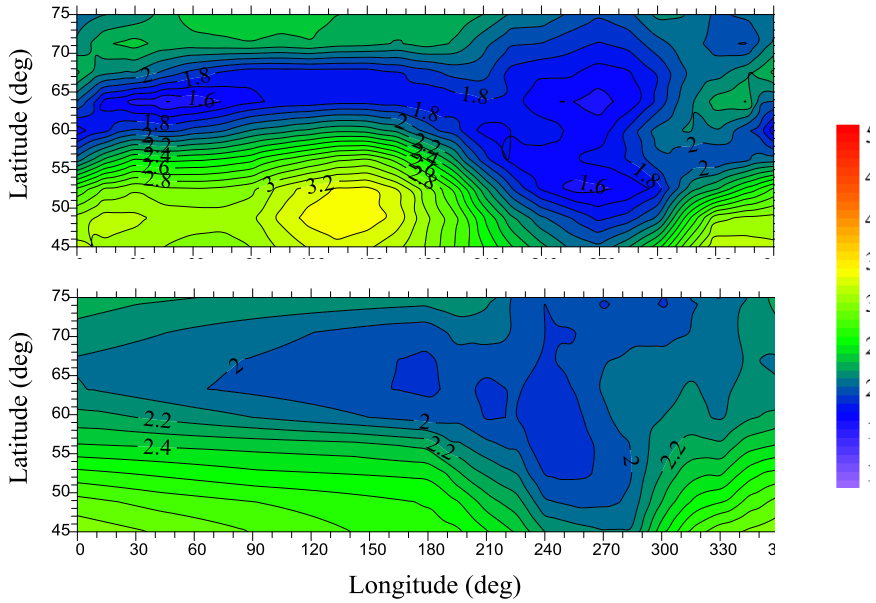

FIGURE 4. Spatial distribution of the *foF*2 obtained using MIT model (top) and statistical processing of radio occultation data (bottom).

Acknowledgments. *These investigations were performed with financial support of the Russian Foundation for Basic Research Grants No. 14-05-00788 and 15-35-20364 and within the project "Physical mechanisms of the reaction of the upper atmosphere and ionosphere on the processes in the lower atmosphere and on the Earth surface" (State task Education and Science Ministry of the Russian Federation, the competitive part of the task No. 3.1127.2014/K).*

1. W. B. Jones and R. M. Gallet, The Representation of Diurnal and Geographic Variations of Ionospheric Data by Numerical Methods, *Telecomm. J.*, 1962, 5, pp. 3—23.

2. M. W. Fox and L. F. McNamara, Improved World-Wide Maps of Monthly Median foF2, *J. Atmos. Terr. Phys*., 1988, 50, 1077.

3. I. A. Galkin, B. W. Reinisch, X. Huang et al., Assimilation of GIRO Data into a Real-Time IRI, *Radio Sci.*,2012, 47, RS0L07, doi:10.1029/2011RS004952.

4. N. Jakowski, R. Leitinger, and M. Angling, Radio occultation techniques for probing the ionosphere, *Ann. Geophys*., 2004, 47(2—3), pp. 1049—1066, doi:10.4401/ag-3285

5. L.-T. Lee, W. Wang, J. Liu et al., The ionospheric midlatitude trough observed by FORMOSAT-3/COSMIC during solar minimum, *J. Geophys. Res.*, 2011, 116, A06311, doi: 10.1029/2010JA015544.

Validation of the Technique for Estimation of Absolute Total Electron Content and its Gradients

Anna A. Mylnikova[1], Yury V. Yasyukevich[1,2]

[1] Institute of Solar-Terrestrial Physics of Siberian Branch of Russian Academy of Sciences, Irkutsk, Russia.
[2] Irkutsk State University, Irkutsk, Russia

Introduction. It is mandatory to have accurate values of ionospheric parameters for solution of theoretical and applied ionospheric physics problems when entire electron profile is unknown. The most common parameters for radio physics problems are F2 layer peak height and F2 layer critical frequency. Also, total electron content (TEC) is recently recognized as yet another important parameter.

Ionospheric TEC is estimated by using GPS and GLONASS dual-frequency code and phase measurements of pseudo ranges. TEC derivation is performed using the code and phase measurements simultaneously since phase measurements are ambiguous and code measurements are noisy[1].

We present the technique for estimation of absolute vertical TEC, its horizontal gradients and differential code biases (DCB). DCB is systematic error in TEC caused by the difference in processing time for L1 and L2 signals in satellite and receiver hardware. The validation of the technique was performed using IRI 2012 and data from Global Ionospheric Maps (GIM) computed by CODE.

Data. For the validation we use GLONASS/GPS receivers data, vertical TEC values as given by GIM and slant TEC derived from IRI-2012 model. Slant TEC data derived from IRI are obtain for geometry GLONASS/GPS satellite-receiver and are referred as *modeled STEC*. Modeled STEC is calculated using line integrated electron density given by IRI along path satellite-receiver. Absolute vertical TEC is evaluated from modeled STEC using our technique is referred as I_{V_IRI}. For validation we calculated vertical TEC over receiver *IRI_VTEC* and compared to I_{V_IRI}. The aforementioned can be understood as verification of the technique.

Further we compared absolute vertical TEC evaluated from GLONASS/GPS measurements (I_V) and TEC obtained from GIM computed by CODE (*GIM_VTEC)*.

Absolute vertical TEC estimation technique. Algorithm for absolute vertical TEC, its gradients and DCB estimation is based on dual-frequency GLONASS/GPS measurements. It is developed in ISTP and called TayAbsTEC [2]. It is based on Taylor expansion and has following structure:

- The calculation of STEC based on the dual-frequency code and phase measurements [1, 3].
- The division of data into continuous series.
- The detection and elimination TEC series discontinuities such as outliers and jump discontinuity caused by cycle slip.
- The elimination of the phase measurement ambiguity.
- The estimation of absolute vertical TEC, TEC gradients and DCB using a TEC measurement model.

We used the following TEC measurement model, where parameters are vertical TEC (I_V) and TEC uncertainty related to DCB (I_{BLAS}):

$$I_M = S_j^i \begin{Bmatrix} I_V(\phi_0, l_0, t_0) + G_\varphi \cdot \Delta\varphi_j^i + G_{q\_\varphi} \cdot (\Delta\varphi_j^i)^2 + G_l \cdot \Delta l_j^i \\ +G_{q\_l} \cdot (\Delta l_j^i)^2 + G_t \cdot \Delta t_j^i + G_{q\_t} \cdot (\Delta t_j^i)^2 \end{Bmatrix} + I_{BIASj} \quad (1)$$

The model is a classical second-order Taylor series expansion of I_V in space and time. Mapping function (S_j^i) which converts slant TEC into vertical one.

$$S_j^i = \left[cos\left\{\arcsin\left(\frac{R_E}{R_E + h_{max}} \sin[\alpha \cdot (90 - \theta_i^j)]\right)\right\}\right]^{-1}, \quad (2)$$

whereθ_i^j — satellite elevation angle, R_E — Earth radius, h_{max} is the height of the thin spherical layer (450 km). Then we estimated I_V and I_{BLAS} by mean of least squares between measured STEC and I_M. Some researches [4] introduced $\alpha < 1$ in mapping function to increase accuracy of vertical TEC estimation. Moreover, α depends on the height of the thin spherical layer. We found α dependence on the geographical coordinates. It originates form the fact that slant TEC depends on elevation in different manner for different regions of Earth.

We should mention that other algorithms and models for absolute vertical TEC estimation also exist and use approximations of a thin one layer [4, 5] and two layer ionosphere [6].

Results: absolute TEC derived from IRI-2012. IRI_VTEC is computed in coordinate range 27°—76° N и 79°—128° E with longitude and latitude step 2.5°. I_{V_IRI} is estimated by TayAbsTEC above the IRKJ station (52.3° N., 104.3° E.) and some distance away from the station with longitude and latitude step 2.5°. TEC in the station vicinity was obtained using I_{V_IRI} and TEC gradients. We calculated difference (*dI*) between I_{V_IRI} and *IRI_VTEC* in each point with latitude step 2.5° on longitude of station (Fig. 1a) and with longitude step 2.5° on latitude of station (Fig. 1b).

Figure 1a shows that *dI* increases with distance is increasing. The highest values of *dI* are at distance more than 20° to South and North from the station for 4—9 UT (11—16 LT). *dI*increases faster towards equatorial ionosphere than toward high latitude ionosphere.

Figure 1b shows that *dI* weakly depends on distance from station, so dependence of *dI* on longitude is less than its dependence on latitude. There is a clear dependence of *dI* on time. The maximum *dI* is observed during the period 2—4 UT and 12—16 UT, or in local time it would be 10—12 LT and 20—24 LT at 128 E and 1—4 LT on next day at 80 E. The minimum *dI* (~0 TECU) is observed at 18.5 LT.

dI depends more on latitude than on longitude. It causes bigger gradients along meridian especially in the daytime when equatorial anomaly is more pronounced.

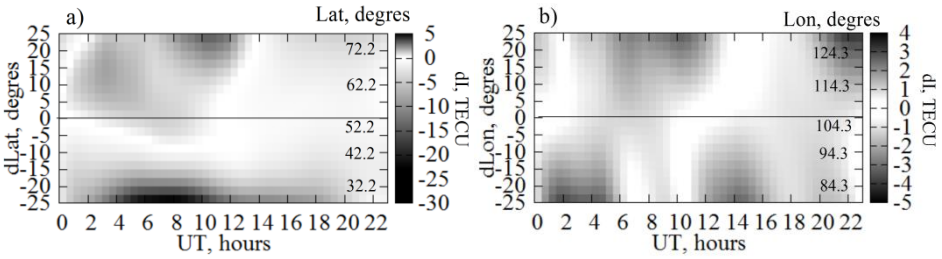

FIGURE 1. Dependence of *dI* on time and distance from station on latitude (*dLat*) (a) and on longitude (*dLon*) (b).

Comparison of observation derived absolute TEC and GIM. Here we compare estimated VTEC by TayAbsTEC (I_V) and VTEC data from GIM computing by CODE (GIM_VTEC) are used for testing. I_V is derived using GLONASS/GPS measurements from Australian network receivers (ftp://ftp.gagov.au/geodesy-outgoing/gnss/data). Similar to the previous section difference (*dI*) between I_V and GIM_VTEC is computed and plotted versus distance from station along latitude and longitude. *dI* is computed for two stations: MAC1 (54.49° S. 158.93° E.) and LORD (31.52° S. 159.06° E.). MAC1 station is taken into account when GIM is calculated, LORD station is not part of the data gone into GIM. Moreover there are no stations near lord station used to calculate GIM.

dI is plotted versus latitude (a) and longitude (b) on Figures 2 and 3. *dI*is presented for the geomagnetic quiet day — March 5, 2015 Kp = 1.3 (Fig. 2) and for geomagnetic storm — March 17, 2015 Kp=7.7 (Fig. 3). Zero value corresponds to location of a station. Gray dotted lines present *dI* dependence on *dlat* for LORD station, black solid lines present that for MAC1 station. Each line corresponds to specific time, time step is 2 hours.

Figures 2a and 3a show that *dI* values at away from station latitude-wise are much higher for LORD than for MAC1. We remember that LORD is not taken into account for GIM calculation and MAC1 is. During geomagnetic storm *dI* is scattered more than on the geomagnetic quiet day for same station but does not exceed *dI* scattering for the day during geomagnetic storm for LORD station. The highest LORD station's *dI* is observed at 13 LT both on the geomagnetic quiet day and during geomagnetic storm.

On Fig. 2b and 3b *dI* almost does not depend on distance along longitude for both stations LORD and MAC1. However *dI* is scattered stronger for LORD than for MAC1. During geomagnetic storm (Fig. 3b) *dI* scattering increases in comparison to *dI* on the geomagnetic quiet day for both stations LORD and MAC1.

Big difference between *dI* for MAC1 and LORD is probably due to the fact that GIM_TEC data near LORD station is result of interpolation and not direct measurements. Data from LORD station and nearest stations are not gone into GIM calculation, so these GIM_TEC data are less precise as compared with GIM_TEC data near MAC1 station, data of which go into GIM calculation.

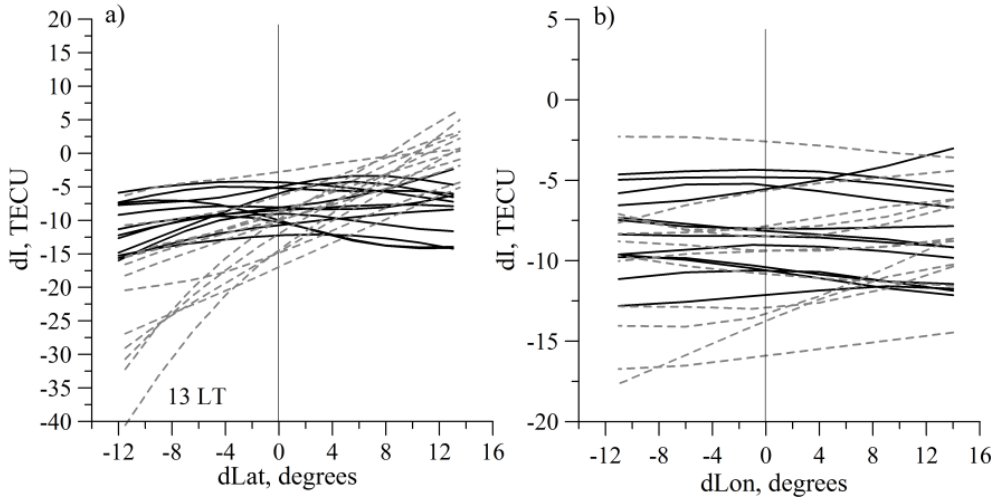

FIGURE 2. Dependence of *dI* on time and distance from station on latitude (a) and on longitude (b). March 5, 2015 (Kp=1.3). Black solid lines — mac1 station (54.49° S.158.93° E.), gray dotted lines — lord station (31.52° S. 159.06° E.).

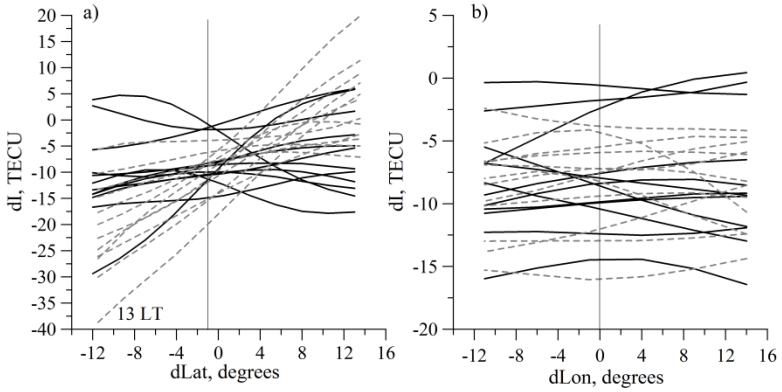

FIGURE 3. The same as in Fig 3, but for the March 17, 2015 (Kp=7.7).

Conclusion. Validation of the technique TayAbsTEC is performed on the base of IRI-2012 and absolute vertical TEC from GIM. It was found that *dI* increases with distance from station along latitude. Also, *dI* increases faster equator-ward rather than towards high latitudes. The maximum *dI* is observed at the distance more than 20° to North and South from station during 11—16 LT. *dI* almost does not depend on a distance along longitude, but there is clear time dependence of *dI*.

As a result of comparison VTEC data estimated by TayAbsTEC and VTEC from GIM it can be concluded that for region where there are no GNSS stations are used to calculate GIM, *dI* higher than for region where stations are present. On the day during geomagnetic storm *dI* much higher than on the geomagnetic quiet day. This difference is due to the fact that GIM data near station not used for computing GIM is result of interpolation rather than direct measurements.

Based on these results, we conclude that using spatial gradients given by TayAbsTEC for regional TEC maps is possible. The ranges of confident TEC prediction with use of gradients are 10° along latitude from station and 20° along longitude.

Acknowledgements.*The study was supported by the Russian Foundation for Basic Research, project no. 16-35-00051_mol_a.*

1. E. L. Afraimovich, E. I. Astafyeva, V. V. Demyanov et al., A review of GPS/GLONASS studies of the ionospheric response to natural and anthropogenic processes and phenomena, *J. Space Weather Space Clim.*, 2013, 3, A27.

2. Yu. V. Yasyukevich, A. A. Mylnikova, and A. S. Polyakova, Estimating the total electron content absolute value from the GPS/GLONASS data, *Results in Physics*, 2015, 5, pp. 32—33.

3. B. Hofmann-Wellenhof, H. Lichtenegger, and J. Collins, Global Positioning System: Theory and Practice, New York, Springer—Verlag Wien, 1992, 327 p.

4. S. Schaer, Mapping and Predicting the Earth's Ionosphere Using the Global Positioning System, Dissertation, Astronomical Institute, University of Berne, Berne, Switzerland, 25 March 1999.

5. N. Jakowski, C. Mayer, M. M. Hoque, and V. Wilken, Total electron content models and their use in ionosphere monitoring, *Radio Sci.*, 2011, 46(6), RS0D18, doi 10.1029/2010RS004620

6. M. Hernandez Pajares, J. M. Juan, and J. Sanz, New approaches in global ionospheric determination using ground GPS data, *J. Atmos. Sol.—Terr. Phys.*, 1999, 61(16), pp. 1237—1247.

Investigation of Geomagnetic Storm and Sudden Stratospheric Warming Impact on HF Radio Wave Propagation

Daria S. Kotova[1,2], Maxim V. Klimenko[1,2], Vladimir V. Klimenko[1], Veniamin E. Zakharov[2], Yuriy N. Korenkov[1], and Fedor S. Bessarab[1,2]

[1]West Department of Pushkov IZMIRAN, RAS, Kaliningrad, Russia
[2]Immanuel Kant Baltic Federal University, Kaliningrad, 236041, Russia

Introduction. In slightly inhomogeneous medium for description of HF radio wave propagation the geometric optic approximation is applicable. Ionosphere is three dimensional anisotropic inhomogeneous medium for HF radio wave propagation. There are a lot of reasons for variability in plasma electron density. One of the sources of such variability is geomagnetic storm that has a global and continuance impact to ionospheric variability. Earlier using rocket observation it was shown that stratospheric warming and other processes may influence to upper atmospheric layers. Understanding the relation between the lower atmosphere and thermosphere/ionosphere system through mesosphere is a very important scientific objective for knowledge of upper atmosphere physics and forecast of the ionosphere and HF radio wave propagation (RWP). Sudden Stratospheric Warming (SSW) represents large meteorological event that is associated with global essential anomalies that occur at heights from the troposphere to the lower thermosphere.

Earlier we realized the program software for numerical calculation of radio ray path in the ionosphere that can used any modeled medium [1—3]. In the given report we used numerical results obtained from Global Self-consistent Model of the Thermosphere, Ionosphere and Protonosphere (GSM TIP) model as propagation environment for HF signals. The comparison of the modeled/data *F* region peak parameter behavior during the periods of geomagnetic storm on September 26—29, 2011 [4] and SSW 2009 [5] revealed a fairly good qualitative agreement at different longitudes and latitudes. The aim of this paper is to investigate the impact of considered events on HF radio communication.

SSW influence on radio wave propagation. The prolonged continuous minimum of solar and geomagnetic activity 2007—2009 allows careful examination of the relationship between the processes in the middle and upper atmosphere, as this

period minimized solar and magnetospheric sources in upper atmosphere variability. The January 2009 presents a unique major Stratospheric Warming event that was very strong and long-lasting. Ionospheric effects in Russia's Asia region during SSWs in the winters 2008/2009 were presented in [6]. Several scientific groups using different models and various additional techniques (assimilation, nudges, etc.) attempted to reproduce the observed equatorial electromagnetic drift and total electron content disturbances during 2009 SSW event, with different level of success [7—9]. The new approach for reproducing of the ionospheric response to 2009 SSW event with setting an additional upward and downward electromagnetic plasma drift velocities close to Jicamarca observations [5] indicates that the GSM TIP can reproduce the observed low-latitude pre-noon positive and daytime negative *TEC* disturbances.

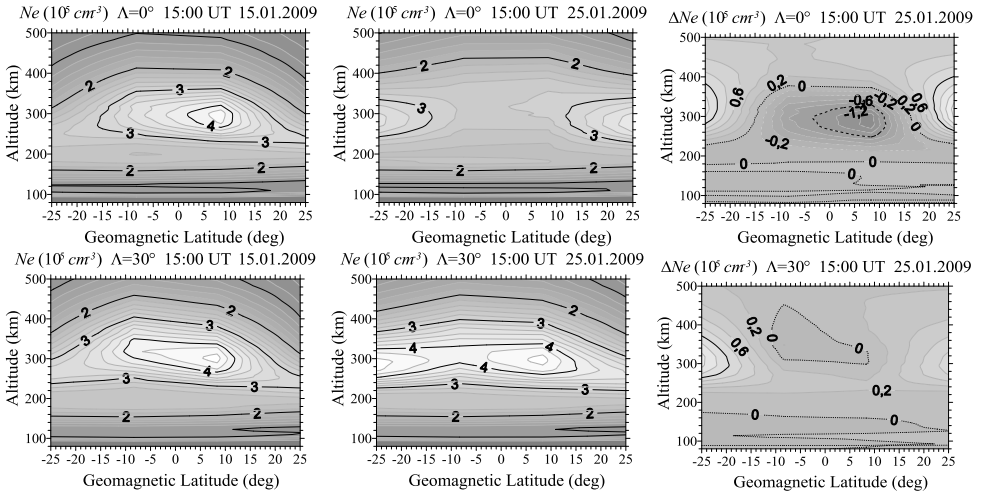

FIGURE 1. Modeled from -25º to 25º altitudinal dependence of latitudinal profiles of electron density at 15:00 UT on 15 January (left panel), on 25 January (middle panel) and their differences (right panel) at 0º (top panel), 15º (middle panel) and 30º (bottom panel) geomagnetic longitudes.

To simulate the thermospheric/ionospheric parameters during major 2009 SSW event we used the algorithm presented in [5]: (1) the stratospheric anomalies during SSW event were modeled by specifying the temperature and density perturbations at the lower boundary of the TIME-GCM (height of 30 km) according to data from European Centre for Medium-Range Weather Forecasts (ECMWF); (2) TIME-GCM output at 80 km was used as lower boundary conditions for driving GSM TIP model runs; (3) we have set the additional electric potential in its equation in the GSM TIP model at all geomagnetic latitudes to test the generation mechanism of large ionospheric effects due to increasing vertical ion drift and performed the model simulation. We performed joint TIME-GCM and GSM TIP model runs and ob-

tained thermospheric and ionospheric parameters: for January 15, 2009 (undisturbed conditions); and for January 25, 2009 (the day with SSW response). Figure 1 represent modeled near-equatorial latitude-altitude slice of electron density and its disturbances at three different longitudes. It is evident the most essential electron density disturbances occurred at *F* region heights (equatorial ionization anomaly (EIA) enhancement). The electron density response to SSW event is almost absent below 220 km.

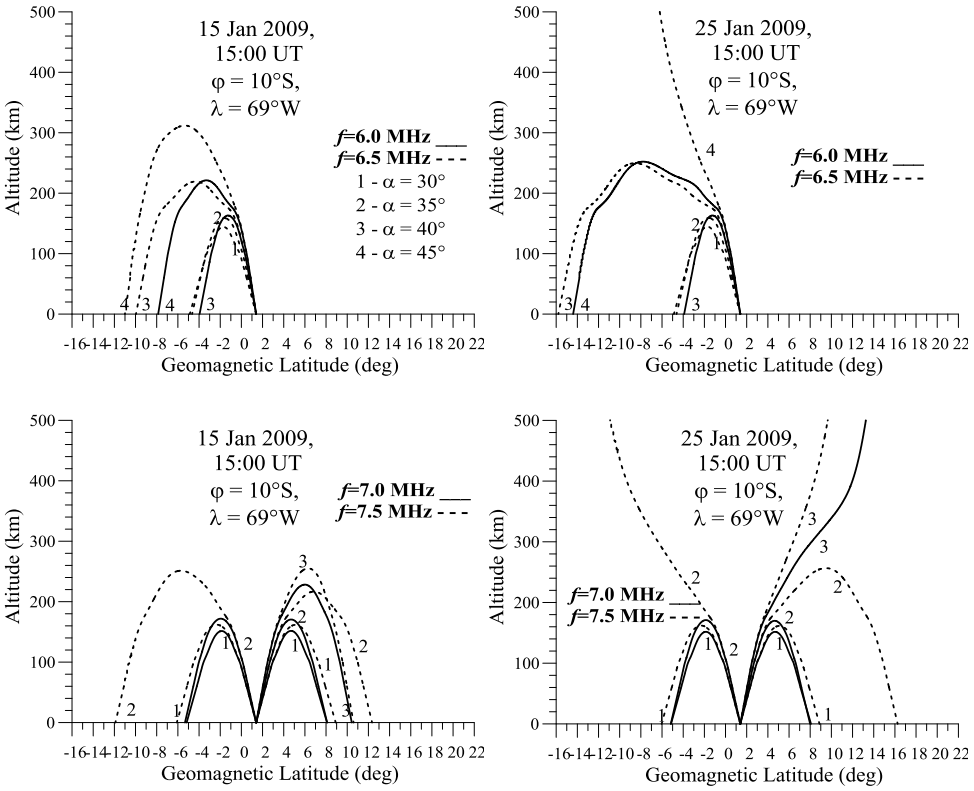

FIGURE 2. The beam structures obtained in model calculation results for radio wave with different frequencies and elevation angles at 15:00 UT on 15 January (left) and 25 January (right).

In order to study the influence of this event on radio wave propagation, we used GSM TIP modeled ionospheric parameters and numerical RWP model [10] with different carrier frequencies. The joint using GSM TIP and RWP models was previously allow to investigate the changes in radio wave propagation during geomagnetic storm events [1—3].

Figure 2 presents the model calculation results of radio wave ray-paths with different frequencies and elevation angles for a hypothetical low-latitude transmitting station with geographic coordinates (10°S, 69°W) at 15:00 UT on 15 and

25 January 2009. The station emits in two directions — northward and southward. These calculations were performed for 15 and 25 January with the same frequency and elevation angle of the transmitter. It may be noted that the number of paths leaving the ionosphere on January 25 is greater than on January 15. The range of radio wave propagation and the reflection height are changed during SSW event. As for the ground radio communications only incoming rays are important, we can conclude that during sudden stratospheric warming the radio communication have deteriorate.

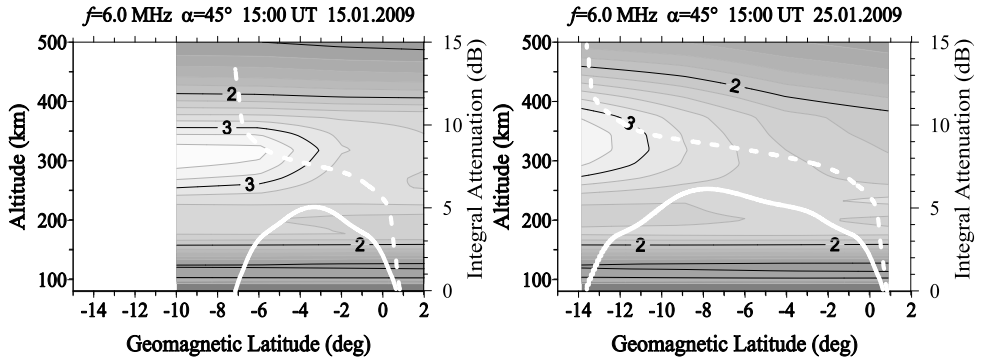

FIGURE 3. Two top panels: Calculated trajectories (white solid lines) and integral dampings (white dashed lines) of radio waves with the frequencies f =6.0 MHz at 15:00 UT on 15 January (left panel) and 25 January (right panel). The electron density vertical profiles are constructed along the trajectories.

Figure 3 shows the geomagnetic latitude-altitude projection of the calculated ray-paths of radio waves, their integral attenuation and the vertical profiles of the electron density along the ray-paths. There are EIA crest displacements from equator and decrease in electron density at the previous locations of the equatorial ionization anomaly crests during SSW event. This leads to the increase in distance of the considered one-hop ray-path. It is well seen that the operating frequency of the radio wave decreases significantly. The attenuation reaches the maximum values in the lower part of the *D* and *E* layers. Strong influence of the non-deflecting attenuation, in which the ray deformation is small and the attenuation is significant, is observed here.

Geomagnetic storm impact to radio communication. The variability of HF signals (its path and attenuation) from an equatorial transmitter during geomagnetic storm on 26—29 September, 2011 is presented in [2]. Here we considered mid- and high-latitude ionosphere during most significant *F* region ionospheric disturbances at 20:00 UT. The modeled transmitter was located at Irkutsk due to good model/data agreement of *F* region ionospheric disturbances at these locations [4]. We used two azimuths for transmission — 0° and 330°. We considered different radio wave frequencies and elevation angles (Fig. 4). In quiet condition almost all considered radio path return to the Earth. During main storm phase due to significant increase (~100 km) in *F*2 peak height and expansion of the main ionospheric

trough toward mid-latitude, all considered radio ray with azimuth 330° does not reflected from the ionosphere (except radio ray with 7 MHz and elevation angle of 10° — that is a high (Pedersen) ray in this case). At radio wave transmission in northward direction the geomagnetic storm lead to increase of radio rays reflection height on ~ 100 km and increase in number of insignificant rays for radio communication. In addition it is evident that all considered rays return to the Earth to the very limited area of latitudes 65°-67.5°.

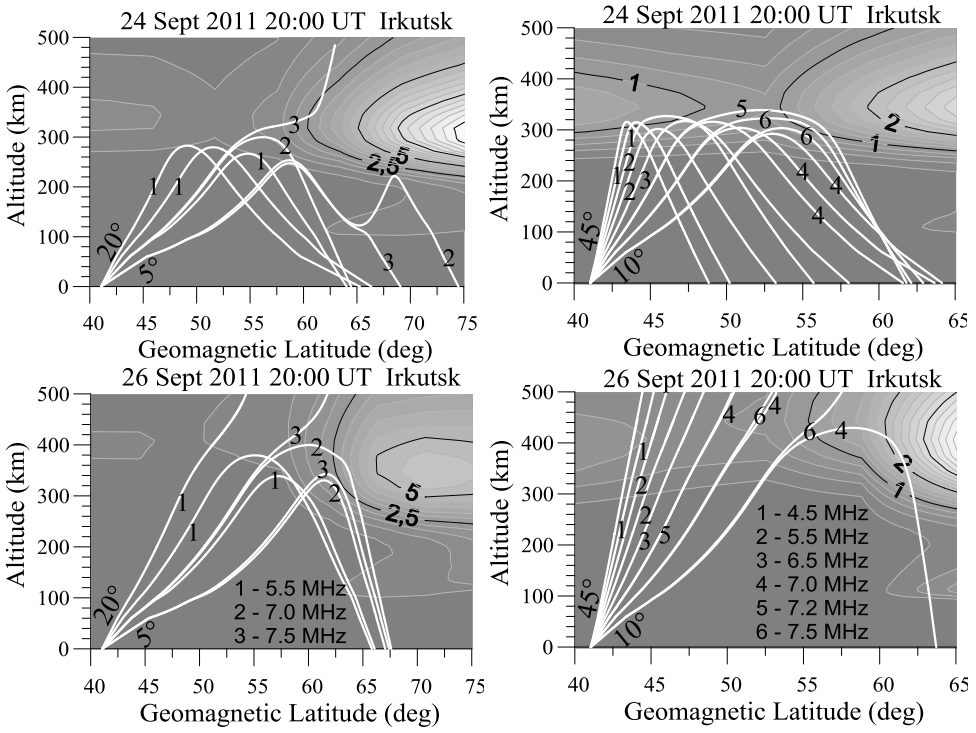

FIGURE 4. Calculated trajectories (white solid lines) of radio waves with different frequencies at 20:00 UT on 24 September (top panels) and 26 September (bottom panel). The electron density vertical profiles are constructed along the trajectories. Left panel — $\beta = 0°$, right panel — $\beta = 330°$. The elevation angle step is 5°.

Conclusion. We considered in more detail the features of the radio ray paths in the equatorial ionosphere during 2009 SSW event. During the event under consideration there has been a decrease of the electron density along the radio ray-paths in the crests of the equatorial anomaly, which leading to the deterioration of the radio communication. During SSW the calculation results have revealed a slight increased attenuation (5%), primarily due to the changes in the composition of the neutral thermosphere during warming. During main storm phase due to significant increase (~100 km) in *F*2 peak height and expansion of the main ionospheric trough toward mid-latitude there is increase in number of insignificant rays for radio communication. The impact of considered geomagnetic storm on HF radio

communication is much greater at high latitudes in comparison to low latitudes. In general the low-latitudes effects during 2009 SSW are more sufficient in comparison to geomagnetic storm effects.

Acknowledgments.*These investigations were supported by RFBR Grants No. 14-05-00578, No. 15-35-20364. The reported study was funded by RFBR according to the research project No. 16-35-00590 мол_а. The work was partially performed in the scope of the project "Physical Formation of the Response of the Upper Atmosphere and Ionosphere to the Processes in the Lower Atmosphere and on the Earth's Surface" (State Order of the Ministry of Education and Science of the Russian Federation, competitive part, order 3.1127.2014/K).*

1. D. S. Kotova, M. V. Klimenko, V. V. Klimenko, and V. E. Zakharov, Numerical simulation of the influence of the May 2—3, 2010 geomagnetic storm on HF radio-wave propagation in the ionosphere, *Radiophysics and Quantum Electronics*, 2014, 57(7), pp. 467—477, doi: 10.1007/s11141-014-9529-2.

2. D. S. Kotova, M. V. Klimenko, V. V. Klimenko et al., Using IRI and GSM TIP model results as environment for HF radio wave propagation model during the geomagnetic storm occurred on September 26—29, 2011, *Adv. Space Res.*, 2015, 56(9), pp. 2012—2029, doi:10.1016/j. asr.2015.05.009.

3. D. S. Kotova, V. E. Zakharov, M. V. Klimenko, and V. V. Klimenko, Development of the Model of HF Radiowave Propagation in the Ionosphere, *Russ. J. Phys. Chem. B*, 2015, 9(6), pp. 983—991, doi: 10.1134/S1990793115050218.

4. M. V. Klimenko, V. V. Klimenko, F. S. Bessarab et al., Influence of Geomagnetic Storms of September 26—30, 2011, on the Ionosphere and HF Radiowave Propagation. I. Ionospheric Effects, *Geomagn. Aeron.*, Moscow, 2015, 55(6), pp. 744—762, doi:10.1134/S0016793215050072.

5. M. V. Klimenko, V. V. Klimenko, F. S. Bessarab et al., Study of the thermospheric and ionospheric response to the 2009 sudden stratospheric warming using TIME-GCM and GSM TIP models: First results, *J. Geophys. Res. Space Physics*, American Geophysical Union, 2015, 120(9), pp. 7873—7888, doi:10.1002/2014JA020861.

6. A. S. Polyakova, M. A. Chernigovskaya and N. P. Perevalova, Ionospheric effects of sudden stratospheric warmings in eastern Siberia region, *J. Atmos. Sol.—Terr. Phys.*, 2014, V. 120, pp. 15—23, doi: 10.1016/j. jastp.2014.08.011.

7. T. Fuller-Rowell, H. Wang, R. Akmaev et al., Forecasting the dynamic and electrodynamic response to the January 2009 sudden stratospheric warming, *Geophys. Res. Lett.*, American Geophysical Union, 2011, 38(13), L13102, doi:10.1029/2011GL047732.

8. H. Jin, Y. Miyoshi, D. Pancheva et al., Response of migrating tides to the stratospheric sudden warming in 2009 and their effects on the ionosphere studied by a whole atmosphere-ionosphere model GAIA with COSMIC and TIMED/SABER observations, *J. Geophys. Res. Space Physics*, American Geophysical Union, 2012, V. 117, A10323, doi:10.1029/2012JA017650.

9. N. M. Pedatella, H.-L. Liu, F. Sassi et al., Ionosphere variability during the 2009 SSW: Influence of the lunar semidiurnal tide and mechanisms producing electron density variability, *J. Geophys. Res. Space Physics*, American Geophysical Union, 2014, 119(5), pp. 3828—3843, doi:10.1002/2014JA019849.

10. V. E. Zakharov and A. A. Cherniak, Numerical model of radio paths of HF radio waves in the ionosphere, *I. Kant BFU News*, Kaliningrad, 2007, No. 3, pp. 36—40. (in Russian).

Aurora as Indicator of the Ionospheric Impact on Trans-Ionospheric Navigation Signals

Sergey A. Chernouss[1], Irk I. Shagimuratov[2], Igor B. Ievenko[3], Mikhail V. Filatov[1], Ivan I. Efishov[2], Mikhail V. Shvets[1], and Nikolay V. Kalitenkov[4]

[1]Polar Geophysical Institute, Murmansk-Apatity, Russia
[2]Kaliningrad Filial of IZMIRAN, Kaliningrad, Russia
[3]Yakutsk Institute of Cosmophysic Research and Aeronomy RAS, Yakutsk, Russia
[4]Murmansk State Technical University, Murmansk, Russia

Absrtact. The comparative analysis of the ionospheric total electron content (TEC) and an aurora intensity, which characterized the polar ionosphere during substorm, is presented. TEC data were obtained from the network of GPS-GLONASS stations over auroral and subauroral zones and auroral images in different emissions were obtained from numerical optical observations data. Temporal and spatial distribution of rate of TEC index (ROTI) and optical aurora were also constructed on the base of the famous models. It is shown similarity of the auroral ovals and distribution of TEC irregularities. Detail analysis of the comparison was done for the event of January 7, 2015. Optical measurements in this day were provided by the spectral images in main auroral emissions OI 555.7, OI 630.0, N_2^+ 470.9 and H 486.1 nm at subauroral Yakutsk and auroral Poker Flat stations. The day January 7, 2015 is characterized by high activity in the time 07—13 UT. During this time both auroral activity and quantity of irregularities sharply increased in the same sector of local time. Moreover sometime temporary variations show similarity in details. That was observed both in Alaska and Yakutia, where GPS and optical receivers running in real time. Picture with ROTI, calculated from signals of all satellites in the receiver field of view have a good correlation both for red aurora and blue ones. The attempt of prediction of ionospheric TEC irregularities appearance was done by using model of aurora prediction. The auroral oval was predicted with the model NORUSKA designed by Russian and Norwegian scientist in the joint project and this oval position was compared with position of ionospheric irregularities from GPS measurements in numerical stations, Possibility of optical auroral measurement using for the forecasting of positioning errors is under consideration too.

1. Introduction. The scintillations of trans-ionospheric radio signals is very well known indicator space weather condition. The electron density irregularities presented in high latitude ionosphere may experience phase and amplitude fluctuations of GPS signals [1]. The low frequency GPS phase fluctuations may be directly due to electron density changes along the radio ray path, or the total electron content (TEC) changes. Strong TEC fluctuations can complicate phase ambiguity resolution; increase the number of undetected and uncorrected cycle slips [2, 3].

The loss of signal lock in GPS navigation was associated with aurora [4]. The experimental evidence of positioning errors connected with spatial and temporal variations in the intensity of auroral arcs was demonstrated in [5].

2. Instrument and methods. The information about TEC fluctuations were obtained using the regular GPS observations provided by the International GPS Service (IGS). The world wide and numerous network GPS stations are very opportunely to monitor the spatial distribution of ionospheric irregularities in planetary scale [6, 7, 8]. In this report GPS measurements of global IGS network were used to study the substorm time occurrence of phase fluctuations (TEC changes) in the high latitude ionosphere during January 7 2015 event. The GPS stations with geomagnetic coordinates higher than 55°N and different longitudes were involved in this investigation. Dual-frequency GPS measurements for individual satellite passes served as raw data. As ameasure of fluctuation activity the rate of TEC (ROT, in the unit of TECU/min, 1 TECU=10^{16} electron/m^2) at 1 min. interval was used, as the measure of intensity of TEC fluctuations do index ROTI [10]. Detailed study produced by data of several auroral and subauroral stations AB18 (66.71N 162.61W) TIXI (71.38N 128.52E) KIR0 (67.51N 21.03E) NNVN (61.47N 44.90W) Figure 1. Optical data on aurora (Fig.1) were obtained from the NORUSKA model [9] on the base of the auroral oval calculation by Starkov [10]. This program permit to make forecasting of the auroral oval wth time prediction of about several hours. Other part of optical data obtained by direct measurements in the main auroral emission OI 555.7, OI 630.0, N_2^+ 470.9 and H 486.1 nm by optical imagers in the auroral observatory Poker Flat (65.12N 147.43W) [11] and subauroral Yakutsk (62.03N 129.73E). Comparison of these data with the GPS data on ionosperic irregularities is in the next chapter.

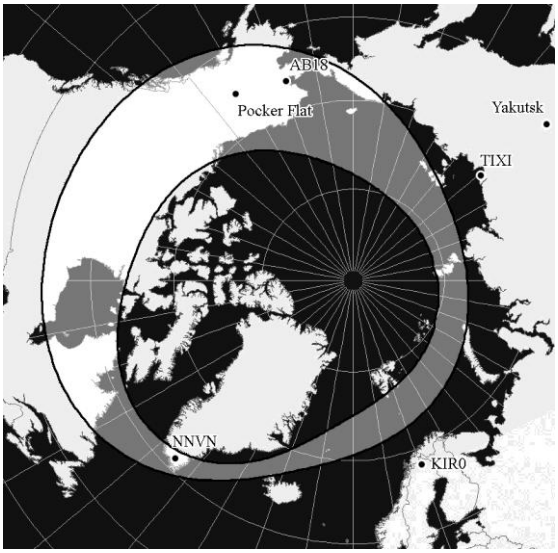

FIGURE 1.Map of auroral oval and a position of the main observation stations used.

3. Results and discussion

3.1 Solar and geomagneic conditions. Dst, Kp and AE indices, which characterize intensity of geomagnetic storm over period 5—10 January 2015, are presented in Fig. 2. This storm was rather short but enough. intensive. Maximal value of the index Dst reached near -100 nT, Kp reached about 6. Maximal auroral activity (index AE) was observed 09—12 UT when driven phase of the storm was developed. Sudden commencement of storm is occurred near 04 UT. There is good reason to believe that previous time interval was quiet. 3.2 Optical ovals and ovals of TEC irregularities

Overlapping of optical aurora and spatial-temporal distribution of the TEC irregularities during January selected events presented in Fig. 3.

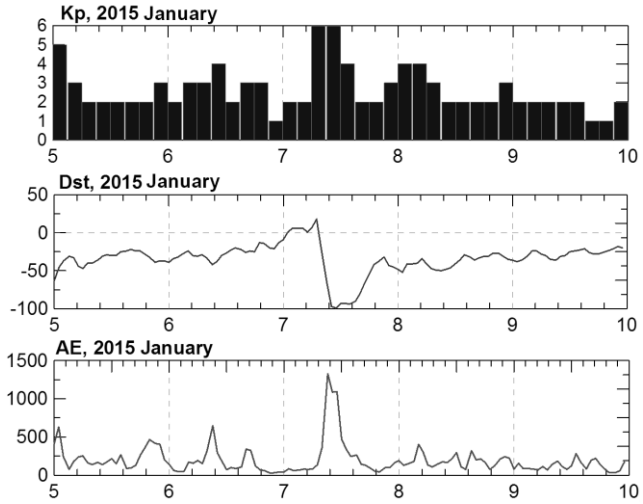

FIGURE 2. Kp, Dst, AE in January 2015.

The aurora position over the station calculated from the model data based on the average height of the aurora about 110 km by made cross-section of the auroral oval from the NORUSKA pictures as imaging in Fig.1. The irregularities space-time distribution was build on the base of dual frequency GPS receiver data obtained at a single station in supposition of irregularities height about 400 km. Figure 3 demonstrate relatively quiet day of 6 January data and disturbed day of 7 January. The difference of auroral and TEC data distribution in the same day clearly shown in Figure 3 too. Obviously it is difficult to see a good coincidence of auroral and ionospheric irregularity distribution because of the different heights. But in spite of that we can see some similarity in these distributions. Joint feature observed from the Figure 3 is widening of space and intensity both distribution in the night sector that points out on asymmetry of both distribution, This could be explained by the magnetosphere asymmetry, which usually indicates by auroral

ovals. Moreover this asymmetry related mainly to discrete auroral forms like rayed auroral arcs which rays are spaced along magnetic field lines. Some great discrepancy of two distributions for example data at the Tixie station where diurnal dependence of auroral occurency is significally smaller of irregularities oval. It could be explained by using of two dimentional models of aurora and ionosperic irregularities at fixed heights. Obviosly we need take into account curvature of the Earth magnetic field since precipitation particles moved along field lines and we will do/that in further work.

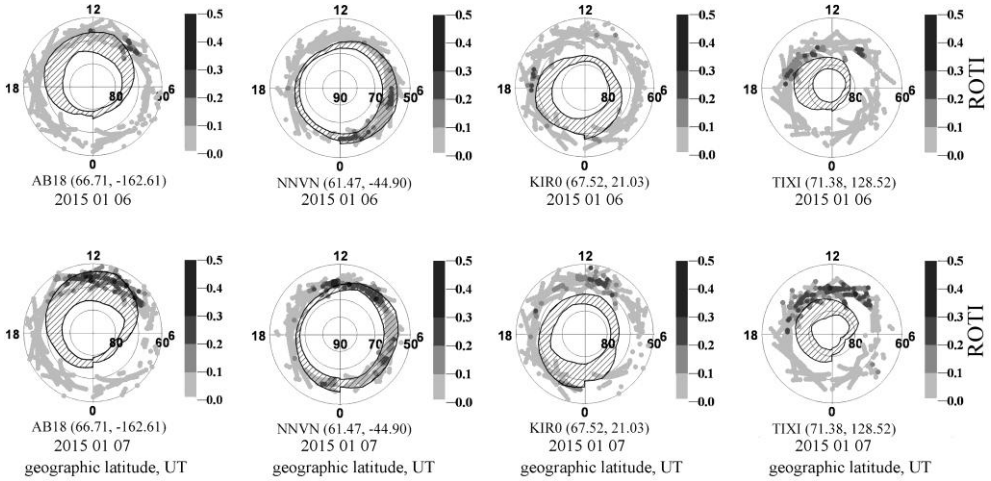

FIGURE 3. Optical and irregularities ovals in geographic coordinates at auroral stations.

The occurrence of TEC fluctuations essentially depend on geomagnetic latitude. Geomagnetic Latitude behavior of TEC was analyzed using ROTI measurements over stations located at different longitudes. It was formed images ROTI in the Geomagnetic latitude and UT coordinates for spatial and temporal distribution of TEC fluctuations. In figure 4 images of ROTI for 6—8 January 2015 at different longitudinal sectors are presented. In storm day the intensity of fluctuations increases at all longitudes. The increase took place simultaneously (around 12 UT) at all stations. The maximal intensity was at station when auroral disturbance occurred at local night time. Based on the daily GPS measurements from 130—150 selected stations, the images of spatial distribution TEC. fluctuations (index ROTI) in Corrected Geomagnetic Latitude (CGL) and Magnetic Local Time (MLT) coordinates was formed. These images demonstrate the irregularity oval similar to the auroral oval, as it is shown in figure 1. Thus the occurrence of the irregularity oval relates with auroral oval. The irregularity oval expands equatorward as the auroral one with increase of the magnetic activity.

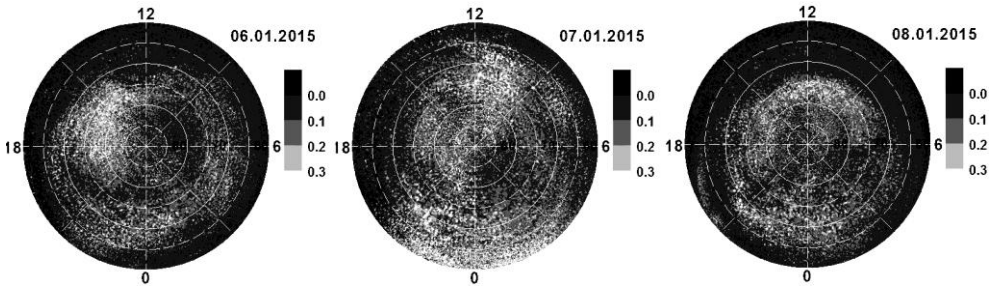

FIGURE 4. Irregularityovals constructed by data of GPS stations network in geomagnetic coordinates.

3.2 Temporal and spatial development of TEC fluctuations and aurora. The occurrence of TEC fluctuations associated with auroral oval. On figure 5, 6 it is presented development TEC fluctuations over subauroral Yakutsk and auroral Alaska stations (Poker Flat. and AB18).

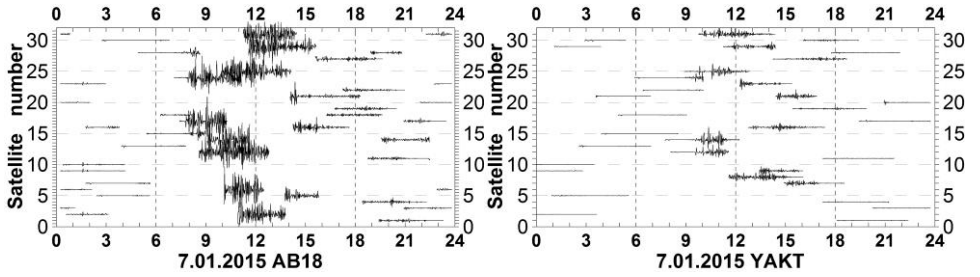

FIGURE 5.a) Development of TEC fluctuations at subauroral and auroral (Alaska) and b) subauroral (Yakutsk) stations for disturbed day.7 January 2015.

In Fig. 6, 7 the keograms of the Poker Flat and Yakutsk are presented. The stations located in auroral and subauroral area. During January 7 more intensive luminosity variations were registered around 12—15 UT. The intensity of aurora decrease from north to south, but they were observed even at latitude of 60.5°N. Obviously, the time course of ROT coincides with the auroral intensity variations at both stations in Alaska and Yakutsk. It confirms that fluctuation of GPS signals are controlled by auroral disturbances.

Strong fluctuations were observed in 09—12 UT during driven phase of the 7 January storm. In this time sharply increase also AE index (Fig. 2) and auroral activity, registered by optics (Fig. 6, 7).

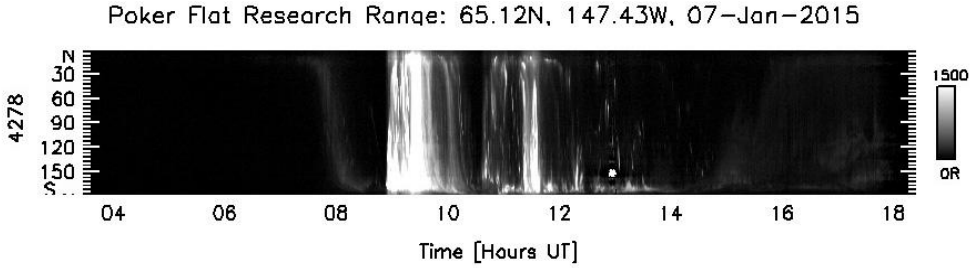

FIGURE 6. Keogram of auroral enission N_2^+ 427.8 nm in Poker Flat (Alaska).

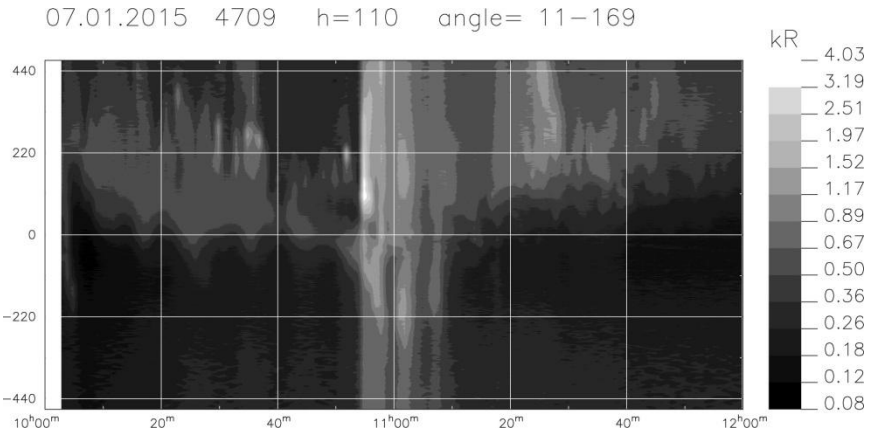

FIGURE 7. Keogram of auroral enission N_2^+ 470.9 nm in Yakutsk.

Conclusion. It was checked a possibility of irregularity spatial and temporal distribution of ionospheric irregularities pediction on the base of auroal oval prediction. First of all it was shown identity forms of auroral and irregularity ovals in general. Analysis shoved that fluctuation activity of GPS signals in the high latitude ionosphere is depended on geomagnetic conditions. Similarly to the auroral oval and the spatial distribution of the TEC fluctuations is shown. The occurrence of intensive aurora can be used as indicator of violation functioning space navigation systems and perhaps auroral forecasting will be possible to use for forecasting of TEC irregularity variations and positioning errors in Arctic.

Acknowledgment.*We thank grants of RFBR 14-05-98820 r-sever-a and 15-45-05090r_vostok-a.*

1. I.Shagimuratov., S. Chernous, Iu. Cherniak et al., Phase fluctuations of GPS signals associated with aurora, *Proc. 9th European Conf. on Antennas and propagation (EuCAP)*, Lisbon, 12—17 April 2015, paper 1570053943.

2. B. Forte and S. Radicella, Geometrical control of scintillation indices. What happens for GPS satellites, *Radio Sci.*, 2004, 39.

3. S. A. Chernouss and N. V. Kalitenkov, The dependence of GPS positioning deviation on auroral activity, *International J. Remote Sensing*, 2011, 32(1), pp. 3005—3017.

4. A. M. Smith, C. N. Mitchell, R. J. Watson et al., GPSscintillation in the high arctic associated with an auroral arc, *Space Weather*, 2008, 6, S03D01.

5. S. Chernouss, M. Shvec, M. Filatov et al., Study of GPS positioning deviations during aurora, *Absrt.of IV Intern. Conf. "Atmosphere, Ionosphere, Safety" (AIS-2014)*, Kaliningrad, Russia, 2014, pp. 243—251.

6. J. Aarons, GPS system phase fluctuations at auroral latitudes, *J. Geophys. Res.*, 1997, 102, A8, pp. 17219—17231.

7. X. Pi, A. J. Manucci, U. J. Lindqwister, and C. M. Ho, Monitoring of global ionosheric irregularities using the worldwide GPS network, *Geophys. Res. Lett.*, 1997, 24, pp. 2283—2286.

8. I. I. Shagimuratov, A. Krankowski, I. Efishov et al., High latitude TEC fluctuations and irregularity oval during geomagnetic storms, *Earth Planets Space*, 2012, 64(6), pp. 521—529.

9. F. Sigernes, M. Dyrland, P. Brekke et al., Real time aurora oval forecasting — SvalTrackII, *Optica Pura y Aplicada (OPA)*, 2011, 44, pp. 599—603.

10. G. V. Starkov,Mathematical model of the auroral boundaries, *Geomagn. Aeron.*, 1994, 34(3), pp. 331—336.

11. http://optics.gi.alaska.edu/optics/realtime

Statistical Study of Medium-Scale Traveling Ionospheric Disturbances using Hokkaido East and Ekaterinburg HF Radar Data

Alexey V. Oinats[1], Nozomu Nishitani[2], Pavlo Ponomarenko[3], Oleg I. Berngardt[1], Konstantin G. Ratovsky[1], Maxim V. Tolstikov[1]

[1]Institute of Solar-Terrestrial Physics SB RAS, 664033, Lermontov St., 126a, P. O. Box 291, Irkutsk, Russia.
[2]Institute for Space-Earth Environmental Research, Nagoya University, Furo-cho, Chikusa-ku, Nagoya 464—8601, Japan.
[3]University of Saskatchewan, Saskatoon, SK, Canada

Medium-scale traveling ionospheric disturbances (MSTIDs), which are wave-like electron density disturbances with horizontal wavelengths of about several hundreds of kilometers and periods of 15 minutes up to 1 hour, have been being investigated for many decades using different techniques and observational facilities (see e. g. [1, 2]). Daytime MSTIDs are generally connected with atmospheric gravity waves (AGWs), propagating at ionospheric heights, whereas nighttime mid-latitude MSTIDs are likely to be associated with Perkins instability [3].

In the current study we used the multi-year datasets of two mid-latitude high frequency (HF) radars, the Hokkaido East (43.53°N, 143.61°E) and Ekaterinburg

(56.42°N, 58.53°E), to obtain statistically significant distributions of the MSTID main characteristics [4,5]. MSTIDs manifest themselves as periodic variations of the ground backscatter (GB) power received by HF radar. We used automated technique based on cross-correlation analysis of GB minimum slant range variations to determine the MSTID azimuth, horizontal phase velocity, period, horizontal wavelength, and relative amplitude. Calibrated elevation measurements for the Hokkaido East radar allowed us to study the disturbances propagating in the E and F regions of the ionosphere separately. Comparison of the MSTID characteristics obtained from measurements by two radars and for two ionospheric regions could provide important information about the regional (latitudinal and altitudinal) characteristics of the AGWs.

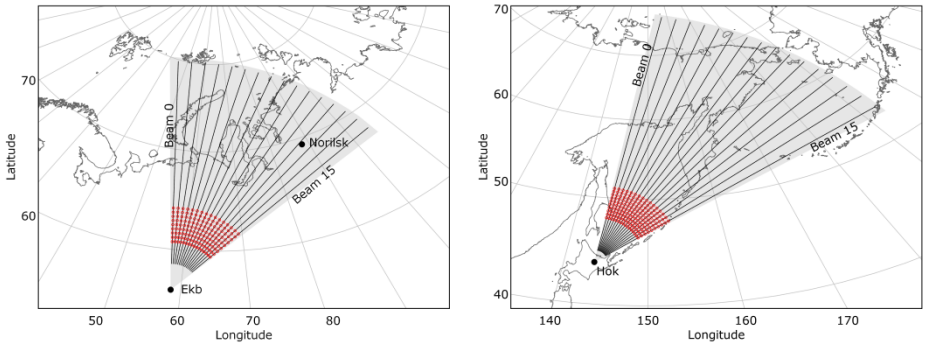

FIGURE 1. Location of the Ekaterinburg and Hokkaido East HF radars and their FOV. Approximate location of the ionospheric reflection points is shown by red circles.

Instrumentation and data processing. The radars provide measurements of range-time dependencies of the power, Doppler velocity, Doppler spectral width, and elevation angle (elevation measurements had not been provided yet by the Ekaterinburg radar) at each of 16 azimuths, called "beams", with a temporal resolution of 1—2 minutes. All beams form an approximate 50°-width field-of-view (FOV). Figure 1 show a map of the radar locations and their FOVs. In this study we used only one-hop GB echoes recorded from 2007 to 2014 by the Hokkaido East radar and from 2013 to 2014 by the Ekaterinburg radar (see [4, 5] for more details). In this study we used radar data obtained at the operational frequency of ~11 MHz as it was most usable frequency during the period under consideration.

The main idea of the processing technique is to fit the TID analytical model to GB minimum slant range variations observed on different radar beams [4]. We suppose the disturbance has a plane phase front within the radar FOV, and the phase velocity vertical component is equal to zero. We consider that the ionosphere mainly influences on GB in the propagation trajectory apogee where reflection occurs. Therefore, the slant range variations are directly connected with the ionosphere variations in the reflection point. To determine the time lags between varia-

tions in two reflection points, we use cross-correlation analysis with statistical sampling size equivalent to 6 h. We construct a two-dimensional squared deviation which includes the observed time lags and coordinates of the reflection points. Minimization of the deviation gives us appropriate azimuth and horizontal velocity of the disturbance. Other parameters of the disturbance are determined by averaging over beams used in minimization. Period is calculated as a median of a set of variation prevailing periods. Horizontal wavelength is defined from the calculated period and velocity. The amplitude is expressed as an average of the slant range deviation RMS. Relative amplitude is equal to the ratio between the amplitude and average slant range.

The processing was carried out for each local time and date. As a result, we obtained the diurnal dependencies of five MSTID characteristics for each date under the period of consideration.

Results and discussion. Diurnal occurrence rate of the MSTID characteristics were calculated for each of three ionosphere regions: the E and F regions for the Hokkaido East radar (Hok-E and Hok-F) and the F region for the Ekaterinburg radar (Ekb-F). We should note that there is no GB data at all during nighttime for the E region due to its low critical frequency. Therefore, we determine the occurrence rate as a ratio between the observation duration of a given value of the MSTID parameter and the general observation interval at a certain local time. The analysis showed that the most frequent daytime velocities are as follows: 60—100 m/s, 110—180 m/s, and 30—90 m/s for Hok-E, Hok-F, and Ekb-F, respectively. The most frequent daytime wavelengths are as follows: 300—550 km, 450—800 km, and 150—400 km for Hok-E, Hok-F, and Ekb-F, respectively. The most frequent period for all regions is in the range of 60—100 min.

Nighttime values of velocity, period, and wavelength for the F ionosphere region are somewhat greater than those during the daytime. This is consistent with results of [6], and can be related with the increased HF reflection height during the nighttime in comparison with daytime. Velocity of GW propagating upward is expected to increase with altitude to compensate for the decreasing atmospheric density. On the other hand, GWs with longer wavelength/period are less attenuated and can propagate for longer times and reach greater heights before their dissipation [7].

The relative amplitude varies within the range of 3—8 % for Hok-F; it reaches a minimum near noon and maximums at about 6 LT and 20 LT. In case of Ekb-F, the amplitude has a similar behavior, but varies within a greater range, from ~4 % near noon to ~13 % at 8 LT and 22 LT. For Hok-E, the amplitude is somewhat greater and varies within the range of 4—9 %. Similar diurnal behavior of the MSTID relative amplitude was reported by Afraimovich E. L. [8] who showed that the relative amplitude of TEC variations at night significantly exceeds that of the daytime; in addition, the relative amplitude is a few times greater at higher latitudes as compared to mid- and low-latitudes.

Contours on Fig. 2 show the diurnal variations of occurrence rate of the MSTID propagation azimuth. Left, center, and right columns correspond to Hok-E, Hok-F, and Ekb-F regions, respectively. Blue, red, and magenta curves represent constant occurrence rates of 3.3 %, 5 %, and 10 %, respectively. There are four

dominant directions with enhanced occurrence for the F region: morning northeastward (from 20° to 50° at 4—6 LT), daytime southeastward (from 100° to 140° at 7—15 LT), nighttime and evening southwestward (from 190° to 220° at 15—18 LT and 21—3 LT), and evening northwestward (from 280° to 310° at 18—21 LT). There are three dominant directions for the Hok-E region: morning northeastward (from 20° to 50° at 6—9 LT), daytime northwestward direction (from 280° to 320° at 8—16 LT), and evening southwestward (from 190° to 215° at 13—16 LT). We have indicated a good agreement between them and results of many other studies (please, see [4, 5] for details).

Comparison between Hok-F and Ekb-F occurrence patterns shows that they are very close to each other. However, there is a difference in the absolute values of the occurrence rate. For example, the most prominent Hok-F southeast daytime peak is rather weak for the Ekb-F, and the Ekb-F late-evening northwest peak are significantly stronger than that of Hok-F. In addition, the peaks for the Ekaterinburg radar are shifted slightly to greater local time. The shift can be partially explained by the fact that the registration region of the Hokkaido East radar is located mainly to the east from the radar site in a different time zone (+1 h).

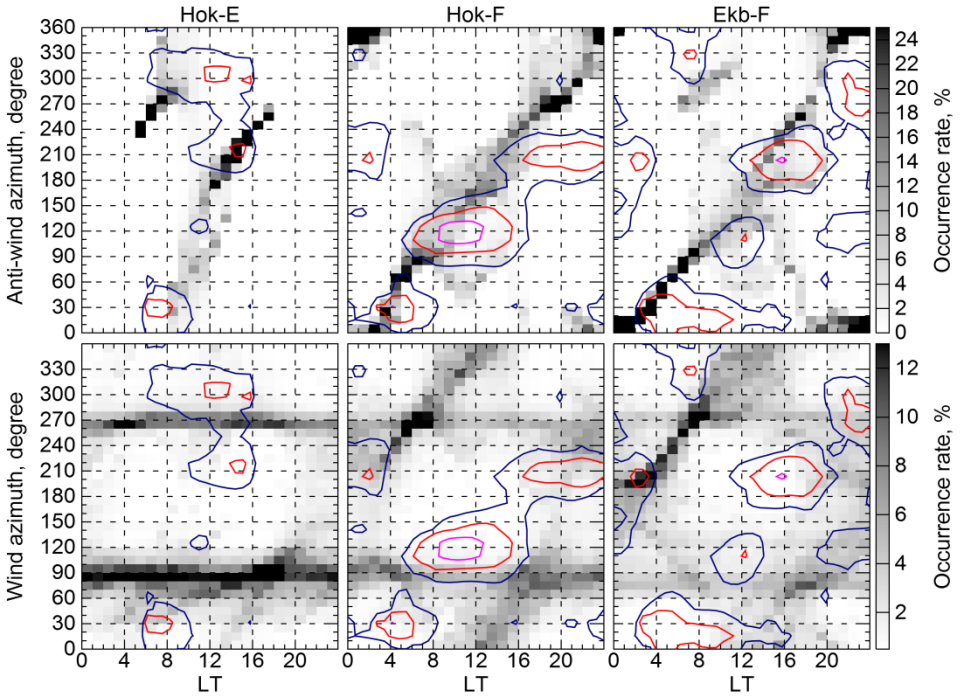

FIGURE 2. Diurnal dependence of the anti-wind (top) and wind (bottom) direction occurrence rate calculated using HWM07 and GB model. Left, center, and right columns correspond to the Hokkaido E and F region, and the Ekaterinburg E+F region, respectively. Blue, red, and magenta curves are the levels of constant MSTID azimuth occurrence rate of 3.3 %, 5 %, and 10 %, respectively.

According to the theoretical concept, if neutral wind has a component parallel to the wave vector, it causes a Doppler shift of GW frequency [9]. Depending on the mutual orientation of the wave, wind, and their parameters, critical coupling or reflection may occur. Therefore, not all GWs originating from the lower atmosphere (troposphere) and initially having all possible directions can reach the ionosphere. This results in the appearance of a certain diurnal pattern of the observed MSTID azimuths. Many researchers have reported observational evidences of this effect (see i. e. [9, 10]).

To check the filtering effect of the neutral wind, we calculated the relative occurrence rate for the neutral wind direction using the horizontal wind model HWM07 [11]. The wind azimuth is calculated for the whole period under consideration at heights, where the "measurements" of MSTID characteristics are provided by the HF radar. The height and coordinates are taken from GB model (GBM, see [12]) and correspond to the HF true reflection height and coordinates of the reflection point for the radar central beam (beam #8). The occurrence rates are shown on the top panels of Fig. 2 by the gray color according to the color bar to the right of the plots. Since the Ekaterinburg radar did not provide elevation angles, we used the combined Ekaterinburg GBM for the E and F channels (E+F). Similar to Fig. 2, the occurrence rate is determined as a ratio between the predicted duration of a given wind azimuth and the general interval of GBM prediction at a certain local time. Vertical and horizontal axes show the anti-wind azimuth (anti-parallel to the wind direction) and local time, respectively.

As seen from Fig. 2 (top), there is a distinct pattern of wind direction depending on the ionosphere region. Almost all contours of enhanced MSTID occurrence qualitatively agree with the wind "tracks" (they overlap or lay very closely to the corresponding wind tracks). The largest difference is related to the nighttime southwestward MSTIDs, which have no corresponding wind track. The size of some "spots" and the relation between wind and MSTID occurrence rate values do not agree well. Another difference is that the MSTID occurrence rate represents a set of localized spots distributed over the azimuth—local time plane. On the contrary, the azimuth pattern calculated from HWM07 consists of relatively smooth tracks extended in local time. In other words, there is some kind of "gap" in the MSTID azimuthal pattern. The gaps on Hok-F and Ekb-F pattern are located near the exact north, south, east, and west directions.

To understand the cause of the "gaps" we also calculated the occurrence pattern of the neutral wind direction within an altitude range that GWs are expected to propagate through. In contrast to the anti-wind pattern (described above) indicating "permissive" directions, the second one should indicate "prohibitory" directions. For each local time wind azimuth was calculated for a set of heights from 10 km to 100 km for the E region and from 10 km to 250 km for the F region with the step of 10 km. The resulting occurrence rate was divided by corresponding number of azimuth values within a set (10 and 25 for the E and F region pattern, respectively). The calculated occurrence patterns are presented on the bottom panels of Fig. 2 by the gray color according to the color bar to the right of the plots. On the patterns

the darker color indicates the greater occurrence of the wind "prohibiting" the GWs. As seen from the patterns, almost all MSTID spots mostly lay in the regions with low occurrence of the prohibiting wind (the regions with white or light gray color) and again excepting the nighttime southwestward MSTIDs. Moreover the shape of some MSTID contours repeats the shape of the regions with low wind occurrence. For example, the latter can be clearly seen for the morning northeast and daytime southeast spots of Hok-F; for the morning northeast-northwest and evening southwest spots of Ekb-F. Thus, at least eastern and western "gaps" in the MSTID diurnal pattern most probably might be associated with the existence of the fair neutral wind elsewhere within the altitude range of GWs propagation. The fair wind could attenuate and break the GWs before they reach the heights where HF radar can observe their effect.

Conclusion. Thus, our analysis of the multi-year HF radar datasets showed that the observed MSTIDs are mostly caused by GWs propagating in the thermosphere (except for the nighttime southwestward MSTIDs). The dominant MSTID propagation directions match well with the enhanced occurrence of anti-wind direction at the height of observation and with the low occurrence of the wind direction within the expected altitude range of GWs propagation. The values and diurnal behavior of the MSTID horizontal velocity, wavelength, period, and relative amplitude agree well with the results published earlier, and are consistent with the properties of the GWs propagating at corresponding heights. On the contrary, the nighttime southwestward MSTIDs likely propagate in the same direction with the neutral wind. The latter is not consistent with the AGW theory.

Acknowledgements.*The work was supported by Russian Scientific Foundation (project 14-37-00027). We grateful Nagoya University and ISTP SB RAS for the provided experimental data.*

1. R. D. Hunsucker, Atmospheric gravity waves generated in the high-latitude ionosphere: a review, *Rev. Geophys. Space Phys.*, 1982, 20(2), pp. 293—315.

2. K. Hocke and K. Schlegel, A review of atmospheric gravity waves and travelling ionospheric disturbances: 1982—1995, *Ann Geophys*., 1996, 14, pp. 917—940.

3. K. Shiokawa, Y. Otsuka, C. Ihara et al., Ground and satellite observations of nighttime medium-scale traveling ionospheric disturbance at midlatitude, *J. Geophys. Res.*, 2003, 108(A4), pp. 1145.

4. A. V. Oinats, V. I. Kurkin, and N. Nishitani, Statistical study of medium-scale traveling ionospheric disturbances using SuperDARN Hokkaido ground backscatter data for 2011, *Earth Planets Space*, 2015, 67(22).

5. A. V. Oinats, N. Nishitani, P. Ponomarenko et al., Statistical characteristics of medium-scale traveling ionospheric disturbances revealed from the Hokkaido East and Ekaterinburg HF radar data, *Earth Planets Space*, 2016, 68(8).

6. J. A. Waldock and T. B. Jones, HF Doppler observations of medium-scale travelling ionospheric disturbances at mid-latitudes, *J. Atmos. Terr. Phys.*, 1986, 48(3), pp. 245—260.

7. S. L. Vadas, Horizontal and vertical propagation and dissipation of gravity waves in the thermosphere from lower atmospheric and thermospheric sources, *J. Geophys. Res.*, 2007, 112, A06305.

8. E. L. Afraimovich, N. P. Perevalova, and I. V. Zhivetiev, Relative amplitude of the total electron content variations depending on geomagnetic activity, *Adv. Space Res.*, 2008, 42, pp. 1231—1237.

9. J. A. Waldock and T. B. Jones, The effects of neutral winds on the propagation of medium-scale atmospheric gravity waves at mid-latitudes, *J. Atmos. Terr. Phys.*, 1984, 46(3), pp. 217—231.

10. A. D. Kalikhman Medium-scale traveling ionospheric disturbances and thermospheric winds in the F-region, *J. Atmos. Terr. Phys*., 1980, 42, pp. 697—703.

11. D. P. Drob, J. T. Emmert, G. Crowley et al., An empirical model of the Earth's horizontal wind fields: HWM07, *J. Geophys. Res*., 2008, 113, A12304.

12. A. V. Oinats, N. Nishitani, P. Ponomarenko, and K. G. Ratovsky, Diurnal and seasonal behavior of the Hokkaido East SuperDARN ground backscatter: simulation and observation, *Earth Planets Space*, 2016, 68(18).

The Results of Comparison of Vertical Motion Velocity and Neutral Atmosphere Temperature at the Lower Thermosphere Heights

Nataliya V. Bakhmetieva, V. N. Bubukina, Valeriy D. Vyakhirev, Gennady I. Grigoriev, Elena E. Kalinina, and Ariadna V. Tolmacheva

Radiophysical Research Institute, 25/12a, Bol'shaya Pecherskya St., Nizhniy Novgorod,603950, Russia

The upper mesosphere-lower thermosphere region (MLT) is the region of transition, where an energy exchange between the atmosphere and its upper layers acts. Dynamics of this region depends on many processes ensuring energetic coupling between the different layers. The study of these processes is necessary for an understanding of the physical phenomena in the MLT-region. To get a full picture of these processes, it is necessary to know the state of the medium: its temperature, density, composition, electron concentration, velocities of the horizontal and vertical movements, characteristics of turbulence. Simultaneous measurements of many parameters with good temporal and spatial resolution are a main task of the experimenters. Theoretical interpretation of the measurements becomes difficult due to the influence of many factors. In present time, it is known that a significant contribution to dynamics of the mesopause region the excitement of the internal gravity waves (IGW) brings as a result of the convectional and dynamic instabilities. Dissipation of the gravity waves occurs for various reasons, including because of the saturation and breaking of the waves, as well as with an increase in the kinematic viscosity and thermal conductivity in the area of their propagation. Energy and momentum of the waves, in turn, are transmitted into the environment and can cause turbulence and also vertical thermal flows near the mesopause [1, 2]. According to our study, similar processes could occur in the region located above

95—100 km. In this regard, we set a aim to match the velocity of the vertical motion and the neutral atmosphere temperature, and their variations at these heights. Our experimental data were obtained by the method based on resonance scattering of the radio waves from the artificial periodic irregularities (API) of the ionospheric plasma (the API techniques).

Determination of the atmospheric parameters by the APItechniques. The artificial periodic irregularities of ionospheric plasma were discovered during the active heating experiments in Radiophysical Research Institute. The API arecreated in the ionosphere illuminated by a high power HF radio wave. Powerful standing radio wave is formed by interference of the incident into the ionosphere and the reflected wave from it. The periodic structure is created at the heights of about 60 km to the level of reflection of the power radio wave. The API are generated in the antinodes of the standing wave. Their vertical scale is equal to one half of wavelength λ of the power wave. In the E-region the API are formed by action electron pressure redistribution caused by electron thermal diffusion. Diagnostics of the API is based upon the observation the Bragg backscatter of the pulsed probe radio waves from the periodic structure. If the pulses backscattered by the periodic structure are added in phase, their easy to stand out from the background noise. In our experiments Bragg condition leads to the equality of the wavelengths of the powerful and probe waves. The API are probed in the pauses between turnings on of the heater transmitters. The diagnostic facility is situated near powerful transmitters. Receiving of the backscattered signals is performed using one section of an antenna of the heating facility. The amplitudes and phases of the scattered signals are registered in dependence on virtual altitude and time. The signal /noise ratio is about 10—100 for the pulses coming from the heights of the E region. Virtual height *h* is equal cΔt/2, Δt is the delay time of the pulse, c is velocity of light. Every minute is done two to four measurements. Registration is carried out with a spatial resolution of 0.7 or 1.4 km.

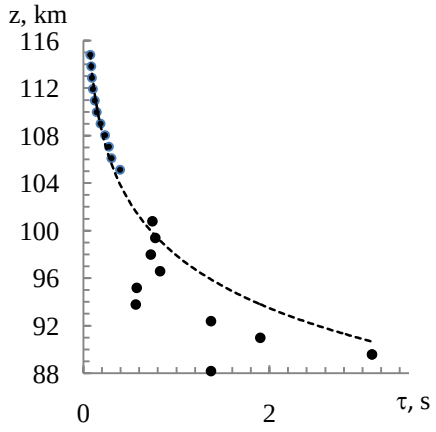

FIGURE 1. The API relaxation time 6.10.2014 at 11:20.

The methods for determining ionospheric and atmospheric parameters in the E-region of the ionosphere: the temperature T and density ρ of the neutral atmosphere and vertical velocity have been developed in Radiophysical Research Institute. To determine the neutral atmosphere temperature the API relaxation times after turning off the powerful transmitters are calculated. The relaxation time τ is determined as the decrease amplitude of the scattered signal in *e* times. Fig.1 shows a typical example of altitude dependence of the API relaxation time τ(z), here z is usual altitude. Fig. 1 shows that up to 101 km the relaxation time τ(z) increases with decreasing altitude exponentially, below 101 km

τ decreases due to the turbulence and at height 90 km τ increases due appearance of the E sporadic layer. Relaxation of the irregularities at the E-region heights occurs by diffusion $\tau = (K^2 D_\alpha)^{-1}$. Here $K = 2\pi/\Lambda$, Λ is a vertical scale of the periodic structure,D_α is an ambipolar diffusion coefficient. In turn, the ambipolar diffusion coefficient depends on the medium characteristics: the electron (T_e) and ion (T_i) temperatures and the frequency of collisions of ions and molecules (ν_{im}):

$$D_\alpha = k_B(T_e + T_i)/(M_i \nu_{im}),$$

where k_B is Boltzmann constant and M_i is the average ion mass. The characteristic scale at which the relaxation time decreases by e times with increasing height corresponds to atmospheric scale height H. This experimental fact is the basis of the method for determining the neutral atmosphere temperature and density at altitudes E layer of the ionosphere. Detail processing method represented in [4]. We used the average value of the relaxation times and velocities for 5 min.

The vertical motion velocities were also determined using the API. The neutral gas motion influences the processes of the API relaxation and therefore observations of the Doppler shift of scattered signal's frequency can be used for the measurements of the vertical motion velocities. We measured the phase Φ of the scattered signals. Then $d\Phi/dt = 2\pi F_D = 4\pi V/\lambda$ and we get:

$$V = \frac{\lambda}{4\pi}\frac{\Delta\Phi}{\Delta t} = \frac{c}{4\pi fn}\frac{\Delta\Phi}{\Delta t}.$$

Positive sign of V corresponds to downward motions.

It must be note that the velocity variations include both wave and convective motions. The velocity lower the turbopause level includes also the turbulent component. But if value the turbulent component becomes large we cannot obtain the velocity enough exactly. Beside we cannot determine the temperature lower a turbopause level.

The results of the experimental data analysis. Main characteristics of the experiments: date, frequency of the powerful and probe transmitters, the observation periods (Moscow time) and the height interval for which these data were obtained are shown in Table 1.

TABLE 1. Date, frequency of the powerful action and probe waves, the observation periods (Moscow time) and the height interval where data were obtained.

Date	Frequency, MHz	Moscow time	Height interval
1.09.2014	5.6	17.00—18.40	97—112
2.09.2014	5.6	17.30—20.15	96—111
6.10.2014	5.6	10.40—12.45	98—112
7.10.2014	5.6	10.40—16.30	100—113
18.09.2010	4.7	11.30—16.30	99—114

The most common cases which were fixed in the process in comparison of the temperature and velocity variation are following.

1. There are wave-like variations T(z) and V(z), minima of velocity corresponds with the maxima of temperature (Variation of the temperature and velocity is in antiphase). Such profiles for 1.09.2010 are shown in Fig. 2a and Fig. 2b. The spatial periods could be from 5 to 7—9 km.

2. Variations of the temperature and velocity are in phase, i. e. the maximum temperature reached at same height as the maximum velocity. The examples of such variations are shown in Fig.3a (18.09.2010) and Fig.3b (6.10.2014). 18.09.2010 the spatial periods L were equal to ~6 and 9 km and 6.10.2014 L was about 3—4 km.

In both these cases, one can speak about the wave movements. It must be noted that variations occurred 18.09.2010 when convective instability was observed [4].

3. In some cases we have seen the occurrence of deep temperature minimum.

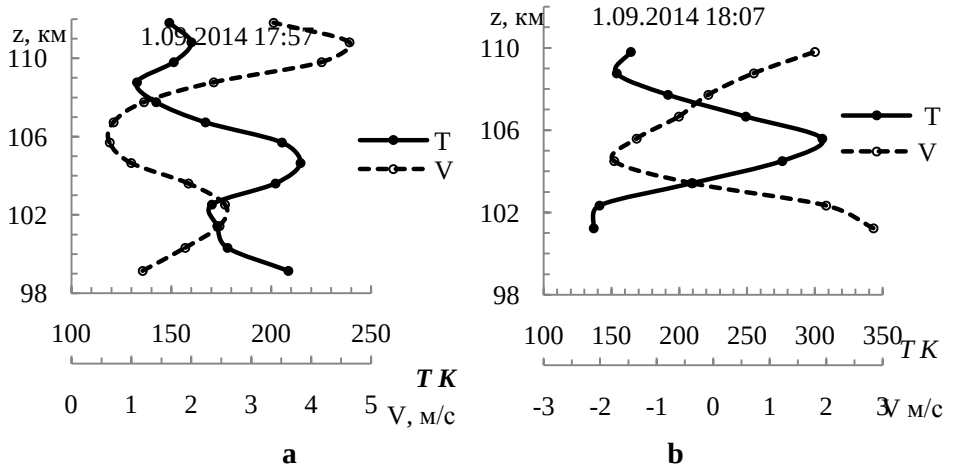

FIGURE 2. The altitudinal variations of T(z) and V(z) in antiphase.

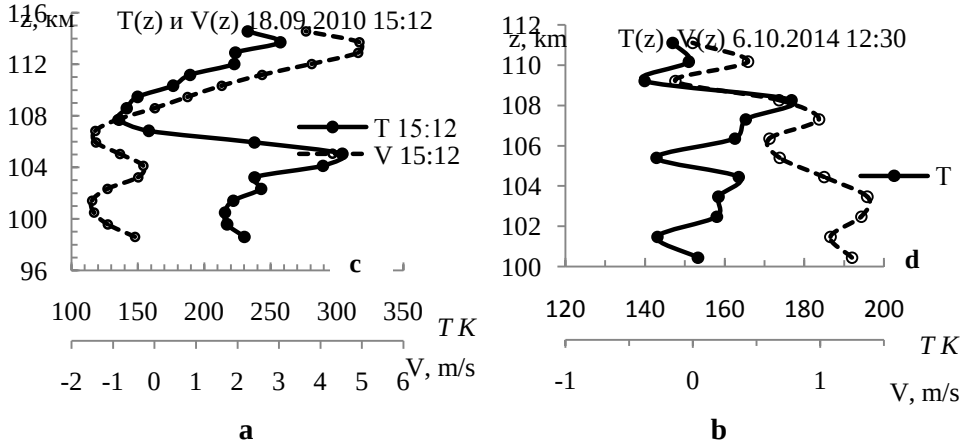

FIGURE 3. The altitudinal variations of T(z) and V(z) in phase.

Figure 4 shows the height profiles of the temperature and velocity 02.09.2014, at 18:40. As can be seen from Fig. 3, the temperature minimum takes place at heights 101—103 km and it is equal 130 K. At the same heights the vertical velocity is close to 0. Below and above this level the temperatures and velocities increased, but the velocities have the different directions: below level where the temperature reaches 0 the velocity is directed upward, and above this level the velocity is downward. At the same time the sporadic layer E was formed at heights 95—100 km, possibly due to wind shear caused by these motions. Also we observe large negative temperature gradient in lower part of the temperature profile, exceeding adiabatic gradient. In turn, increase of negative temperature gradient creates a condition that favors the occurrence of convective instability and generation the IGW. Really wave-like temperature variations were observed above 100 km 2.09.2014 after 19:10. Their space scale was equal about 3.5 км.

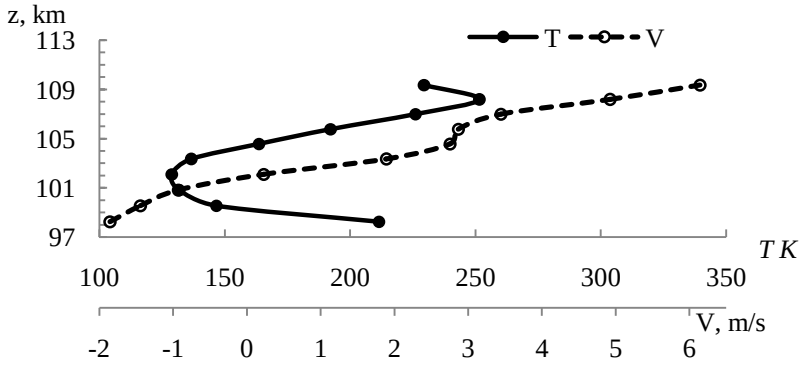

FIGURE 4.2.09.2014 18:40.

4. Convective instability was also observed 18.09.2010 [4] and then super adiabatic gradient of the temperature took place also. At the same time temporal variations of the velocity with periods of 10—12 minutes were observed lower 100 km between 90 and 100 km). Such periods are close to the periods corresponding to the frequency of the Brunt-Vaisala. We observed similar time variations in velocity below the turbopause also on October, 6 and wave nature of the process was clearly expressed in both cases.

Convective instability has also appeared 07.10.2014. Unfortunately, in this day the velocities were not measured. But sequence of the events was the same as 18.09.2010. Apparently the minimum of temperature T ~ 100—110 K was formed at the altitude of 106.8 km even before the observations and super adiabatic gradient occurred at the bottom of the temperature profile. Half an hour later, the variations

T (z) have appeared. At 12: 30—12:50 the maximum temperature at the altitude of ~ 108 km had risen to 275 K and at 14 hours up to 400 K. In addition to a significant increase in temperature in the altitude range 105—109 km, instability manifested in the intensifying wave-like temporal variations of temperature at these

altitudes. Figure 5 shows the temporal variations of the temperature at altitudes of 105 and 108 km. They have periods of 10 to 15 minutes.

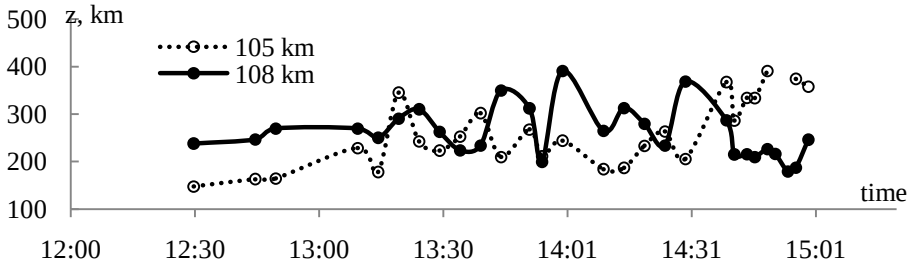

FIGURE 5. Temporary variability in neutral temperature at altitudes of 105 and 108 km during convective instability on 07/10/2014.

5. In many cases, we observed no noticeable correlation between T(z) and V(z) and this may be due to several factors. Firstly, when signals backscattered from the API are diminished, the measurement error increases. Secondly, the turbopause height varies and this can increase the contribution of the turbulent velocity into the measured value. Third, the convective flows from both above and below are superimposed on the wave variations and distort their appearance.

Conclusion. Comparison of measured temperatures and the vertical motion velocities above 100 km gave following results. The undulating temperature variations and vertical motion velocity variations often observed in the same time. In the absence of wave-like variations there is a tendency to temperature increase when the value of velocity regardless its direction increases that could be connected with presence of the thermal flows from the turbulent region, where IGW propagate. IGW can transfer energy to the environment due to dissipation. In the presence of thermal flows a structure may be formed with a deep minimum temperature. In this case the occurrence of the super adiabatic temperature gradient is possibly, that favors the occurrence of GW instability above the turbulence level. This hypothesis does not contradict the available experimental and theoretical studies. In the future, we are going make estimations of the possibility of the energy transfer from the region situated below turbopause on to overlying heights.

The work was supported in part by Russian Foundation for Basic Research, project 13-05-00511 and in part within the public tasks of the Ministry of Education and Science of Russia.

1. J. Weinstock, *J. of the Atmos. Sci.*, 1987, 44(2), pp. 410—419.

2. D. C. Fritts, B. P. Williams, B. P. She et. al., *Gephys. Res. Lett.*, 2004, 31, L24S06.

3. V. V. Belikovich, E. A. Benediktov, A. V. Tolmacheva, and N. V. Bakhmet'eva, Ionospheric Research by means of artificial periodic irregularities. Translated by Drs M. Förster and M. Rietveld.Copernicus, Katlenburg-Lindau, Germany. 2002.

4. A. V. Tolmacheva, N. V. Bakhmetieva, G. I. Grigoriev, and E. E. Kalinina.*Adv. Space Res*., 2015, 56, pp. 1185—1193.

Generation of the Super Small Scale Artificial Ionospheric Irregularities and its dependence on the Magnetic Zenith Effect

Ilya A. Bolotin[1], Vladimir L. Frolov[1,2], Gennady G. Vertogradov[3], and Vitaliy G. Vertogradov[3]

[1]Radiophysical Research Institute, 25/12a Bolshaya Pecherskaya str, Nizhny Novgorod, 603950, Russian Federation
[2]Kazan Federal University, 18 Kremlyovskaya str, Kazan, 420008, Russian Federation
[3]Southern Federal University, 105/42 Bolshaya Sadovaya tr., Rostov-on-Don, 344006, Russian Federation

Introduction. HF heating at frequencies close to multiples of the electron gyrofrequency leads to generation of the super small scale artificial ionospheric irregularities (SSSI) in the plasma density with scale size of 10 cm. According to the model described in [1], during the ionosphere heating at frequencies a bit higher than the electron gyrofrequency harmonic, the Bernstein waves are excited inside artificial decameter ionosphere irregularities. These waves form the standing wave with $l_{\perp} = \lambda_B/2 = 10$—$20$ cm. As the amplitude of the standing wave is high enough, it forms the plasma density grid, elongated along the geomagnetic field lines ($l_{\parallel} \approx 1$ km), through the strictional pushing of plasma from the regions of electrical field maximums,

The purpose of this paper is introduction of new experimental proofs of SSSI detection and the study of the magnetic zenith influence on their generation.

Experimental setup. The experiments discussed in this paper were carried out in March 2010, 2011, 2013 and in August 2010, 2011, 2012, 2013 in evening and day time on Sura heating facility, located in 120 km to the east from Nizhny Novgorod, Russia (geographic coordinates: 56.15° N, 46.1° E; operating frequencies band: 4.3—9.5 MHz; effective radiation power: 80—300 MW). The ionosphere heating was performed using the frequencies close to the 4^{th} or 5^{th} harmonic of electron gyrofrequency with a detuning $\Delta f = f_{Pump} - nf_{ce} \approx 40$ kHz, matching the maximum power of *Broad Upshifted Maximum* component in Stimulated Electromagnetic Emission (SEE) spectrum. According to [1], such conditions should satisfy the requirements for SSS generation. The radiation pattern of the facility was tilted at 12° from vertical (to the magnetic zenith area for pumping wave), to increase the effectiveness of pumping wave interaction with the ionosphere plasma. The experiments were accompanied by the SEE measurements, which allows to determine the harmonic of electron gyrofrequency accurately, using the effect of the main SEE component suppression when $\Delta f \approx 0$ Hz.

The results of SSSI sounding using the GPS satellites signals. For SSSI detection the method of excited area sounding by the GPS satellites signals was used. The method allows to evaluate the variations of Total Electron Content (TEC) along the signal propagation path and thereby evaluate the variations of ionosphere plasma density. For these experiments the heating was performed with the schedule: 5s — heating, 5s — pause or 10s — heating, 10s — pause. The appearance of fluctuations of the sounding signal with the period equal to the heating period under such conditions can indicate the existence of SSSI [3—5]

Figure 1 illustrates the example of carried out experiments, which was held in 21st of August 2011, when the heating was performed using frequency f_{Pump}=5400 kHz, with $\Delta f = f_{\text{Pump}} - 4f_{\text{ce}} \approx 40$ kHz. Here, in Fig 1(a) the satellite's PRN22 flight path across the main lobe of the radiation pattern of the Sura facility in geographic coordinates is illustrated. Figures 1(b) and 1(c) show the time dependence of TEC variations value and its wavelet analysis respectively. It can be seen that Fig.1(b) has evident maximum, i. e. under the gyroharmonic ionosphere heating strong fast variations of GPS satellites signal phase appear. After the wavelet analysis of these variations, the spectral maximums can be found on the periods consistent with the Sura facility operation schedule.

The comparison of the moments of such variations appearance with the satellites flight paths have shown that every time when the variations appeared the underionospheric point, taken on the height of pumping wave reflection, was shifted to the south-west from the center of the radiation pattern near the area of magnetic zenith. The obtained results allow to conclude that the generation of SSSI is more efficient in the magnetic zenith area.

The amplitude of TEC variations in our experiments was about ~ 0.02 TECU, what, according to [4], corresponds to variations of ionosphere plasma density in SSSI ~ 10 %.

The relation between the widening of the scattered on the decameter irregularities signal spectrum and the magnetic zenith effect. As it was shown in [5], the value of widening of the scattered on the decameter irregularities signal spectrum depends heavily on the location of the scattering surface in the excited area of ionosphere and on the fact whether it passes through the magnetic zenith. The widening itself, according to [1], is connected with generation of SSSI. So, the discovering of the dependency between the scattered signal widening and the distance from magnetic zenith to the scattering surface can give information about the area of mostly effective SSSI generation. To determine the moments when the scattering surface passes through the magnetic zenith one can use the effect that the strength of decameter irregularities (and, therefore, the intensity of the scattered signal) has its maximum right in the area of magnetic zenith [6]

During the experiments on gyroharmonic heating the scattered signals of Moscow station RWM at frequencies 9996 kHz and 14996 kHz, and of a number of broadcasting stations in band 15—22 MHz were detected in the observation point, located near Rostov-on-Don.

The results of processing of scattered signals received in the observation point for eight measurement series are summarized in Table 1. As the characteristics of

the scattered signal depend heavily on the value of detuning Δf, for each measurement series the characteristics of scattered signals, received under constant $\Delta f \approx 40$ kHz, were chosen for analysis.

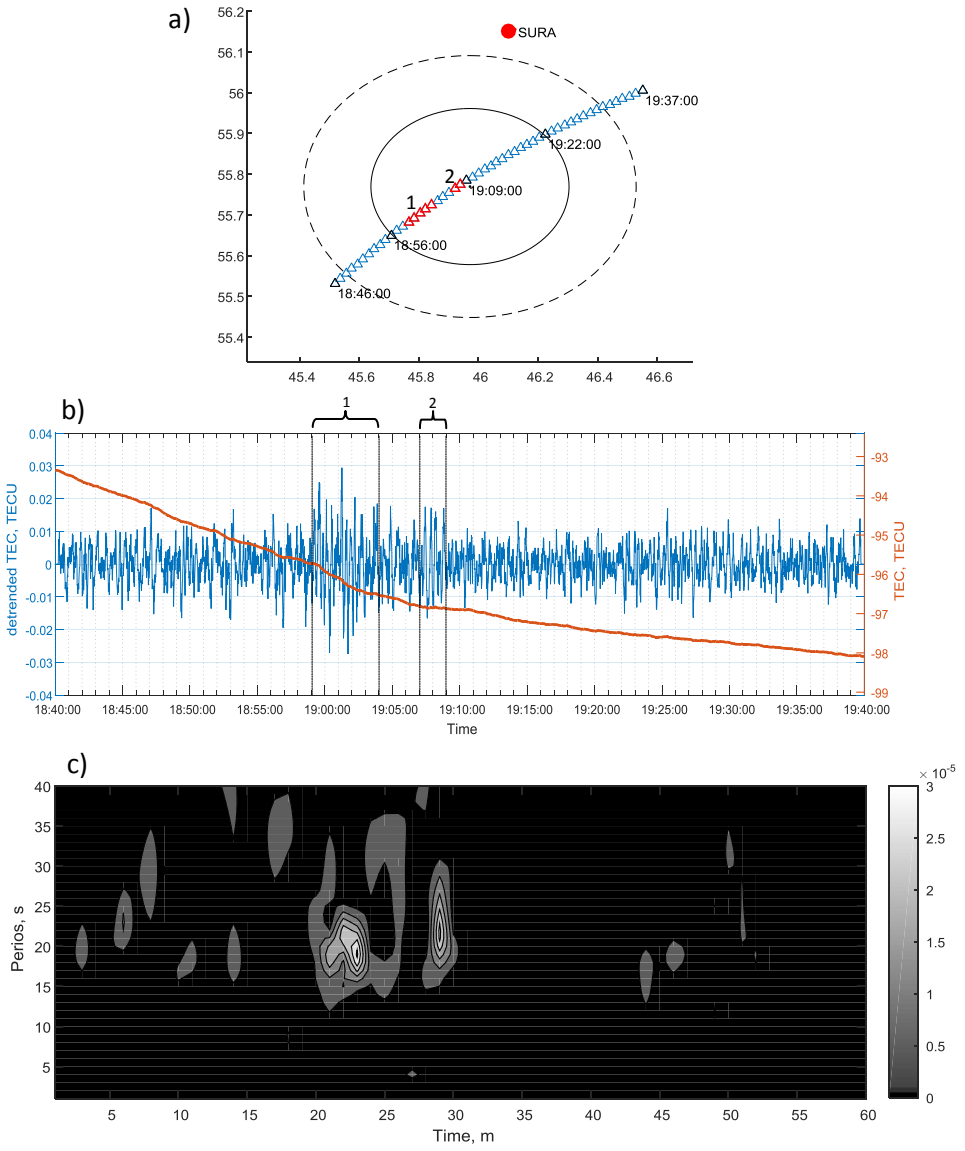

FIGURE 1. Experiment held on 21st of August 2011: (a) the satellite's PRN22 flight path across the main lobe of the radiation pattern of the Sura facility in geographic coordinates; (b) time dependence of TEC variations value during the satellite's flight across the excited area of ionosphere; (c) the results of TEC variations wavelet analysis.

TABLE 1. The results of processing of scattered signals received in the observation point for eight measurement series.

№	S_{max}, dB	δf_{20}, Hz	Δf, kHz	№	S_{max}, dB	δf_{20}, Hz	Δf, kHz
1	-83.7	2.2	40	5	-54.51	2.53	50
	-87.4	1.78	40		-51.6	2.93	50
	-72.1	5.82	40		-55.87	3.24	50
2	-66.6	4.23	40	6	-53.88	3.49	55
	-64.8	4.53	40		-41.32	6.75	55
3	-64.32	2.28	40	7	-46.21	4.35	45
	-62.34	7.67	45		-38.59	6.12	45
	-62.34	7.61	40	8	-42.19	0.71	40
4	-60.81	1.51	30		-39.59	6.83	40
	-51.46	3.33	30		-41.57	3.17	45

Figure 2 shows the dependency of the scattered signal spectrum widening vs. its intensity, for all measurements, introduced in Table 1. As it can be seen from Fig.2, together with the increase of the scattered signal power, more spectrum widening was detected.

Considering that the increase of scattered signal intensity under the constant detuning Δf indicates the approaching of the scattering cone to the magnetic zenith, we can conclude that the widening of the scattered signal spectrum (and, therefore, more effective SSSI generation) has its maximum in the magnetic zenith area.

FIGURE 2.The dependency of the scattered signal spectrum widening vs. its intensity.

Conclusion. As a result of the measurements held on the Sura facility it was found that under the periodic (±5s or ±10s) HF heating of ionosphere at frequen-

cies a bit higher than the electron gyrofrequency harmonic, fast variations of ionosphere plasma density are observed, which can be caused by artificial SSSI with c $l_{\perp} \approx 10$ cm and $\Delta N/N \approx 10\%$. Their generation is mostly effective in the magnetic zenith area.

This work was done under the financial support of RSF grant № 14-12-00556.

1. A. V. Gurevich and K. P. Zybin, Strong field aligned scattering of UHF radio waves in ionospheric modification, *Phys. Lett. A*, 2006, 358, pp. 159—165.

2. I. A. Bolotin, V. L. Frolov, A. M. Padokhin, and V. E. Kunitsyn, Results of the experiments on super small scale artificial ionospheric irregularities detection by means of GPS signals, *XXIV Russian conference "Radio Wave Propagation"*, Irkutsk, 29 June — 5 July 2014. *Conference proceedings*, 3, pp. 41—46.

3. G. M. Milikh, A. V. Gurevich, K. P. Zybin, and J. Secan, Perturbations of GPS signals by the ionospheric irregularities generated due to PF-heating at triple of electron gyrofrequency, *Geophys. Res. Lett*., 2008, 35, L22102, doi:10.1029/2008GL035527.

4. A. C. Najmi, G. Milikh, J. Secan et al., Generationand detection of super small striations by F region HF heating, *J. Geophys. Res. Space Physics*, 2014, 119, pp. 6000—6011, doi:10.1002/2014JA020038.

5. V. L. Frolov, I. A. Bolotin, G. P. Komrakov at al., The gyroharmonic properties of artificial ionospheric irregularities generation, *Radiophysics and Quantum Electronics*, Nizhny Novgorod, 2012, 55, pp.393—420.

6. N. I. Budko, V. V. Vaskov, G. P. Komrakov at al., Features of the small scale irregularities excitation in the resonance area of ionosphere plasma under the oblique ionosphere exposure by the powerful radiowave, *Geomagn. Aeron.*, 1989, 29(6), pp. 973—980.

Ionosphere Response to Intense ULF Waves as observed by GPS/TEC and EISCAT Instruments

Vladimir B. Belakhovsky[1], Viacheslav A. Pilipenko[1], D. Murr[2], Evgeniy N. Fedorov[1], and Alexander E. Kozlovsky[3]

[1]Institute of Physics of the Earth, Moscow
[2]Augsburg College, Minneapolis
[3]Sodankyla Geophysical Observatory of the University of Oulu

Abstract. Earlier studies demonstrated that the monitoring of the ionospheric total electron content (TEC) by global satellite navigation systems is a powerful method to study the propagation of transient disturbances in the ionosphere, induced by internal gravity waves. This technique has turned out to be sensitive enough to detect ionospheric signatures of magnetohydrodynamic (MHD) waves as well. However, the effect of TEC modulation by ULF waves is not well examined a responsible mechanism has not been firmly identified. During periods with intense Pc5 waves distinct pulsations with the same periodicity were found in the

TEC data from high-latitude GPS receivers in Scandinavia. We analyze jointly responses in TEC variations and EISCAT ionospheric parameters to global Pc5 pulsations during the recovery phase of the strong magnetic storms on Oct. 31, 2003. Comparison of periodic fluctuations of the electron density at different altitudes from EISCAT data shows that main contribution into TEC pulsations is provided by the lower ionosphere, up to ~150 km, that is the E-layer and lower F-layer. This observational fact favors the TEC modulation mechanism by field-aligned plasma transport induced by Alfven wave, though energetic electron precipitation and ionosphere Joule heating might be involved too.

Introduction. The ionosphere represents an inner boundary of the near-Earth environment where the energy exchange occurs between the neutral atmosphere and the plasma of outer space. MHD waves provide an effective channel of the energy transfer from the outer magnetosphere to the bottom of the ionosphere. The interaction between the solar wind and magnetosphere acts as a permanent source of various types of MHD waves in the ultra-low-frequency (ULF) band, which fill the entire magnetosphere and reach its inner boundary, the ionosphere. While ground magnetometers and magnetospheric satellites provided tremendous amount of information about ULF wave properties in the magnetosphere and on the ground, the wave properties in the ionosphere remained unavailable to in-situ observations. The ever-growing array of global satellite navigation systems (GPS, GLONASS, etc) provide information on variations of a radiopath-integrated ionospheric parameter — the total electron content (TEC).

The GPS/TEC technique turned out to be sensitive enough to detect ionospheric signatures of ULF waves. The TEC modulation by intense Pc5 pulsations was found by [1, 2]. Thus, the standard TEC/GPS technique is sufficiently sensitive to detect ULF waves in some cases. However, a physical mechanism of TEC periodic modulation associated with ULF waves has not been established yet.

Here we analyze a unique event when the same global Pc5 waves were detected in the ionosphere by the GPS/TEC technique [1] and EISCAT radar [3]. We analyze these observations simultaneously which has provided an additional information on the relationship between geomagnetic and ionospheric variations.

Observational data. We use the standard TEC data with 30-sec resolution from an array of GPS receivers in Scandinavia. The slant TEC along a radiopath can be converted into the vertical vTEC, denoted here as N_T, by assuming the altitude of pierce points to be 250 km. As a measure of columnar density N_T the TEC unit (1 TECu = 10^{16} m^{-2}) is used.

Magnetometer 10-s data from the IMAGE array, covering the range of geographic latitudes from ~79^o to ~58^o, are used. The magnetometer observations are augmented with the multi-beam IRIS riometer data from Kilpisjarvi (KIL). The magnetometer data have been decimated to a common 30-s step with TEC data.

We use the data with 30-s cadence from the UHF radar EISCAT. The EISCAT radar system measures the altitude profile of electron density $N_e(z)$, ion temperature $T_i(z)$, and electron temperature $T_e(z)$ along the beam up to ~400 km.

Oct. 31, 2003 ULF event. During the recovery phase of large magnetic storm on Oct. 31, 2003 very intense (up to a few hundred nT) global quasi-mo-

nochromatic Pc5 waves were observed [4]. During the periods 1100—1200 UT and 1200—1300 UT with elevated Pc5 activity, TEC fluctuations have been compared with ground geomagnetic variations at station KIR (geographic latitude 67.8^{o}) and ionospheric parameters determined by EISCAT radar.

The TEC data show gradual variations around 30—40 TECu with superposed small-scale fluctuations. To highlight these fluctuations the TEC data have been detrended with a cut-off frequency of 1 mHz. Quasi-periodic TEC pulsations have been revealed over a wide latitudinal range. The comparison for the period 1100—1330 UT of TEC fluctuations along paths GPS7/KIRU, GPS9/KIRU with magnetic variations at KIR and EISCAT-derived ionospheric density N_e in the lower ionosphere, shows the occurrence of persistent periodicity in all these parameters (Fig. 1). The peak-to-peak amplitudes of oscillations of the TEC are ΔN_T ~0.6 TECU (GPS07/KIR), and ~1.0 TECU (GPS09/KIRU), and magnetic pulsations ΔB~400 nT (X-component) at KIR. Visual inspection of Fig. 1 shows that magnetic (X-component) and TEC variations are approximately out-of-phase. At the same time, the riometer data do not demonstrate the periodicity evident in magnetometer data (bottom panel in Fig. 1).

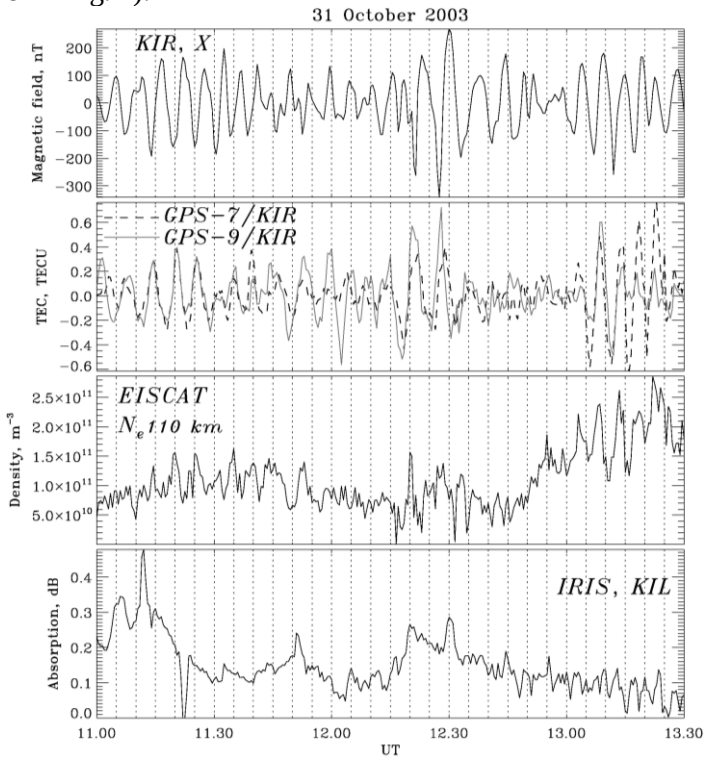

FIGURE 1. Multi-instrument observations of Pc5 waves during Oct. 31, 1100—1330 UT: (upper panel) X-component (in nT) of geomagnetic pulsations at KIR; (b) detrended (with a 1 mHz cut-off frequency) TEC fluctuations (in TECu) along radio paths GPS07/KIRU (dotted line) and GPS09/KIRU (solid line); (c) EISCAT N_e fluctuations at h = 110 km; and (d) cosmic noise absorption from KIL riometer.

Spectral analysis confirmed the occurrence of the same periodicity with f~2.4 mHz in variations of the geomagnetic field, TEC (GPS07, GPS09), and EISCAT N_e [3]. Cross-spectral analysis also showed a good correspondence between TEC and B variations. During the 1130—1300 UT time interval the spectral coherency of TEC fluctuations at GPS09/KIRU and magnetic pulsations at KIR around the frequency 2.5 mHz was high, $\gamma(f)$~0.8. The ratio between the spectral densities of TEC and X-component magnetic variations at this frequency was $\Delta N_T(f)/\Delta B(f) \sim 2 \cdot 10^{-3}$ TECu/nT. Magnetic pulsations (X-component, KIR) and EISCAT electric field E_x had coherency γ~0.8. The cross-correlation between TEC variations from GPS09/KIRU and EISCAT field E_x had a high coherency $\gamma(f)$~0.86. The ratio between spectral amplitudes at this frequency was $\Delta N_T(f)/E_x(f) \sim 4 \cdot 10^{-3}$ TECu/(mV/m).

An important parameter of ULF wave structure is its scale in the latitudinal (radial) and longitudinal (azimuthal) directions. The longitudinal propagation characteristics are characterized by the azimuthal wave number m, which can be determined from a cross-correlationtime shift $\Delta\tau$ between two detrended time series with periodic variations with period T at sites separated in longitude by $\Delta\Lambda$, as follows $m=(\Delta\tau/T)(360°/\Delta\Lambda)$. The cross-correlation function $R(\Delta\tau)$ for magnetic and TEC variations has been estimated using the magnetic stations KIR-LOZ at latitude ~67.8°, longitudinally separated in geographic coordinates by $\Delta\Lambda$~15.4°, and the longitudinally separated pierce points along receiver/satellite paths TROM/GPS9 and VARS/GPS28 at geographic latitude ~69.7° and separated in longitude by $\Delta\Lambda = 27.2°$. For the wave frequency f~2.5 mHz the azimuthal wave number $m \approx 0.9$ for magnetic data, $m \approx 0.5$ for TEC data. Thus, though both magnetic and TEC data show a Pc5 wave propagation in the same direction, the m-values from ionospheric TEC data are somewhat lower than those from ground geomagnetic data.

To find out which altitudes contributes most to the TEC variations, we have integrated ionospheric Ne(z) data from EISCAT over two different altitude range: the bottom ionosphere from 103 km to 152 km; and the F-layer from 152 km to 415 km. Comparison between height-time diagram of $N_e(t)$ variations, and altitude-integrated ionospheric densities $<N_e>$ (in TECu) are compared with actual TEC variations for time interval 1100—1200 UT (Fig. 2). Comparison of these fluctuations with periodic variations of TEC shows that main contribution is provided by lower ionosphere, up to ~150 km (that is the E-layer and lower F-layer).

Discussion. Long-period pulsations are the most powerful wave process in the near-Earth environment. The radar observations showed that Pc5 waves can noticeably modulate the ionospheric plasma: the electric field E, plasma convection velocity V, E-layer electron density N_e and the ionosphere conductance Σ, and electron T_e and ion T_i temperatures in both F- and E-layers (see references in [1]). Recent observations by [1, 2] have demonstrated that Pc5 waves are capable to modulate TEC as well.

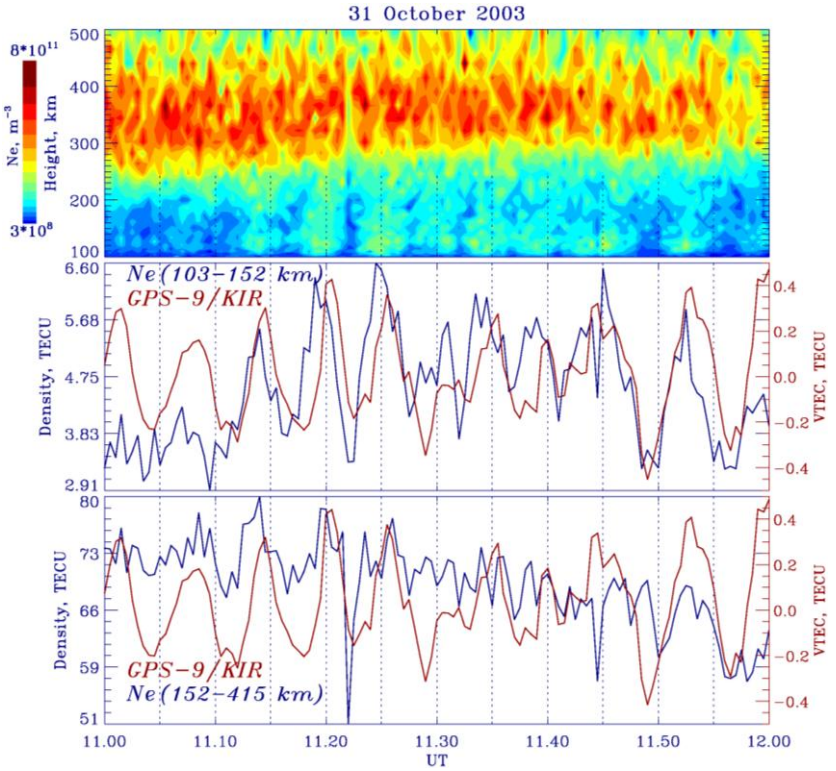

FIGURE 2. Time variations of the EISCAT electron density during 2003, Oct. 31, 1100—1200 UT: (upper panel) altitude-time plot; (middle panel) Ne variations (blue line) altitude-integrated over altitude range 103—152 km (in TECu), and superposed TEC variations (red line) from GPS9/KIRU; (bottom panel) Ne variations altitude-integrated over altitude range 152—415 km (in TECu) and superposed vTEC variations GPS9/KIRU.

One may expect that all the Pc5 wave-induced fractional variations of plasma and magnetic field should be of the same magnitude, like in any linear wave. However, GPS observations have revealed that the depth of periodic TEC modulation is sometimes even somewhat larger (e. g., in the event of Oct. 31, 2003 $\Delta N_T/N_T$ ~ 2.5 %) than the geomagnetic field modulation ($\Delta B/B_0$ ~ 1 %). In principle, ULF modulation of energetic electron precipitation, inducing an additional periodic ionization of the lower ionosphere, can cause periodic TEC variations with much higher depth than geomagnetic field variations [2]. However, during the event under consideration no periodic electron precipitation occurred as evidenced by simultaneous riometer observations.

Consideration of possible mechanisms of TEC modulation by magnetospheric Alfven waves has shown that in principle the plasma heating, vertical plasma drift, steep gradient, and field-aligned electron transport can provide a noticeable input into the observed TEC variations transport [1]. The field-aligned current transported by an Alfven wave, incident onto the ionosphere from the magnetosphere,

provides an additional periodic plasma flow in/out the ionosphere. As a result, the plasma density in the bottom ionosphere periodically increases/decreases. Moreover, the mechanism of the field-aligned plasma transport by Alfven waves can produce relative amplitudes of TEC variations, $\Delta N_T/N_T$, larger than that of geomagnetic pulsations, $\Delta B/B_0$.

A feature of the field-aligned plasma transport mechanism is that it contributes mainly into the bottom layers of the ionosphere, in accordance with the combined GPS/EISCAT/magnetometer observations. Surely, any conclusive judgments can be stated only after more detailed studies with the use of other ionospheric instruments that will provide more detailed information about ionospheric plasma parameters.

Conclusion. Long-period Pc5 pulsations being the most powerful wave process in the terrestrial environment can significantly modulate the local densities of the magnetospheric and ionospheric plasma. Even radiopath-integrated TEC has turned out to be sensitive enough to response to intense Pc5 waves. So far, the effect of TEC modulation by ULF waves is a challenge for the MHD wave theory, because responsible mechanisms of such modulation have not been firmly established yet. Analysis of the altitude profile of the electron density fluctuations derived from EISCAT data during the global Pc5 wave event has shown that main contribution into the periodic TEC variations is provided by lower ionosphere, up to ~150 km, that is the E-layer and lower F-layer. This observational fact favors the field-aligned plasma transfer induced by Alfven wave as a dominant modulation mechanism.

Acknowledgements. *This study was supported by the RFBR grants N 16-35-60049 mol_a_dk (BV), N 14-05-00588 (VP), and N 15-05-01814 (EF), and NSF grant ATM-0827903 to Augsburg College (DM). Dual-frequency 30-s rate GPS measurements are freely available as daily data files in RINEX format from the IGS (ftp://cddis.gsfc.nasa.gov). We are indebted to the staff of EISCAT for operating the facility and supplying the data. We thank the institutes who maintain the IMAGE magnetometer array (www. ava. fmi. fi/image). The riometer data originated from the IRIS, operated by the Lancaster University (UK) in collaboration with the Sodankyla Geophysical Observatory.*

1. V. Pilipenko, V. Belakhovsky, D. Murr et al., Modulation of total electron content by ULF Pc5 waves, *J. Geophys. Res*., 2014, 119, pp. 4358—4369.

2. C. Watson, P.T. Jayachandran, H.J. Singer et al., Large-amplitude GPS TEC variations associated with Pc5—6 magnetic field variations observed on the ground and at geosynchronous orbit, *J. Geophys. Res.*, 2015, 120, doi:10.1002/2015JA021517.

3. V. Pilipenko, V. Belakhovsky, A. Kozlovsky et al., ULF wave modulation of the ionospheric parameters: Radar and magnetometer observations, *J. Atmosph. Solar-Terr. Physics*, 2014, 108, pp. 68—76.

4. N. G. Kleimenova and O. V. Kozyreva, Spatial-temporal dynamics of Pi3 and Pc5 geomagnetic pulsations during the extreme magnetic storms in October 2003, *Geomagn. Aeron.*,2005, 45, pp. 71—79.

Longitudinal Variation of Winter Anomaly in the *F*2 Peak Electron Density and its Manifestations in Topside Ionosphere, Plasmaspheric and Total Electron Content

Maxim V. Klimenko[1,2], Vladimir V. Klimenko[1], Irina E. Zakharenkova[1], Konstantin G. Ratovsky[3], Yury V. Yasyukevich[3], Anna S. Polyakova[3], Nicolai V. Chirik[2], and Renata Yu. Lukianova[4,5]

[1]West Department of Pushkov IZMIRAN, RAS, 236017, Kaliningrad, 41 Pobeda Av., Russia
[2]Immanuel Kant Baltic Federal University, 236041, Kaliningrad,14 A. Nevsky Str., Russia
[3]Institute of Solar-Terrestrial Physics, SB RAS, 664033, Irkutsk P/O Box 291, 126a Lermontov Str., Russia
[4]Geophysical Center, RAS, 119296, Moscow, 3 Molodezhnaya Str., Russia
[5]Space Research Institute, RAS, 117997, Moscow, 84/32 Profsoyuznaya Str, Russia

Winter anomaly (WA) is a mid-latitude ionospheric *F* region phenomenon. WA is identified as an anomalous daytime winter/summer *foF*2 (MHz) or N_mF2 (m^{-3}) = $1.24\times10^{10}foF2^2$ ratio, when at the similar level of solar and geomagnetic activity the daytime winter *foF*2 or N_mF2 values exceed the daytime summer values [1—3]. The formation mechanism of winter anomaly in the *F*2 peak electron density *(N_mF2)* is presented in [4]. According to [4] at a fixed geographic latitude a winter anomaly is stronger developed at longitudinal sectors that most closest to geomagnetic pole.

We analyzed the winter anomaly in N_mF2 and its manifestation in the topside ionospheric electron density, plasmaspheric and total electron content (*TEC*) according to satellite data and first-principle model results. We used 1998—2015 data of Global Ionospheric Maps (GIM) for the TEC analysis; COSMIC, CHAMP and GRACE radio occultation data for the N_mF2 analysis during 2001—2015; CHAMP in-situ measurements of electron density; GRACE K-band ranging system (KBR) in situ topside ionospheric electron density data; data of GPS recoder onboard GRACE satellites for plasmaspheric electron content estimation. The maps of the winter anomaly intensity in *TEC* were obtained using observation data for different solar and geomagnetic activity levels. In the present study we evaluated the degree of reproduction of the winter anomaly that is obtained using a Global Self-consistent Model of the Thermosphere, Ionosphere, and Protonosphere (GSM TIP) [6]. GSM TIP model runs for winter and summer solstice at low ($F_{10.7}$ = 80) and moderate ($F_{10.7}$ = 125) solar activity were performed using empirical model of field-aligned currents [7] that developed according to Magsat and Ørsted satellite data.

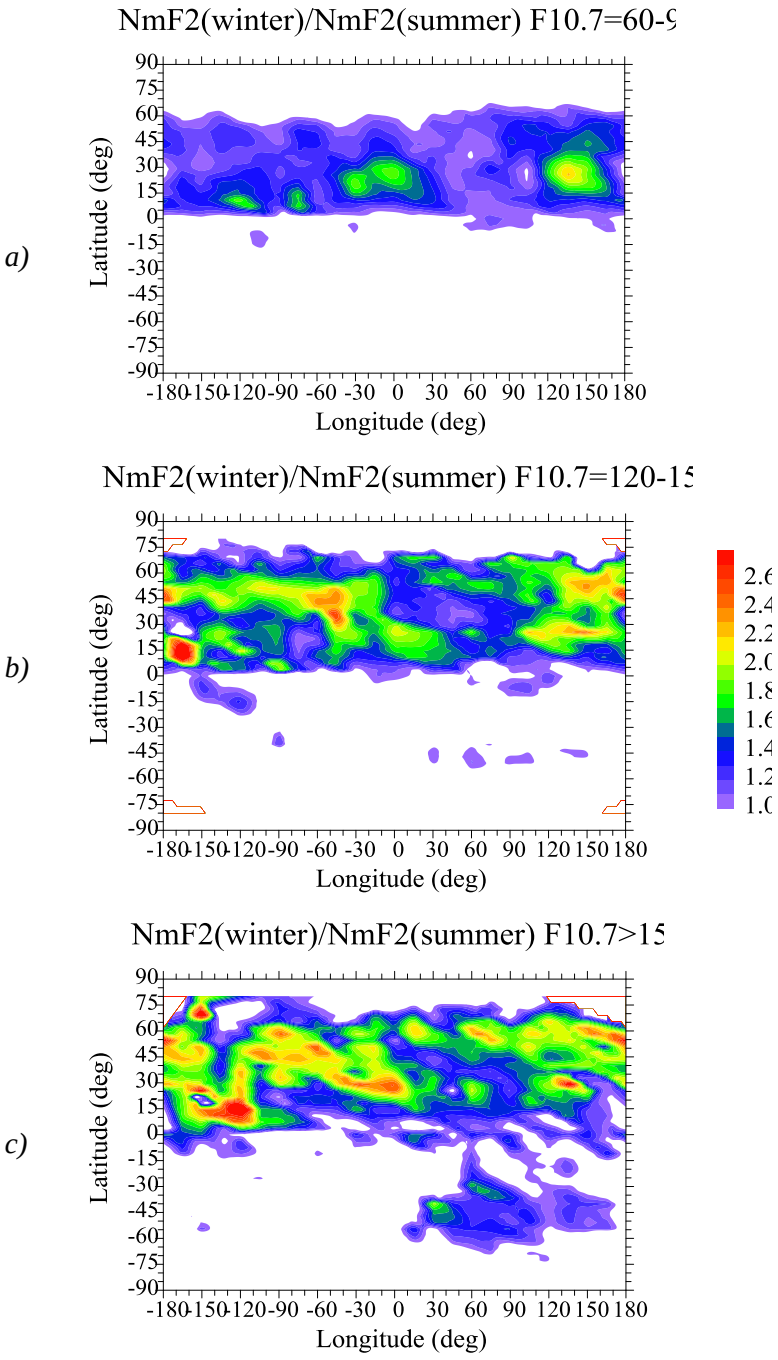

FIGURE 1. Winter-to-summer ratio of noon N_mF2, obtained using radio occultation technique at low ($F_{10.7}$ ~ 60—90 sfu), middle ($F_{10.7}$ ~ 120—150 sfu) and high ($F_{10.7}$> 150 sfu) solar activity.

As a quantitative characteristic of winter anomaly intensity we used the daytime winter-to-summer ratio of all considered parameters. Winter and summer periods determined as a solstice day ±30 days.

Figures 1 and 2 present the maps of winter/summer N_mF2 and *TEC* ratios obtained using radio occultation and GPS measurements at low, moderate and high solar activity. Figure 3 presents the maps of winter/summer N_mF2 and *TEC* ratios obtained using GSM TIP model for low and moderate solar activity.

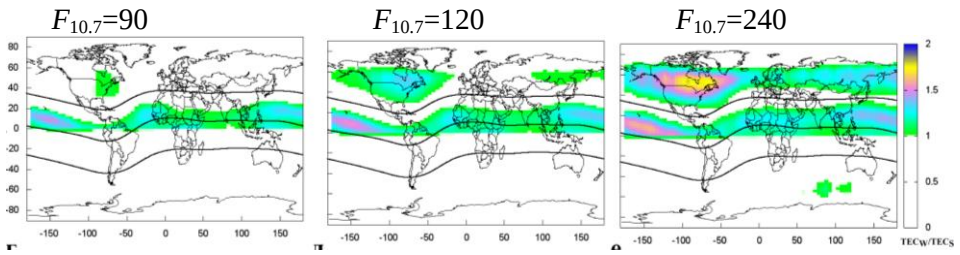

FIGURE 2. Maps of Winter-to-summer ratio in daytime *TEC*. GPS observation data.

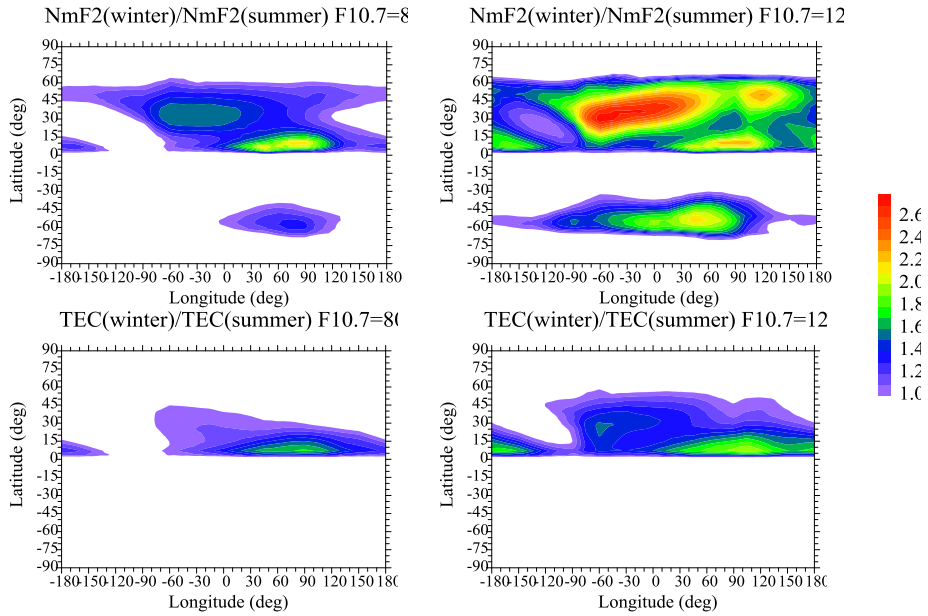

FIGURE 3. Maps of winter/summer ratios of the noon N_mF2 (top) and *TEC* (bottom) values, obtained in GSM TIP model for low ($F_{10.7}$=80 — left) and moderate ($F_{10.7}$=125 — right) solar activity.

It is shown that the winter anomaly intensity is higher in N_mF2 than in *TEC*. We found that the winter anomaly in *TEC* is absent at solar activity minimum for both Northern and Southern hemisphere. According to observation data the winter

anomaly in *TEC* starts forming at $F_{10.7}$ ~ 90 sfu for Northern hemisphere mid-latitudes and at $F_{10.7}$ ~ 240 sfu for the Southern hemisphere mid-latitudes. The model/data comparison have shown that (1) GSM TIP model and radio occultation data don't reproduce the extreme high values of winter anomaly intensity thatwas registered by ground-based ionosonde data [1]; (2) the GSM TIP model reproduces the main longitudinal features of winter anomaly formation; (3) winter anomaly is more pronounced in Northern Hemisphere than in Southern one. These results are consistent with the well-known experimental facts [4, 5]. On the other hand these results disagree with [6], where the proposed formation mechanism of winter anomaly does not lead to the any differences in WA intensity in Northern and Southern hemisphere. The most significant intensity of winter anomaly is appeared in American-Atlantic longitudinal sector. The same longitudinal variation of winter anomaly manifested in electron density according to CHAMP (height of ~300 km) satellite data and GRACE plasmaspheric electron content (integral electron density in the height region from 480 km up to 20,200 km) (see Fig. 4).

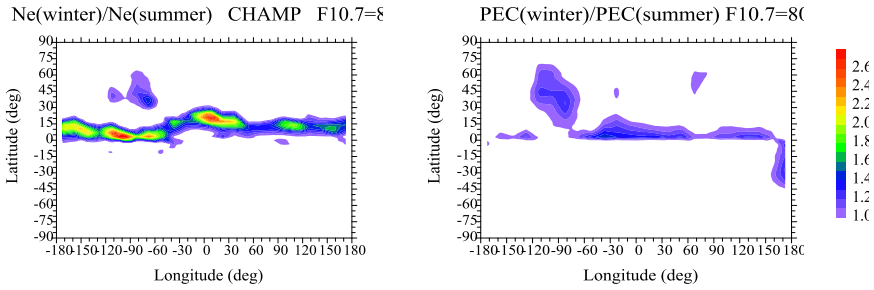

FIGURE 4. Maps of winter/summer ratios of the noon N_e values (left) and electron content in height region from 480 km up to 20,200 km(right) according to observations of CHAMP and GRACE satellites for low ($F_{10.7}$=80) solar activity.

Acknowledgments. *Authors thank the Jet Propulsion Laboratory for the provision of Global Ionospheric Maps (GIM) TEC and also Pavlov A. V. and Pavlova N. M., which results were used in our study. These investigations were performed with financial support of the Russian Foundation for Basic Research Grants No. 16-35-60018 and 14-05-00788.*

1. A. V. Pavlov and N. M. Pavlova, Variations in statistical parameters of the NmF2 winter anomaly with latitude and solar activity, *Geomagn. Aeron.*, 2012, 52(3), pp. 335—343.

2. H. Rishbeth, How the thermospheric circulation affects the ionosphere, *J. Atmos. Solar-Terr. Phys.*, 1998, 60, pp. 1385—1402.

3. M. R. Torr and D. G. Torr (1973), The seasonal behaviour of the F2-layer of the ionosphere, *J. Atmos. Terr. Phys.*, 1973, 35, pp. 2237—2251.

4. H. Rishbeth, I. C. F. Muller-Wodarg, L. Zou et al., Annual and semiannual variations in the ionospheric F2-layer: II: Physical discussion, *Ann. Geophys*., 2000, 18(8), pp. 945—956.

5. A. J. Mannucci, B. D. Wilson, D. N. Yuan et al., A global mapping technique for GPS-derived ionospheric TEC measurements, *Radio Sci.*, 1988, 33(3), pp. 565—582.

6. A. A. Namgaladze, Yu. N. Korenkov, V. V. Klimenko et al., Global numerical model of the thermosphere, ionosphere, and protonosphere of the Earth, *Geomagn. Aeron.*, 1990, 30(4), pp. 612—619.

7. R. Lukianova and F. Christiansen, Modeling of the global distribution of ionospheric electric field based on realistic maps of field-aligned currents, *J. Geophys. Res*., 2006, 111. A03213, doi:10.1029/2005JA011465.

Discrete Radio Source Scintillations as Method for Ionosphere Study at Irkutsk Incoherent Scattering Radar

Roman V. Vasilyev, Mariia V. Globa, Dmitry S. Kushnarev, Andrey V. Medvedev, and Konstantin G. Ratovsky

Institute of solar-terrestrial physics SD RAS, Russia, 664033, Irkutsk p/o box 291; Lermontov st., 126a

We present some latest results of observation of Cygnus-A radio source in quiet and disturbed geomagnetic condition at Irkutsk incoherent scattering radar (IISR). Scintillation method applied for ionosphere testing at IISR confidently defines Fresnel frequency and power cutoff — the spectral characteristics usually related to the velocities and spatial spectra of ionospheric plasma disturbances. We also connect our data to IGFR magnetic field model in order to show possible relation between shape of discrete radio source scintillation spectra, radio source position and geomagnetic field.

Irkutsk incoherent scattering radar (IISR) is able to perform observations of the discrete cosmic radio sources in continuous regime during long time interval, up to the several hours per day during several months. Variations of radio source intensity at the time scale from tens to hundreds of seconds appearing due to ionospheric disturbances are frequently arise at radio astronomical or satellite observations. The phenomenon, also referred to as scintillation of radio signal in the ionosphere, was well studied in the last century [1]. The shape of scintillation spectra reflects spatial spectra of ionospheric disturbances, and relative velocity of disturbances and radio source. Scintillations of radio signal from discrete cosmic radio source are also observed and preliminary studied at IISR [2]. In that work we showed necessity to increase time resolution in order to get spectral characteristics able to show ionospheric disturbances parameters.

At the moment we have improved time resolution of our observations from 18 to 4.5 seconds and frequency resolution also have increased significantly (several times). This allows us to distinguish radio source signal from ambient noise more precisely and get spectral parameters of ionospheric scintillations with better resolution. We performed passive observations within 14 days from 18 June to 01 July

2015 and extracted variations of Cygnus-A radio galaxy intensity during that period. Example of scintillation spectrum is shown in Fig. 1. One can see the Fresnel frequency peak of the spectrum and power law behavior of the left part of the spectrum.

From our observation we found that scintillation index S4 tends to increase in the limited time domain, except case of geomagnetic storm 22 June 2015, when we see two maxima of S4 during observation time. In work [3] was shown the peculiar behavior of ionospheric scintillations concerned with angle α between magnetic field and line of sight to the radio source. We supposed the same mechanism to be responsible for increasing of S4 in our observations. Figure 2 shows behavior of superimposed S4 indices for all of observational days and α in local stellar time for

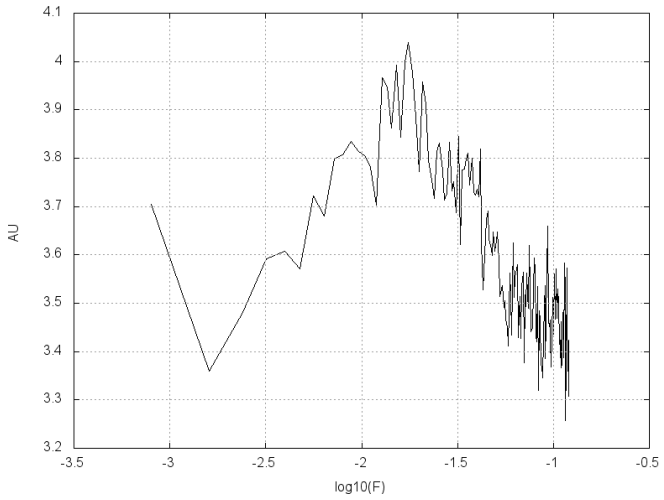

FIGURE 1. Spectrum of scintillation obtained with new IISR technique for June 24, 2015. Fresnel frequency is about 16.7 mHz, exponent from 16 mHz and higher — 1.066 Hz.

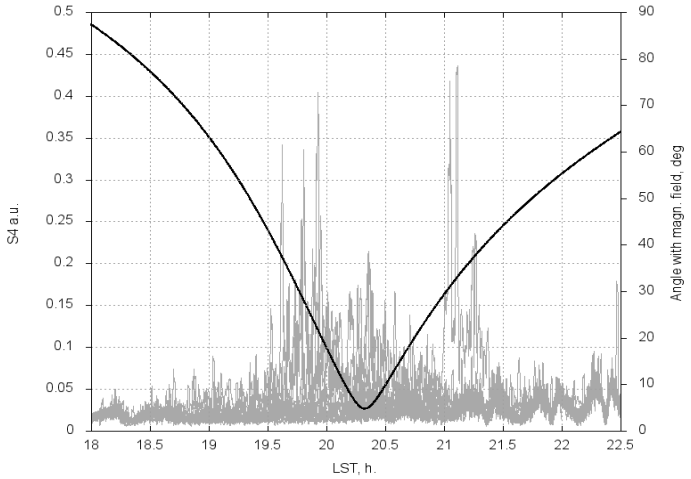

FIGURE 2. Gray lines — S4 indices vs local stellar time for IISR location for all observational days. Black line — angle between magnetic field and line of sight to the radio source.

IISR location. It is clearly seen that scintillations intensity increases with α decreasing, and became maximal when we look to the radio source along the magnetic field. Angle α was calculated from IGRF model using WMM2015 coefficients set.

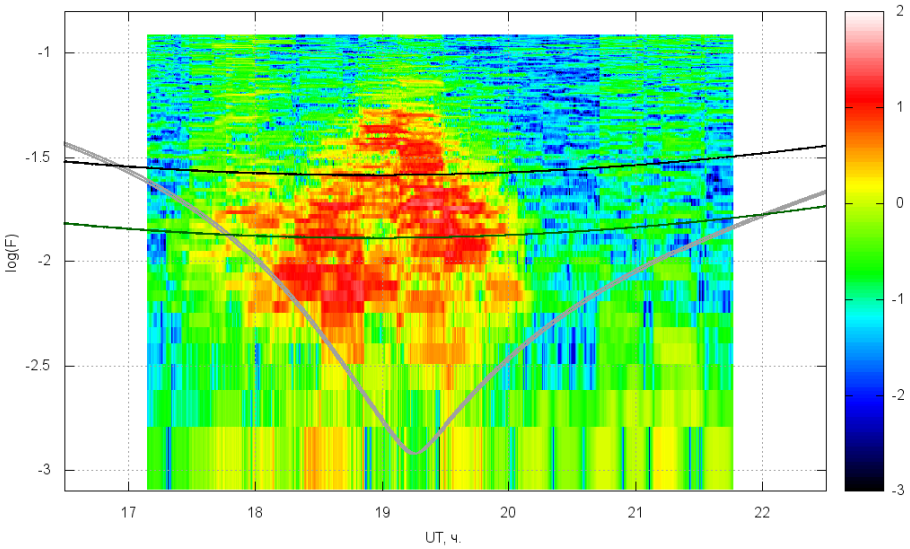

FIGURE 3. Running spectra of scintillations for June 24, 2015. Coincident grey lines show variation of angle between magnetic field and line of sight to the radio source, black line corresponds to velocity in (1) for R = 400 km, green line corresponds to velocity in (1) for R = 100 km.

The running spectrum of scintillations with respect to the α for one day of observation is presented at Fig. 3. The exponent of scintillation spectrum for frequencies higher than Fresnel frequency changes with α and has minimum value when α is close to zero. Obviously it is the reason of S4 increasing with α decreasing for our observations. Other interesting feature of such approach is the comparison of the Fresnel frequency of spectrum with some theoretical frequency obtained from velocity of motion of some point through ionospheric disturbances at fixed height. The height also defines size of disturbances as a size of Fresnel zone for IISR wavelength. Point coordinates are calculated from the intersection of line of sight from IISR to the radio source with some sphere. The sphere is concentric with the Earth and has a radius bigger than the Earth radius on value of desirable height. Velocity vector of such point is almost perpendicular to the magnetic field for whole observation period, and frequency is defined as:

$$F_t = V_\perp \sqrt{\lambda R} \qquad (1)$$

where$F_t$is the (calculated) theoretical frequency, $V_\perp$ is the component of intersection point velocity normal to the magnetic field, λ is the wavelength of received

electromagnetic radiation (2 m.) and R is the distance from IISR to intersection point. F_t behavior for different heights is shown at Fig. 3 with black and green lines. The Fresnel frequency of the spectrum changes from the theoretical frequency corresponding to 100 km to the values F_t corresponding to intermediate R between 100 and 400 km.

One should remark that we do not include motion of disturbances itself in the described picture of observed phenomena yet. In our geometry IISR observe part of Cygnus-A trajectory which predominantly lay along parallel. Due to this fact in case of meridional motion of disturbances with the velocity less than $V_\perp$ the Fresnel frequency will show only radio source motion through ionospheric disturbances as (1). If meridional velocity of disturbances will increase to the values significantly more than $V_\perp$ the observed Fresnel frequency starts to exhibit motion of the ionospheric disturbances, rather than radio source motion. Zonal motion of the ionospheric disturbances for IISR observation geometry can significantly increase or decrease Fresnel frequency in spectra in dependence of motion direction. Disturbances moving from East to West lead to decrease of observed Fresnel frequency, whereas opposite direction of motion increases it. In case of Fig. 3 one can say that in the first stage (18—19 UT) there was observed East-West motion of the ionospheric disturbances, and in second stage (19—20 UT) they stopped or changed the direction of motion.

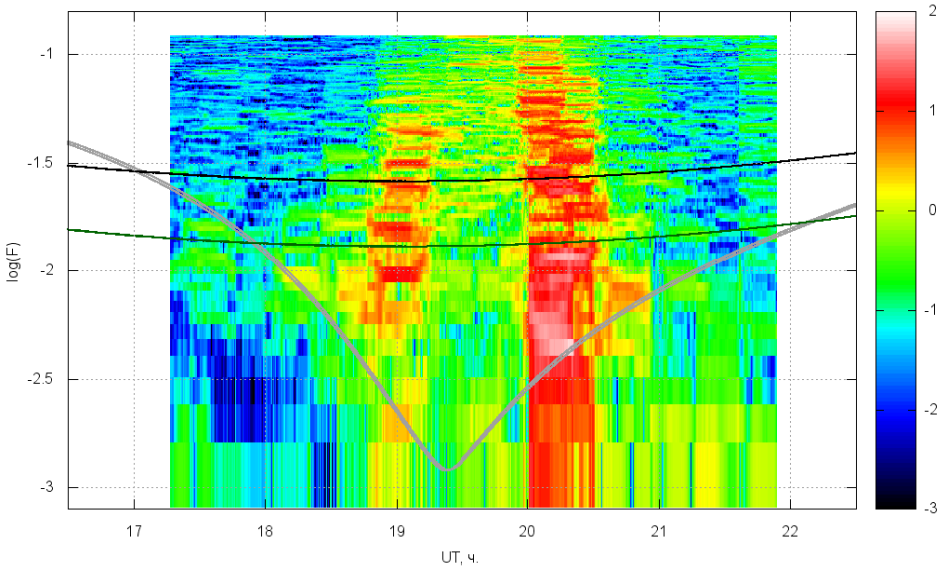

FIGURE 4. Running spectrum of scintillations for June 22, 2015. Coincident grey lines show behavior of angle between magnetic field and line of sight to the radio source, black line corresponds to velocity in (1) for R = 400 km, green line corresponds to velocity in (1) for R = 100 km.

All of processed data from 18 June 2015 to 01 July 2015 show similar behavior. There is dependence of spectral width on angle between magnetic field and line of sight to the radio source, except for the day with geomagnetic storm on 22 June 2015, see Fig. 4. Begin of the dataset shows expected behavior, whereas starting from 20 UT spectra significantly grow in intensity and expand to higher frequencies. Fresnel frequency splits into two peaks and the lowest one moves down possible due to the East — West motion of the disturbances. This fact makes some confusion. Obviously, the source of the ionospheric disturbances lays in the North direction in this case. Explanation could be in the phenomenon when large scale (hundreds and thousands kilometers) ionospheric disturbances generate the small scale (from meters to kilometers) disturbances [4] and they move independently from parent large scale wave.

Described analysis of scintillation data requires more attention than was paid. It is based on assumption that scintillations appear due to field aligned disturbances, but that fact limits the height range — we should take into account only plasma without significant collisions. Disturbances appearing at the heights where collisions play significant role would form another kind of scintillations spectra. In order to clarify possibilities of the method one should perform modeling with set of known ionospheric plasma parameters and different directions of disturbances motion.

Irkutsk incoherent scatter radar could make significant contribution in the ionosphere monitoring by radio astronomical observations. The observation time window of IISR is sliding during the day due to fixed scan view. Unfortunately, this closes the possibility to make seasonal observation of radio wave scintillations in the ionosphere, mostly appearing at the local night at IISR latitudes. Nevertheless operations in couple with other instruments (GPS stations, ionosondes, optical monitoring) opens up extensive possibilities, in particular for searching of mid-latitude radio wave scintillations sources in the ionosphere.

The work was supported by RFBR grant 15-05-03946 A.

1. Kung Chie Yeh and Chao-Han Liu, Radio wave scintillations in the ionosphere, *Proceedings of the IEEE*, April 1982, 70(4), pp. 324—360, doi:10.1109/PROC.1982.12313.

2. R. V. Vasilyev, D. S. Kushnarev, V. P. Lebedev et al., Perspectives of usage of Irkutsk incoherent scatter radar (IISR) as an imaging riometer and radio-heliograph, *J. Atmos. Sol.—Terr. Phys*., 2013, 105, pp. 273—280, doi:10.1016/j. jastp.2013.06.012.

3. B. N. Gershman, L. M. Eruxhimov, and Yu.Ya.Yashin, Wavy Phenomena in the Ionosphere and Cosmic Plasma, Moscow, Nauka, 1984 (in Russian).

4. E. I. Astafyeva, E. L. Afraimovich, and S. V. Voeykov, Generation of secondary waves due to intensive large-scale AGW traveling, *Adv. Space Res.*, 2008, 41(9), pp. 1459—1462, doi: 10.1016/j. asr.2007.03.059.

Polar Wind Outflow Characteristic at ~20000 km Altitude

Dmitry V. Chugunin[1], Maxim V. Klimenko[2,3], and Vladimir V. Klimenko[2]

[1]Space Research Institute of RAS, 117997, Profsoyuznaya 84/32, Moscow, Russia
[2]West Department of Pushkov IZMIRAN RAS, 236017, Kaliningrad, 41 Pobeda Av., Russia
[3]Immanuel Kant Baltic Federal University, 236041, Kaliningrad, 14 A. Nevsky Str., Russia

Polar wind is the process of plasma flowing out along the high-latitude magnetic tubes from the ionosphere, where the plasma pressure is rather high, into the magnetosphere in which the plasma pressure is very low. According to the classical theory [1], the thermal energy of electrons and ions in the ionosphere is a source of energy for the polar wind. This means that the ions move upwards into the magnetosphere only due to the pressure gradients of the electron and ion gas acting against the gravity force.

Over the period of studying the polar wind, many numerical models of this phenomenon were developed in which the authors tried to take into account all the known factors which could influence such an outflow of ions from the polar cap ionosphere. They were both hydrodynamic [2, 3] and kinetic [4, 5] models, however, it is not yet found exactly (especially at high altitudes) to what degree their results coincide with real characteristics of the polar wind. In the first place, it is caused by the fact that at high altitudes measurements of the ion distribution functions of the polar wind are very complicated due to the positive potential of satellites relative to the ambient plasma. As a result, a substantial part of the distribution function of cold ions in the polar wind cannot be measured.

Until recently the main source of data with which the modeling results were compared were the measurements conducted onboard the Akebono satellite. The averaged densities and velocities of ions in the polar cap according to the data of the SMS instrument installed onboard this satellite were presented in [6, 7]. After launching the Image satellite, the results of sounding the magnetospheric plasma by electromagnetic waves of the RPI instrument were published. Unfortunately, such a method does not make it possible to determine the field-aligned velocities of ions and their temperature.

The published characteristics of the polar wind obtained by these satellites are a result of averaging measurements in the polar cap depending on height and geomagnetic activity. In this case, as a rule, all that lies above a given invariant latitude was taken as the polar cap. Latitudes of 77° and 70° were taken in [7] and [8], respectively. However, in [9] it was noted that in the polar cap at high altitudes, one can distinguish several types of ionospheric ions outflow and only one of them is caused by the polar wind mechanism. These flows could be caused by the follow-

ing processes: the outflow of ions in the region of auroral currents and fields (mainly in the auroral oval); the "cleft ion fountain" where direct penetration of energetic particles from the magnetosheath, which leads to formation of intense conic beams (conics) convected to the polar cap; and interested to us the polar wind.

The most accurate selection of measurements corresponding to criteria of the region where polar wind flows could be observed was performed in [9]. Unfortunately, the Interball-2 satellite whose measurements are used in this paper did not reach invariant latitudes higher than 81°. According to [9], it was found that the selected segments of measurements on which the presence of the polar wind was possible were located in the nighttime part of the polar cap and almost coincided with the Ion Depletion Zone. The sensitivity of the SMS instrument onboard the Akebono satellite in this region was not sufficient to determine characteristics of fluxes of cold ionospheric ions, that is, the fluxes in this region almost were not included into the statistics of these measurements. The ion flows measured onboard the Interball-2 satellite in the chosen segments of orbits were split into types which differed strongly between themselves. Four of them could be referred to as polar wind flows. Here is their description: (1) cold and rather intense flows of H+ ions, while O+ ions do not reach the detector (we denote them as **H**); (2) the same flows of H+ ions, but simultaneously fluxes of O+ ions are detected (**Ho**); (3) very weak fluxes of H+ ions in the absence of O+ ions (**h**); and (4) ions do not reach the detector, that is, the positive potential of the satellite together with the weak intensity of the fluxes do not make it possible to conduct their measurements (**na**). It was shown in [15] that in summer periods there existed only fluxes **H** and **Ho**, and **h** and **na**took place only in winter seasons. This fact manifests an obvious dependence of the polar wind flux intensity on the illumination of the ionosphere. A hypothesis was also put forward that the O+ ion fluxes depend on the polar rain. This paper is a continuation of the studies the results of which were presented in [17], and an attempt is undertaken here to find the difference between the **H** and **Ho** flows and also to obtain characteristics of ionospheric ion fluxes in the polar cap in summer period.

The measurements of the Hyperboloid energy—angle mass-spectrometer installed onboard the Interball-2 satellite (Auroral Probe) were used. Hyperboloid measured the three-dimensional distribution function of the main ion species H+, He+, O++, and O+ within the ~1—80 eV energy range. The complete 3D-distribution function was measured during the period of the satellite rotation (2 min). The majority of measurements in the polar cap were at altitudes of the satellite apogee which was approximately 20,000 km. Moreover, the measurements considered here were made in 1996—1997, i. e., during the solar activity minimum.

For every 2-min measurement, moments of the distribution function (n, V, $T_\perp$, T) were calculated with allowance made for possible satellite potential. Unfortunately, the inverse problem of reconstructing from measurements the real distribution function of the ions having passed through the electric field surrounding the satellite in the plasma has not been solved yet for real configuration of the satellite.

Nevertheless, an algorithm of calculation of moments of the distribution function of ions on the basis of the Hyperboloid instrument data was developed. The potential at which the calculated density corresponded to the current balance equation was found by the iteration method. The obtained potential was further used also for calculation of the field-aligned velocity and temperature of ions. As a result, more than 300 values of the field-aligned group velocity of O+ and He+ ions were obtained, as well as more than 700 values of moments for H+ ions.

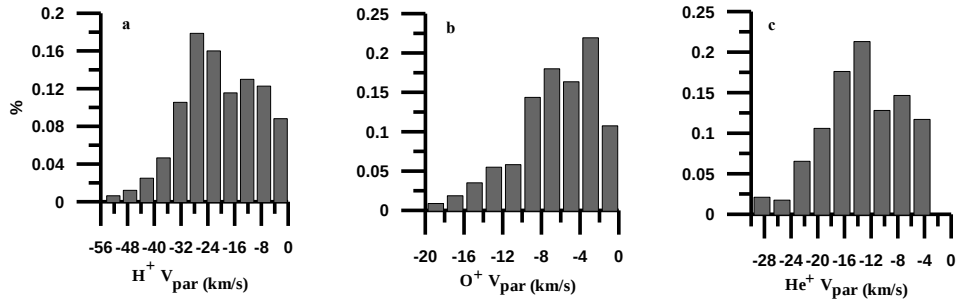

FIGURE 1. Distributions of the obtained field-aligned velocities of H+, He+, and O+ ions.

Figure 1 presents the distributions of the obtained field-aligned velocities for H+, He+, and O+ ions. The values for O+ ions are presented for flows of the **Ho** type, the values for H+ and He+ ions include measurements for both the **H** and **Ho** types. It follows from the data of these distributions that the average field-aligned velocities of H+, He+, and O+ ions are 21±10, 14.2 ±7, and 7 ±4 km/s, respectively. The large scatter of the values of the field-aligned velocities (which is about 50 %) is caused by two factors: imperfection of the method of determination of the moments from the measurements; the real scatter of values in the measurements.

When comparing the distributions of the field-aligned velocities of the H+ and He+ fluxes, the first thing which should be paid attention to is the fact that two graphs are very similar to each over. Helium ions behave exactly in the same way as hydrogen ones. There could be two explanations to this fact. First, helium is a light ion and should without any resistance from the Earth's gravity field follow hydrogen along open magnetic field lines. In this case, helium fluxes would differ from hydrogen fluxes only by the relative concentration in the ionosphere and by the flow velocity which depends on the ion mass. The second: H+ ion could find the way to the detector of He+ ions. However, in the latter case the velocities of helium and hydrogen ions should differ by a factor of 4. In our case, the velocities differ by a factor of 1.5—2. Thus, the graphs in Fig. 1 show that He+ ions behave identically to H+ ions. However, there are cases when He+ ions are not detected. Unfortunately, the Hyperboloid instrument operated in the regime when only measurements of H+ and O+ ions were permanently conducted. The channel of He+ measurements was sometimes switched off, so we cannot present reliable statistics of the He+ flux difference between the **H** and **Ho** types.

The statistical distribution of O+ ions velocities has no well pronounced peak as in the cases of H+ and He+ ions. The major part of measurements falls on velocities of 9—3 km/s, and after that there occurs a sharp decrease of the probability in the distribution. The velocities above 9 km/s with a high degree of probability are overestimated (that is, our method provided a wrong determination of the distribution function moments), so we can exclude them out of consideration. The distribution peak falls on 3 km/s. This is most probably due to the fact that the O+ ions with lower velocities just do not reach the detector because of the satellite's positive potential to overcome which their energy is not sufficient. A maximum at such low energies points to the fact that in the majority of cases we cannot determine exactly the field-aligned velocity of O+ ions because of the satellite potential and/or low intensity of the fluxes. The mean velocity of O+ ions at such statistical distribution is 7 km/s. If all said above is true, this velocity is overestimated, though it is impossible to determine its exact value because of measurement errors. If one takes only the velocity values below 10 km/s, then the average value of the field-aligned velocity of O+ ions is 5 km/s. We accept this value as the most correct and following from the measurement data.

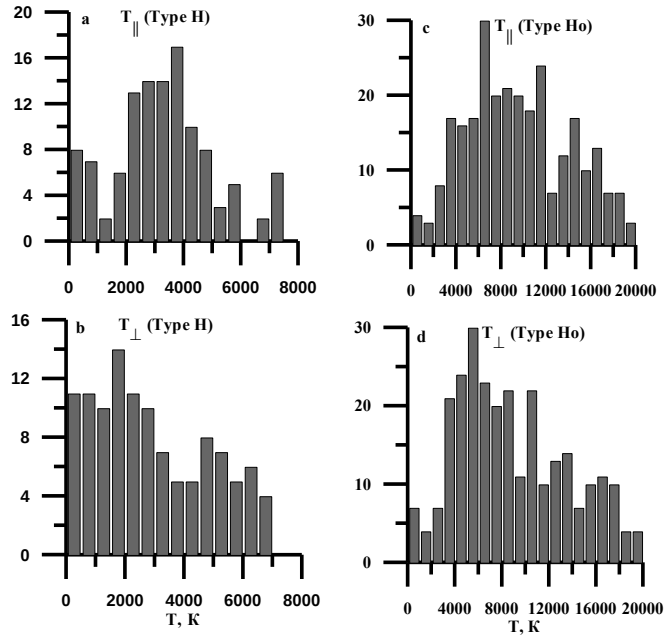

FIGURE 2. Distributions of the parallel and perpendicular temperatures of H+ ions.

The most reliable determinations of the temperature are for H+ ions. Figure 2 shows statistical distributions of the parallel and transverse temperatures of H+ ions for the **H** (Figs. 2a and 3b) and **Ho** (Figs. 2c and 2d) types. The temperature in Kelvins and the number of events in which such temperatures were determined are

shown on the abscissa and ordinate, respectively. It follows from these graphs that for the flows of the **H** type, the maxima of the parallel and perpendicular temperatures fell on 3500 and 2000 K, respectively. As it should be expected at high altitudes, when there is no heating across the magnetic field due to conservation of the first adiabatic invariant, $T_{\perp}<T_{\parallel}$. Accordingly, the $T_{\perp}/T_{\parallel}$ratio mainly is higher than 1, however, there are cases in which the temperature ratio was higher than 1. There are also measurements in which $T_{\perp}$ decreased down to 1000 K and even lower. It follows from the comparison of the left-hand and right-hand parts of Fig. 3 that the temperature of beams of the **Ho** type is higher than the temperatures of beams of the **H** type. The maxima in the distribution for the **Ho** type fall on $T_{\parallel}$~6500 K and $T_{\perp}$~5500 K. The temperature ratio is approximately equal to 1. This increase in the temperatures and their ratio is indicative of the fact that below the satellite a weak heating of H+ ions takes place, unlike the situation when the flows could be referred to as the **H** type. This heating slightly influences the outflow velocity of H+ ions, because their energy at the ionospheric level is sufficient to overcome the gravitation barrier. All this serves as an additional proof of the fact that the flows of the **H** and **Ho** types differ in their physical nature, and extra heating of ionospheric ions often occurs at low altitudes in the polar cap. Due to inaccuracy of the method of determination of the distribution function moments for weak fluxes, it was found impossible to present the same temperature distributions for He+ and O+ ions.

Table 1 presents a comparisons of measurements with polar wind characteristics simulated by the TUBE-7 model and modified Global Self-Consistent Model of the Thermosphere, Ionosphere and Protonosphere (GSM TIP) [10, 11]. The modeling results are a steady-state solutions of outflow of ionospheric ions.

TABLE 1. Comparisons Hyperboloid measurements with TUBE-7 and GSM TIP model.

	Interball-2. Summer 1997	TUBE-7 model. Solar minimum	GSM TIP
N_H	0.5—2 cm^{-3}	0.6 cm^{-3}	0.5 cm^{-3}
V_H	21 km/s	23 km/s	15—25 km/s
T_H	$T_{\parallel}$=3500 K $T_{\perp}$=2000 K *Type* **H** $T_{\parallel}$=6500 K $T_{\perp}$=5500 K *Type***Ho**	2500 K	3200 K
N_{He}	-	0.15 cm^{-3}	
V_{He}	14 km/s	10 km/s	
T_{He}	7500 K	2500 K	
N_O	0.1 cm^{-3}	0.4 cm^{-3}	0.05 cm^{-3}
V_O	5 km/s	1 km/s	
T_O	10000 K	1000 K	

The concentration and velocity coincide very well with the values calculated by the models. The results of calculations of the H+ ions temperature according to the models agree well with the temperature measurements in the flows of the **H** type.

The values of 2500 and 3200 K calculated by the models are in the middle between the obtained values of $T_{\parallel}$ and $T_{\perp}$. If one considers particular cases, in some measurements the temperature was even substantially lower than the model one. It testifies that the flows of the **H** type can be reliably referred to as a classical polar wind. The temperature of the flows of the **Ho** type was found by a factor of more than two higher than the model one. This indicates that the flows of the **Ho** type are not the classical polar wind: the ions have undergone an extra heating at lower altitudes, but this heating influenced the field-aligned velocity of H+ ions rather slightly.

The detected fluxes of O+ ions turned out to be much more energetic and intense than the fluxes obtained as a steady-state solution of the equations describing the polar wind. There is a physical mechanism which heats ionospheric ions in the polar cap region where precipitation is small and the energy income from the magnetosphere is minimal.

After the analysis of the moments of the distribution function of H+, He+, and O+ ions, it has been found that flows of the **H** type are those of the polar wind, while flows of the **Ho** type underwent at lower altitudes an extra heating and acceleration, that is, at a height of 20,000 km on the nighttime side of the sunlit polar cap upwelling flows of H+ ions were detected which agree very well with the polar wind models. O+ ions of the polar wind have too low energy to overcome the positive potential of the satellite.

It is shown that current models of the polar wind describe this event fairly reliably and, moreover, this event actually exists, this fact often having been doubted because of complications in measurements of such low-energy ions.

The work was supported by the RFBR 15-35-20364.

1. A. J. Dessler and F. C. Michel, Plasma in the Geomagnetic Tail, *J. Geophys. Res.*, 1966, 71, pp. 1421—1426.

2. S. A. Grigoriev, L. V. Zinin, I. Yu. Vasilenko, and V. E. Lynovsky, Multi-Ion One-Dimensional MHD Models of Upper Ionospjere Dynamics: 1. A Mathematical Ionospheric Model with Seven Positive ion Species, *Kosm. Issled.*, 1999, 37(5), pp. 451—462.

3. H. G. Demars and R. W. Schunk, Seasonal and Solar Cycle Variations of the Polar Wind, *J. Geophys. Res.*, 2001, 106, pp. 8157—8168.

4. S. W. Y. Tam, F. Yasseen, T. Chang, and S. B. Ganguli, Self-Consistent Kinetic Photoelectron Effects on the Polar Wind, *Geophys. Res. Lett.*, 1995, 22, pp. 2107—2110.

5. Y.-J. Su, J. L. Horwitz, G. R. Wilson et al., Self-Consistent Simulation of the Photoelectron-Driven Polar Wind from 120 km to 9Re Altitude, *J. Geophys. Res.*, 1998, 103, pp. 2279—2296.

6. A. W. Yau, B. A. Whalen, W. K. Peterson, and E. G. Shelley, Distribution of Upflowing Ionospheric Ions in the High-Altitude Polar Cap and Auroral Ionosphere, *J. Geophys. Res.*, 1984, 89, pp. 5507—5522.

7. T. Abe, A. W. Yau, S. Watanabe et al., Long-Term Variation of the Polar Wind Velocity, *J. Geophys. Res.*, 2004, 109, doi: 10.1029/2003JA010223.

8. P. A. Nsumei, X. Huang, B. W. Reinisch et al., Electron Density Distribution over the Northern Polar Region Deduced from IMAGE/Radio Plasma Imager Sounding, *J. Geophys. Res.*, 2003, 108, doi: 1029/2002JA009616.

9. D. V. Chugunin, L. V. Zinin, Yu. I. Galperin et al., Polar Wind Observations on the Nightside of the Polar Cap at Altitudes of 2—3 *R*E: Results of the *Interball-2* Satellite, *Kosm. Issled.*, 2002, 40(4), pp. 416—433.

10. A. A. Namgaladze et al., Global model of the thermosphere-ionosphere-protonosphere system, *Pure and Applied Geophysics* (PAGEOPH), 1988, 127(2/3), pp. 219—254.

11. M. V. Klimenko, V. V. Klimenko, and V. V. Bryukhanov, Numerical simulation of the electric field and zonal current in the Earth's ionosphere: The dynamo field and equatorial electrojet, *Geomagn. Aeron*., 2006, 46(4), pp. 457—466.

Geometric Description of Ionospheric Conductivity in the Auroral Ionosphere

Alexander A. Chernyshov[1], Boris V. Kozelov[2], and Michail M. Mogilevsky[1]

[1]Space Research Institute of the Russian Academy of Sciences, Profsoyuznaya Street 84/32, 117997, Moscow, Russia
[2]Polar Geophysical Institute of the Russian Academy of Sciences, Akademgorodok 26a, 184209, Apatity, Murmansk region, Russia

The understanding of fractal geometry of Nature can hardly be overrated. The term "fractal" was introduced in science by Mandelbrot to quantify the geometric features of a variety of natural objects whose fine-scale structure is statistically self-similar [1]. Unlike Euclidean geometry, he refused the implicit assumption about the smoothness of the object. Many object are in fact characterized by well-defined power-law spatial correlation function. In many cases, such power-law behavior could be associated with the fine-scale structuring in the system and the hierarchy of structures on many spatial scales could be then approximated by geometric sets termed fractals. Application of the fractal approach have led to considerable progress in many branches of science including problems of space physics, for instance, the study of processes on the Sun, solar wind, interplanetary magnetic field turbulence, stochastic substorm dynamics, Earth's distant magnetotail, the auroral structures and many others (for example, see [1—4]).

Recently dynamic properties of the percolating networks near the critical threshold have received a good deal of attention. This insight along with the substantial advances in the geometric formulation of the critical phenomena have opened new perspectives on the topological methods in the theory of percolation. This has led to an possibility of the geometric description of the dynamical phenomena involving the formation of the percolating structures. This approach has important advantages, because it allows one to consider a wider class of structures than has traditionally discussed. The geometric parameters of percolated clusters near the percolation threshold depend weakly on the details of the small-scale

structure, which makes the percolation theory a promising tool for studying the properties of the medium. The relevance of the topological ideas applied to the auroral ionosphere has been recently demonstrated [2, 3]. In the present study, we use a geometric approach based on fractal theory and percolation theory to describe the Hall conductivity of the auroral zone ionosphere. Actually this study is a continuation of work initiated in the previous articles [2, 3] where well-known in the literature empirical relations were applied for determination of fractal parameters in auroral ionosphere and main attention was paid to the Pedersen conductivity. The obtained theoretical results for the Pedersen conductivity were in good agreement with electromagnetic field data from the satellites and ground-based observations of aurora. Using Spiro's relations [2] and Robinson's relations [3], different fractal results were determined for Hall conductivities. Therefore, it is necessary to find solutions in general form and to perform an analysis of obtained results. The Hall conductivity is important parameter in the auroral ionosphere because Hall current flows in auroral arcs [5]. This is the subject of this work.

The E-region of nightside Earth's ionosphere at altitudes of 80—150 km and at latitudes where the major part of energetic particles precipitation is observed and these particles result in auroras are considered. In this region, particle precipitation isthe main cause of ionization in the nightside and, consequently, of increased conductivity. Using typical values of electron and ion gyro-frequencies and also the maximum values of the collision frequencies in E-layer of ionosphere, the expressions for the Hall conductivity in the E-region ionosphere are simplified and take the following form:

$$\sigma_H = \frac{qn}{B} \propto n \tag{1}$$

where, n, q and B indicate electron density, electron charge and geomagnetic field strength. In the absence of other ionization sources the electron density is determined by ionization by auroral particles. The rate of ionization caused by auroral particles collisions with atmospheric gases varies smoothly along the magnetic field lines; therefore, the nontrivial fractal structure can form only in the spatial distribution transverse to the magnetic field.

By usual assumption of thin ionosphere we can go to height-integrated ionosphere and to height-integrated conductivity $\sum_H = \int dz\sigma_H$, where z is the vertical coordinate. In the general case, the height-integrated Hall conductivity $\sum_H (W, \varepsilon)$ at given magnetic field line is a function of the average energy W and the energy flux ε of precipitating electrons. The dependence on the average energy is simply understandable because more energetic electrons penetrate deeper to the Hall current layer. According empirical models this dependence has a power law form $\propto W^z$ with a bit different power index z. The dependence on energy flux has a form $\propto \sqrt{\varepsilon}$ due to recombination features at ionospheric E-region altitudes. In important case of the region of intense field-aligned currents both W and ε depend on

the current intensity. The field-aligned current $j_{\parallel}$ generates transversal currents in the ionosphere and the corresponding transverse electric fields $E_{\perp}$. If α is the transverse characteristic scale, the change of potential drop in the ionosphere, we can obtain the following relation for the Hall conductivity:

$$\frac{\Delta\phi_{\perp}}{\Delta\phi_{\parallel}} \propto \frac{\alpha_H^2}{\sum_H} \tag{2}$$

Now we need two additional facts about fractal sets and percolation. Firstly, the transverse potential drop is proportional to resistance and the scaling of the resistance, where ζ is the resistance exponent. The exponent is determined by $\zeta = 2 + \theta - d_f$. Secondary, the criticality condition of the percolation threshold (the Alexander-Orbach conjecture) ensuing from the universal value theorem [3]. We will use this condition in form of inequality to estimate the values of fractal parameters that are necessary for the ionospheric current percolation:

$$\frac{2d_f}{2+\theta} \geq \frac{4}{3} \tag{3}$$

Then, using the derivations discussed in detail in [3] from (1), (2) and (3) we can obtain the following estimations for the fractal dimension and connectivity index in the general form:

$$d_H^f \leq \frac{8m-4}{3m-2} \text{ and } \theta_H \leq \frac{6m-2}{3m-2} \tag{4}$$

In order to better understand these obtained expressions, Figure 1 shows the graphs of dependence critical scaling index (connectivity index θ_H and fractal dimension d_H^f) for Hall conductivity from scaling index in empirical approximation. In Fig. 1, for clarity sake, dotted lines represent values of Spiro's and Robinson's empirical relations used in [2, 3]. As would be expected, the different empirical relations for conductivities lead to different results. It is worth noting that despite the fact that different results for the Hall conductivity are obtained by using different empirical relationships, there is such a state where a negative connectivity index $\theta < 0$ but fractal dimension $d^f \geq 1$. Such interesting class of fractal objects are called as asymptotically path-connected set [4]. Asymptotically path-connected fractals combine properties of path-connectedness and disconnectedness because these fractals can be conceived as disconnected distributions of path-connected subsets. Because the Hausdorff dimension of each such subset cannot be smaller than one, the particles may freely migrate along the set remaining within the limits of the 'their own' path-connected component. They are prohibited from leaving the chosen component because the entire fractal is disconnected, $\theta < 0$. A set is called path-connected if along with any pair of points it also contains a path connecting these points [4]. The Hausdorff dimension of a path-connected fractal set has $d^f \geq d_\theta \geq 1$ and $\theta > 0$.

As illustrated in Fig.1, depending on the specific value of θ_H, persistent (superdiffusive) or antipersistent (subdiffusive) processes are possible. For an antipersistent process ($\theta > 0$), a discontinuity emerges and the particle 'is stuck' in the turbulent field. On the other hand, persistent processes ($\theta < 0$) elapse more rapidly movement. The corresponding dynamical phenomena occur with an accelerated rate that does not allow particles to stay long in different points of the turbulent region. For $\theta \neq 0$, the processes in fractal space are essentially non-Markovian and therefore effects of memory, nonlocality, and intermittency should be taken into account, that is, these effects go far beyond the conventional Gaussian statistics.

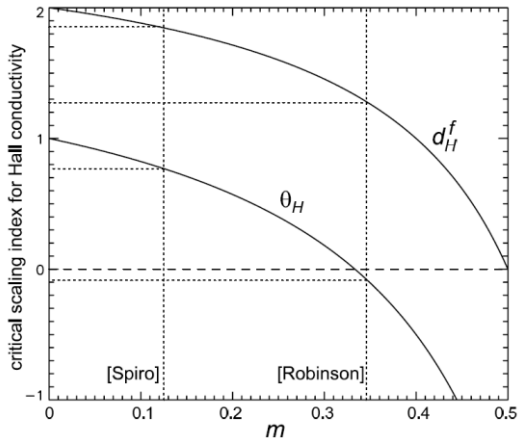

FIGURE 1. Dependence critical scaling index for Hall conductivity (connectivity index and fractal dimension) from scaling index in empirical approximation.

The asymptotically path-connected behavior is possible for the Hall current in the auroral ionosphere. It is known that Hall current flows in auroral arcs [5]. The multiple arcs system is observed often rather than one auroral arc. Various observations have shown that in bright areas Hall conductivity has maximum values, while in the dark areas there is very low Hall conductivity. Since the asymptoticallypath-connected set with $d^f \geq 1$ and $\theta < 0$ occurs in the ionosphere, Hall conductivity appears to be associated with "channeling" of particle motion. Moving along the "allowed" channels, ionized by auroral particles, the ionospheric carriers of Hall current collide with neutral atoms only within these narrow channels. For multiple arc structure of the dimension d^f, the dimension of cross section perpendicular to arcs can be estimated as

$$d_{cs} = d^f - 1 = \frac{\alpha - 2}{2} \tag{5}$$

Here α is the scaling index obtained by the logarithmic diagrams constructed using a discrete wavelet decomposition [2] and the corrections due to aspect angle distortions discussed in are taken into account. We demonstrated (not shown) the overlapped polar plots present angular dependence of the scaling index. The index value is expressed by radial distance and the angle indicates the direction of a linear cross section of the image used for index calculation. The dotted circles mark the extreme values of the scaling index. The direction perpendicular to the arcs corresponds to the North-South (N-S) direction. Development of the multiple arc structure is well seen from the auroral keogram constructed by N-S cross sections of the camera images during interval 18:00-18:09 UT (not shown). As may be inferred from our study, in this case the main dynamics is observed in the perpendicular structure. We studied time dynamics of the Hurst index $H = d_{cs}$ estimated from the scaling index α of the perpendicular structure by the expression (5). For the presented case, the values $d_{cs} \leq 0.85$ that always corresponds to value $d_{cs} = d_H^f - 1$ expected from Spiro's relation. Sometimes, for example, near 18:04 UT, the d_{cs} value satisfies the conditions $d_H^f - 1 \leq 0.27$ expected from the Robinson's approximation. Then, crossing the precipitation region in the direction perpendicular to the arcs one should observe the structure of the precipitation which looks like a generalized Cantor set.

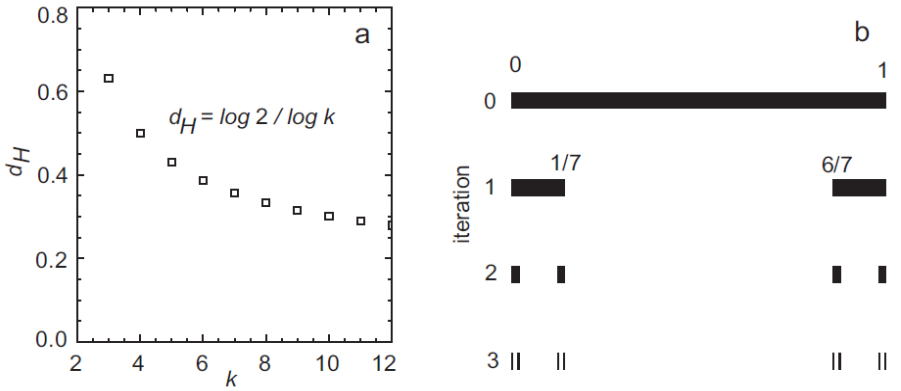

FIGURE 2.(a) Dependence of the generalized Cantor set dimension on parameter k. (b) Sample of iterative construction of the generalized Cantor set for k = 7.

As is known, generalized (regular) Cantor set in contrast to the classical Cantor set can be constructed in different ways with various fractal dimensions. There is a simple method for constructing of generalized Cantor sets. D_k is the collection of sets defined in terms of k, for $k \geq 2$, in which each set in the sequence is formed by the repetitive removal of an open interval of length (1—2/k) from the center of each closed interval starting with [0;1], with intervals of length 1/k remaining on each side. Notice that each of the sets $D_k$are self-similar sets and Hausdorff (fractal) dimension in this case *log* 2/*log k*. The dependence of the dimension on k is shown

in Fig. 2. It is interesting that if $k = 6{,}7..10$, we obtain fractal dimension $0.3 \div 0.4$ that agrees well with the experimental and theoretical estimates. As an example of the generalized Cantor set derived in this way, the case when $k = 7$ is depicted in Fig. 3. It is evident that the higher k value leads to "poorer" set D_k.

It should be mentioned that different results are presumably obtained for the fractal estimations for the Hall conductivity due to the formation of the altitude dependence of the Hall conductivity on the energy of electrons. In this case, an exponential growth of the atmospheric density with decrease in height is superimposed on a power drop of the total cross-section of interaction of electrons with increasing energy, and this leads to the fact that the spectrum of the electrons may be different. Thus, this, in turn, causes to different topological results for Hall conductivity.

In this work, values of the fractal dimension and the connectivity index, characterizing the structure of Hall conductivities on the night side of the auroral zone were obtained. Restrictions imposed on fractal structure of the ionospheric conductivity were analyzed in terms of the percolation of the ionospheric Hall currents. In fact, these topological parameters define the structure of a percolation cluster when there are current flows in the ionosphere, that is, backbone of the percolation cluster. Backbone includes all the nodes lying on all possible trajectories of nonselfintersecting random walk starting at node (nodes) injection and ending on the boundary [1]. Form of backbone of percolation cluster depends on how the places of energetic particle precipitations and field-aligned currents are located. In the analysis of transport phenomena in percolation clusters there are many different estimates of fractal dimension. In fact, it manifests itself as multifractal behavior.

Using various empirical relationships, we obtain generally different fractal dimensions (and connectivity indexes) for the ionospheric conductivities (namely, Hall conductivity). This is because the choice of a particular physical process that occurs in a fractal medium is actually equivalent to the choice of measure of this fractal set. Therefore, the study of physical phenomena on fractal sets leads naturally again to the concept of multifractals.

This work was supported by Russian Foundation for Basic Research (№ 15-35-20364).

1. J. Feder, Fractals, Plenum Press, New York, 1988.

2. A. A. Chernyshov, M. M. Mogilevsky, and B. V. Kozelov, Fractal approach to the description of the auroral region, *Plasma Physics Reports,* 2013, 39, pp.562—571.

3. A. A. Chernyshov, M. M. Mogilevsky, and B. V. Kozelov, Use of fractal approach to investigate ionospheric conductivity in the auroral zone, *J. Geophys. Res.*, 2013, 118, pp. 4108—4118.

4. L. M. Zelenyi and A. V. Milovanov, Fractal topology and strange kinetics: from percolation theory to problems in cosmic electrodynamics, *Physics-Uspekhi*, 2004, 47(8), pp. 749—788.

5. O. Marghitu, Auroral Arc Electrodynamics: Review and Outlook, *Geophysical Monograph Series*, 2012, 197, pp. 143—158.

Effects of 1997—1998 Global Parameters Leap in Total Electron Content

Ilya K. Edemskiy

Institute of Solar-Terrestrial Physics, SB RAS, Irkutsk, Lermontov st. 126a, Russia

Calculation of total electron content (TEC) based on parameters of global navigation satellite system (GNSS) is widely used for ionosphere investigation [1]. Methods developed by prof. E. L. Afraimovich allow us to define TEC along line-of-sight (LOS) to GNSS satellite, which usually is elevated over horizon during 4—8 hours.

Authors of [2] present calculation method of vertical TEC disturbances average amplitude index or Wtec index. The method allows us to obtain long-term series of ionosphere characterizing data for LOS-crossed area and make it possible to investigate long-term global geophysical phenomena as solar activity cycle influence of ionosphere, for example.

Some GNSS receivers of International Geophysics Service (IGS) have been recording data since 1990th and its data is available via Internet for free. In this paper we used data of Canadian stations YELL (Yellowknife, 62.5ºN, 245.5ºE) and ALBH (Victoria, 48.4ºN, 236.5ºE) to calculate Wtec for long period of 1992—2012. The data were prefiltered with 30s-10min window.

Upper part of figure 1 presents Wtec index daily variations during the whole period and at the bottom one can see its standard deviation (STD) calculated for each day of the period. There is a good correlation between Wtec and cyclic solar activity: average amplitude is higher in period of activity maximum (2001—2002) and lower in periods of minimal activity. Solar activity-connected dynamics of disturbance intensity is more clear in variations of its standard deviation. Figure 2 presents Wtec standard deviation from YELL (grey) and ALBH (red) data for 1995—2004. Yellowknife station is located in high latitudes and that could explain why Wtec STD is higher in average than the Victoria station one.

That is really interesting to see sharp leap of average YELL Wtec STD within 1997—1998. We can conclude that TEC disturbances amplitude range was sharply reduced during this period. It is known [3] that big variety of global geophysical parameters (such as the angular Earth velocity, the level of the ocean, the average annual temperature, the frequency of volcanic eruptions, etc.) has a step-like variation in this period. So presented features of Wtec dynamic apparently was produced by the same cause or source.

Figure 3 presents temporal variations of gravitation field, measured by superconductive gravimeters (black line) and absolute gravimeters (circles) in micro-Gals [4]. Time period between 1997 and 1998 contains quite obvious leap of gravitation. It is really interesting that the moment of gravitation leap time as almost coincide with the standard deviation of Wtec fall during 1997—1998.

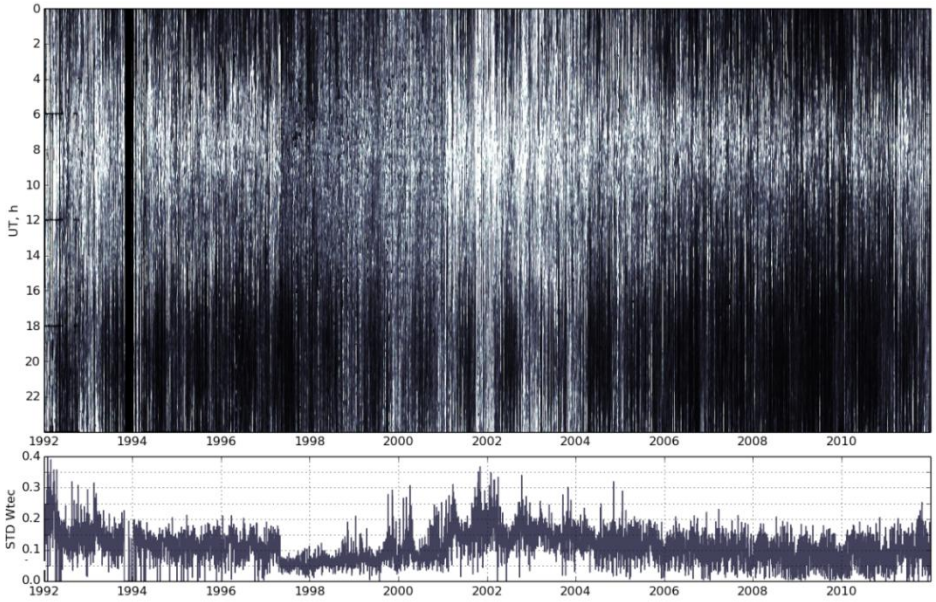

FIGURE 1. YELL Wtec variation (top) and its standard deviation (bottom).

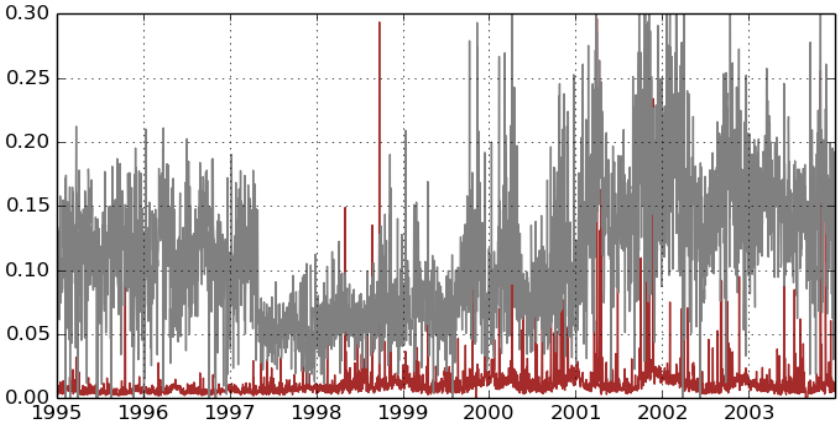

FIGURE 2. Variations of Wtec standard deviation during 1995—2004 from YELL (grey) and ALBH (red) data.

The mechanism of such ionosphere disturbances activity decrement and its connection with gravitational variations as not quite clear now. Authors of [4] interpret the sharp increase in gravity of about 3 microGal during 1997 in terms of mass/density variations in conjunction with the occurrence of local and regional seismic activity. In the same way some authors think that such a global effect could be driven only by some planetary scale influence, for example, some outer-space impact.

Meanwhile presented here STD Wtec data show us that even if the geospheric parameters leap was global, it was not appeared in the same way in different places. We can conclude that the same observations and data analysis should be made for other long-term GNSS data. It is necessary to estimate dependence of such ionosphere characterizing parameters as Wtec on station latitudinal and geographical location, its distance from ocean, etc. Geospheres interconnection and energetic exchange between them are really important to reveal for our planetary dynamics inderstanding and this type investigations will be surely continued.

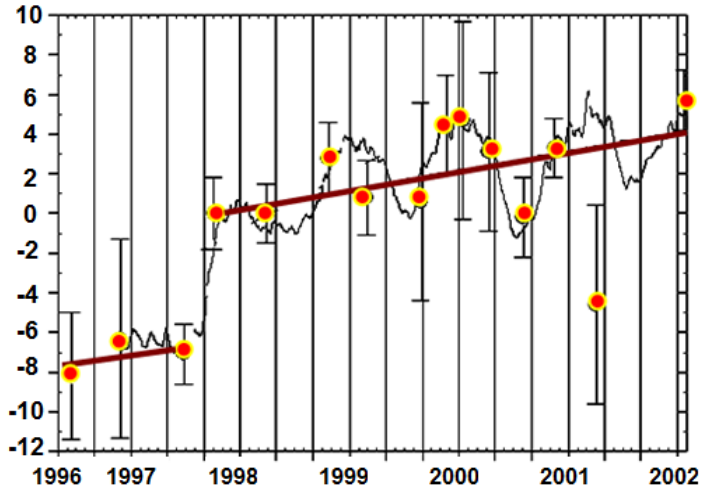

FIGURE 3. Gravitation leap by Medicina (Italy) station data. OY values is given in microGals for absolute gravimeters (circles) and superconductive gravimeters (black line) [4].

Author thank Gennady Ya. Smolkov for fruitful discussions, and Anna Mylnikova and Sergey Voyeykov for data preparation. The study was supported by the Russian Foundation for Basic Research, project No. 16-35-00051_mol_a.

1. E. L. Afraimovich and N. P. Perevalova, GPS monitoring of the Earth's upper atmosphere, SC RRS SB RAMS, Irkutsk, Russia, 2006, 480 p (in Russian).

2. S. V. Voyeykov, O. I. Berngardt, and N. V. Shestakov, Vertical TEC variation disturbance index as instrument of Chelyabinsk meteorite investigation, *Geomagn. Aeron.*, 2016, 56(2), pp. 1—10.

3. Yu. B. Barkin, Interpretation of global ocean level variations of sea level and ocean average levels variations in Northern and Southern hemispheres during a century, *MSU Review, Sec. 3: physics and astronomy*, 2011, 4, pp. 75—83 (in Russian).

4. S. Zerbini et. al. Height and gravity variations by continuous GPS, gravity and environmental paameter observations in the southern Po Plain, near Bologna, Italy, *Earth and Planetary Science Letters*, 2001, 192, pp. 267—279.

Using Network Technology for Studying the Ionosphere

Ilya V.Zhivetiev[1,2], Yury V.Yasyukevich[3]

[1]Institute of Cosmophysical Research and Radio Wave Propagation FEB RAS, Paratunka, Russia
[2]Kamchatka State Technical University, PetropavlovskKamchatsky, Russia
[3]Institute of Solar-Terrestrial Physics of Siberian Branch of Russian Academy of Sciences, Irkutsk, Russia

Introduction. One of the key problems of the ionosphere physics is the problem of coupling of different regions of the ionosphere. We suggest a network technology for studying the connection of ionosphere dynamics change in different regions. We used the data of global ionosphere GIM maps produced by CODE for 2005—2010. Distribution of cross-correlation function maximum values of total electron content (TEC) change is not simple. This distribution allows us to reveal two levels of ionosphere coupling: "strong" ($r > 0.91$) and "weak" ($r > 0.76$) ones. Ionosphere of the arctic region higher than 50° MLat is characterized by "strong" coupling. For the southern hemisphere the similar region is bigger. "Weak" coupling is typical for the whole southern hemisphere. In the North America region there is an area where TEC dynamics is "strongly" correlated inside and is not correlated with other regions of the ionosphere.

Investigation of complex systems by networks holds a firm place in many areas of science. In particular, to investigate the neutral atmosphere, networks have been used during the last decay [1, 2]. A network is a set of coupling and connected nodes. Any chosen parameter may be a feature of the connection: locked link in a computer network, family tiers in human society and so on. After having determined the «nodes» in an object domain and the «connection» between them, it is possible to form a network. When studying the network characteristics, we can obtain new data on general dynamics of the system as a whole, in this case on the ionosphere.

Technique. The paper suggests a method to investigate the ionosphere based on networks. We apply the data of Global ionospheric maps (GIM) (ftp://cddis. gsfc. nasa. gov/gps/products/ionex/). GIM maps are estimated by several laboratories all over the world. There is a systematic discrepancy between the maps drawn by different laboratories [3], but the general dynamics is similar on the whole. We use CODE maps in this paper.

GIM data are distributed on a network from – 180° to 180° longitudinally and from – 87.5° to 87.5° latitudinally. The network resolution is 5° latitudinally and 2.5° longitudinally, the total number of cells is 5183. Each cell contains the data on vertical total electron content (TEC) with two-hour time resolution. A GIM elementary cell is a network node. TEC «anomaly» is chosen as the parameter under investigation. Hereafter, an «anomaly» is the deviation of TEC mean diurnal value

from its mean annual value. Mean annual value for a current day is estimated within the window of ±182 days. Thus, there are 5183 series for the period from 2005 to 2015, the length of each is 2191 values.

Correlation value between the corresponding series of TEC anomalous values is used as the criteria of the connection between two nodes. Fig. 1 illustrates distribution of cross-correlation function maximum values r_{xy} for all the nodes. It is clear that the values are distributed quite evenly to r≈0.76. Then, there is a sharp increase, the maximum is r≈0.96, decrease of the maximum by √2 times corresponds to the value 0.91. Based on that, we distinguished the following criteria of the connection: r_{xy}<0.76 — no connection; r_{xy}>0.76 — «weak» connection; r_{xy}>0.91 — «strong» connection. Having determined the criteria, we constructed two networks with «weak» and «strong» connection.

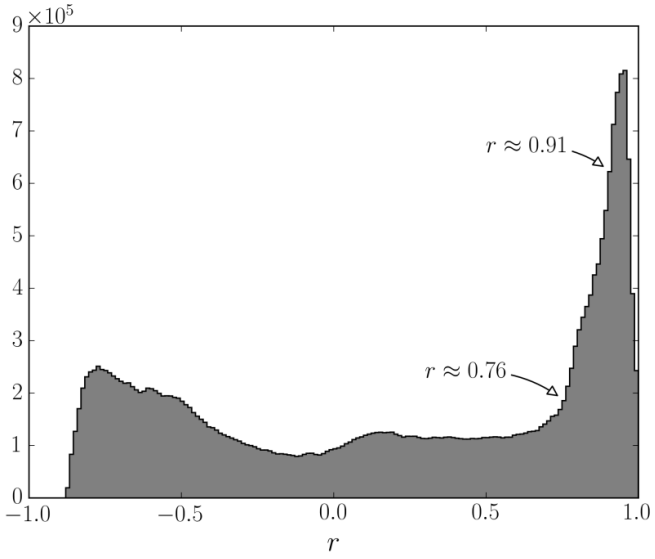

FIGURE 1. Distribution of maximum values of TEC anomaly cross-correlation functions for all the nodes.

Ionospheric network. In Fig. 2 the color indicates the number of connections (so called deg) for each network node. Fig. 2a is weak connection; Fig. 2b is strong connection. We see in Fig. 2a that there are three main regions with the boundary at ±14°MLat: equatorial anomaly region [4], northern and southern hemispheres. The average number of the connections inside the regions with other nodes is close. There is a separate region in the northern hemisphere, in the South of the North America, which is characterized by a small number of connections. This region covers a part of the Gulf of Mexico, of the Atlantic Ocean, and reaches 50° MLat.

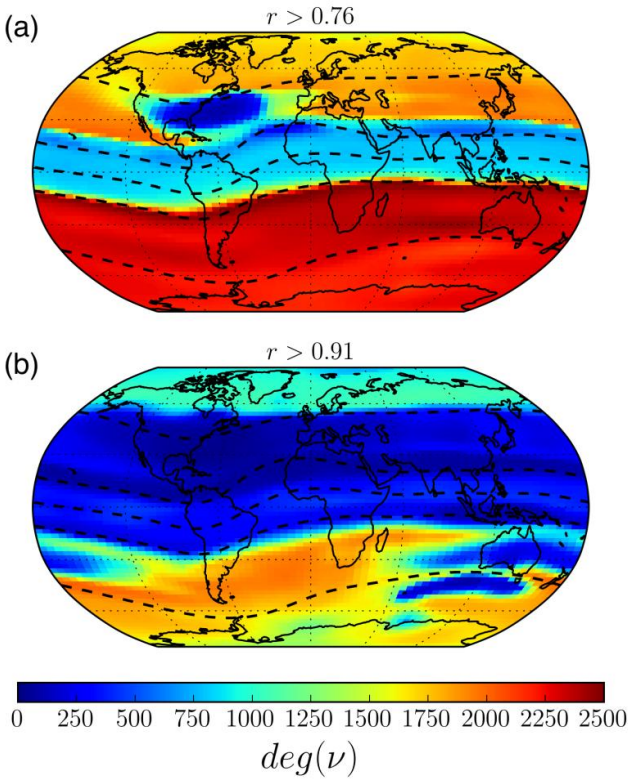

FIGURE 2. Spatial distribution of the number of connections for each network node: (a) weak connection, (b) strong connection. Dashed lines show geomagnetic equator and geomagnetic parallels (±14°MLat, ±50°MLat).

Analysis of the number of «strong» connections (Fig. 2b) shows considerable asymmetry of the northern and the northern hemispheres. Partially, that may be associated with the method of GIM map construction. There are fewer stations in the southern hemisphere which are used to make the GIM maps. In the result of data interpolation, the nodes are connected stronger with each other. However, the number of stations in the South of Africa and South America is quite enough, but the number of «strong» connections for the nodes in this region is also large. Moreover, the Australian region is characterized by a fewer number of connections than in the southern hemisphere on the average. This may show that the density of stations does not significantly affect network characteristics.

We can also see it in Fig 2b that the ionosphere of the Arctic region of the northern hemisphere is «strongly» connected higher than 50° MLat. In the southern hemisphere, polar latitudes are pronounced much weaker. When r≈0.76 (Fig. 2a), almost the whole southern hemisphere is connected.

There is a region in the South of the North America, where TEC changes correlate with each other. Their dynamics differs considerably from that in the rest mid-latitudinal ionosphere of the northern hemisphere. According to the data given in [5],

we can see that the strongest effects in this region are observed during magnetic storms analyzed in the paper. Low correlation with other regions may be caused by that.

This isolated region is geographically located in the region of formation of the Gulf Stream warm main flow. However the dimensions of the region are quite large and significantly exceed the region of the formation. It was shown in the paper [6] that carbon dioxide concentration increases over the Gulf Stream zone. Peculiarities of temperature and atmosphere neutral content may result in the peculiarities in the dynamics of electron concentration. Thought in this case, it would be likely to register the anomaly along the whole Gulf Stream. To reveal the real mechanism of formation of the isolated region characterized by its own ionospheric dynamics, further investigations are necessary.

Acknowledgements.*The study was supported by the Russian Foundation for Basic Research, project no. 15-05-03946_a.*

1. A. A. Tsonis and P. J. Roebber, The architecture of the climate network, *Physica A*, 2004, 333, pp. 497—504.

2. V. Stolbova, P. Martin, B. Bookhagen et al., Topology and seasonal evolution of the network of extreme precipitation over the Indian subcontinent and Sri Lanka, *Nonlin. Processes Geophys*., 2014, 21, pp. 901—917.

3. E. I. Astafyeva, E. L. Afraimovich, A. V. Oinats et al., Dynamics of global electron content in 1998—2005 derived from global GPS data and IRI modeling, *Adv. Space Res*., 2008, 42, pp. 763—769, doi:10.1016/j. asr.2007.11.007.

4. E. V. Appleton, The anomalous equatorial belt in the F2-layer, *J. Atmos. Terr. Phys*., 1954, 5, pp. 348—351.

5. W. Wang, J. Lei, A. G. Burns et al., Ionospheric response to the initial phase of geomagnetic storms: Common features, *J. Geophys. Res*., 2010, 115, A07321, doi: 10.1029/2009JA014461.

6. J. L. Buffon, Evidence for atmospheric carbon dioxide variability over the Gulf Stream, *Geophys. Res. Lett*., 1984, 11, pp. 1141—1143.

Investigation of Singular Points in Optical Path Functional for High and Low Rays in Ionospheric Radio Path

Igor A. Nosikov[1,2], Maxim V. Klimenko[1,2], and Pavel F. Bessarab[3]

[1]Immanuel Kant Baltic Federal University, 236041, Kaliningrad, Russia,
[2]West Department of Pushkov Institute of Terrestrial Magnetism, Ionosphere and Radio Wave Propagation of the Russian Academy of Sciences, 236017, Kaliningrad, Russia
[3]Royal Institute of Technology KTH, SE-16440, Stockholm, Sweden

There are two approaches of radio path calculation with securing end-points. The most popular approach is homing method [1, 2]. It required searching direction

of emission radio waves to provide for point-to-point ray tracing. Nowadays homing method is widely used for problem of radio path calculations in an ionosphere, although it has some disadvantages [3]. There is another method to solve this boundary problem. In particular, in [1] refers to the possibility of calculating ray paths using variational methods, which are based on Fermat's principle of minimizing the functional optical ray path

$$S[\gamma] = \int_A^B n(\bar{r})dl\,. \qquad (1)$$

Integration is performed along the curve γ, which joins boundary points *A* и *B*; $n(\bar{r})$ — refractive indexes in each point of curve γ with $\bar{r} = (x, y, z)$; dl — the length of the element along γ. According with Fermat's principle the functional of the ray path must satisfies to the expression

$$\delta S = 0\,. \qquad (2)$$

But until recently, variational methods were not performed for ionospheric radio path problems. The variant of variational method was proposed in paper [5]. In current work we use the nudged elastic band (NEB) method as an optimization method, which is widely used in different areas of science [6, 7]. The particular case of NEB method is the method of transvers displacements described in [8] that is recently used for radio path calculations.

However, as the author of the paper [5], the proposed approach has several limitations, primarily related to the impossibility of obtaining low rays. The first calculation results performed by our method, led to the same conclusion — inability to obtaining low rays by standard minimization procedure that allowed to talk about the fact that the low rays does not correspond to minimum of optical path length. So we have a question: what mean low and high ray in term of the functional of optical path length. For answer to this question the method of express analysis of optical path length has been developed. This method allows demonstrating the qualitative distribution of functional of the radio path length that defined using three points: the boundary conditions and the apex (hypothetical reflection point). To obtain spatial distribution of optical path length the apex point consistently changes its location in the nodes of the selected grid during express analysis procedure. As example Fig. 1 present the calculation results using an express analysis for radio wave frequencies 10—15 MHz. These results were obtained in the modeled ionosphere, where the electron density profile has a parabolic form (see description in [8]). The considered frequencies correspond to the interval $f_{cr} < f < MUF$, where MUF — maximum usable frequency. In accordance with Fig. 1, the functional of high rays corresponds to the minimum and the functional of low rays corresponds to the saddle points for all cases. This result explains the robust determination of the high rays by variational methods, as well as the problems associated with finding the low rays. Since the low rays are not a minimum, thus optimizing methods based on the minimization of a radio path length, cannot find there.

Problems associated with finding of saddle points in a multidimensional space of parameters considered in [11], where the mechanisms of their determination by the NEB method were proposed. In the future it is planned to implement a method of optimization for ionospheric problem based on search, as a minimum, and saddle points.

Also Fig. 1 shows the dynamics of changes in the functional distribution of the rays with increasing frequency from 10 to 15 MHz range. As the frequency increases, the difference in reflection heights of the high and low rays decreases until MUF is reached. In considered case the minimum and saddle point mergesas a result the functional for 15 MHz has no stationary points, which corresponds to the case where the MUF exceeded and radio path with this frequency unavailable.

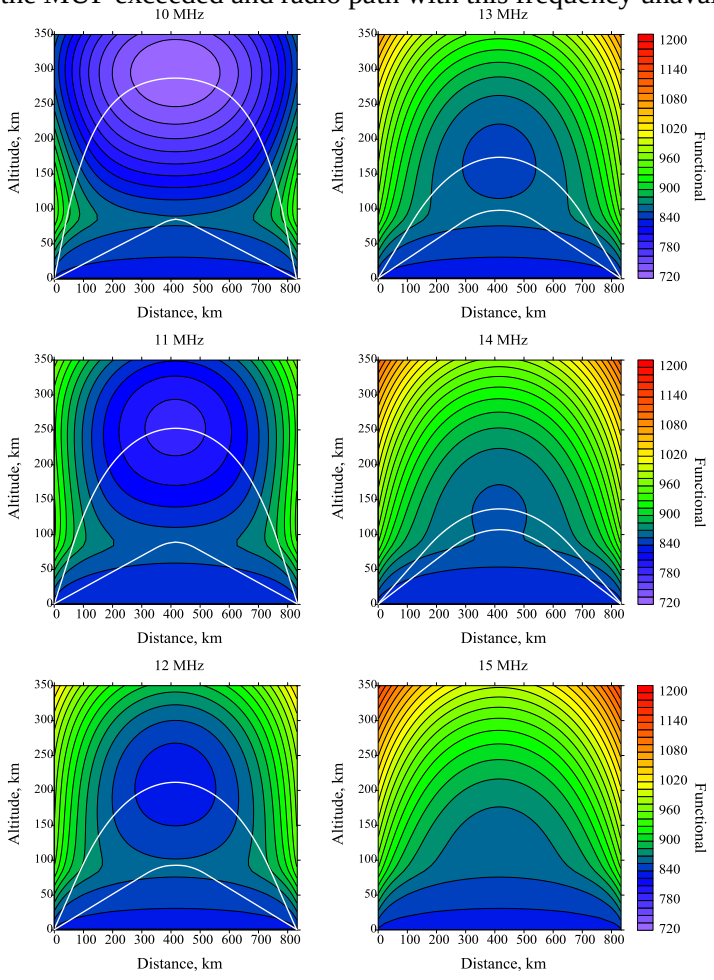

FIGURE 1. Functional maps of optical ray paths for 10—15 MHz in modeled ionosphere, where the electron density profile has parabolic form; white solid lines are known solutions (high and low rays).

Thus, the functional distribution of the optical path has been investigated for modeled ionosphere. The analysis of preliminary results in terms of the calculus of variations showed that the high ray is the minimum of optical path functional and the optical path of the low ray corresponds to a saddle point. This result shows that the use of the functional optimization methods based on searching for the minimum optical path in problems of calculating radio paths is possible only for the high rays. It should be pointed out that for the low rays optimization methods may be applied taking into account the search of saddle point. Solving the problem of determining the lower rays [6] will expand the possibilities of using optimization methods for the calculation of HF radio paths.

This investigations were performed with financial support of the Russian Foundation for Basic Research Grants No. 16-35-00590 and № 15-35-20364. This work was partially carried out within the project "Physical mechanisms of the reaction of the upper atmosphere and ionosphere on the processes in the lower atmosphere and on the Earth surface" (State task Education and Science Ministry of the Russian Federation, the competitive part of the task No 3.1127.2014/K).

1. N. Y. Zaalov, E. M. Warrington, and A. J. Stocker, *Radio Sci.*, 2003, 38(3), pp. 1052—1058.
2. D. V. Blagoveshchensky, M. Yu. Andreyev, V. S. Mingalev et al., *Adv. Space Res.*, 2009, 43(12), pp. 1974—1985.
3. N. N. Kalitkin, *Science*, 1978, pp. 266—276.
4. Y. A. Kravtsov and Y. I. Orlov, *Science*, Moscow, 1980, 304 p.
5. C. J. Coleman, *Radio Sci.*, 2011, 46, RS5016.
6. I. A. Nosikov, P. F. Bessarab, and M. V. Klimenko, *Radiophysics and Quantum Electronics*, 2016, 59(1).
7. G. Mills and H. Jónsson, *Phys. Rev. Lett.*, 1994, 72, pp. 1124.
8. G. Henkelman and H. Jónsson, *Phys. Rev. Lett.*, 2003, 90, p. 116101.
9. L. Xu, G. Henkelman, C. T. Campbell, and H. Jónsson, *Surface Phys. Rev. Lett.*, 2005, 95, pp. 146103.
10. P. F. Bessarab, V. M. Uzdin, and H. Jónsson, *Phys. Rev. B*, 2013, 88, pp. 214407.

The Experimental Data on the Effectiveness of Compensation Atmospheric Effects for UHF Radar through median NeQuick model

Vladimir B. Ovodenko

Joint Stock Company Scientific research institute of long-distance radio communication, 127083, Moscow, 8th March 10—1

Abstract. The study of compensation radar range errors is presented. We have used a monthly median atmospheric models for calculating corrections for the UHF radar measurements of calibration satellites. We have studied range error obtained with and without applying corrections. The experimental data were obtained at two

UHF radars with different field of view orientation in mid-latitudes. The experimental results presented in this paper show that applying corrections calculated with non-updated NeQuick model reduce range error.

1. Introduction. The Earth atmosphere significantly impact on the radiowave propagation. This impact mainly results to the refraction and radiowave group delay cause to radar range and elevation angle errors for different radiowave bands [1].

The objective of this paper is to investigate the effectiveness of atmospheric effects compensation in the Ultra High Frequency (UHF) radar based on the experimental data of tracking calibrations satellites equipped with retroreflectors. The UHF radar, discussed in this paper, tracks calibration satellites on a regular basis. The residuals between real UHF radar measurements and reference measurements were used during this study.

We used two types of the residuals. The first type corresponds to the case when corrections were not applied to radar measurements. The second type corresponds to the case when corrections were applied to the radar measurements.

2. Calculating the corrections and radar range error evaluation. It is necessary to know three-dimensional distribution of the refractive index in the radar field of view for correction calculation. The algorithm described radiowave propagation is also required. The refractive index can be calculated with data from empirical neutral atmosphere model [2] at height up to 60 km. The input data are geographical coordinates (latitude, longitude) and month. The refractive index calculated with data from the global ionosphere model NeQuick [3] at height more than 60 km. The input data are geographical coordinates, date, time and solar activity level. The R12 index of solar activity was used to drive the NeQuick model in the current case.

The two-dimensional ray tracing scheme is used for calculating radiowave propagation [4]. All calculations are carried out in local topocentric coordinate system related to the radar antenna. The apparent elevation angle and azimuth are initial data for correction calculation. The atmosphere is divided into spherical layers with constant refraction index value it the each layer. The radiowave bending and the group delay are calculated for each layer. Thus, the algorithm allows to calculate full group delay and real elevation angle through neutral atmosphere and ionosphere.

It should be noted that corrections were calculated for this case correspond to monthly median conditions. The ionosphere model updating with operational ionosphere data was not performed.

3. The experimental data. At this paper we consider the data obtained at the two UHF radars located at mid-latitudes with different field of view orientation. The first radar ("radar-1") is located close to Krasnodar (45°N, 39°E) with field of view oriented to the south-west. The second radar ("radar-2") is located close to Kaliningrad (54.4°N, 20.3°E) with field of view oriented to the west. The experimental measurements at the first radar were carried out from 28 to 31 March 2015 and from 2 to 20 August 2015 at the second radar respectively.

The coordinate measurement error is defined as the difference between measured and reference data. We used real radar measurements obtained by tracking calibration satellites: Beacon-C, Starlette, Ajisai, Stella, Larets, Jason-2, Cryosat-2, Haiyang 2A.

We used a three-dimensional corrections array for processing experimental data. The corrections are presented in the system described by the three arrays of range, elevation and azimuth. The correction value for the measurements of satellite position is calculated by interpolation between neighboring array elements.

The range errors are presented in Fig. 1a, 1b. The data from radar-1 are presented in Fig. 1a, and from radar-2 in Fig. 1b respectively. The range errors without atmospheric compensation are shown with "No correction" legend. The range errors with applied corrections for given satellite coordinates are shown with " NeQuick corr". All range errors are expressed in conventional units (c. u.).

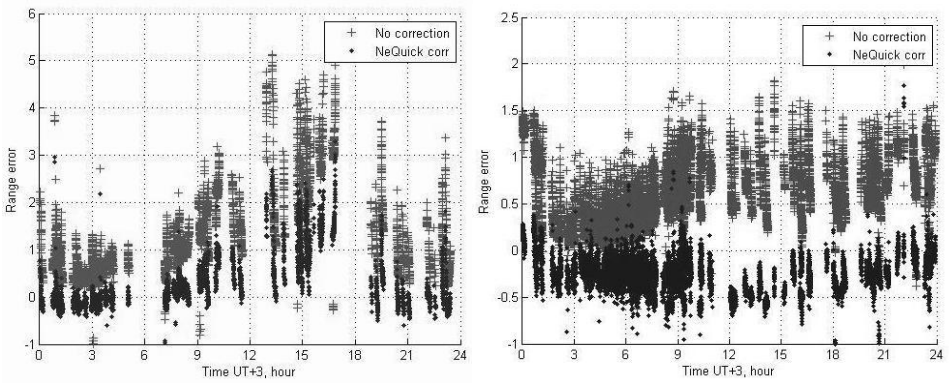

FIGURE 1. The dependence of range on time four two cases: without applying corrections (red dots, “No correction”) and with corrections (blue dots, “NeQuick corr”) for radar-1 (a) and radar-2 (b).

There is a clearly expressed diurnal variation of the range error for radar-1 data. The most probable source of such variation is daily changes in the ionosphere electron density in the radar field of view. In the daytime (10—18 UT) the range error reach values of 2—5.5 c. u. that is approximately 1.5—2 times greater than during the nighttime.

The diurnal variation of range error not clearly expressed as it seen from radar-2 experimental data. The absolute range error values for radar-2 are less than for radar-1. The absolute range error values are in the range from 0.5 to 1.5 c. u. throughout all time of the day.

This difference in the range error values can be explained by the difference between two radars in latitude and field of view orientation. The applying corrections reduce range error. For radar-1 and radar-2 range error value is close to zero during nighttime. There is a positive residual error about 1—2 c. u. for radar-1 and a negative residual error about up to -0.5 c. u. for radar-2 during daytime.

The residual error can be caused the difference between real ionosphere state from monthly median conditions specified with NeQuick model for both radars. The ability to reduce the residual error by updating ionosphere model was shown in previous papers [5].

The statistical characteristics of range errors — mean and standard deviation (SD) are presented in Table 1 and 2. The first line of table corresponds to the error without any corrections. The second line corresponds to the case when corrections were applied to the radar measurements.

TABLE 1. Range error for radar-1.

	Mean	**SD**
Without compensation	**1.36**	**1.00**
With compensation	0.32	0.67

TABLE 2. Range error for radar-2.

	Mean	**SD**
Without compensation	0.58	0.33
With compensation	-0.25	0.18

The mean range error decreased by 76.4 % and by 51.7 % for radar-1 and radar-2, standard deviation decreased by 33 % and 45 % respectively.

4. Conclusion. The main results of this paper are the following. The study of the effectiveness of compensation showed that applying corrections reduce mean range error and its standard deviation. The different range error values are obtained for two radars with different field of view orientation. We note that the results obtained in this study relate to monthly median corrections calculated with the NeQuick model.

1. H. Millman, Atmospheric Effects on VHF and UHF Propagation, *Proceedings of the IRE*, Aug. 1958, 46(8), pp. 1492—1501, doi: 10.1109/JRPROC.1958.286970.

2. K. S. Sokolov, V. V. Trekin, V. B. Ovodenko, and E. S. Patronova, The method of operational accounting of propagation medium on trajectory measurements.*Achievements Mod.Radioelectron*, 2012, 2, pp. 17—21 (In Russian).

3. G. D. Giovanni and S. M. Radicella, An analytical model of the electron density profile in the ionosphere, *Adv. Space Res.*, 1990, 10(11), pp. 27—30.

4. R. S. Berkowitz, Modern Radar: Analysis, Evaluation, and System Design. JohnWiley, 1965.

5. V. B. Ovodenko, V. V. Trekin, N. A. Korenkova, and M. V. Klimenko, Investigating range error compensation in UHF radar through IRI-2007 real-time updating: Preliminary results, *Adv. Space Res.*, 2015, 56 (5), pp. 900—906, doi:10.1016/j. asr.2015.05.017.

Comparison of the Rotational Temperature of the Hydroxyl at the Height of the Mesopause Measured at Two Different Stations

Igor I. Koltovskoi[1], Petr P. Ammosov[1], Galina A. Gavrilyeva[1], Anastasia M. Ammosova[1]

[1]Yu. G. Shafer Institute of Cosmophysical Research and Aeronomy of Siberian Branch of the Russian Academy of Sciences (ShICRA SB RAS), 31, Lenina av, Yakutsk, 677980, Russia

Abstract: The report presented a comparison of the rotational temperatures of the OH band(3,1) at an altitude of about 87 km measured with two spectrographs installed at the optical stations: Maimaga (63°N, 129.5°E), which is located 120 km North of Yakutsk and Tiksi (71.6°N, 128.7°E).

Introduction: The infrared spectrograph in the station of Tiksi (71.6°N, 128.7°E) was installed in September 2015. Software developed by us allows the unit to operate in fully automatic mode. The device automatically starts recording the night sky, with the angle of dip of the Sun > 9º, and with the beginning sunrise is stopped. Using the internet every morning data is transmitted to the institute. Thus, the station Tiksi and Maimaga have the exact same infrared spectrograph, recording the band OH is(3,1) in the far infrared region (about 1.5 μm). This paper presents the comparison of the rotational temperatures of the OH band(3,1) measured with two spectrographs installed on different optical stations during 4 months (September-December 2015).

Equipment's and stations: From 2014 permanent registration bands of hydroxyl OH (3.1) is conducted in the optical station Maimaga (63° N, 129.5° E) of the Institute of Cosmophysical Research and Aeronomy in the far infrared (1.5 micron). Optical station Maimaga is located in the ~ 120 km to the north of Yakutsk. Infrared spectrograph consists of a monochromator Shamrock SR-303i, equipped with highly sensitive infrared iDus InGaAs photodiode array detector DU490A-1.7 ANDOR, operating wavelength range 1490—1544nm, cooling – 60°C, the angle of ~ 3º, spectrograph resolution 0.2mm width of the entrance slit is 0.8nm. Hydroxyl molecule spectra of OH (3,1), radiates at an altitude of about 87 km, registered in the automatic mode when the angle of the sun dipping > 9 ° every minute of every day and transmitted via the Internet to the server of the Institute. From September 2015 the same infrared spectrograph was installed at the station Tiksi (71.6°N, 128.7°E). According to many recent works OH band (3.1) is well thermalizing and corresponds to the neutral atmosphere at the height of its radiation. Selecting the hydroxyl emission band in the far infrared is due to three factors. Firstly, the greatest intensity of the hydroxyl emission in this spectral region, and secondly, a smaller contribution of stray light from the stars and the moon, in the third auroral emissions is absence.

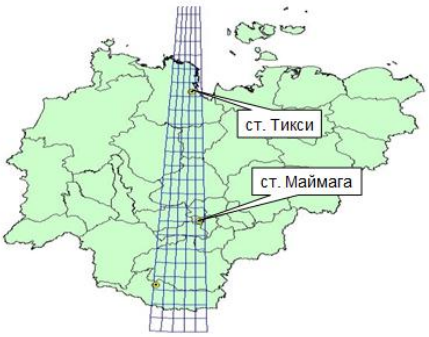

FIGURE 1. Location optical station Maimaga (63.04° N, 129.51° E) and Tiksi (71.58° N, 128.77° E).

Measurement and selection: Measurements were carried out at night, when the angle of the sun dipping> 9°, in cloudless and cloudy weather. Emission recorded hydroxyl OH (3,1) c 60 seconds exposure. Further, using a known technique, we find the temperature of the rotational emission hydroxyl OH (3.1). Evaluation method of molecular rotational temperature of emissions is based on the fit of the model spectra constructed taking into account the hardware functions of the device to different, predetermined temperature, the measured spectrum to the actual method of least squares. In assessing the rotational temperature by hydroxyl band were used transition probabilities calculated in Mies, F. H., 1974.

Method for determining the OH rotational temperature: The method for determining the temperature from the hydroxyl emission spectrum is based on the fact that the intensity distribution in the lines of the rotational bands is related to "excitation" temperature according to the formula

$$S(\lambda,T) = const \cdot \lambda^{-4} I(J') \cdot \exp[-F(J') \cdot c \cdot h/kT],$$

where F (J') — excitation energy, T — rotational temperature, J' — rotational quantum number, I (J') — the intensity factor, k — Boltzmann constant, c — velocity of light, λ — wavelength, h — Planck's constant. A comparison of the actual measured spectrum with the synthetic, calculated taking into account the parameters of the optical system, allows us to estimate the temperature at which the excitation occurred.

Evaluation begins with the calculation of line spectrum of the molecular band hydroxyl S (λ, T) at a given temperature. Since the actual spectrum is estimated by summing up the columns of the matrix, the output of the device have a discrete set S (i, T) equally spaced wavelengths, where i — pixel number. The spectral parameters of the rotational lines of the hydroxyl bands were taken from the "Collection of Nightglow Emission Spectra".

It then calculates the synthetic circuit S (i) at a predetermined temperature value, for which the model range of the molecular band S (i, T) is rolled with the real function of the transfer device:

$$S/(i) = \Sigma S(i,T) \cdot z(i - j),$$

where z (i) — transfer function of the spectrograph, i — pixel number, j — Width, in pixels, of the transfer function.

The real spectrum of emission lines in addition to the hydroxyl, also contains continuous component. This part includes the inherent nightglow emission (continuum), and components of different nature: twilight, moonlight, stellar component and others.

These parts include a continuous simulated spectrum S"(i) as a term, a linear function having the form:

$$S"(i) = A+B(i) + C \cdot S/(i),$$

where A + Bi — continuous component of the spectrum, C — adjustment factor.

It is assumed that the temperature at which the sum of squares of deviations from a synthetic spectrum actual values F (T) is minimal, corresponds to the actual rotational temperature:

$$MinF(T) = \Sigma[(E(i) - S"(i,T))]^2,$$

where E(i) — actual spectrum;

Conditions minimizing function F(T) leads to a system of linear equations in the fitting parameters A, B and C for a given temperature. Trimming circuits produced at given temperatures of from 100 to 300 K in steps of 2K. The result is a series of values of F(T), corresponding to the minimum temperature at which the synthetic spectrum best reflects the spectrum obtained in the spectrograph.

Discussion and comparison: During the day, due to the dynamic processes occurring in the atmosphere, such as planetary waves, variations associated with age of the moon, tides and IGW, the rotational temperature is subject to significant fluctuations. For example, in Figure 2a,b,c shows a few nights comparing the rotational temperature bands of hydroxyl OH (3.1) overnight, where you can see clearly through the different waves. There is an opportunity to follow one or the other wave. It is known that the model estimates the rotational amplitude of daily temperature fluctuations should decrease with increasing latitude, which is clearly seen in Figure 2c.

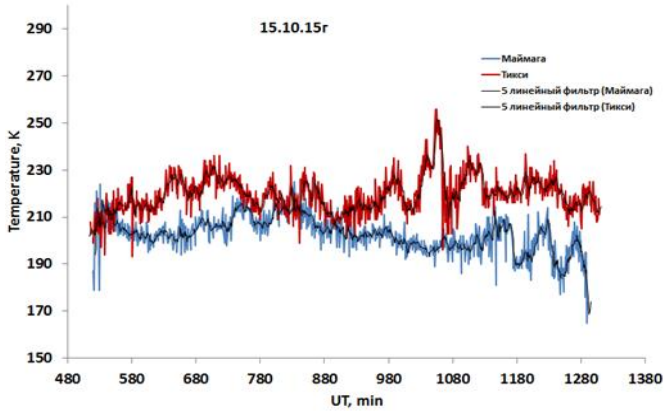

FIGURE 2a. Comparisons of overnight rotational temperature bands of hydroxyl OH (3.1)

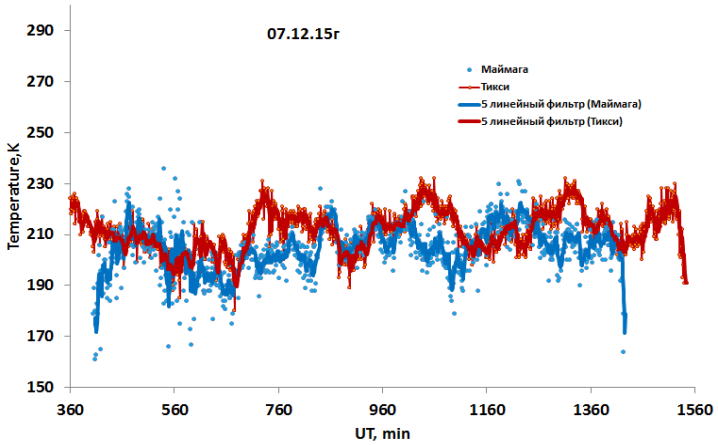

FIGURE 2b. Comparisons of overnight rotational temperature bands of hydroxyl OH (3.1)

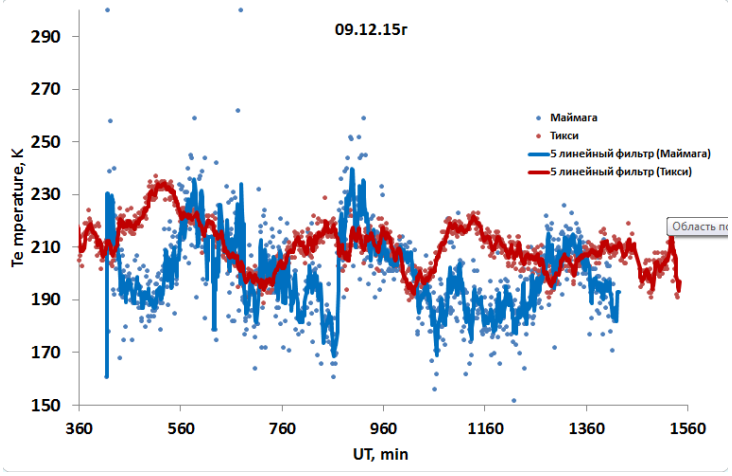

FIGURE 2c. Comparisons of overnight rotational temperature bands of hydroxyl OH (3.1)

For comparison, Figure 3 shows the rotational mean nights temperatures OH (3,1) measured at various latitudes during 4 months 2015. Although the observation period of 4 months, the seasonal variation is clearly seen rotational hydroxyl temperature. Thus, the temperature is heated from 150K in the middle of August to 210K during the winter months. Although in the September Tiksi have a few data, resulting temperature a little lower than the temperature obtained Maimaga. In October temperature obtained Tiksi becomes higher than Maimaga. When comparing the average monthly temperature hydroxyl rotational temperatures with those obtained from an empirical model CIRA (COSPAR International Reference Atmosphere ftp://nssdcftp. gsfc. nasa. gov/models/atmospheric/cira/cira86/) there is a good correlation with the exception of December (Figure 4). It can be seen that although the overall seasonal variation corresponds to the model, temperatures coincide only in November.

Fig. 3 can also be seen with the short-term variations in the periods of a few

days, associated with the existence of planetary waves. In further work is planned to identify and assess the parameters of these variations. Try to understand their origin, etc.

Conclusion: Thus, the light-sensitive infrared spectrograph, registration OH band (3.1) in the far infrared (1.5 micron) is set to station Tiksi (71.58° N, 128.77° E).Preliminary results of measurements of the hydroxyl rotational temperatures at an altitude mesopause for 4 months (September, October, November, December) 2015. It is shown comparison of the results with the data obtained on Maimaga station (63.04 ° N, 129.51 ° E). Average rotational hydroxyl temperature compared with temperatures derived from the empirical model CIRA (COSPAR International Reference Atmosphere. Ftp://nssdcftp.gsfc.nasa.gov/models/atmospheric/cira/cira86/).

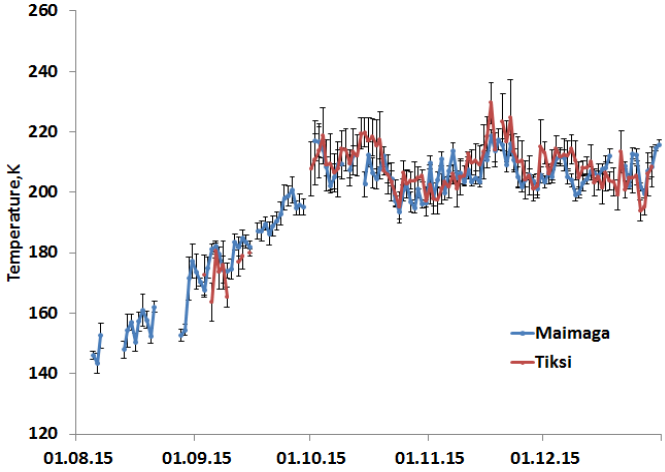

FIGURE 3. Comparison of the mean night temperature rotational OH band (3.1) measured on different optical stations within 4 months of 2015.

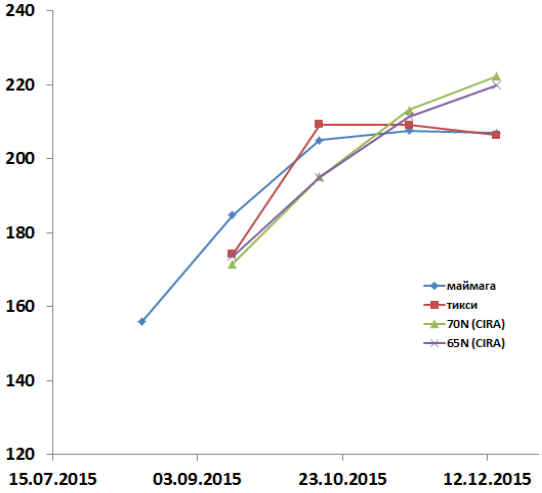

FIGURE 4. Comparison the average monthly temperature hydroxyl rotational temperatures with those obtained from an empirical model CIRA

Despite the difference in latitude, there is a very good correlation between the hydroxyl rotational temperatures measured in Maimaga and Tiksi. It was assumed that the polar cap temperature hydroxyl rotational temperatures in the winter should be higher in the summer months below. In general, according to our data is a pattern described with the exception of the second half of December. The reason for this decrease mesopause temperature may be absence of different activities. (11-year solar cycle to a minimum).

When measuring the rotational temperature of hydroxyl from different geographical locations it is possible to explore the complex spatial and temporal variations, depending on their type. For example, the division of migratory or non-migratory tides, the direction of propagation of the planetary and internal gravity waves, etc. It planned to do in the future work.

This work was supported by the Russian Foundation for Basic Research №16-35-00204mol_a, №15-05-05320a, №15-45-05066r_vostok_a.

Impact of Forbush Decreases of Galactic Cosmic Rays on Stratospheric Circulation

Irina Artamonova[1,2], Alexey Eliseev[3,4]

[1]Main Astronomical Observatory, Russian Academy of Sciences, St.-Petersburg, Russia
[2]A. I. Voeikov Main Geophysical Observatory, St.-Petersburg, Russia
[3]A. M. Obukhov Institute of Atmospheric Physics, Russian Academy of Sciences, Moscow, Russia
[4]Kazan Federal University, Kazan, Russia

Variations of galactic cosmic rays are considered as one of possible cosmic agent which can transfer the energy of solar disturbances into the Earth atmosphere [e. g., 1]. It was shown that solar and galactic cosmic ray variations could affect the pressure field in troposphere and influence the development of extratropical cyclones and anticyclones [2—3]. The aim of this work is to analyze the changes of the different parameters of stratosphere (geopotential height, temperature, zonal and meridional wind components) in association with short-term variations of galactic cosmic rays (GCRs), known as Forbush decreases.

We analyzed 20 Forbush decreases of GCRs with the amplitude exceeding 2.0% relative to the undisturbed level according to the Apatity neutron monitor data (67°N, 33°E) for the period 1991—2004. The daily averaged values of geopotential height (GPH), temperature (T), zonal (u) and meridional (v) wind components on main isobaric levels 200, 100, 30, 10, 3, 1 hPa were taken from the United Kingdom Meteorological Office (UKMO) data. An epoch analysis was used to calculate mean deviations from the undisturbed level, which was obtained by averag-

ing the data over 10 days before the event onset. The day of the event onset was considered as an initial day. Significance of deviations was calculated using the Monte-Carlo (MC) and False Discovery Rate (FDR) methods.

Significant variations of geopotential height, temperature, zonal and meridional components of wind during Forbush decreases of galactic cosmic rays were revealed on the isobaric levels 100, 30, 10, 3, 1 hPa over the middle and polar latitudes of the Northern and Southern hemispheres. The maxima of variations of all parameters under consideration were observed on the isobaric level 10 hPa (altitude ~30 km, the height of the maximum ionization of the atmosphere by GCRs) on the 4^{th}—8^{th} days after the event onsets. Results of calculations for the isobaric level 10 hPa on the 4^{th} day after 20 Forbush decreases during 1991—2004 are presented in Fig. 1. The amplitude of geopotential height deviations was + 250 gp. m and —200 gp. m in the Northern hemisphere and +175 gp. m and —130 gp. m in the Southern hemisphere. The maximum amplitude of temperature variations was 4 K over the North Atlantic region and -3 K over the Eastern Europe. The significant variations of zonal (u) and meridional (v) wind components were revealed over Greenland, north Atlantic and Europe. Amplitude of variations was + 9 m/c and – 12 m/c for the u-wind component and + 12m/c and – 8 m/c for the v-wind component.

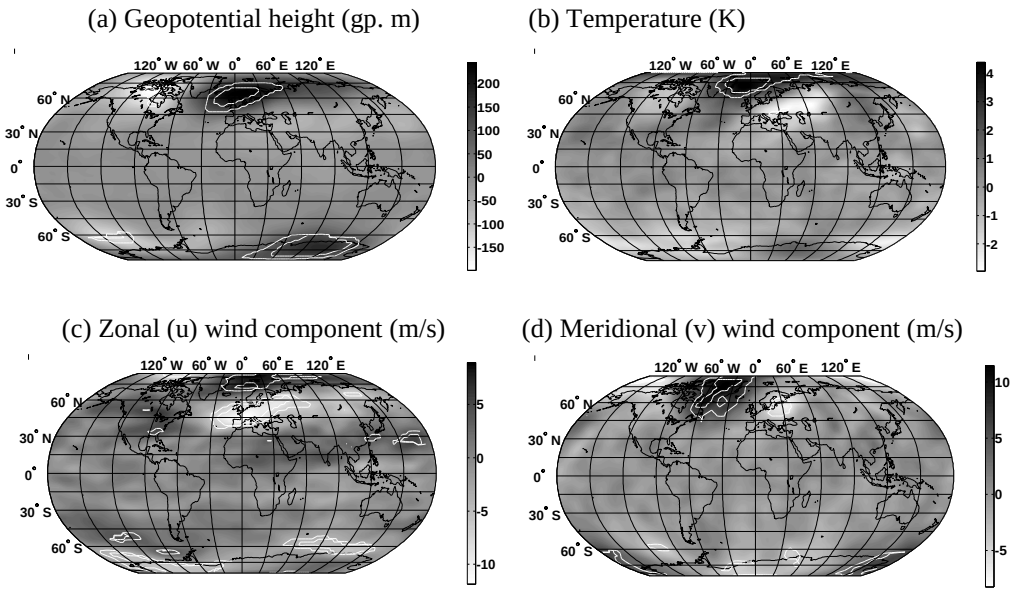

FIGURE 1. Composites of geopotential height (a), temperature (b), zonal (c) and meridional (d) wind components on the isobaric level 10 hPa (altitude ~30 km) on the 4^{th} day after 20 Forbush decreases of GCRs during 1991—2004. White lines depict the significance levels 0.95 and 0.99 as calculated by the MC and FDR.

The minimum energy of galactic cosmic rays precipitating in the regions of revealed disturbances of analyzed stratospheric parameters (GPH, T, u and v wind

components) was estimated according to data [4] about values of geomagnetic cutoff rigidities. It was revealed that minimum energies of precipitating particles in the regions of most significant stratospheric parameter deviations vary from ~10 MeV to ~ 1 GeV in the Northern hemisphere and from ~10 MeV to ~3 GeV in the Southern hemisphere. The data above suggest that the detected changes in geopotential height, temperature, zonal and meridional wind components are due to variations of the low-energy component of galactic cosmic rays strongly modulated by solar activity [e. g., 5].

The physical mechanism of the observed effects could be associated with variations of stratosphere ionization caused by cosmic rays flux variations during Forbush decreases.

1. B. A. Tinsley, G. W. Deen, *J. Geophys. Res*., 1991, 96, pp. 22283—22296.
2. I. V. Artamonova, S. V. Veretenenko, *J. Atm. Sol-Terr. Phys.*,2011, pp. 366—370.
3. I. V. Artamonova, S. V. Veretenenko, *Adv. Space Res.*, 2014, 54, pp. 2491—2498.
4. M. A. Shea, D. F. Smart, *18th Int. Cosmic Ray Conf. Pap*, 1983, 3, pp. 415—418.
5. G. A. Bazilevskaya, *Adv. Space. Res*, 2005, 35, 458 p.

Features of the Annual Gamma-Ray Variation in the Ground Level of the Atmosphere

Alexey V. Germanenko, Yuriy V. Balabin, B. B. Gvozdevsky

Laboratory of Cosmic Rays, golo, 26a, Academgorodok St., Apatity, 184209, Russia

The monitoring of secondary cosmic rays, including the surface gamma radiation background (GRB) arriving from the upper hemisphere, has been carried out by the Polar Geophysical Institute since 2009. Scintillation detectors on NaI(Tl) crystals are used. The energy range of 20 keV — 5 MeV is covered by two crystals, of Ø62×20 mm and Ø150×110 mm. The first crystal is effective within the range of 20—400 keV, integral output channels >20 keV and >100 keV are used; the second crystal is effective within the range of 0.2—5 MeV. Based on the second crystal the device to measure the differential energy spectrum was developed.

The GRB variations not related to an atmospheric precipitation have been detected. First of all, it is the annual variation whose amplitude is 25% and 50% in Apatity and Barentsburg, respectively. Additional measurements and experiments showed that the annual variation is related to the changes in the energy spectrum up to 450 keV only. In addition, the annual and day variations in other components of secondary cosmic rays have been studied.

The transformation of the GRB differential spectrum of of 0.2—5 MeV range into subranges (200—400 keV, 400—600 keV, etc.) allowed us to reveal different bands having the different barometric coefficients increasing with the energy. That means that the radiation within the range of 0.2—5 MeV is generated by different

mechanisms and originated from different types of particles. A noncontradictory hypothesis explaining the observed effect is suggested.

1. Introduction. The neutron, electron and muon, electromagnetic components (with energies of tens MeV and more) of secondary cosmic rays are investigated for many years. Much less studied soft gamma radiation (up to few MeV) in the surface layer of the atmosphere. Our 6 years data of the complex unit at the Apatity and Barentsburg stations is quit enough to carry out of studying and comparison. At the Apatity station data from detectors: neutron monitor (18-NM-64), leadless section of neutron monitor (i.e. bare NM, bNM), charged particle detector (CPD) and scintillation gamma-ray detectors (SGRD) were used. Conventional neutron monitor 18-NM-64 detects neutrons with energies above 50 MeV. Leadless neutron monitor 4-NM-64 is sensitive to neutrons with energies up to hundreds of keV [Dorman]. Charged particle detector (muons, electrons and positrons) with energies above ~7 MeV. Scintillation gamma-ray detectors (small one is Ø60×20 mm NaI(Tl) crystal and big one is Ø150×110 mm NaI(Tl) crystal) measure the flux of electromagnetic radiation on the 4 energy levels: >20, >100, >200 keV and > 1 MeV. Besides, by means of the scintillation detector Ø150×110 mm NaI(Tl) crystal, the differential spectrum of ground gamma-radiation (GR) within the range of 0.2—5 MeV. The period of one spectrum gathering is set 30 minutes. At the Barentsburg station two types of detectors were only used: NM and small SGRD with output channels > 20, > 60, > 100, > 200 keV. The function block-diagram is given in Fig. 1.

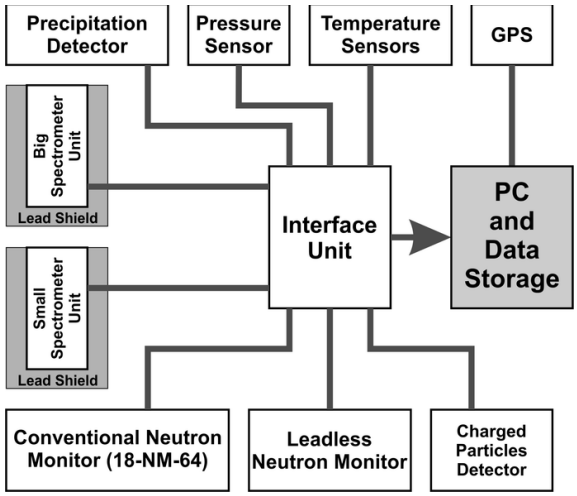

FIGURE 1. The function block-diagram of the unit in Apatity.

The various regular and stochastic variations in cosmic rays flow were detected. This paper is focus on the annual variation observed in some components of SCR (Secondary Cosmic Rays).

2. Annual variation in some components of SCR. The annual GR-variation has been detected just after a one-year observation, with its amplitude being high and readily observed. It makes up tens of percent. The origin of this considerable

variation is not clear yet. Results are given for the search for possible similar variations in other components.

It is obvious the seasonal variations on NM and CPD are absent. It is observed a monotonic decrease of intensity. This is due to the 11-year solar cycle modulation of cosmic ray in the heliosphere because the period 2009—2015 is from the Sun minimum to maximum. The same trend is observed at bNM, however, in the each cold season there is a decrease of the neutron flux. With warm weather coming this flux is reduced to its usual level corresponding to NM level. As it was mentioned above, huge variation is present at GR. The variation amplitude is ~25% in Apatity and ~50% in Barentsburg). It can't be explained by the radon evolution.

The point is that deep soil freezing in the area where Apatity station is located, occurs in November-December. It should result in that radon stops emanating from the ground. By this period of time the snow cover is 50—60 cm deep. Besides there is no any geological fault within the area of Apatity station location, hence, the amount of the radon emanated is minimal. But the gamma-ray flux during a winter (from October till April) is falling down continuously.

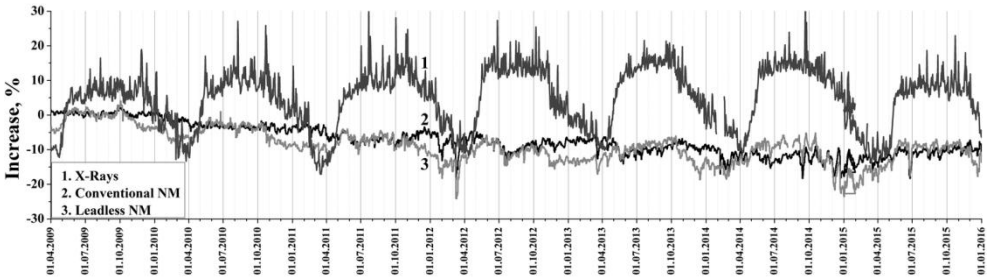

FIGURE 2. The intensity profile of secondary cosmic rays. "Piloseness" in the GR profile corresponds to the increases of GR connected to precipitation [1, 2].

General argument against "radon cause" is the annual variation of GR in Barentsburg. Barentsburg is on latitude 78° N. This is the permafrost zone. The radon evolution from the soil in such conditions is not possible. However the annual variation amplitude at Barentsburg is twice more than at Apatity (see Fig.3a) and up to 50%. At the same time the phase and the profile shape of annual variations on these two stations are close enough. We suggest to be another causes.

First of all, the method of epoch superimposition has been applied to obtain a more accurate annual variation profile, i. e. it allowed an average annual bNM and SGRD profile over a seven-year period (Fig.3b) to be obtained. The daily average data on the snow cover depth [3] and the epoch superimposition have been used to obtain an average profile of the snow cover thickness in Apatity and Barentsburg stations location. The bNM and SGRD profiles are different in amplitude but sur-

prisingly exact in their shape. In addition they follow the snow cover thickness profile. It is clear that the bNM and SGRD intensity increases in snow melting in spring, by the late April (~ 120-th day the year). The level of bNM becomes normal. In autumn, with the snow cover formation (~300-th day of the year) the level

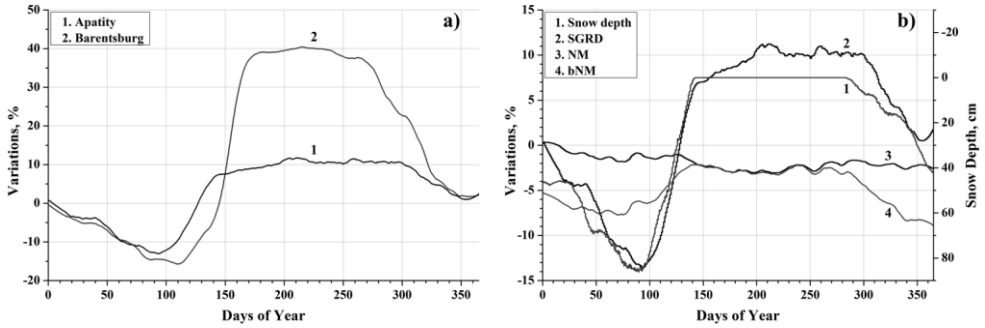

FIGURE 3.a) Comparison of SGRD variations in Apatity and Barentsburg. **b)** Annual variation of various radiation components in the Apatity station relative to the snow depth.

of bNM decreases again. So good correlation of annual variations with the snow cover thickness seems to confirm the radon hypothesis. However, it is better not to make such conclusions yet. The state of the ground may produce some effect, resulting in a certain part of variations in the warm season (a radon component). But to completely explain an annual variation by this way is impossible. Within all the winter period the GR-flow decreases and after an abrupt "rise" in spring, which coincides with the snow cover melting, it continues increasing until the midsummer.

As it was mentioned, bNM is sensitive to neutrons, with energies ranging from thermal one to hundreds keV. Neutrons have got such small energies as a result many collisions with the atomic nuclei of the environment. [4,5]. For brevity, these neutrons are possible to be referred to as the scattered or albedo ones. The process mainly occurs in a dense medium, i. e. in the ground. The snow cover reflects neutrons, just like an exterior layer of polyethylene on NM [4]; the thickness of polyethylene on NM is 8 cm, the snow cover of 1 m thick approximately corresponds to a 12—15 cm water layer.In this case water (H_2O)and polyethylene $(CH_2)_n$are close in efficiency to decelerate and reflect neutrons because the content of protons (hydrogen nuclei) in a unity of their volume is approximately equal. Thus, the annual variation on bNM is related to that the snow cover prevents the scattered neutrons from emanating from the ground.If this is a real reason of the annual variation on bNM, one is sure to observe the effect of saturation: it is when the snow cover completely prevents neutron emanation from ground, with further increase of the snow cover in depth making no longer effect. It is obvious that with snow cover thickness of ~ 50 cm and over, the decrease in counting of bNM stops. This effect is clearly observed from the ratio between the counting rate and the snow cover thickness Fig. 4a. It should be pointed out that a conventional NM is specially designed so

that neutrons of smaller energies, which are scattered in their environment render no effect on it [4]. That is why the energy threshold for the NM is 50 MeV.

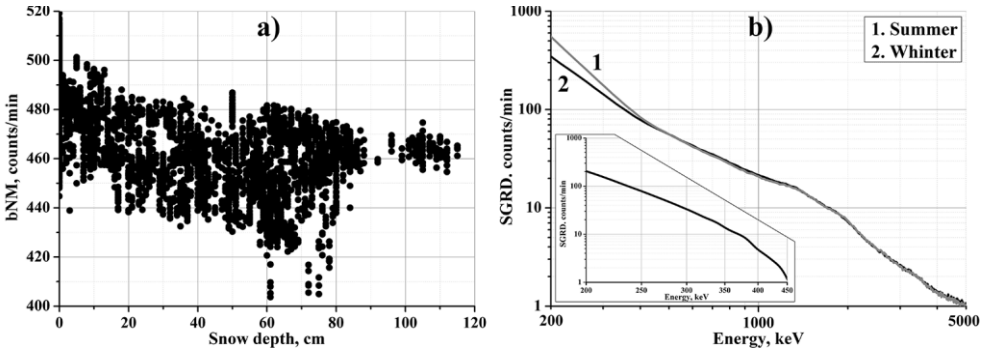

FIGURE 4.a)bNM count rate depends on snow depths; **b)** Differential gamma-ray spectra at a summer (1) and a winter (2). In the inset there is a difference between these spectra. Upper limit of energy is clear observed at 450 keV.

In addition to GR- recording in 4 integral channels measurement there are continuous measurement of the differential GR-spectrum in the range 0.2—5 MeV with 30 minutes time resolution are carried out. Each measured spectrum is recorded in a separate file. Some days with clear weather marked in March-April, 2015 were selected. Clear weather is necessary to avoid the change of the GR-flow, which is related to precipitation [1]. An average spectrum in the minimum of the annual variation has been calculated from the recordings obtained during all the days selected. The same operation was carried out in July-August, i.e. in the maximum of the GR-annual variation. The differential spectra of the minimum and maximum are given on Fig.4b. One can see the change of the GR-flux, which is related to the annual variation, occurs only in energies up to 450 keV. GR with the energy higher than 450 keV show no seasonal changes.

To verify the results obtained, an additional study has been carried out. The differential spectrum recorded was divided into subdivisions: 200—400 keV, 400—600 keV, 600—800 keV, etc. The measurements within the limits of one subdivision were summed up to obtain a quanta flow within the given subdivision. Handling the data files obtained over a year, we had an annual profile of the GR-flow for rather narrow energy ranges instead of integral channels used before. Just in the subdivision of600—800 keV,the annual variation is very poor, practically absent, as it does not exceed the fluctuation and variations induced by other reasons (first of all, by increases in precipitation).

It is possible to note that a convincing result has been achieved: the annual variation and increases while precipitations are absolutely different phenomena. Though the amplitude of variation (25%) and the increases in precipitation (up to 50%, typical 20—30%) are comparable, the annual variation is related to the changes of the GR-spectrum in energies up to 450 keV. In comparison, increases in precipitation cause the corresponding change of the GR-spectrum up to 2.5 MeV[1].

The true reason of both the increases in precipitation and the annual variation is not clear yet. Some facts however are clearly established. The GR-spectrum has the same power form at any time within a year and a day.Within this spectrum there are no any characteristic lines of radionuclides. The threshold of 450 keVis close to a well known value of 510 keV, i.e. to the energy of positron annihilation; especially because the energy measurement accuracy on this type of a crystal is less than 17%. In our opinion, the affinity of the threshold energy to the energy of positron annihilation is a rather important fact specifying the nature of an annual variation. It is possible to propose the following as a working hypothesis. The elastic interaction with the atomic nuclei of the environment is known to cause albedoparticles to originate.The same is true for neutrons, as it has been mentioned above. This is the way a flux of albedo positive muonsμ^+reflected from the earth's surface, originate. Muons originate in the atmosphere mainly at height of over 10 km above the earth's surface, with only very energetic muons being able to achieve the earth's surface. As the lifetime of muons is 2.2 μs, practically all the albedo μ^+decay in the atmosphere. The albedo μ^+ decay into three particles, of which one is positron.A positron like an electron loses its energy for air ionization and bremsstrahlung radiation. Slowing down, a positron eventually annihilate, resulting in origination of two quanta with energies of 510 keV[6, 7]. The presence of the snow cover similarly impedes the emanation of the albedo μ^+into the atmosphere. The snow is certainly not an effective inhibitor forμ^+because the proton mass (in molecule of H_2O) is 9 times greater than the rest mass ofμ^+. However, it is necessary to note that having reached the earth's surface, muons have very high energy (a few GeV), so these are the relativistic ones, and their complete mass may be comparable withor may even exceed the rest mass of a proton. Though seeming unnatural, the hypothesis proposed coordinates all the established facts: the absence of lines of radionuclides in the spectrum of a variation, the upper threshold amount of energy of a variation in 450 keV, a strong correlation with the depth of snow cover, and the presence of a same reason of a variation in neutron and electromagnetic components.

3. Conclusions. Seasonal variations in different components of the secondary cosmic rays during 2009—2015 have been measured. Seasonal variation on the HM is completely absent, there is only a gradual decrease caused of the solar activity increase. The general trend at bNM is the same as at NM, however, in the cold season there is a decrease on some percents. It is consider being moderation effect of a snow cover. Annual variation in the soft gamma-ray is huge (~25% at Apatity, ~50% at Barentsburg). These variations are in good coincidence with snow cover depth. Based on the superimpose method we have studied annual variations in the different components of the secondary cosmic rays.

The measurements of the differential GR-spectrum in the minimum of the annual variation and in the maximum have shown that the annual variation is caused exclusively by an increase of the gamma-quanta flow, with energies not exceeding 450 keV. The hypothesis is proposed which consistently coordinates all the facts revealed.

1. Y. V. Balabin, A. V. Germanenko, B. B. Gvozdevsky, E. V. Vashenyuk, Variations in the natural X-ray background in the polar atmosphere, *Geomagnetism and Aeronomy*, 2014, 54(3), pp. 347—356.
2. A. V. Germanenko, Yu. V. Balabin, B. B. Gvozdevsky et al., High-energy photons connected to atmospheric precipitations, *Astrophys. Space Sci. Trans.*, 2011, 7, pp. 471—475.
3. https://rp5.ru/Weather_archive_in_Apatitovaya
4. L. I. Dorman, Experimental and Theoretical Foundations of Cosmic Ray Astrophysics, Nauka Publ., Moscow, 1975, 463 p.
5. L. I. Dorman, Meteorological Effects of Cosmic Rays, Nauka Publ., Moscow, 1972, 211 p.
6. S. Hayakawa, Cosmic Ray Physics. Nuclear and Astrophysical aspects, Wiley-Interscience, New York, 1969, 774 p.
7. V. S. Murzin, Introduction to the physics of cosmic rays, MSU Publ., Moscow, 1988, 320 p.

Electromagnetic Disturbances in the Frequency Range 5—20 Hz in the Upper Ionosphere and on the Ground

Nataliya S. Nosikova[1,2], Nadezda V. Yagova[1], Vyacheslav A. Pilipenko[1], Heilig Balazs[3],and Alexander Yu. Schekotov[1]

[1]Institute of Physics of the Earth of the Russian Academy of Sciences, B. Gruzinskaya, 10, Moscow 123242, Russia
[2]National Research Nuclear University "MEPhI", Kashirskoe highway, 31, Moscow, 115409, Russia
[3]Tihany Geophysical Observatory MFGI, Tihany, Hungary

The frequency band from ~ 5 Hz to ~ 25 Hz is the "blind spot" in the physics of magnetospheric-ionospheric ULF waves. Electromagnetic ULF disturbances in the band below ~5 Hz is typically formed by ion-cyclotron waves generated in the near-equatorial regions of the magnetosphere. Besides them, there is a theoretical possibility of occurrence in the upper ionosphere of electromagnetic structures with somewhat higher frequencies:

— A part of energy of powerful atmospheric emission — Schumann resonance (SR) with the fundamental tone ~7.8 Hz and higher harmonics can leak into the night side upper ionosphere [1]. Indeed, electric field observations on low-orbiting satellites found spectral bands corresponding to SR harmonics [1,4];

— wave modes of the ionospheric Alfven resonator (IAR) with frequencies extending from ~1 Hz to the fundamental SR tone occupy the altitude region from ionospheric E-layer up to the reflection point in the upper ionosphere at ~ 1000 km [2, 3].

— At auroral latitudes in the region of intense field-aligned currents intense MHD turbulence occurs. A turbulent region is observed on a low-orbiting satellite as a disturbance with power-law spectra [4]. An occurrence possibility of spectral

peaks, corresponding to some highlighted quasi-periodic spatial structures, on this turbulent background is still unclear.

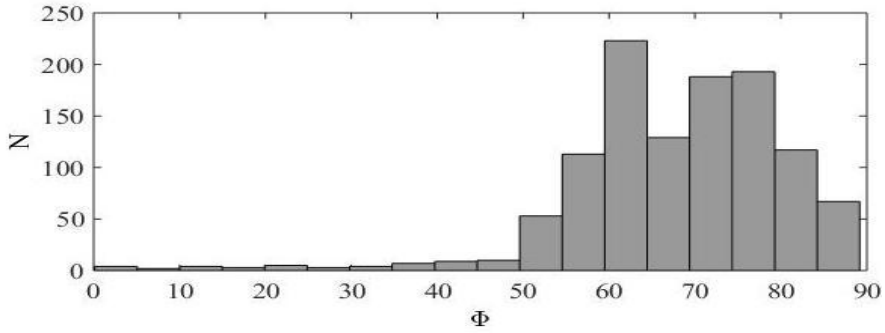

FIGURE 1. Latitudinal distribution of the numbers N of quasi-periodic sig-nals in the 7—8 Hz frequency band as measured by CHAMP in both hemispheres

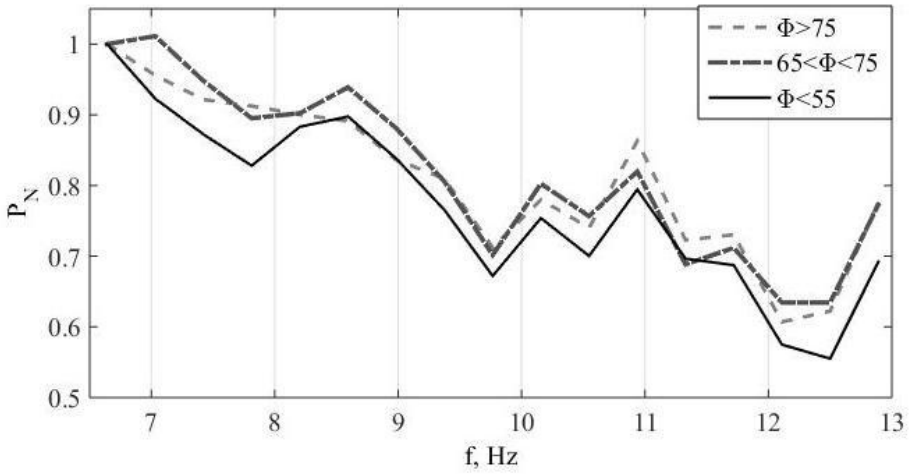

FIGURE 2. Normalized frequency distribution of the occurrence rate P_N of quasi-periodic signals in the polar cap (grey dashed line), at auroral (bold dot-dashed line) and middle (solid line) latitudes. See geomagnetic latitude boundaries in the insert.

Thus, there remains the problem that has not been resolved yet: Are there any highlighted frequencies/scales in the upper ionosphere in the range around the SR fundamental tone? To answer this question, in this paper we examine quasi-periodic signals in the frequency band 5—20 Hz recorded simultaneously in the upper ionosphere by CHAMP satellite and on the ground at Karymshino station (Kamchatka). We analyze their relation to world-wide thunderstorm activity, on the one hand, and to plasma parameters of the outer magnetosphere, on the other hand.

CHAMP [5] was launched in 2000 at quasi-circular orbit with inclination 87^o. The altitude during the operation was continuously decreasing and reached ~370 km in 2002. Magnetic field at CHAMP is measured with 3-component flux-gate magnetometer with sampling rate 50 Hz. Karymshino (KAR) station (geographic coordinates 52.8N, 158.1 E, and L=2.1) is equipped with 3-component search-coil magnetometer with the initial sampling rate 150 Hz, which has been reduced to 50 Hz. Seven days in the summer of 2002 are taken for the analysis.

A program for the automatic detection of quasi-periodic signals analyzes 2s time intervals, and selects events when a spectral maximum in a given frequency band exceeds a prescribed threshold. The signal occurrence rate at a given frequency is the ratio of selected intervals number to total number of intervals.

Magnetic field variations in 5—20 Hz frequency range recorded simultaneously in the upper ionosphere and on the ground are characterized by the following properties.

Figure 1 shows the corrected geomagnetic (CGM) latitudinal distribution of signals in the 7—8 Hz frequency band, distributions for other frequencies are similar. A highest occurrence rate is observed at auroral ($65^o<\Phi<75^o$) and polar cap ($\Phi>75^o$) latitudes. Probably, this statistical result is due to a significant contribution of events when the satellite crossed spatial structures of a kilometer scale.

In order to discriminate spatial variations dominating within the auroral zone from possible time-periodic signals the frequency distribution of the occurrence rate $P_N(f)$ has been calculated for three latitudinal zones: polar cap, auroral oval, and mid-latitude (Fig. 2). A maximum is seen at f~8 Hz atmiddle and auroral latitudes. A maximum at f~11 Hz can be seen in all three zones. An enhancement of P_N at f~8 Hz could be a result of SR leakage into the upper ionosphere.

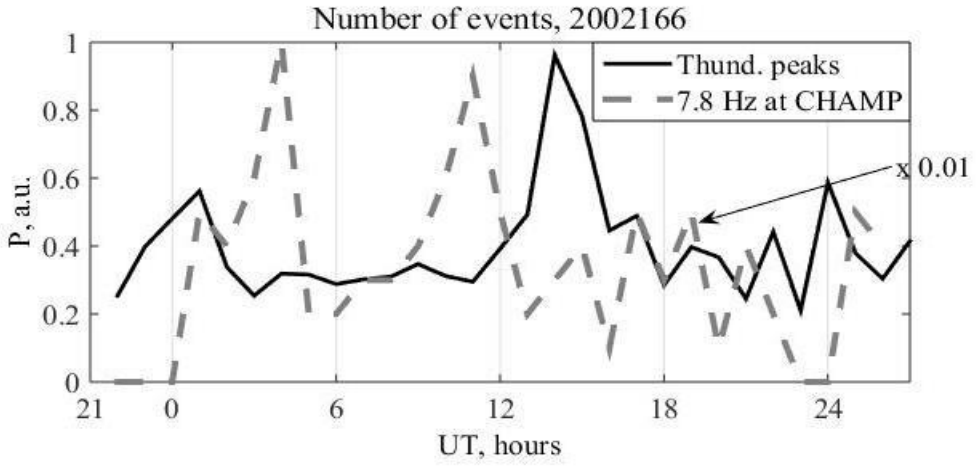

FIGURE 3. Occurrence rate of ~8 Hz signals and the normalized number of lightning strokes, recorded by the WWLLN network for day 2002 166.

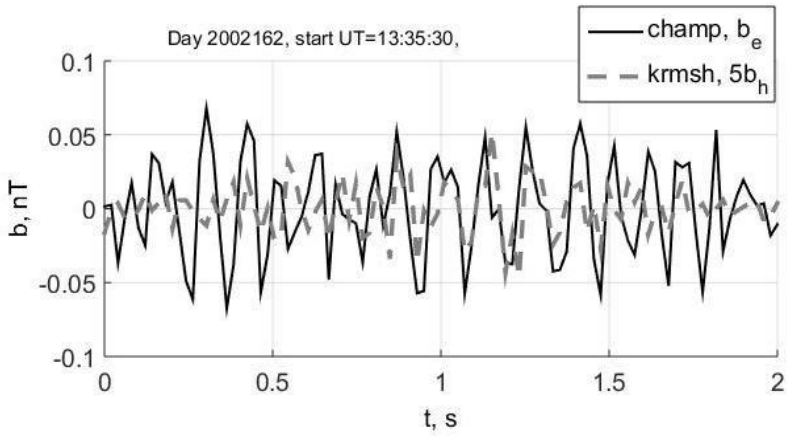

FIGURE 4.An example of coherent oscillations of the magnetic field at CHAMP and KAR in near conjugate location (CHAMP CGM coordinates are -55.2, 218.5). The KAR signal is multiplied by 5.

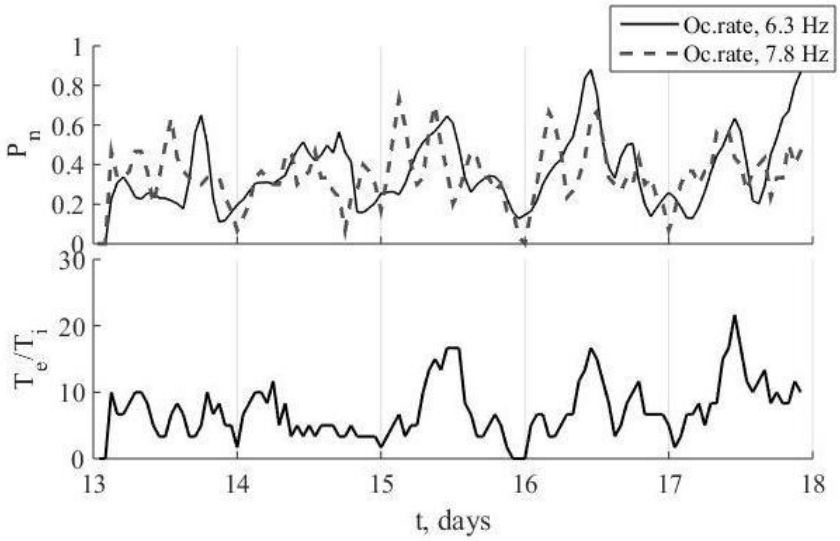

FIGURE 5. Normalized occurrence rate of harmonic signals at CHAMP and Te/Ti ratio at the geostationary orbit as measured by LANL in June 2002.

To check the hypothesis on SR leakage, the occurrence rate of 8 Hz signals has been compared with the hourly number of world-wide lightning strokes registered by the WWLLN network. The comparison (Fig. 3) shows no correlation between thunderstorm activity and the occurrence rate of 8 Hz signals in the upper iono-sphere.

Waveforms of the signals detected in the upper ionosphere also do not support the hypothesis of their thunderstorm origin. An example of coherent fluctuations of the magnetic field recorded simultaneously in the ionosphere and on the ground during the interval of quasi-conjugated CHAMP-KAR location is shown in Fig. 4. Contrary to typical impulsive waveforms of SR, the recorded event demonstrates long-lasting quasi-harmonic oscillations. Moreover, the signal amplitude in the ionosphere is higher than that on the ground.

The latitude maximum of the occurrence rate latitude distribution shown in Fig. 1 is projected into the outer magnetosphere. The occurrence rate P_N of quasi-periodic signals with frequencies in the bands centered at 6.3 and 7.8 Hz in the F-layer is shown in Figure 5 (upper panel). Enhancements of P_N correspond rather well to increases of the electron to ion temperature ratio at geostationary orbit (Fig. 5, bottom panel). Thus, the occurrence of quasi-periodical signal at 6.3 Hz is predominantly controlled by the plasma parameters in the outer magnetosphere. However, no such correspondence can be seen in the occurrence rate of signals at 7.8 Hz.

Discussion and conclusion: During some satellite observations, events with ~8 Hz disturbances in the ionospheric F-layer were observed [6]. They interpreted these observations as the result of SR penetration into the upper ionosphere. However, those disturbances in the F-layer can be of ionospheric or magnetospheric origin and their relation to SR is still open.

The observed enhancements of ULF waves at ~8 Hz and ~11 Hz in the upper ionosphere are puzzling. Excitation of SR by a magnetospheric source seems questionable. Indeed, SR is the electric mode trapped in the Earth-ionosphere waveguide. Any electric mode is weakly excited by a magnetospheric source, because of low penetration of the ionospheric field-aligned currents into the low-conductive atmosphere. In the outer magnetosphere the 5—15 Hz frequency range corresponds to the lower ion-electron hybrid frequency. The SR leakage hypothesis has not been unambiguously confirmed by our analysis of CHAMP magnetic data. However, there are arguments both pro and con this hypothesis. SR hypothesis is supported by some increase of the occurrence rate at nearly 8 Hz (Fig. 2). The polar maximum in the latitude distribution (Fig. 1) allows both SR and magnetospheric interpretations. It corresponds to the latitude minimum of lightning activity, but the propagation is more effective at high geomagnetic latitudes [1].

However, no correlation with world thunderstorm activity, amplitude decrease from the ionosphere to the ground, quasi-sinusoidal waveforms that are not typical for thunderstorm generated signals, and correlation of plasma temperatures in the outer magnetosphere with the signal occurrence favor the magnetospheric origin of the observed signals. Some combination of both mechanisms can be suggested.

Acknowledgements: *This study is partly supported by the RFBR grant № 15-55-45064. The authors thank Dr. H. Luehr for supplying CHAMP magnetic field data. The CHAMP mission was sponsored by the Space Agency of the German Aerospace Center (DLR) through funds of the Federal Ministry of Economics and Technology. We acknowledge CDAWEB for LANL data, NASA contract NAS5-02099.*

1. V. V. Surkov, N. S. Nosikova, A. A. Plyasov et al., Penetration of Schumann resonances into the upper ionosphere, *J. Atmospheric and Solar-Terrestrial Physics*, 2013, pp. 65—74.

2. D. Dudkin, V. Pilipenko, V. Korepanov et al., Electric field signatures of the IAR and Schumann resonance in the upper ionosphere detected by Chibis-M microsatellite, *J. Atmospheric Solar-Terr. Physics*, 2014, 117, pp. 81—87.

3. V. Pilipenko, D. Dudkin, E. Fedorov et al., IAR signatures in the ionosphere: modeling and observations at microsatellite Chibis-M, *J. Atmospheric Solar-Terr. Physics*, 2015.

4. I. V. Golovchanskaya, A. A. Ostapenko, B. V. Kozelov, Relationship between the high-latitude electric and magnetic turbulence and the Birkeland field-aligned currents, *J. Geophys. Res*., 2006, 111, A12301.

5. http://www. gfz-potsdam. de/en/section/earths-magnetic-field/infrastructure/champ/

6. B.-B. Ni, Z.-Yu Zhao, Spatial observations of Schumann resonance at the iono-spheric altitude, *Chinese Journal of Geophysics*, 2005, *48*, pp. 818—826.

Linear and Dual Linear Regression Model of Mid-Latitude Daytime N_mF2 Dependence from Solar and Geomagnetic Activity

Alisher R. Abdullaev[1], Maxim V. Klimenko[1,2], Alexander V. Markov[1], Konstantin G. Ratovsky[3], Nina A. Korenkova[1], Vladimir S. Leshchenko[1], and Valerii A. Panchenko[4]

[1]Immanuel Kant Baltic Federal University, 236041, Kaliningrad,14 A. Nevsky Str., Russia
[2]West Department of Pushkov IZMIRAN, RAS, 236017, Kaliningrad, 41 Pobeda Av., Russia
[3]Institute of Solar-Terrestrial Physics, SB RAS, 664033, Irkutsk P/O Box 291, 126a Lermontov Str., Russia
[4]Pushkov IZMIRAN, RAS, 142190, Troitsk, Moscow Region, Russia

Introduction: The F2 layer peak electron density (N_mF2) is larger for higher solar activity and is proportional to sunspots number and the $F_{10.7}$ index [1]. Solar activity dependence of diurnal and seasonal variations of ionospheric F region parameters in the East-Siberian region in details is investigated in [2]. It was shown, that higher solar activity leads to the N_mF2 growth, which is the greatest in the afternoon at winter solstice. Contrary, N_mF2 weakly depends on solar activity in the nighttime winter ionosphere which mainly depends on the diffusion plasma flows from the plasmasphere. In [3] it was concluded that N_mF2 in winter above Millstone Hill at 12:00 LT increases linearly with increasing of solar activity proxy $F_{10.7}$ index. Hence, linear function can be used to represent the N_mF2 and proxy

$F_{10.7}$ correlation. In this paper we examined N_mF2 dependence on the different kind of averages solar and geomagnetic activity in January 2008—2015 at different locations.

Data analysis results: We analyzed the daily $F_{10.7}$ index data obtained from the web-site http://lasp. colorado. edu/lisird/tss/noaa_radio_flux. html and geomagnetic activity index *Ap* obtained from the web-site http://wdc.kugi.kyoto-u.ac.jp/kp/index.html for January 2008—2015. We obtained 27-day and 81-day averaged values of solar ($<F_{10.7}>_{27}$ and $<F_{10.7}>_{81}$) and geomagnetic $<Ap>_{27}$ activity indices for 15 January of each year (see Table 1). $<Ap>_{27}$ showed that the considered periods were geomagnetically quiet. We used the N_mF2 observation data from the Irkutsk, Moscow and Kaliningrad ionosondes. The data were obtained from the manually scaled ionograms using interactive ionogram scaling software, SAO Explorer [4, 5] in the cases of the Irkutsk and Moscow ionosondes and PARUS software [6] in the case of the Kaliningrad ionosonde. On the basis of 27-day average January daytime N_mF2, $<N_mF2>_{27}$, for each station, $<F_{10.7}>_{27}$ and $<F_{10.7}>_{81}$ for 2008—2015 the linear regressions of daytime $<N_mF2>_{27} = a_0 + a_1 \times (<F_{10.7}> — 70)$ have been constructed. The analysis of the obtained linear regressions and observation data has revealed the following paradox: in January 2014, when values of solar activity indices $<F_{10.7}>_{27}$ and $<F_{10.7}>_{81}$ were larger than in 2015, the daytime $<N_mF2>_{27}$ have appeared smaller.

TABLE 1. 27-day and 81-day averaged values of the $F_{10.7}$, 27-day averaged *Ap* index and daytime N_mF2 over Irkutsk, Kaliningrad and Moscow for 15 January 2008—2015.

Year	$<F10.7>_{27}$	$<F10.7>_{81}$	$<Ap>_{27}$	daytime (10—14 LT)$<N_mF2>_{27}$		
				Irkutsk	Kaliningrad	Moscow
2008	72	71.88	8.4	3.69	2.76	-
2009	67.7	66.8	4	3.3	2.44	2.91
2010	79.4	79	3.1	3.81	2.96	3.25
2011	81	85	5.9	4.61	4.28	4.19
2012	131	124	7.2	9.77	7.41	8.09
2013	126.5	111.2	5.3	8.59	7.65	8.18
2014	153	154.5	5.5	9.78	9.10	9.42
2015	130	137.3	9.6	10.94	10.44	10.57

For an illustration of this paradox we present in Fig. 1 the dependence of daytime $<N_mF2>_{27}$ on solar activity and results of linear regressions of daytime $<N_mF2>_{27}$. It is visible that the linear regressions have the greatest deviations from observation data in 2014 and 2015. Having analyzed these greatest deviations of observed daytime $<N_mF2>_{27}$ from their linear regressions and $<Ap>_{27}$ values for eight years (see Table 1), we have come to a conclusion that the underestimation of linear regression of daytime $<N_mF2>_{27}$ values in 2015 corresponds to the level of geomagnetic activity increased this year, and the linear regression overestimated the daytime $<N_mF2>_{27}$ in 2014 due to the lowered level of geomagnetic activity. On

the basis of it the conclusion is drawn on a positive contribution of geomagnetic activity to January daytime $<N_mF2>_{27}$.

TABLE 2. Coefficients and mean squared errors (MSE) for linear and dual linear regression for all years obtained using $<F_{10.7}>_{27}$ index.

Station	Linear regression			Dual linear regression			
	a_0	a_1	MSE	b_0	b_1	b_2	MSE
Kaliningrad	2.837	0.091	1,02	3.664	0.082	0.323	0,60
Moscow	3.093	0.09	0,79	2.911	0.071	0.510	0,19
Irkutsk	3.535	0.093	0,78	3.080	0.088	0.325	0,38

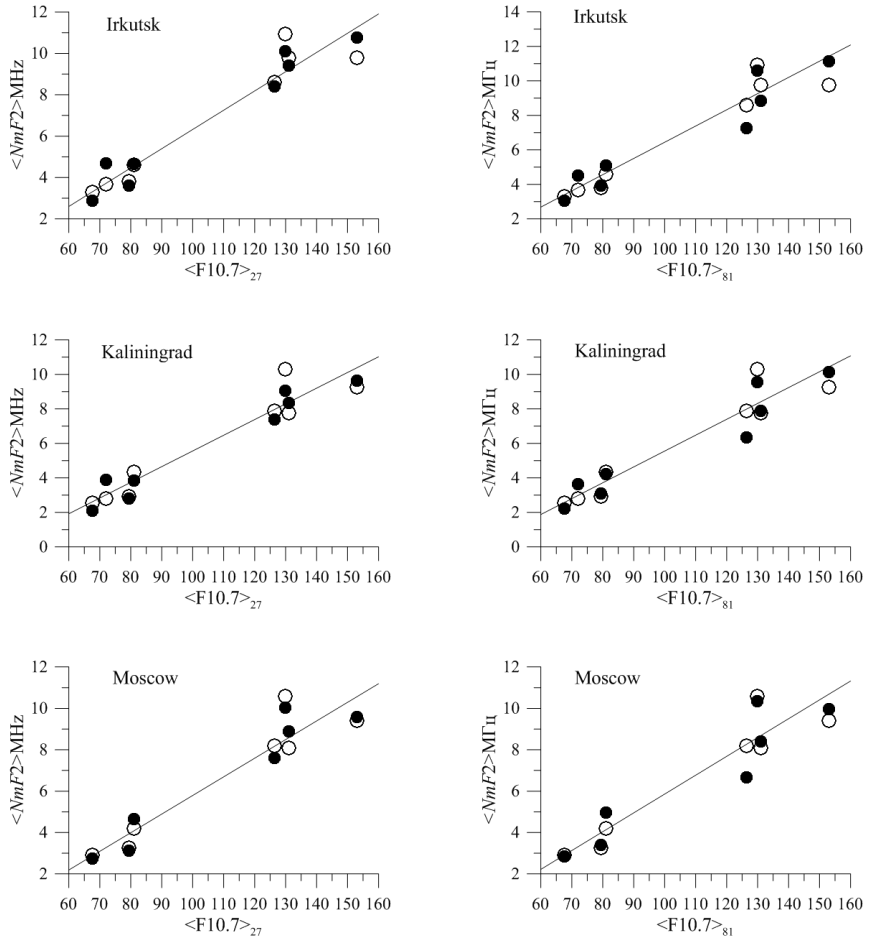

FIGURE 1. Daytime $<N_mF2>_{27}$ dependence on the solar activity indices $<F_{10.7}>_{27}$ (top) and $<F_{10.7}>_{81}$ (bottom) observed at 3 considered stations (light circles) and obtained by linear (solid lines) and dual linear (black circles) regressions of data for 15 January 2008—2015.

TABLE 3. The same as in Table 2, but obtained using $<F_{10.7}>_{81}$ index.

Station	Linear regression			Dual linear regression			
	a_0	a_1	MSE	b_0	b_1	b_2	MSE
Kaliningrad	2.802	0.092	0,75	2.497	0.086	0.223	0,57
Moscow	3.132	0.091	0,75	3.086	0.074	0.405	0,42
Irkutsk	3.629	0.094	0,89	3.336	0.088	0.233	0,70

We carried out the verification of the version about a positive contribution of geomagnetic activity to daytime $<N_mF2>_{27}$ on the basis of the constructed dual linear regression: daytime $<N_mF2>_{27} = b_0 + b_1 \times (<F_{10.7}>_{27}—70) + b_2 \times (<Ap>_{27}—4)$. The comparison of dual linear regression with observed daytime $<N_mF2>_{27}$ and linear regression (Fig. 1) has revealed smaller deviations of dual linear regression from data that confirms a conclusion about a positive contribution of geomagnetic activity to January daytime $<N_mF2>_{27}$.

Coefficients and mean squared errors of linear and dual linear regression for all stations on $<F_{10.7}>_{27}$ and $<F_{10.7}>_{81}$ are specified in Tables 2 and 3. The mean squared errors obtained using a formula:

$$MSE = \frac{1}{n}\sum_{i=1}^{n}(< N_mF2 >_{27}^{*} - < N_mF2 >_{27})^2 ,$$

where$<N_mF2>_{27}$ is the result of linear regression or dual linear regression, and daytime $<N_mF2>_{27}$ are the observed values.

Comparison of mean squared errors with use the $<F_{10.7}>_{27}$ and $<F_{10.7}>_{81}$ shows that:

1) the results of dual linear regression describe daytime $<N_mF2>_{27}$ much better, than results of linear regression;

2) the advantages of use the $<F_{10.7}>_{27}$ or $<F_{10.7}>_{81}$ for the creation of linear regression don't revealed;

3) for the dual linear regression using the $<F_{10.7}>_{27}$ leads to a smaller MSE, than using $<F_{10.7}>_{81}$.

Acknowledgements.*The investigations are performed with financial support of Grants of the Russian Foundation for Basic Research No. 14-05-00788 and 14-05-00578.*

1. B. E. Bryunelli and A. A. Namgaladze, Physics of the Ionosphere, M.: Nauka, 1988, 526 p.

2. K. G. Ratovsky, A. V. Oinats, and A. V. Medvedev, Similitaries and differences between regular variations of F2-layer parameters of the polar and midlatitude ionosphere in east Siberian sector, *Solar-Terr. Phys.*, 2015, 1(2), pp. 70—79.

3. J. Lei, L. Liu, W. Wan et al., Variations of electron density based on long-term incoherent scatter radar and ionosonde measurements over Millstone Hill, *Radio Sci.*, 2005, 40, RS2008.

4. B. W. Reinisch, I. A. Galkin, G. M. Khmyrov et al., Automated collection and dissemination of ionospheric data from the digisonde network, *Adv. Radio Sci.*, 2004, 2, pp. 241—247.

5. G. M. Khmyrov, I. A. Galkin, A. V. Kozlov et al., Exploring digisonde ionogram data with SAO-X and DID Base, Proc. AIP Conf, *Radio Sounding and Plasma Physics*, 2008, 974, pp. 175—185.

6. A. L. Karpenko and N. I. Manaenkova, Nonlinear time series analysis of the ionospheric measurements, *Geologishe Rundshau*, 1996, 85(1), pp. 124—129.

Stationary Solution for Resonant Interaction of Internal Gravity Waves

Nataliya V. Bakhmetieva, Victor G. Lapin, and Gennady I. Grigoriev

Radiophysical Research Institute (NIRFI), 25/12a, Bol'shaya Pecherskaya St., Nizhny Novgorod, Russia

The main objectives of the study is experimental diagnostics of eddy ordered structures at the lower ionosphere, such as that occur when internal gravity waves (IGWs) propagate in stratified flows in the atmospheric boundary layer. In [1, 2] we considered the impact of the eddy motions in the mesosphere and the lower thermosphere on the relaxation time and the frequency of the artificial periodic irregularities. In this paper we study the nonlinear interaction of internal gravity waves in the atmosphere, taking into account a horizontal wind uniform height. We are taking into account nonlinear terms up to the third order in the IGW equations. It allowed us to determine the type and conditions of the existence of soliton solution.

The equation for the velocity of the medium in the presence of a uniform horizontal wind can be written [3, 4] as:

$$\frac{\partial \mathbf{v}}{\partial t} + (\mathbf{V}\cdot\nabla)\mathbf{v} = -\left(\frac{1}{\rho_0}\nabla p - \frac{\rho}{\rho_0}\mathbf{g}\right)\cdot\left(1 - \frac{\rho}{\rho_0}\left(1 - \frac{\rho}{\rho_0}\right)\right) - (\mathbf{v}\nabla)\mathbf{v}, \qquad (1)$$

where V is the horizontal wind velocity.

It takes into account the relationship between the equilibrium pressure and density of the atmosphere ($\nabla p_0 = \mathbf{g}\cdot\rho_0$) and keep the disturbance to the cubic terms. We use the incompressibility condition to describe the waves of low frequency. Therefore we get the continuity equation

$$\frac{\partial \rho}{\partial t} + (\mathbf{V}\cdot\nabla)\rho - \frac{\rho_0}{\mathrm{g}}N^2 w = -(\mathbf{v}\nabla)\rho, \qquad (2)$$

$$\nabla\mathbf{v} = \mathbf{0} \qquad (3)$$

In equation (2) N- the frequency of Brunt — Vaisala, which in the case of an incompressible and isothermal atmosphere is:

$$N^2 = -\frac{\mathrm{g}}{\rho_0}\frac{d\rho_0}{dz} = \frac{\mathrm{g}}{H}\text{for}\rho_0 = \rho_{00}\cdot\exp\left(-\frac{z}{H}\right).$$

Replacement $\{u',w'\} = \{u,w\}\cdot\exp\left(-\frac{z}{2H}\right)$ и $\{R,P\} = \frac{\{\rho,p\}}{\rho_{00}}\cdot\exp(\frac{z}{2H})$ allows you to get rid of the variable coefficients in the linearized equations. As a result, we obtain the system of the equations:

$$\widehat{D}u' + \frac{\partial P}{\partial x} = e^{z/2H}\left[R\frac{\partial P}{\partial x} - \left(u'\frac{\partial}{\partial x} + w'\frac{\partial}{\partial z} + \frac{w'}{2H}\right)u'\right], \widehat{D} \equiv \frac{\partial}{\partial t} + U\cdot\frac{\partial}{\partial x}$$

$$\widehat{D}w' + \left(\frac{\partial}{\partial z} - \frac{1}{2H}\right)P + \mathrm{g}R = e^{\frac{z}{2H}}[-\left(u'\frac{\partial}{\partial x} + w'\frac{\partial}{\partial z} + \frac{w'}{2H}\right)w' +$$

$$+(\mathrm{g}R^2 + R(\frac{\partial}{\partial z} - \frac{1}{2H})P)(1 - Re^{z/2H})] \quad (4)$$

$$\frac{\partial u'}{\partial x} + \left(\frac{\partial}{\partial z} + \frac{1}{2H}\right)w' = 0, \widehat{D}R - \frac{N^2}{\mathrm{g}}w' = -e^{z/2H}\left[u'\frac{\partial R}{\partial x} + w'\left(\frac{\partial}{\partial z} - \frac{1}{2H}\right)R\right]$$

Left parts of the equations (4) contain linear terms in the wave perturbations. We obtain the dispersion equation assuming that all the quantities are determined by the factor *exp(–iwt + i(k$_x$x + k$_z$z))* and we are omitting quadratic and cubic terms:

$$\Omega^2 = N^2\frac{k_x^2}{k^2+(2H)^{-2}}, \Omega \equiv \omega - k_x U, k^2 = k_x^2 + k_z^2, \quad (5)$$

as well as the relationship between the complex amplitudes of the wave disturbances

$$u \approx -\frac{k_z}{k_x}\cdot w';\ R \approx \frac{i}{\Omega\cdot\mathrm{H}}\cdot w';\ P \approx -\frac{k_z\Omega}{k_x^2}\cdot w'. \quad (6)$$

Synchronism conditions $\omega_3 = \omega_1 + \omega_2$, $\mathbf{k}_3 = \mathbf{k}_1 + \mathbf{k}_2$were investigated, and for the dispersion relation (5) it was found a resonance triplet corresponding to a doubling of frequency:

$$k_1/k_{x1} = k_2/k_{x2} = 2;\ k_{z1} = -k_{z2};\ \mathbf{k}_{x1} = \mathbf{k}_{x2} = \mathbf{k}_3/2. \quad (7)$$

Wave vectors lie in the same vertical plane xz and wave k_3 propagates horizontally along ox axis. Vectors $\mathbf{k}_1$ and $\mathbf{k}_2$form an angle with the vertical equal to $\pm\pi/6$.

It will be convenient to exclude all variables in the left part of the equation (4) except the linear terms of vertical velocity *W*. Then we get one equation. The 'prime is omitted for brevity leaving only the main members on the parameter $(k\cdot H)^{-1} << 1$:

$$\left[\widehat{D}^2\cdot\Delta + N^2\frac{\partial^2}{\partial x^2}\right]W =$$

$$= e^{z/2H}\left\{\left(u\frac{\partial}{\partial x}+W\frac{\partial}{\partial z}\right)\left[\frac{\partial^2}{\partial x^2}\left(\mathrm{g}R-\widehat{D}W\right)-\widehat{D}\frac{\partial^2}{\partial x\partial z}u\right]-\widehat{D}\frac{\partial^2}{\partial x\partial z}R\frac{\partial P}{\partial x}\right\}+$$

$$+e^{z/2H}\widehat{D}\frac{\partial^2}{\partial x^2}\left[\left(1-R\cdot e^{\frac{z}{2H}}\right)\left(\mathrm{g}R^2+R\frac{\partial P}{\partial z}\right)\right] \quad (8)$$

Let us analyze (8) in form of wave triplet with slowly changing complex amplitudes $W_j(t,x,z)$

$$W(t,x,z)=\frac{1}{2}\sum_{j=1}^{3}\left[W_j(t,x,z)\cdot\exp\left(-i\omega_j t+i\mathbf{k}_j\mathbf{r}\right)+\text{k. c.}\right]$$

Further we apply the standard asymptotic methods of weak turbulence to equation (8) and we get the system of truncated equations for slowly changing amplitudes of wave triplet (7) taking into account cube members:

$$\left[\frac{\partial}{\partial t}+U\frac{\partial}{\partial x}\right]W_3 =$$

$$=\frac{5}{4H}\cdot e^{\frac{z}{2H}}W_1\cdot W_2-\frac{3i}{8NH^2}\cdot e^{\frac{z}{H}}W_3(4|W_1|^2+4|W_2|^2+|W_3|^2),$$

$$\left[\frac{\partial}{\partial t}+\left(U+\frac{3N}{8k_{x1}}\right)\frac{\partial}{\partial x}-\frac{\sqrt{3}N}{8k_{x1}}\frac{\partial}{\partial z}\right]W_1 =$$

$$=-\frac{5}{32H}e^{z/2H}W_3W_2^*-\frac{3i}{32NH^2}e^{z/H}W_1(2|W_1|^2+4|W_2|^2+3|W_3|^2), \quad (9)$$

$$\left[\frac{\partial}{\partial t}+\left(U+\frac{3N}{8k_{x1}}\right)\frac{\partial}{\partial x}-\frac{\sqrt{3}N}{8k_{x1}}\frac{\partial}{\partial z}\right]W_2 =$$

$$=-\frac{5}{32H}e^{z/2H}W_3W_1^*-\frac{3i}{32NH^2}e^{z/H}W_2(2|W_2|^2+4|W_1|^2+3|W_3|^2),$$

We will analyze the presence of stationary decisions of this system. It means time derivatives are equal to zero ($\frac{\partial}{\partial t}=0$). For simplicity we will be limited to research of decisions homogeneous along a vertical axis, supposing z << H and casting aside z derivatives in the left part of equations. Thus the system looks like investigational in a monograph [5]. We express complex amplitudes through actual values (module a_j and phase φ_j). Then system (9) goes to (10):

$$a_3^{'}=\mathrm{v}_{12}\cdot a_1\cdot a_2\cdot cos\Phi,\Phi\equiv\varphi_3-\varphi_1-\varphi_2,\mathrm{v}_{12}\equiv\frac{5}{4HU}$$

$$a_1^{'}=\mathrm{v}_{23}\cdot a_3\cdot a_2\cdot cos\Phi,G\equiv U+\frac{3N}{8k_{x1}},$$

$$a_2^{'}=\mathrm{v}_{13}\cdot a_3\cdot a_1\cdot cos\Phi,\mathrm{v}_{23}=\mathrm{v}_{13}\equiv-\frac{5}{32HG}, \quad (10)$$

$$\Phi^{'}=-\delta k-\left[\mathrm{v}_{12}\frac{a_1\cdot a_2}{a_3}+\mathrm{v}_{23}\frac{a_2\cdot a_3}{a_2}\right]\cdot sin\Phi,$$

$$\delta k=-(\beta_1a_1^2+\beta_2a_2^2+\beta_3a_3^2)$$

where the 'prime denotes the derivative function of the coordinate x. Additional marks are entered as:

$$\beta_1 = \beta_2 \equiv -\frac{9}{16N\cdot H^2 G}\left(1-\frac{8G}{3U}\right), \beta_3 \equiv -\frac{9}{16N\cdot H^2 G}\left(1-\frac{2G}{3U}\right) \quad (11)$$

Values in the formula (11) determine the contribution of cube elements into the decision. It is easy to check, that the followings integrals are fulfilled from (10):

$$\frac{a_1^2}{v_{23}} - \frac{a_2^2}{v_{13}} = M_{12}, v_{13} = v_{23},$$
$$\frac{a_3^2}{v_{12}} - \frac{a_1^2}{v_{23}} = M_{31}, \quad (12)$$
$$a_1 a_2 a_3 sin\Phi + \frac{1}{4}\left[\frac{\beta_1}{v_{23}} a_1^4 + \frac{\beta_2}{v_{13}} a_2^4 + \frac{\beta_3}{v_{12}} a_3^4\right] = \Gamma,$$

where right parts of the equations are constants of the integration. Coefficients, included in the first two expressions can change signs, for example, at the change of direction of wind ($U>0 \Rightarrow U<0$). It changes sense of second from these integrals drastically. The sum of intensities is saved if $\nu_{12v}\cdot\nu_{23}<0$, and in opposite case $\nu_{12v}\cdot\nu_{23}>0$ the difference of intensities of waves is saved. This leads to simultaneous growth of intensities of waves. Then we will consider an event, when following conditions are fulfilled:

$$\mathrm{U} < 0, G \equiv U + \frac{3N}{8k_{x1}} = \frac{3N}{8k_{x1}} - |U| > 0, \quad (13)$$

when group velocities of waves have opposite directions. We will examine exactly this case (13).

Putting $M_{12} = M_{31} = \Gamma = 0$ we received from formula (12):

$$a(x) = a_3(x), a_1(x) = a_2(x) = a(x)\cdot\left|\frac{v_{23}}{v_{12}}\right|^{0.5}$$
$$sin\Phi = -\frac{1}{4}\left[2\frac{\beta_1}{v_{12}} + \frac{\beta_3}{v_{23}}\right]a, \quad (14)$$
$$a' = \pm\chi a^2\cdot\sqrt{1-\gamma^2 a^2}, \gamma = \frac{1}{4}\left|2\frac{\beta_1}{v_{12}} + \frac{\beta_3}{v_{23}}\right|, \chi = \left|\frac{5}{32HG}\right|$$

The sign in expression can change at the appeal of root in a zero. It determines the utmost value of amplitude:

$$a_{max} = 1/\gamma = 4\left|\frac{2\beta_1}{v_{12}} + \frac{\beta_3}{v_{23}}\right|^{-1} \quad (15)$$

The decision of the equation system (14) is a solitary wave (a soliton) and can be written in a kind (see [5]):

$$a(x) = \frac{1}{\sqrt{\gamma^2+\chi^2(x-x_1)^2}} \quad (16)$$

Position of the soliton maximum $x_1 = \left(\chi a(0)\right)^{-1}\sqrt{1-\gamma^2 a^2(0)}$ is due to the magnitude of the "seed" amplitude.

Soliton width Δx is deviation from the point of maximum where amplitude in two times less than α_{max}:

$$\Delta x = \sqrt{3}\frac{\gamma}{\chi} = \frac{\sqrt{3}}{5} \cdot 32HG\gamma \quad (17)$$

We express the soliton characteristics through waves parameters. Using denotations τ we get:

$$\gamma = \frac{3}{40NH}(20 + 8 \cdot \tau + 3 \cdot \tau^{-1}), \tau \equiv \frac{G}{|U|} \equiv \frac{3N}{8k_{x1}|U|} - 1 \quad (18)$$

Magnitude γ has a minimum at $\tau = \tau_m = 3/8$. It means (18) that maximal soliton amplitude will be realized under to condition:

$$[k_{x1}|U|]_m = \frac{3}{11}N \quad (19)$$

Maximal amplitude and width of soliton, as follows from (15), (17) are formulas:

$$(a_{max})_m = 1/\gamma_{min} = \frac{40}{93}NH, (\Delta x)_m \approx 7.5 \cdot \frac{|U|}{N} \quad (20)$$

A more general solution to the system of equations (10) may be the periodic nonlinear wave periodic in the space. Such solutions include another important parameter such as a period. These aspects, as well as accounting of the vertical structure of the solution is planned to analyze further.

So, it was analyzed the resonance interaction of packets of internal gravity waves propagating in the isothermal atmosphere in the presence of the uniform horizontal wind.We found conditions of existence of stationary solution in the form of a solitary wave and determined its parameters.

Acknowledgments. *The work was founded in part by Russian Foundation for Basic Research under grants No 14-05-00565. The work of N. V. Bakhmetieva was supported by Russian Science Foundation under grant No 14-12-00556.*

1. N. V. Bakhmetieva, G. I. Grigoriev, and V. G. Lapin, *Radiophysics and Quantum Electronics*, 2014, 57(5), pp. 360—371.

2. N. V. Bakhmetieva, G. I. Grigoriev, and V. G. Lapin, XXIV[th] Russian Scientific Conference "Wave Propagation", Irkutsk, 2014, *Conference Proceedings*, 3, pp. 29—32.

3. K. B. Dysthe, C. Juren, and L. Stenflo, *Physica Scripta*, 1974, 9, pp. 226—228.

4. P. V. Dvoryakovsky, N. Petrukhin With., and S. M. Feinstein, *Physics of atmosphere and ocean*, 1976, 14(1), pp. 21—26.

5. X. Wilhelmson and J. Wayland, Coherent nonlinear interaction of waves in plasma, Moscow, Energoizdat, 1981, 223 p.

The Analysis of Methods of Determination the Scattering Parameter of the Inhomogeneous Fluctuating Ionospheric Screen

Sergey Yu. Belov[1], Iya N. Belova[2]

[1]M. V. Lomonosov Moscow State University, Physics Department, 1, Leninskie gory, GSP-1, 119991, Moscow, Russia
[2]A. M. Obukhov Institute of Atmospheric Physics, Russian Academy of Sciences, [3]Pyzhevsky Lane, 119017, Moscow, Russia

Introduction: A new method for estimating the parameter noncoherent signal/noise β_K of ionospheric signal is offered. A comparative analysis is carrying out. This new method exceeds an order of magnitude widely used standard one by analytical (relative) accuracy of determining a parameter β_K. It has the same order as the well-known coherent methodology.

Parameter of returned partially scattered ionospheric signal β_K is of interest to an important characteristic of the "perturbation" and "turbidity" of statistically inhomogeneous ionospheric plasma and to the work index of reliability of ionospheric communication channels including diagnostic one. Prompt and reliable estimate of the parameter β_K is of interest to radio physics, geophysics, and optics. Specification for ionospheric case is implemented. This range allows us to diagnose sub-surface layer of the earth because scattering parameter is formed by inhomogeneities dielectric permittivity of the subsurface structures.

The problem of measuring and accounting of scattering power of the earth's surface in the short-range radio waves is inportant for solving such challenges as diagnostic properties of the environment by means of methods that use this radio band, when in the channel there is an intermediate reflection (scattering) of the earth's surface, which is of interest for exploration and environmental studies.

Selection of the working sensing range and the impact of environment on the passing radiation are an important issues for using space-based tools, for environmental management and environmental monitoring.

The most important aspects of using space-based tools for environmental management and environmental monitoring are the choice of the operating range and probing questions about the influence of media on the passing radiation [1]. The problem of this discussion is the "rough" remote diagnostics of the earth's surface and subsurface of the dielectric structures in the SW range [2]. Selection of SW range takes into account the subsurface layer (thickness of the order of the wavelength of the incident signal). Interpretation of the data is based on a statistical multiplicative model of the signal [3]. Testing the method of obtaining a signal/noise ratio in this model was produced by the example of a double reflection of the probe signal from the SW ionosphere in a vertical sounding (remember that when using a satellite, the signal passes twice through the atmosphere and iono-

sphere). The work addressed issues of sensitivity of the model parameters that were studied.

The measurement, mapping, and computation of the "rough" Earth Surface Scattering Power (ESSP) in the SW range are of interest for a set of problems (communication, geology, etc.). The ESSP parameter is the signal/noise ratio of the β_K waves reflected from the earth's "rough" backing. There is the back of the β_K-data and measuring method is in SW range. [4] presents the experimental method of β_K determination.

In this paper, this method is tested on the parameter of β_K sensitivity. According to the statistical model (SM), a database ("records" for the numerical experiment) adequate to the real conditions was created. The properties of the "rough" earth area were defined by the theoretical β_K value. Based on the method of [5], β_K (numerical experiment) was determined. Then, the arrays of the β_K and $\beta_K{}^t$ were compared and analyzed. In this paper, the admissible sensitivity and stability of the method [6] were justified. The comparative analysis of the real experimental data and adequate numerical ones were fulfilled. As a result, the plausibility of the ionosphere echo statistical structures used were justified [7].

In this paper, we propose a new method for estimating the parameters of noncoherent signal/noise ratio β_K ionospheric echo [8]. A comparative analysis shows that the analytical (relative) accuracy of the determination of the parameter β_K using the new method exceeds the widely-used standard, and the same order of known coherent methodology [9].

The paper presents the results of comparison of the measurement method from the point of view of their admissible relative analytical errors. The new method is suggested.

Calculation methods: Narrowband random process E(t) in fixed point of reception in the ground in scalar approximation is the superposition of mirror $E_0(t)$ and scattered $E_P(t)$ components distributed by the normal law:

$$\begin{aligned} \mathsf{E}(t) &= \mathsf{E}_0(t) + \mathsf{E}_\Gamma(t) = E_{00} \cdot e^{i\cdot(\omega_0 \cdot t - \varphi(t))} + \mathsf{E}_\Gamma(t) = \\ &= R(t) \cdot e^{i\cdot(\omega_0 \cdot t - \Phi(t))} = \left[E_C(t) + i \cdot E_S(t)\right] \cdot e^{i\cdot\omega_0 \cdot t}, \end{aligned} \tag{1}$$

where $\varphi(t)$, $\Phi(t)$, $R(t)$, $E_m(t)$, m = c,s — shown to slow random processes on the period $T = \dfrac{2\cdot\pi}{\omega_0}$; E_{00} = Const.

Scattering parameter is the ratio:

$$\beta_k^2 = \frac{\text{power mirror components}}{\text{scattered power components}} = \frac{E_{00}^2}{2\cdot \mathsf{E}_\Gamma^2}. \tag{2}$$

Here and below, " — " means statistical averaging. $E_C(t) = R(t)\cdot\cos\Phi(t)$ and $E_S(t) = R(t)\cdot\sin\Phi(t)$ are low-frequency quadrature of the ionospheric signal, R(t) is envelope, $\Phi(t)$ is total phase.

The subscript k = E4, R2, R4 means experimentally recorded primary random processes and appropriate method of their registration: E4 — coherent; R2, R4 — noncoherent amplitude. Index k indicates the primary parameter recorded: E — quadrature, R — envelope of the ionospheric signal.

Standart noncoherent R2-method based on the relationship (3) is widely used for estimating β_K (2) [1]:

$$\frac{\overline{R^2}}{\left(\overline{R}\right)^2} = f\left(\beta_{R2}\right) = \frac{4}{\pi}\cdot\frac{\left(1+\beta_{R2}^2\right)\cdot\exp\left(\beta_{R2}^2\right)}{\left[\left(1+\beta_{R2}^2\right)\cdot I_0\left(\beta_{R2}^2/2\right)+\beta_{R2}^2\cdot I_1\left(\beta_{R2}^2/2\right)\right]^2}. \qquad (3)$$

$I_n(x)$ is Bessel function of n^{th} order of a purely imaginary argument.

Using coherent E4-method and estimating β_{E4} by γ_{E4} kurtosis of quadrature [2, 3]:

$$\gamma_{E4}\left(\beta_{E4}\right) = \frac{\overline{E_m^4}}{\left(\overline{E_m^2}\right)^2} - 3 = -\frac{3}{2}\cdot\frac{\beta_{E4}^4}{\left(1+\beta_{E4}^2\right)^2}; \quad m = c,s. \qquad (4)$$

It should be noted that measured primary parameters are the ratio of moments $\overline{R^2}/\left(\overline{R}\right)^2$, $\overline{E_m^4}/\left(\overline{E_m^2}\right)^2$ respectively. Relations (3), (4) are obtained by taking into account the specific models of structure of the ionospheric signal.

Probabilistic properties of the ionospheric signal (1) of the first multiplicity response is well described by Rice model with a displaced spectrum (RS-model) [4—6]. Expressions (3) and (4) are obtained based on Rice model with a displaced spectrum.

A priori expression (4) of coherent method E4 contributes an order of magnitude higher relative analytical accuracy of the estimation of parameter β_K [7—9].

In this paper, we propose new noncoherent R4-method of determination β_{R4} by γ_{R4} kurtosis of envelope for RS-model [2]:

$$\left(\gamma_{R4}(\beta_{R4}) = \frac{\overline{R^4}}{\left(\overline{R^2}\right)^2} - 3 = \gamma_{R4}(\beta_{R4}) = -1 - \frac{\beta_{R4}^4}{\left(1+\beta_{R4}^2\right)^2}\right) \qquad (5)$$

For compare the given methods in the sense of relative errors permitted in calculating β_K resulting view of functional dependencies $f(\beta)$, $\gamma_{E4}(\beta)$ and $\gamma_{R4}(\beta)$, we obtain expressions (6):

$$\varepsilon_k = \left|\frac{\Delta\beta_K}{\beta_K}\right| = \left|\frac{1}{\beta_K}\cdot\frac{dG_K}{dZ_K}\cdot\Delta\left(Z_K\right)\right|, \qquad (6)$$

whereK = R2, E4, R4; GK = f, γ_{E4}, γ_{R4};$\Delta(Z_K)$— absolute statistical errors of measured values: $Z_K = \frac{\overline{R^2}}{\left(\overline{R}\right)^2}, \frac{\overline{E_m^4}}{\left(\overline{E_m^2}\right)^2}, \frac{\overline{R^4}}{\left(\overline{R^2}\right)^2}$.

Measures of inaccuracy including statistics for the different techniques of determination β_K are:

$$\mathcal{E}_{R2}(\beta)=\frac{\pi}{8}\cdot\frac{\left[\left(1+\beta^2\right)\cdot \mathrm{I}_0\left(\beta^2/2\right)+\beta^2\cdot \mathrm{I}_1\left(\beta^2/2\right)\right]^3}{\beta^2\cdot\exp\left(\beta^2\right)\cdot \mathrm{I}_1\left(\beta^2/2\right)}\cdot\Delta\left(Z_{R2}\right); \quad (7а)$$

$$\mathcal{E}_{E4}(\beta)=\frac{\left(1+\beta^2\right)^3}{6\cdot\beta^4}\cdot\Delta\left(Z_{E4}\right); \quad (7б)$$

$$\mathcal{E}_{R4}(\beta)=\frac{\left(1+\beta^2\right)^3}{4\cdot\beta^4}\cdot\Delta\left(Z_{R4}\right)\cdot \quad (7в)$$

Statistical error $\Delta(Z_K)$ depends on the sample volume N. It may be different at identical sample volume for each of the methods. We normalize (7) on $\Delta(Z_K)$ for focusing on the errors due to differences in functional dependencies (3) — (5).

Dependency Graphs $\mathcal{E}_K^*=\dfrac{\mathcal{E}_K}{\Delta(Z_K)}$ for β_{R2}, β_{E4} and β_{R4} are shown in Fig. 1. $\mathcal{E}_K^*$ will be called analytic (relative) error method.

Experimental distribution $W_Э(\beta)$ determines the range of variation of β. From equation (4) and (5) we conclude that $\mathcal{E}_{E4}^*=\dfrac{2}{3}\cdot\mathcal{E}_{R4}^*$ have the same order and significantly (by order) exceed measurement accuracy of standard R2-method [10, 11].

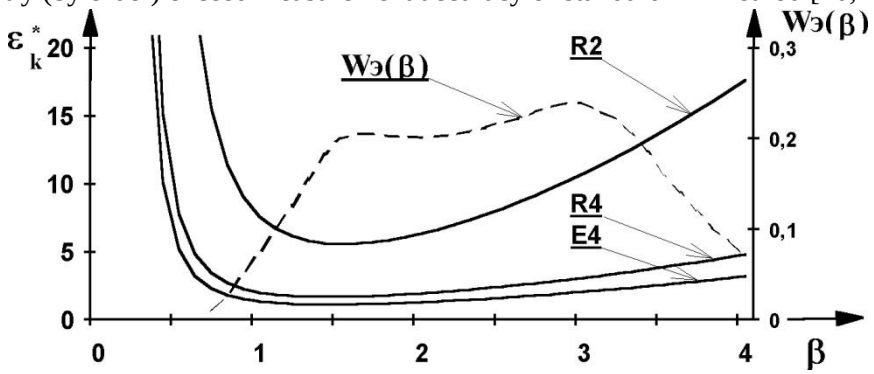

FIGURE 1. Dependency Graphs $\mathcal{E}_K^*$, K = R2, R4, E4 (solid curves) and the experimental distribution $W_Э(\beta)$ (dashed curve) (F2-layer, 4,5—9,5 MHz, single signal).

Analysis of analytical error of estimation of the parameter β_K allowed to recommend R4-method instead of standard R2-method. Sufficiently high analytical (relative) accuracy of parameter estimation β_K can be achieved using noncoherent apparatus using (5) of R4-method. Naturally, the ability to optimize the statistical error by the relevant special digital processing of ionospheric signal is keep on coherent methodology E4.

Conclusion: The comparative analysis of the normalized relative analytical errors $\mathcal{E}_K^*$ of the known methods and the new one was performed [12]. It was shown that errors $\mathcal{E}_E^*$ and $\mathcal{E}_{R4}^*$ have the same order, and both errors significantly exceed the

error $\mathcal{E}_{R2}^{*}$ in comparison with the standard R2-method by a measurement accuracy of β_K [13].

As a result, it was found that sufficient β_K analytical measurement accuracy can be achieved when using an noncoherent apparatus using a new R4-method. But the coherent E-method reserves the possibility of statistical error optimization with a special processing of the ionospheric signal [14].

1. Ya. L. Alpert. Rasprostranenie radiovoln v ionosfere, Moscow, 1960, 480 p.
2. S. Yu. Belov, Parameter assessment methods signal/noise in the SW range of radio waves, *Ekologicheskaya fizika*, 2010, 16, pp. 31—38.
3. S. Yu. Belov, Numerical simulation test in the problem of remote diagnostics scattering power of the earth's surface in the SW range, *Proceedings of the International Youth Scientific Forum "Lomonosov-2015"*, 2015.
4. S. Yu. Belov, On the methods of determining the parameters of the signal/noise ratio at the example of propagation of radio channel Earth—Ionosphere, *Proceedings of theInternational Youth Scientific Forum "Lomonosov-2013"*, 2013, 73 p.
5. S. Yu. Belov and I. N. Belova, Identification of environmental risk in monitoring land surface remote sensing in the SW range, *Proceedings of the II All-Russia Scientific Conference "Ecology and Space" Academician* K.Y. Kondratyev, Y. Kuleshov (ed.). Saint-Petersburg: WCA name Mozhaiskii, 2015, pp. 70—76.
6. S. Yu. Belov and I. N. Belova, On the signal/noise ratio of the measurement method of the inhomogeneous fluctuating diffraction screen, *International Symposium «Atmospheric Radiation and Dynamics» (ISARD-2015)*, Saint-Petersburg, 2015, 104 p.
7. S. Yu. Belov, The distant diagnostics of the Earth Surface Scattering Power in the SW range, *Prospects of Development of Scientific Research in the 21st Century: Proceedings of the 6th International Scientific and Practical Conference*, Makhachkala, 2014, 43 p.
8. S. Yu. Belov, New measurement method of estimation signal/noise parameter. European Geosciences Union General Assembly 2010 Vienna, Austria, *Geophysical Research Abstracts*, 2010, 12, 2233 p.
9. S. Yu. Belov, The distant diagnostics of the Earth Surface Scattering Power in the decameter radio waves, *Physics of Atmosphere*, Tomsk, 2009, pp. 279—280.
10. S. Yu. Belov and I. N. Belova, Functional diagram of the experimental apparatus coherent reception in the tasks of monitoring land surface remote sensing in the short-range radio waves, *III International scientific-practical conference "Applied aspects of geology, geophysics and geo-ecology, using modern information technology"*, Maikop, 2015, pp. 53—58.
11. S. Yu. Belov and I. N. Belova, Monitoring of the Earth's surface by method of remote sensing in SW range, *V International Youth Scientific Conference "Ecology-2015"*, Arkhangelsk, 2015, pp. 6—7.
12. S. Yu. Belov, On some characteristics of the scattering of the earth surface for remote sensing in the short-wave band, *II International Conference «Regional problems of remote sensing of the Earth*, Krasnoyarsk, 2015, pp. 101—104.
13. S. Yu. Belov, About a possibility of increasing the accuracy of measurements of the Earth's surface scattering ability at remote sensing in the short-wave range of radio waves, *24th Scientific Conference "The structure of the substance, the history of the lithosphere Timan-Severouralsk segment"*, Syktyvkar, Geoprint, 2015, pp. 28—31.
14. S. Yu. Belov and I. N. Belova, Environmental aspects of the use of remote sensing of the earth's surface in the short-wave range of radio waves, *IGCP 610 Third Plenary Conference and Field Trip "From the Caspian to Mediterranean: Environmental Change and Human Response during the Quaternary",* Astrakhan, 2015, pp. 29—31.

The Mathematical Description of the Ne Profile in the E-region of the Ionosphere

Yurij N. Korenkov[1], Fedor S. Bessarab[1,2],and Pavel A. Vasiliev[2]

[1]Kaliningrad Department of IZMIRAN, Pobedy av. 41, Kaliningrad, Russia
[2]Immanuel Kant Baltic Federal University, Nevskogo st. 14, Kaliningrad, Russia

The study and the mathematical description of E, F1 ionospheric layers (80—140 km altitude) is carried out for decades. The first quantitative theory of the formation of the ionospheric layers was developed by Chapman [1]. His study is still used as the basis for quantitative estimates and an illustration of the physical processes. Chapman theory has significant limitations, since it allows to count only the concentration of Ne, without a detailed description of the ionic composition. However, in many cases, knowledge of the ion composition in the specified area is redundant, for example: calculating of propagation paths and absorption radiowave, ionosonde data interpretation, etc.

The traditional approach to describe the vertical profile Ne in E-region of the ionosphere looks as follows [2]. It is believed that the main ions are $O_2^+$and NO^+, concentrations of $O^+$and $N_2^+$are several times less. When describing the behavior of major ions, diffusion and transport processes are neglected, and for the ions O + and N2 + are used photochemical equilibrium condition. Then the system of equations for the ion concentrations in the E region of the ionosphere can be written as:

$$\begin{aligned} \frac{dn_1}{dt} &= Q_1 - l_1 n_1, \\ \frac{dn_2}{dt} &= Q_2 - l_2 n_2, \\ n_3 &= Q_3/l_3 \\ n_4 &= Q_4/l_4 \end{aligned} \qquad (1)$$

Here, the index value i corresponds ions O_2^+, NO^+, N_2^+, O^+ in ascending order, Q_i are formation rates of i ions considering photoinization and chemical reactions, and l_i. are losses.

TABLE 1. The list of chemical reactions.

1	$O_2^+ + e \rightarrow O + O$	6	$O^+ + O_2 \rightarrow O_2^+ + O$
2	$O_2^+ + NO \rightarrow NO^+ + O_2$	7	$O^+ + N_2 \rightarrow NO^+ + N$
3	$O_2^+ + N \rightarrow NO^+ + O$	8	$N_2^+ + O \rightarrow NO^+ + N$
4	$O_2^+ + N_2 \rightarrow NO^+ + NO$	9	$N_2^+ + O_2 \rightarrow O_2^+ + N_2$
5	$NO^+ + e \rightarrow N + O$	10	$N_2^+ + e \rightarrow N + N$

As we have said, it is sufficient to know only the concentration Ne in many cases, without specifying the ionic composition in the altitude ~ 100—130 km [3]. In this case, the following method is used. The equations for the major ions are recorded in the form of:

$$\frac{d[O_2^+]}{dt} = q(O_2^+) + \lambda_6[O^+][O_2] + \lambda_9[N_2^+][O_2] - (\lambda_2[NO] + \lambda_3[N] - \lambda_1[O_2^+])[N_e],$$

$$\frac{d[NO^+]}{dt} = q(NO^+) + \lambda_7[O^+][N_2] + \lambda_8[N_2^+][O] + (\lambda_2[NO] - \lambda_5[NO^+])[Ne] \quad (2)$$

In this equation $N_e = \sum_i n_i$ where i is the number of the ion, and $q(O_2^+)$ and $q(NO^+)$ are the rates of ionizations. To calculate the *Ne* concentration system (2) may be simplified by summing the first two equations. Neglecting the contribution of ions N_2^+ and O^+ in *Ne* of the concentrations, we obtain an equation of the form:

$$\frac{dNe}{dt} = \sum_i q_i - \alpha Ne^2. \quad (3)$$

Where α = α = $\lambda_1[O_2^+] + \lambda_5[NO^+])/Ne$, and $\sum_i q_i$ is the total function of ionizationtion. If we neglect the αef dependence on ion concentrations, instead of (2) we get a simplified equation of the type (3) for Ne concentration modeling in the altitude of E and F1 region of the ionosphere.

Applying αef instead α is difficult to substantiate because αef will depend on the ratio of major ions and therefore will be determine the electron density in the E region of the ionosphere. In addition, the system (1) from a mathematical point of view, should be reduced to a single second-order equation. Note that the ratio of O_2^+ /N_2^+ is largely determined by the distribution of a minor neutral component NO, which in this formulation of the problem is an input parameter.

The paper presents the equation for Ne concentration in E-region in the correct mathematical form, ie, second-order equation in time for Ne.

Let's introduce the notation $M^+ = [O_2^+] + [NO^+], n_{34} = n_3 + n_4$ and then sum up the system of equation (1):

$$\frac{dM^+}{dt} = Q_s - (\lambda_1 n_1 + \lambda_2 n_2)n_e,$$

where $Q_s = Q_1 + Q_2 = q_1 + (\lambda_9 n_3 + \lambda_3 n_4)[O_2] + q_2 + (\lambda_8 n_3[O] + \lambda_4 n_4)[N_2]$.

We differentiate the resulting equation on time, and given that λ_i weakly dependent on time and $(\alpha_1 n_1 + \alpha_2 n_2) = (Q_s - dM^+/dt)/n_e$, get a second order differential equation:

$$\frac{d^2M^+}{dt^2} = \frac{dQ_s}{dt} + \frac{dn_e}{dt}\left(\frac{1}{n_e}\frac{dM^+}{dt} - \frac{Q_s}{n_e}\right) - \left(\lambda_1\frac{dn_1}{dt} + \lambda_2\frac{dn_2}{dt}\right)n_e.$$

After simplification, the initial equation is converted into a non-linear first order ODE:

$$\left(mu + \frac{Q_s}{n_e} + (\lambda_1 + \lambda_2)n_e\right)\frac{dM^+}{dt} +$$

$$+\lambda_1\lambda_2\left[(M^+)^3 + \left(2n_{34} + \frac{\mu}{\lambda_1}\right)(M^+)^2 - \left(\frac{Q_1}{\lambda_1} + \frac{Q_2}{\lambda_1} - \left(n_{34} + \frac{\mu}{\lambda_1}\right)n_{34}\right)M^+\right] -$$

$$-\mu Q_s - \lambda_1\lambda_2\left(\frac{Q_1}{\lambda_1} + \frac{Q_2}{\lambda_2}\right)n_{34} - \frac{dQ_s}{dt} = 0.$$

1. S. Chapman, The absorption and dissociation or ionizing effect of monochromatic radiation in an atmosphere on a rotating, *Earth. Proc. Phys. Soc.*, 1931, pp. 26—45.

2. A. Nusinov, The deterministic model of middle-latitude and equatorial E-layer (description and characteristics comparatively accuracy), *Ionospheric Res.*, 1988, 44, pp. 94—99.

3. K. Davis, The radio waves in the ionosphere. Blaisdell Pub. Co., 1969, 460 p.

Research of Acoustic Gravity Waves Over Kaliningrad Region During the Solar Eclipse of March 20, 2015

Olga P. Borchevkina[1], Ivan V. Karpov[1,2], Alexsandra V. Ilminskaya[1], and Aleksey I. Karpov[1]

[1]Immanuel Kant Baltic Federal University, Kaliningrad, Russia
[2]KF IZMIRAN, Kaliningrad, Russia

The study of the complex of processes which implement connections of processes in various atmospheric layers is one of the most important tasks of atmosphere physics. Currently, significant development of experimental studies of the upper atmosphere has allowed to find the connection between the dynamic processes in the lower atmosphere and the parameters of large-scale irregularities of the upper atmosphere and ionosphere [1—4]. For example, the disturbance caused by the development of such phenomena in the lower atmosphere as tropical cyclones, stratospheric warming, seismic activity, etc. were revealed in the course of the ionosphere observations [5, 6]. However, the physical processes that implement such connections have not received an adequate explanation until now.

Currently, the interest of studying the propagation of acoustic-gravity waves (AGWs) and of internal gravity waves (GWs) is due to explain the conntctions between the dynamic processes in the upper and lower layers of the atmosphere.

The analysis of the detected ionospheric features that are caused by the lower atmosphere dynamics, for example, their spatial localization and rate of occurrence, can significantly reduce the range of atmospheric waves that may explain the observed ionospheric irregularities. The greatest interest in this case arouse the short scale GWs and infrasound waves that can propagate almost vertically [4, 7, 8].

To study the variation of the parameters of the lower atmosphere the methods of lidar souding with high information content and high spatio-temporal resolution are widely used. For example, the study of wave processes in the lower and middle atmosphere have revealed the presence of infrasonic waves and the AGWs and their gain during periods of meteorological disturbances [9, 10].

The methods for the analysis of navigation satellite signals, of which is determined ionospheric parameter TEC (Total Electron Content) widely are used in studies of spatial and temporal variations of ionospheric structure. The methods of research TEC variations to determine the characteristics of the wave processes were discussed in works [11—13].

Thus, the study of AGWs characteristics in different layers of the atmosphere and ionosphere will clarify the role of such waves in the implementation of the connection of the lower and upper atmospheric layers more accurately. The solar eclipse represents the special interest for the study of the processes of generation and propagation of AGWs in the atmosphere.

This work presents the results of the analysis of observations of the ionosphere parameters and of the lower thermosphere during the solar eclipse of 20 March 2015.

The results of the observations: The observations of variations in the lower atmosphere and ionosphere parameters were made in Kaliningrad (540 N, 200 E) in the period of solar eclipse 20.03.2015. The ionosphere studies are based on analysis of the TEC variations

The observations in the lower thermosphere were carried out by lidar sensing with the use of two-wavelength lidar LSA-2c produced by LLC «Obninsk photonics». These observations determined the time evolution of the intensity of lidar signal scattered in atmosphere. Partial solar eclipse in Kaliningrad began in 10h49m LT 20.03.2015 and ended at about 13h LT. During the observations, the time series of observations of the ionospheric TEC and the intensity of the scattered lidar signal in lower atmosphere were received.

For the analysis of the observed variations in the parameters the methods of harmonic analysis for determining the frequency ranges of variations that are typical for atmospheric and ionospheric disturbances caused by the solar eclipse at different altitudes were used.

The technique of data analysis, aimed at selection such disturbances is presented in the work [13]. It focuses on the study of the dynamics of AGWs and GWs with periods of 2—16 minutes. It is assumed that such AGWs may propagate to the heights of the upper atmosphere and ionosphere.

Observations of variations of the parameters of the lower atmosphere 20.03.2015 were carried out from 6:20 to 18:20 LT, they were started before sunrise and ended after sunset. The figure 1 shows the change in spectra variations of the scattered lidar signal in the course of observation. As the figure shows, in the lower atmosphere variations the area of variations is clearly seen.

It has periods of 3—5 minutes, which remain the lowest in comparison with the amplitude variations with shorter and longer periods. It is natural to assume that the upper boundary of this area corresponds to the period Brunt-Vaisala for internal gravity waves, and the lower boundary of the region corresponds to the period of the acoustic cutoff. Thus, lidar observations allow to highlight the acoustic (infrasound) and the gravitational branches of the variations in observations of the atmosphere. The similar changes of the TEC spectrs (Fig.1) appears during the passage of the solar terminator (7 h 42 m LT) for which there is observed a decrease in the amplitude variations that clearly expressed in the decrease in the amplitude infrasonic harmonics. Solar eclipse period is also shows a decrease in the amplitude of the infrasonic harmonics and a increasig of harmonic amplitudes with periods of internal gravity waves before the ending and after the eclipse. In general, the changes in the spectra of variations of the lower atmosphere during the eclipse are similar to the spectr observed during the passage of the solar terminator.

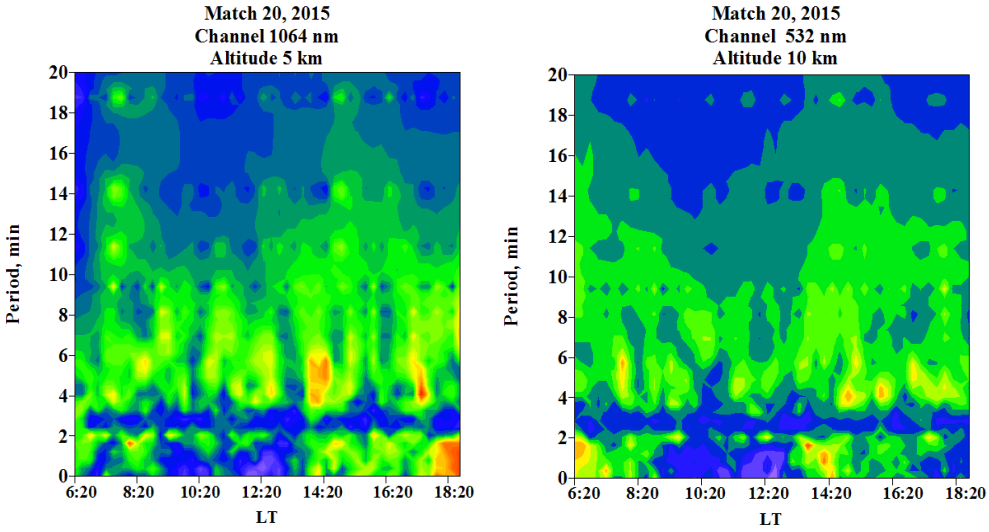

FIGURE 1. The dynamic range of changes the characteristics of the spectral variations during the observations

The time evolution of the spectrum of variations to the time derivative of the value of the TEC obtained in the observations of individual GPS satellites was considered for the analysis of the ionosphere structure variations. This procedure allows to emphasize the high-frequency components of variations of the TEC and to remove low-frequency contribution that determined by the change in position of the satellite in relation to the observation station. The variations in the structure of ionospheric TEC parameter during the solar eclipse, that were obtained from observations of the individual GPS satellite signals are shown in the Fig. 2. The method of study of the spectra of ionospheric variations is similar to the method

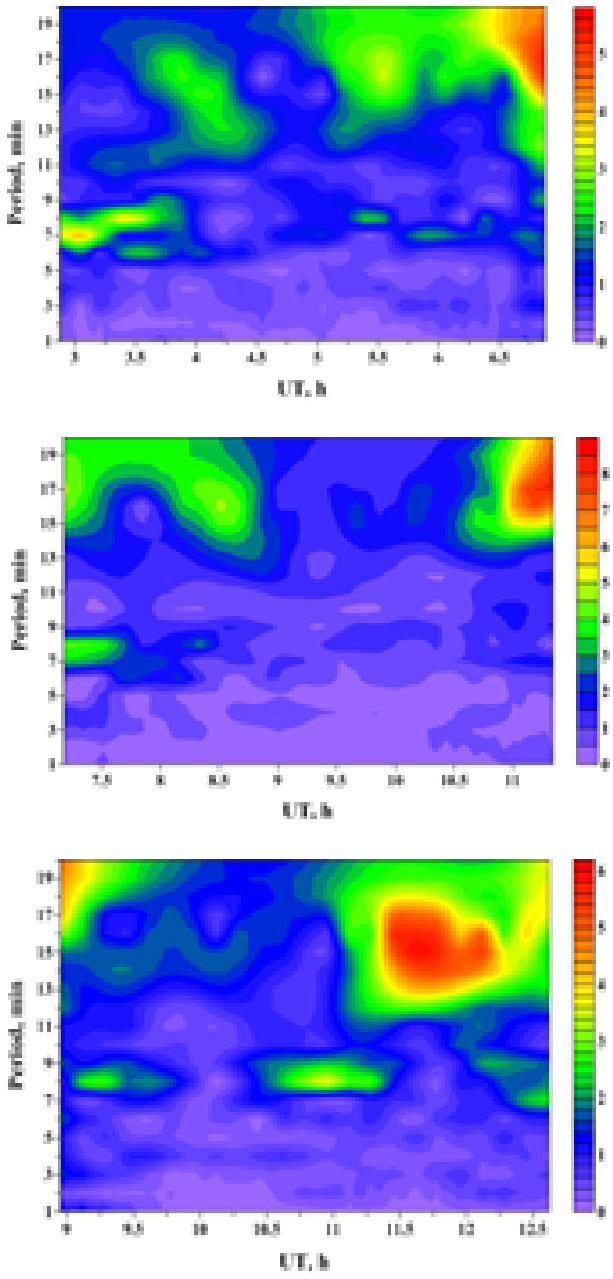

FIGURE 2. The dynamic spectrum of variations of TEC on Kaliningrad station 20 March 2015.

usedduring the analysis of parameter variations in the lower atmosphere and allows to determine the changes in the spectrum of variations during the observation. As

shown in Fig. 2a there is are growing harmonic amplitudes with periods of infrasonic waves (5—7 minutes) and periods of GWs (10—20 min) in the ionosphere during the passage of the solar terminator. In the Fig. 2b, 2c there is a clearly allocated time slot, during which there was a solar eclipse over Kaliningrad. As it can be seen from the figures, during the period of the eclipse there had been a rapid decrease in the amplitudes of the harmonics in the range 7—20 min throughout the analyzed time period. At the same time, in the final phase of the solar eclipse an increase in harmonics deposits with periods of 7—9 minutes before the end of the eclipse (10.5—11.0 UT h), and harmonics with periods of 13—17 min after the end of the eclipse (11—12 UT h) can be noted.

Thus, the results of analysis of observations of variations of TEC implemented along the flown individual satellites, reveal the increasing variation amplitude infrasonic and variations with periods close to the period of the Brunt-Vaisala during the passage of the solar terminator and the solar eclipse.

The analysis of the observation results revealed a number of features in the dynamics of the AGWs during the periods of solar eclipse. The lidar observations show that the main phase of the solar eclipse observed a decrease in the amplitude variations of the atmospheric parameters with periods of AGWs and GWs. At the end of the main phase of a solar eclipse there has been a sharp increase in the amplitude of variations with periods 2—10 min (Fig. 1). The ionospheric observations also noted a similar change in the dynamics of the spectral characteristics variations of TEC (Fig. 2). It is assumed that a change in the nature of the ionospheric variations is associated with the solar eclipse and the propagation of AGWs from the lower layers of the atmosphere.

Acknowledgments. *These investigations were performed with financial support by grant of the RFBR No. 15-05-01665 and State task Education and Science Ministry of the Russian Federation, the competitive part of the task No 3.1127.2014/K.*

1. K. Hocke and K. Schlegel, A review of atmospheric gravity waves and traveling ionospheric disturbances: 1982—1995, *Ann. Geophys*, 1996, 14, pp. 917—940.

2. S. H. Francis, Global propagation of atmospheric gravity waves, areview, *J. Atmos. Sol.-Terr. Phys.*, 1975, 37.

3. V. G. Galushko, V. V. Paznukhov, Y M. Yampolski, and J. C. Foster, Incoherent scatter radar observations of AGW/TID events generated by the moving solar terminator, *Ann. Geophys.*, 1998, 16, pp. 821—827.

4. D. C. Fritts and M. J. Alexander, Gravity wave dynamics and effects in the middle atmosphere, *Rev. Geophys.*, 2003, 41.

5. J. Laštovichka, Forcing of the ionosphere by waves from below, *J. Atmos. Sol.-Terr. Phys.*, 2006, 68.

6. V. P. Antonova, K. E. Dungenbaeva, S. V. Kryukov et al., Difference between the spectra of acoustic gravity waves in daytime and nighttime hours due to nonequilibrium effects in the atmosphere, *Geomagn. Aeron.*, 2006, 46.

7. J. Artru, T. Farges, and P. Lognonne, Acoustic waves generated from seismic surface waves: propagation propoties determinied from Doopler sounding observations and normal-mode modeling, *Geophys. J. Int.*, 2004, 158, pp. 1067—1077.

8. P. Sauli and J. Boska, Tropospheric events and possible related gravity wave activity effects on the ionosphere, *J. Atmos. Sol.—Terr. Phys.*, 2001, 63, pp. 945—950.

9. E. Blanc, T. Farges, A. Le Pichon, and P. Heinrich, Ten year observations of gravity waves from thunderstorms in Western Africa, *J. Geophys. Res.*, 2014, 119(11), pp. 6409—6418.

10. B. Ehard, P. Achtert, and J. Gumbel, Long-term lidar observations of wintertime gravity wave activity over northern Sweden, *Ann. Geophys*., 2014, 32, pp. 1395—1405.

11. E. L. Afraimovich and N. P. Perevalova, GPS monitoring of the Earth's upper atmosphere, SC RRS SB RAMS, Irkutsk, Russia, 2006, 480 p (in Russian).

12. A. S. Polyakova and N. P. Perevalova, Comparative analysis of TEC disturbances over tropical cyclone zones in the North-West Pacific Ocean, *Adv. Space Res.*, 2013, 52(8), pp. 1416—1426.

13. O. P. Suslova, I. V. Karpov, and A. V. Radievskii, Frequency characteristics of the troposphere and ionosphere variations in periods of solar terminator passage,*Russ. J. Phys. Chem. B*, 2013, 7(5), pp. 652—655.

Studing Ionospheric TEC with Signals of Geostationary Navigation and Augumentation Satellites

Gregory A. Kurbatov[1], Artem M. Padokhin[1], Yury V. Yasyukevich[2], and Natalia A. Berbeneva[1]

[1]Faculty of Physics, Lomonosov Moscow State University, Moscow, Russia
[2]Institute of Solar-Terrestrial Physics SB RAS, Irkutsk, Russia

During last two decades data from Global Navigational Satellite Systems (GNSS), such as GPS and GLONASS, are actively used in ionospheric studies. TEC estimations based on dual frequency phase and/or group measurements are the input data for Global Ionospharic Maps (GIM) as well as for 4D spatio-temporal ionospheric tomography procedures. Recently along with widely used GPS/GLONASS satellites there is a possibility to apply geostationary satellites of COMPASS/Beidou navigational system and geostationary satellites of Satellite Based Augumentation Systems (SBAS), such as GAGAN, WAAS and EGNOS, for ionospheric TEC estimations.

The main advantage of geostationary TEC observations compared to GPS/GLONASS is almost motionless ionospheric pierce point (IPP). It provides the possibility to analyze long-term continous data series for the selected "satellite-receiver" pair instead of rather short 2—6h records as for GPS/GLONASS.

Currently there are eleven (three WAAS — prn133, prn135, prn138; two GAGAN — prn127, prn128; one EGNOS — prn136; five COMPASS — C01, C02, C03,

C04, C05) geostationary satellites transmitting signals at pairs of coherent L-band frequencies, which can be used to estimate ionospheric TEC. The number of receiving sites capable to work with the majority of GNSS and SBAS satellites is also rapidly increasing. In common access in particular are the observations of the IGS MGEX network.

In this work we present the results of the comparison of the noise patterns in TEC estimations using signals of these geostationary systems. Fig. 1 (left) shows TEC estimations for the test day at MSU station. Upper pannel presents such estimations for satellites Beidou BDS5 and GAGAN GSAT-8, lower pannel — for satellites Beidou BDS2 and GAGAN GSAT-10 correspondingly. Note that "satellite-receiver" links and IPPs for these satellite pairs are very. Consequently, TEC variations for these satellites well reproduce each other. Fig. 1 (right) presents TEC noise for mentioned above satellites. It is clearly seen that for GAGAN satellites mean TEC noise is ~0.6TECU with maximum values reaching 1.5TECU, when at the same time for COMPASS/Beidou satellites at close elevation angles TEC noise is significantly smaller, with mean and maximum values ~ 0.06TECU and ~ 0.2TECU correspondingly, which is comparable to TEC noise for GPS/GLONASS observations at the same elevations. Note also the distinct diurnal variability in TEC noise for GAGAN satellites, which is mainly due to satellites themselfs. Fig. 2 shows TEC variations and TEC noise for MSU station and EGNOS SES-5 satellite (left) and for STFU station and WAAS Intelsat Galaxy 15 satellite (right) for the same test day. It is clearly seen that TEC noise for SES-5 satellite reaches up to 16TECU, which is not suitable for ionospheric studies. TEC noise for Intelsat Galaxy 15 satellite is ~0.7TECU with maximum up to 1.3TECU, which corresponds to those of GAGAN satellites obsereved at MSU station. Thus, TEC estimations based on geostationary COMPASS/Beidou satellites provide the best noise level among all geostationary GNSS and SBAS systems.

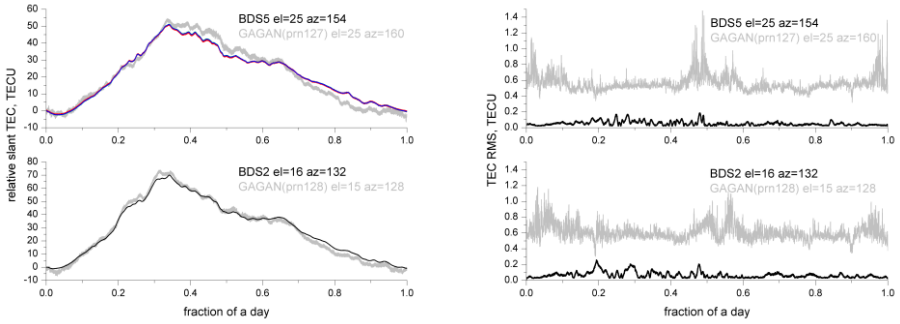

FIGURE 1.TEC variations and TEC noise at MSU station for GAGAN and COMPASS/Beidou satellites.

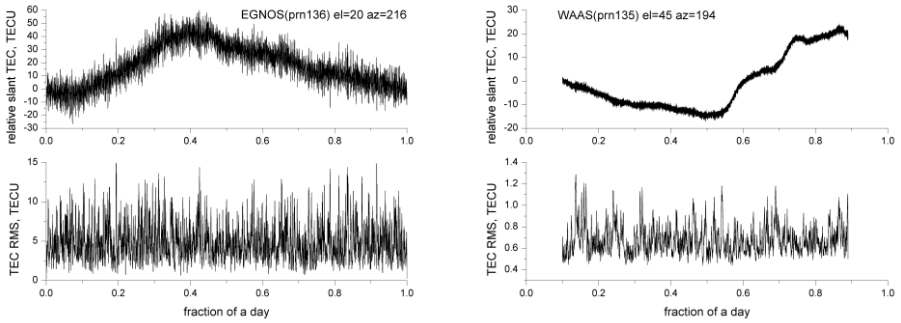

FIGURE 2. TEC variations and TEC noise at MSU station for EGNOS SES-5 satellite (left) and at STFU station for WAAS Intelsat Galaxy 15 satellite (right).

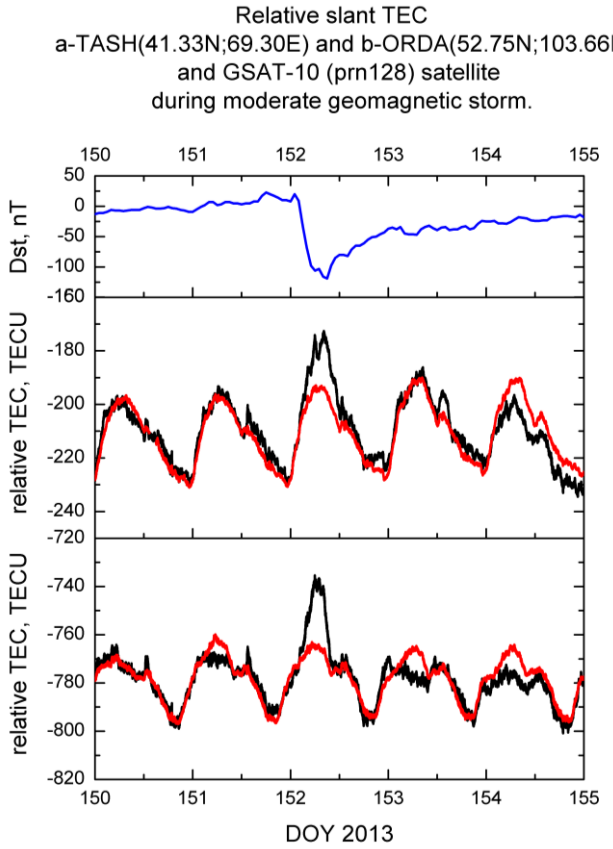

FIGURE 3. Dst index and relative slant SBAS TEC for GAGAN GSAT-10 satellite and ORDA and TASH receiving sites during moderate geomagnetic storm on June 1, 2013.

In this paper we also present some examples of using thus estimated geostationary TEC for the analysis of extreme heliogeophysical events, such as Solar flares and geomagnetic storms. First example we present here is SBAS TEC variations during moderate (Kp~6) geomagnetic storm on June 1, 2013 (see Fig. 3). The Dst index reached the value -119 nT indicating moderate disturbances in midlatitude and near equatorial geomagnetic field. SBAS TEC variations during storm main and start of the recovery phases obtained at two midlatitude stations TASH (Tashkent) and ORDA (Irkutsk) demonstrate strong positive anomaly up to 20—30 TECU compared to undisturbed 4-day mean values.

Finally let us demonstrate the capabilities of SBAS TEC observations in connection with ionospheric effects of Solar flares. Fig. 4 presents the example of processing the SBAS data recorded at MSU (Moscow) and ISTP (Irkutsk) stations during the X1.7-class flare on October 25, 2013. The maximum of the flare occurred at 8:01UT — at 12:01LT and 17:01LT at MSU and ISTP stations correspondingly. A sudden increase in TEC (SITEC) corresponding to variations in the X-ray and EUV radiation during the flare is observed at both stations: SITEC ~4 TECU within 10 min is observed at MSU station, SITEC at ISTP station is ~2.5TECU for prn 127 (GSAT-8) and less than 0.5TECU for prn 128 (GSAT-10) depending on the elevation angle of the Sun at the satellites ionospheric pierce points. The MSU station is in the noon sector while ISTP is in the evening one, so higher MSU TEC variations during this flare is what was expected.

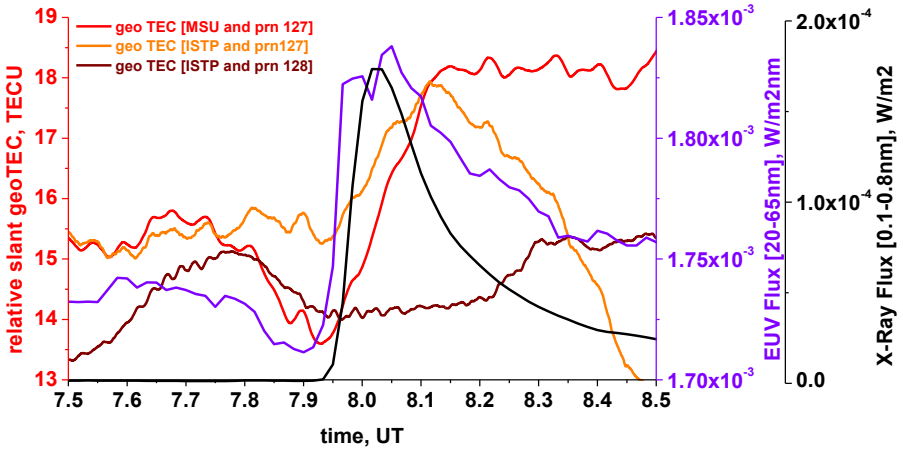

FIGURE 4.SBAS observation during X1.7-class Solar Flare on October 25, 2013

Our results show the capability of using dual-frequency coherent signals from geostationary SBAS and GNSS satellites for continuous monitoring of ionospheric TEC in quite and disturbed geomagnetic conditions. The main advantage of these observations is almost motionless IPP. At the same time, it is necessary to take into account greater level of noise compared to GPS/GLONASS in geostationary TEC

observations. The research conducted in present paper showed that it is preferably to use geostationary COMPASS/Beidou satellites.

Intensively growing number of receivers in multisystems networks and increasing number of dual (and more) frequency geostationary satellites in SBAS and GNSS constellations provide the opportunity in future to incorporate these types of measurements to ionospheric tomography and interferometry routines, if the noise level in geostationary TEC estimations will be reduced.

Acknowledgements. *Authors acknowledge financial support of Russian Scientific Foundation (project 14-17-00637).*

1. V. E. Kunitsyn et al., Investigation of SBAS L1/L5 signals and their application to the ionospheric TEC studies, *IEEE Geoscience and Remote Sensing Letters*, 2015, doi: 10.1109/LGRS.2014.2350037

2. V. E. Kunitsyn et al., Ionospheric TEC estimation with the signals of various geostationary navigational satellites, *GPS Solutions*, 2016, doi: 10.1007/s10291-015-0500-2.

Troposphere and Stratosphere Interacting at Sudden Stratospheric Warmings

Anna Y. Kanukhina, E. N. Savenkova, M. A. Motsakov, and A. I. Pogoreltsev

Russian State Hydrometeorological University,
ave. Malookhtinsky, 98, St. Petersburg, 195196, Russia

On the basis of UK Met Office analysis, we consider the dynamical processes in the stratosphere from the point of view of climate variability over the last decade and stratosphere-tropospheric coupling. Three-dimensional wave activity flux and its divergence were calculated to analyze the dynamical interaction between the stratosphere and the troposphere before, after and during the SSW. Relationship of convective tropospheric activity, planetary wave propagation and circulation processes in the troposphere and stratosphere were considered using the results of radio occultation observations of the COSMIC experiment. Variability of the dynamic regime of the stratosphere can affect the circulation of the troposphere, for example, through the reflection of planetary waves and their subsequent transformation in the troposphere into the regional-scale disturbances. Most strikingly stratosphere-tropospheric coupling occurs during the preparation and development of sudden stratospheric warming (SSW) events [1, 2]. The aim of this work is to study wave interaction between the troposphere and the stratosphere, first of all, during the preparation of the SSW events using the results of radio occultation observation

in the COSMIC/FORMOSAT-3 experiment [3, 4] and data assimilated in the UK Met Office model [5].

Almost all water vapor of the atmosphere is contained in the troposphere, and there are most part of the atmospheric clouds is formed. Convective processes generate a wave packets propagating to the upper latitudes, and then into the stratosphere. Estimation of the atmosphere stability is provided by calculating the value of convective indices. Such diagnostic parameters, which characterize readiness of the atmosphere to the development of convection, like static stability Γ [6], K-index and Total Totals index (TT) [7] were taken.

To investigate the wave interaction between the troposphere and the stratosphere was considered the period from 2007 to 2011. This is due to the fact that the data obtained by experiment COSMIC / FORMOSAT-3 became available to it since 2007 [3, 4]. The GPS (Global Positioning System) Occultation Experiment provides over 2500 atmospheric soundings every 24 hours around the globe. This is about twice the number of daily weather balloon observations (~ 1500 soundings from ~ 850 stations), which are concentrated mostly over land [8].We used files wetPrf which contain the results of the analysis of measurements COSMIC taking into account the presence of water vapor in the atmosphere in the form of vertical profiles relative to the average height above sea level. For a more complete analysis of selected indices (Γ, K, TT) calculations were done at regular intervals of 6 hours.

Estimation of tropospheric convection indices with a connection to SSW events is impossible without a preliminary analysis of stratospheric dynamics. Therefore, first of all, we consider the characteristics of the SSW for the selected period, as well as the distribution of the Elliassen-Palm flux (EP flux) [9] vertical component calculated from the UK Met Office data. Then stratospheric characteristics are compared with the large-scale inhomogeneities in the fields of convective indices.

Winters without expressed SSW events are very rare from 2007 to 2011 years. SSW events in the last decades are observed rather high, at 40—50 km. SSW events may develop due to two reasons: the gain of the wave activity from the lower atmosphere [10], which is accompanied by an increase of flow wave activity from the troposphere into the stratosphere, and due to internal dynamical processes, i. e. due to interaction of waves with mean flow on stratospheric heights [11, 12]. Thus, the relative roles of the different mechanisms of events are considered and in recent years the internal processes associated with nonlinear interaction of PW with mean flow begin to play a predominant role.

Below we present figures and analysis only for 2007 due to limited volume of the paper. Figure 1 shows the characteristics of the SSW occurring in the period from 22.02.2007 to 05.03.2007. The event of sudden stratospheric warming is not expressed clearly: it does not have a so-called "explosive" character but an increase in the SPW (m=1) amplitude and change in direction of general air transfer from the western to the eastern point it to the SSW event. Temperature increase is observed near 20—30 km levels. Strong variability of the zonal flow is not observed, the maximum amplitude of the PW1 constitute only 1750 m in the geopotential

height. Calculated longitude-latitude distribution of the vertical component of wave activity EP flux at an altitude of 20 km are shown in Fig. 2. This distribution corresponds to the time before the development of stratospheric warming, approximately two weeks prior to the SSW, the top figure. Prevailing direction of wave activity is from the troposphere to the stratosphere. Maximum upward EP flow is observed over the West Siberian Plain and the Central Siberian Plateau (longitudinal sector between 60 °E and 135 °E). However, a region of relatively strong updrafts covers almost the whole of Siberia and the Far East. At the same time static instability index Γ distribution (not presented in this paper) with its minimum values corresponding to an unstable atmosphere, covers roughly the same longitudinal sectors (from 30 ° E to 150 °E). Area of maximum convective instability according to Γ index is observed in the sector 110—130 °E both at 6UTC and 18 UTC. The convective instability area in the lower troposphere in the longitudinal sector is coinciding with the observed maximum of upward EP flux of wave activity (Fig.2).

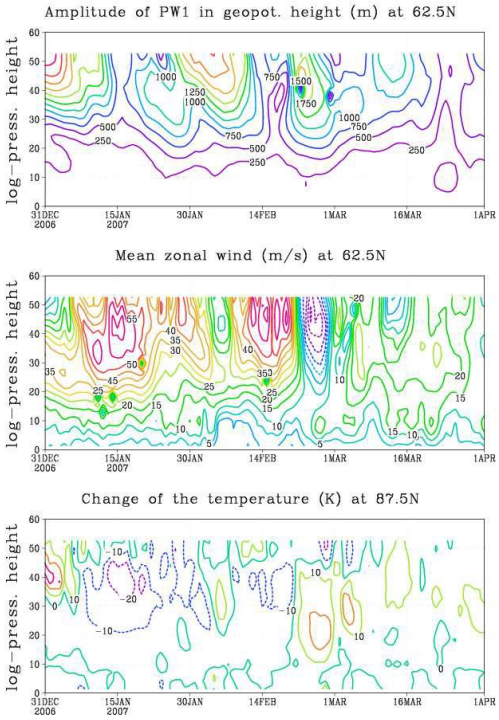

FIGURE 1.The time-altitude cross-sections of the amplitude of the zonal harmonic with m = 1 in the geopotential height and the mean zonal wind at latitude 62.5 N. The changes of the zonal mean temperature during December 2006 —March 2007 at latitude 87.5N are shown in the lower panel.

Areas of static instability according to index Γ correlate well with distribution of K-index values (Fig.3, top). Region of negative values of the static instability

overlay to area of high K-index values more then 35—40 meaning that up to 70 % of the territory is covered with thunderstorm cells. Figure 3, top K-value of the index is above 30 at longitudinal sectors of 30 °E to 150 ° E (upper panel) and from 120 °E to 180 °E (lower panel) with areas of high convective activity in the Western Hemisphere over the territory of the Atlantic, which is consistent with the location of the positive values of the vertical EP flux at an altitude of 20 km two weeks before the SSW in 2007. Similar longitudinal sector of convective instability are depicted with the values of the TT index (Fig. 4, top).

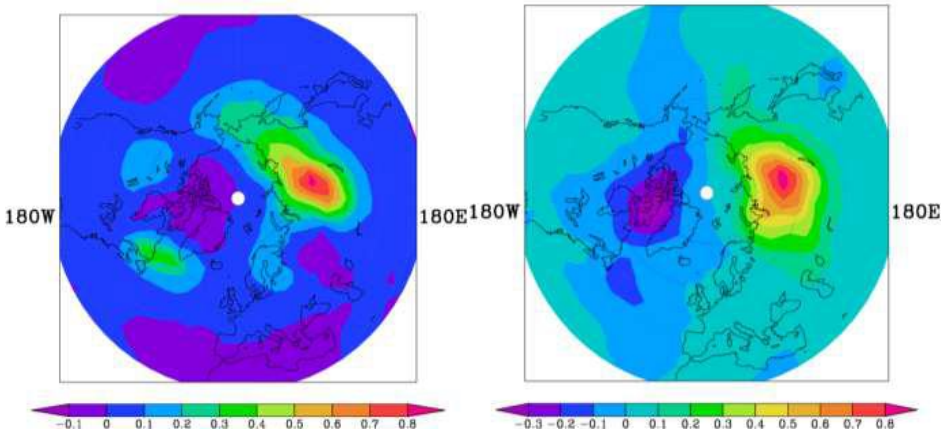

FIGURE2. The longitude-latitude distribution of the vertical wave activity flux at 20 km altitude of for two weeks before and two weeks after the SSW events in winter 2007.

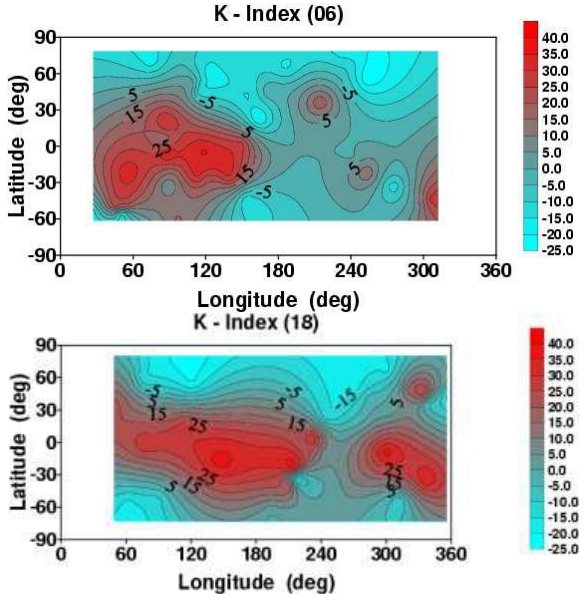

FIGURE3. The distribution of K -index two weeks before the events of the SSW (upper panel) and after the SSW (lower) in 2007.

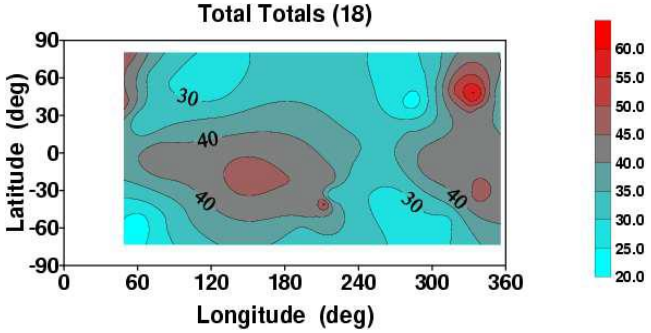

FIGURE 4. The distribution of TT-index two weeks before the events of the SSW in 2007.

The results of UK Met Office data analysis for the 2007—2011 years show that a marked increase of stationary PW activity in the troposphere immediately before the SSW events is actually observed, but not as often. It was also noted that most of the SSW observed in the maximum height of 40—50 km. Relatively "low" SSW (maximum heating of the polar region is observed at an altitude of about 30 km) were considerably less common. Significant warming of the stratosphere at altitudes of upper stratosphere 40—50 km is accompanied usually by weaker secondary SSW at altitudes of 30 km with a time delay of 1—2 weeks. Developments of the SSW in the upper atmosphere indicate the predominance of the internal mechanism, i. e. nonlinear interaction of SPW with the mean zonal flow. Analysis of the UK Met Office data shows that often SSWs happen at higher levels and at altitudes up to 30 km effect of SSW is negligible. Thus, it could be useful to consider SSW as "high" and "low" events too, the warmings, as a rule, also differ in the mechanism of occurrence and development. The first kind of events arises mainly due to the nonlinear interaction of planetary waves with the mean flow at the heights of the upper stratosphere, the second one is initiated mainly due to an increase of wave activity flux from the troposphere into the stratosphere.

Analysis of the convective instability indices distribution in the lower troposphere in January-March 2007—2011 two weeks prior to the first SSW event has shown that in certain longitudinal sectors in the tropics has been increasing wave activity flux from the troposphere into the stratosphere and the area coincide with the areas of tropospheric instability only for low SSWs.

Acknowledgements: *Research is supported by the Russian Foundation for Basic Research № 12-05-33071.*

1. J. R. Holton, The dynamics of sudden stratospheric warmings, *Annual Review, Earth and Planetary Science Letters*, 1980, 8, 169—190.

2. M. E. McIntyre, How well do we understand the dynamics of stratospheric warmings, *J. Meteorological Society of Japan*, 1982, 60, 37—64.

3. C. Rocken, Y.-H. Kuo, S. Sokolovskiy, and R. A. Anthes, The ROCSAT-3/COSMIC Mission and Applications of GPS Radio Occultation Data to Weather and Climate, in Remote Sensing Applications of the Global Positioning System, Edited by Michael Bevis, Yoshinori Shoji, Steven Businger, *Proceedings of SPIE*, 2004, (1—12).

4. R. A. Anthes, P. A. Bernhardt, Y. Chen et al., The COSMIC / FORMOSAT-3 Mission, Early results, *Bulletin of the American Meteorological Society*, 2008, 89, pp. 313—333.

5. R. Swinbank and A. O'Neill, A stratosphere-troposphere assimilation system, *Monthly Weather Review*, 1994, 122, pp. 686—702.

6. I. N. Rusin and G. G. Tarakanov, Very shortrange forecasting, St. Petersburg, RSHU, 1996, 308 p.

7. T. Andersson, M. Andersson, C. Jacobsson, and S. Nilsson, Thermodynamic indices for forecasting thunderstorms in southern Sweden, *Meteorological Magazine*, 1989, 116, pp. 141—146.

8. Chio-Zong, Frank Cheng et al., Satellite Constellation Monitors Global and Space Weather, American Geophysical Union, 2006, l.87(17).

9. R. Plumb, On the three-dimensional propagation of stationary waves, *J. Atmospheric Sciences*, 1985, 42, pp. 217—229.

10. T. Matsuno, A dynamical model of sudden stratospheric warming, *J. Atmospheric Sciences*, 1971, 28, pp. 871—883.

11. R. K. Scott and L. M. Polvani, Internal variability of the winter stratosphere, Part I: Time independent forcing, *J. Atmospheric Sciences*, 2006, 63, pp. 2758—2776.

12. A. I. Pogoreltsev, Generation of normal atmospheric modes by stratospheric vacillations, Izvestiya, *Atmospheric and Oceanic Physics*, 2007, 43, pp. 423—435.

Satellite Observation and Modeling of LongitudinalVariations in thelonosphere *F* Region, Topside Ionosphere, and Plasmasphere during December Solstice

Maxim V. Klimenko[1,2], Vladimir V. Klimenko[1], Alexander T. Karpachev[3], Irina E. Zakharenkova[1,4], Artem M. Vesnin[5], Iury V. Cherniak[6],Ivan A. Galkin[7], Nikolai V. Chirik[2], and Dmitriy V. Chugunin[8]

[1]West Department of Pushkov IZMIRAN, RAS, 236017, Kaliningrad, 41 Pobeda Av., Russia
[2]Immanuel Kant Baltic Federal University, 236041, Kaliningrad,14 A. Nevsky Str., Russia
[3]Pushkov IZMIRAN, RAS, 142190, Troitsk, Moscow Region, Russia
[4]Institut de Physique du Globe de Paris, 75005 Paris, France
[5]Institute of Solar-Terrestrial Physics, SB RAS, 664033, Irkutsk P/O Box 291, 126a Lermontov Str., Russia
[6]University of Warmia and Mazury, 10—719 Olsztyn, Poland
[7]UML Center for Atmospheric Research,University of Massachusetts Lowell, 01854 Lowell, MA, USA
[8]Space Research Institute, RAS, 117997, Moscow, 84/32 Profsoyuznaya Str, Russia

Plasma density distribution in the Earth's ionosphere-plasmasphere system plays the pivotal role in the trans-ionospheric radio waves propagation including the Global Navigation Satellite Systems performance. In order to model the iono-

spheric electron density we need to know the typical longitudinal variations at the quiet conditions. Usually for determination of the typical longitudinal variations of the ionospheric *F* region parameters at different latitudes it is necessary to average these observations from the available datasets. The obtained characteristics can be used as an input database for empirical ionospheric models like IRI [1]. Earlier it was believed that diurnal variations of the ionospheric parameters exceed significantly the longitudinal variations. However, the first satellite observations [2] disprove this. In this report we present the longitudinal variations in *foF*2, *TEC*, plasmaspheric and topside ionospheric electron density at summer and winter solstice conditions to estimate the main longitudinal peculiarity of the ionosphere-plasmasphere system. Regardless of the recent progress on the description of the morphology of the *foF*2 and *TEC* longitudinal structure, there remains lack of results comparing longitudinal variations of these parameters at different latitudinal regions. One of the first results was reported in [3] where the seasonal variations of the plasmaspheric electron density were studied at different *L* shells (*L* — McIlwain parameter). In this paper we present results of the comparison of longitudinal *foF*2 and *TEC* variations derived for all latitudes.

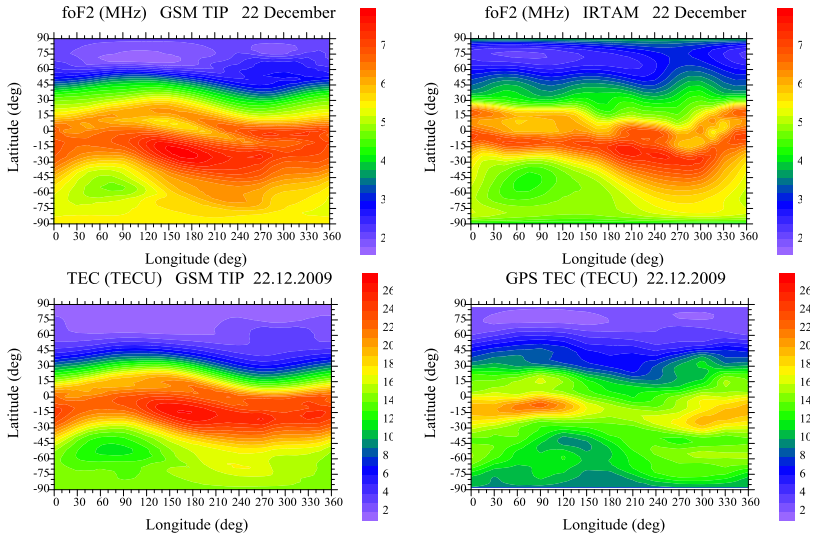

FIGURE 1. Longitudinal varitions of *foF2* and *TEC* at defferent latitudes. Maps show *foF2* and *TEC* on the latitude — longitude grid with 5° latitude step and 15° longitude step. Data are averaged by time for December 22, 2009. Top panels show *foF2* varitions based on the computations of GSM TIP (left) and IRTAM (right). Bottom panels show *TEC* variations based on computations of GSM TIP (left) and GPS measureements (right).

Often, the *TEC* variations are identified with variations of the *F*2 layer critical frequency, *foF*2. This statement bases on the idea of the small contribution of the

plasmasphere to *TEC* and its variability. Recent investigations demonstrate that: 1) disturbances in *foF*2 and *TEC* during a geomagnetic storm can be significantly different especially at a recovery phase[4]; 2) contribution of the topside ionosphere and plasmasphere to *TEC* results in a shift to earlier hours and weakening of the Mid-latitude Summer Evening Anomaly (MSEA) in *TEC* comparing to one in *foF*2 [5]; 3) there are situations when the main contribution of *TEC*is provided by the regions above the *F*2 peak [6], especially during night at the solar activity minimum, where the plasmasphere's contribution to *TEC* can exceed the ionosphere's one [7, 8]. Here we address the following problem. Can we use *foF*2 longitudinal variations to construct the model of *TEC*, and vise versa can longitudinal variations of *TEC* retrieved from ground-based network of GPS receivers be applied for description of the *foF*2 parameters and possible improvement of the ionosphere's empirical models, e. g. IRI?

In this report we present statistical analysis of radio occultation measurements and Interkosmos-19 satellite data for *foF*2, INTERBALL, CHAMP, GRACE electron density and electron content. We involved into analysis absolute total electron content data from the IGS Global Ionospheric Maps (GIM) generated on the basis of world-wide network of GPS/GLONASS ground-based receivers. GIMs have spatial resolution of 5° in longitude and 2.5° in latitude and temporal resolution of 1—2 h. We analyzed data for the solstice conditions at the minimum and maximum of solar activity. We used satellite observational results and simulated results derived from the first-principal, empirical and assimilative empirical models. This comparison allows estimation of the model performance. The first-principle GSM TIP model [9, 10] was developed in the WD IZMIRAN (West Department of Pushkov Institute of Terrestrial Magnetism, Ionosphere and Radio wave propagation of the Russian Academy of Sciences). The total electron content (*TEC*) in the GSM TIP model is calculated by integration of the electron density from bottomside ionosphere to the altitude of GPS/GLONASS satellites (20,200 km). GSM TIP model has already been used to study the longitudinal and UT variations of equatorial electrojet [10], mid latitude and sub-auroral anomalies in *F*2 region electron density at separated longitudes [11]. The second model that we used is IRI-based Real-Time Assimilative Mapping (IRTAM) [12].

IRTAM uses measurements from the Global Ionosphere Radio Observatory (GIRO) and knowledge about ionospheric climatology to now-cast global ionospheric weather. For IRTAM, relative simplicity of the underlying model formalism in comparison to the physics-based models has allowed computations to span past history of model-vs-observation behavior for up to 24 hours. By using 24 hour history of observations rather than one latest measurement we ensure IRTAM robustness to data gabs and autoscaling errors. The empirical model is the NeQuick 2 model. It is a three-dimensional and time-dependent ionospheric electron density model [13, 14]. NeQuick 2 model is able to provide electron density and *TEC* values at different altitudinal regions up to 20,200 km.

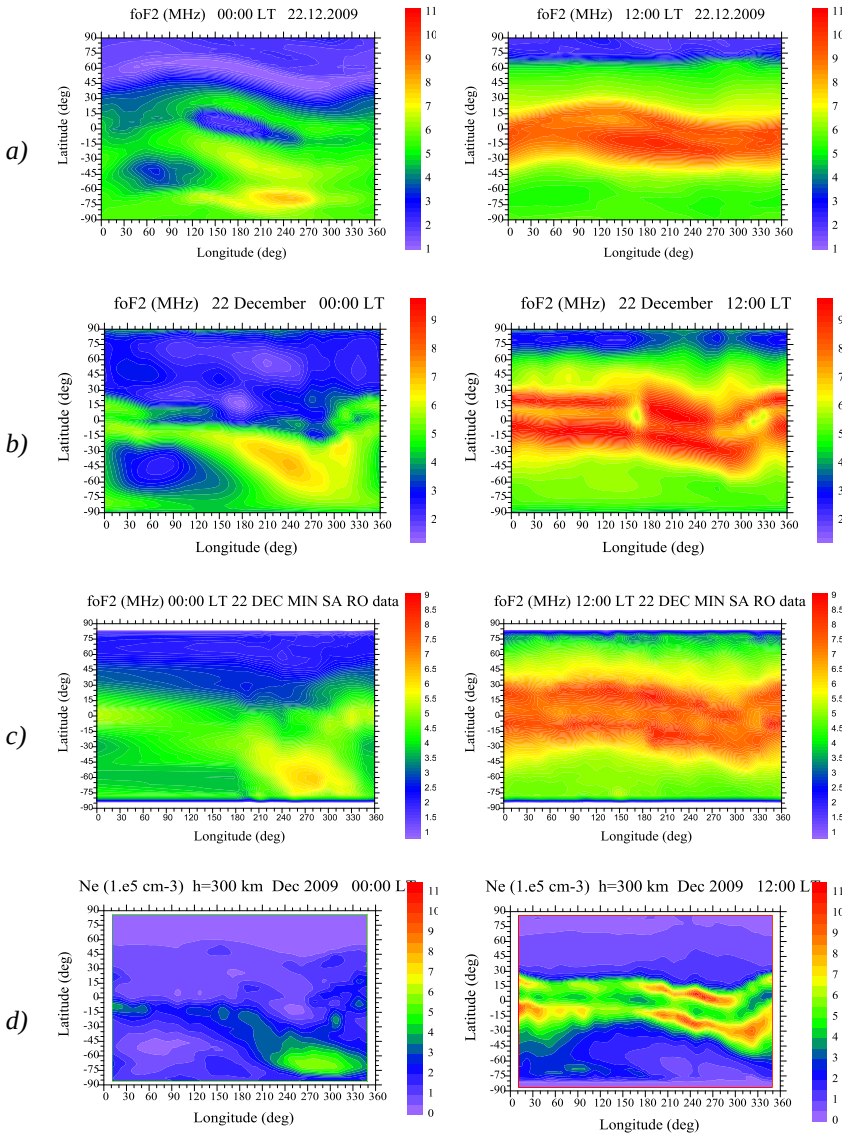

FIGURE 2. Longitudinal variations in *foF*2 (a-c) and electron density $N_e$at height of 300 km (d) for 00:00 LT (left) and 12:00 LT (right). Data are accumulated for December 2009 — January 2010. (a) GSM TIP computations; (b) IRTAM results; (c) radio occultation data; (d) $N_e$variations as shown by the CHAMP observations.

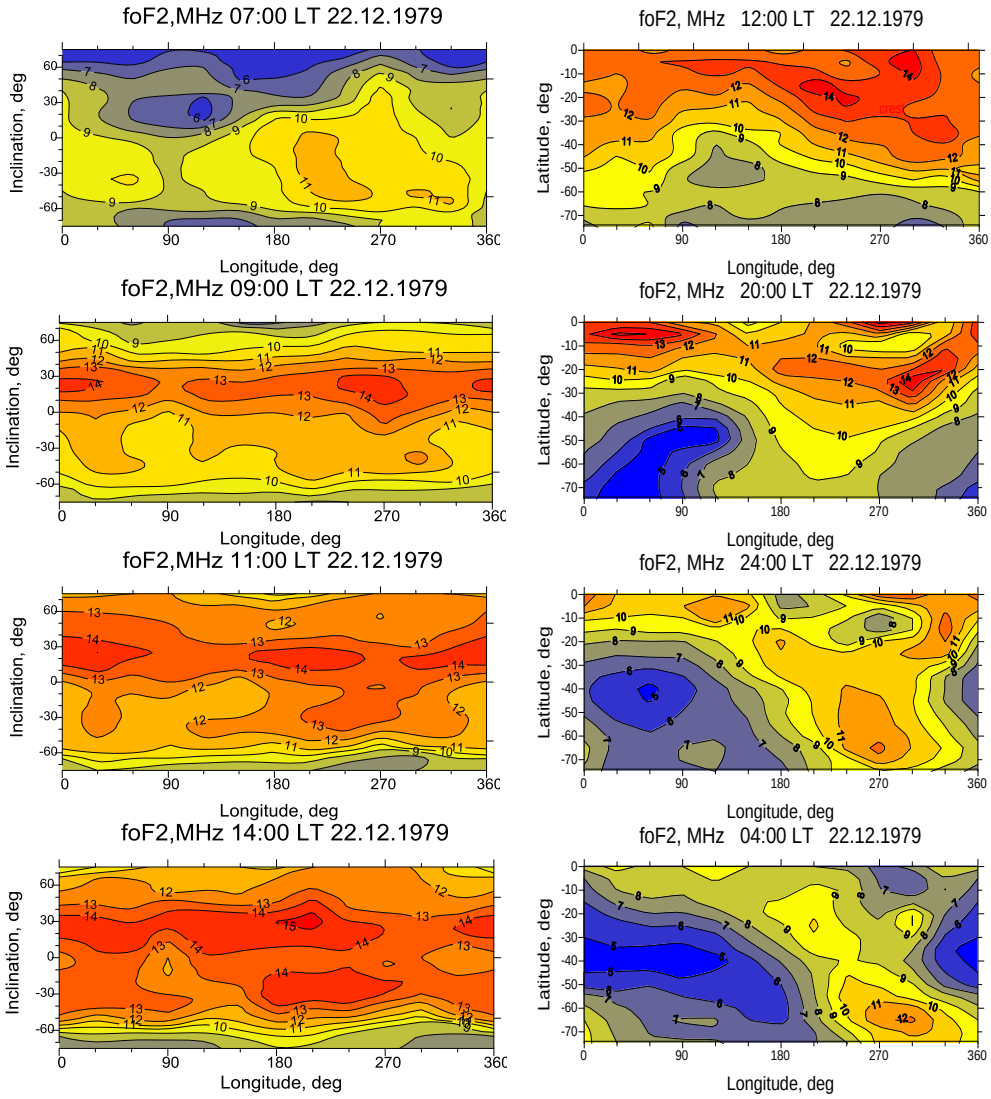

FIGURE 3. Longitudinal variations in *foF*2 in the EIA (left panel) and WSA (right panel) regions for different LT moments. Data are accumulated for December 1979 — January 1980.

Figure 1 recapitulates longitudinal variations in *foF2* and *TEC*. We averaged data over time at the same longitude for 22 December 2009. Both GSM TIP and IRTAM depict each of them. Polar ionospheric cavity appears at 290°E and 270°E longitude in GSM TIP and IRTAM maps, correspondingly. Main ionospheric trough appears to have minimum at 75°N, 130°E as modeled by GSM TIP and at 75°N, 110°E as mapped by IRTAM. In the mid-latitude and low-latitude regions GSM TIP draws one maximum in *foF*2 distribution, but IRTAM draws several

such maxima. This discrepancy can be caused by the limitations any of the models. Both models reproduce minimum of *foF2* in ionospheric anomaly well, except the topology magnetic field that is more accurately reproduces in IRTAM. Also, GSM TIP and IRTAM show the greatest development of equatorial anomaly crests appearance nearly the same longitudinal region: (240°E—300°E) for GSM TIP and (210°E—270°E) for IRTAM. GSM TIP and IRTAM also reveal a good agreement in southern hemisphere. Comparison of longitudinal variations in *TEC* and *foF*2 demonstrates that in general, they are identical and interchangeable in the context of the construction an empirical model of these parameters for quiet geomagnetic conditions. High-latitude *TEC* maximum in American longitudinal sector visible in GPS observations and is reproducible by GSM TIP model can indirectly point out that *foF2* results should also show a spatial maximum close to *TEC* maximum. Such a maximum appears to be on the right place on GSM TIP maps, but is absent on IRTAM maps, which is again can be attributed to insufficient data coverage. Figure 2 presents the examples of longitudinal variation in *foF*2 and $N_e$at height of 300 km during local noon and midnight for 22 December 2009. It is evident the existence of longitudinal variations of the main ionospheric trough and equatorial ionization anomaly (EIA). Also all these maps indicate about Weddell Sea Anomaly (WSA) formation. Figure 3 presents the examples of longitudinal variations during EIA and WSA development at maximum of solar activity according to Interkosmos-19 satellite data.

Acknowledgements.*We are grateful to International GNSS Service (IGS) for GPS data and products (ftp://cddis.gsfc.nasa.gov/pub/gps/). This study was financially supported by RFBR Grants No. 14-05-00788 and 15-35-20364.*

1. D. Bilitza and B. W. Reinisch, International Reference Ionosphere 2007: Improvements and new parameters, *Adv. Space Res.*, 2008, 42(4), pp. 599—609.

2. D. Eccles, J. W. King, and P. Rothwell, Longitudinal variations of the mid-latitude ionosphere produced by neutral-air winds — II. Comparisons of the calculated variations of electron concentration with data obtained from the Ariel I and Ariel III satellites, *J. Atmos. Terr. Phys.*, 1971, 33(3), pp. 371—377.

3. M. A. Clilverd, N. P. Meredith, R. B. Horne et al., Longitudinal and seasonal variations in plasmaspheric electron density: Implications for electron precipitation, *J. Geophys. Res*., 2007, 112, A11210.

4. Iu. V. Cherniak, I. E. Zakharenkova, D. Dzubanov et al., Analysis of the ionosphere/plasmasphere electron content variability during strong geomagnetic storm, *Adv. Space Res.*, 2014, 54(4), pp. 586—594.

5. M. V. Klimenko, V. V. Klimenko, K. G. Ratovsky et al., Mid-latitude Summer Evening Anomaly (MSEA) in F2 layer electron density and total electron content at solar minimum, *Adv. Space Res.*, 2015, 56(9), pp. 1951—1960.

6. E. L. Afraimovich, E. I. Astafyeva, E. A. Kosogorov et al., The mid-latitude fieldaligned disturbances and its impact on differential GPS and VLBI, *Adv. Space Res.*, 2011, 47, pp. 1804—1813.

7. Iu. V. Cherniak, I. E. Zakharenkova, A. Krankowski et al., Plasmaspheric electron content derived from GPS TEC and FORMOSAT-3/COSMIC measurements: solar minimum conditions, *Adv. Space Res.*, 2012, 50(4), pp. 427—440.

8. M. V. Klimenko, V. V. Klimenko, I. E. Zakharenkova et al., The global morphology of the plasmaspheric electron content during Northern winter 2009 based on GPS/COSMIC observation and GSM TIP model results, Adv. *Space Res.*, 2015, 55(8), pp. 2077—2085.

9. A. A. Namgaladze, Yu. N. Korenkov, V. V. Klimenko et al., Global model of the thermosphere-ionosphere-protonosphere system, *PAGEOPH*, 1988, 127(2/3), pp. 219—254.

10. M. V. Klimenko, V. V. Klimenko, and V. V. Bryukhanov, Numerical modeling of the equatorial electrojet UT-variation on the basis of the model GSM TIP, *Adv. Radio Sci.*, 2007, 5, pp. 385—392.

11. M. V. Klimenko, V. V. Klimenko, A. T. Karpachev et al., Spatial features of Weddell Sea and Yakutsk Anomalies in foF2 diurnal variations during high solar activity periods: Interkosmos-19 satellite and ground-based ionosonde observations, IRI reproduction and GSM TIP model simulation, *Adv. Space Res.*, 2015, 55(8), pp. 2020—2032.

12. I. A. Galkin, B. W. Reinisch, X. Huang et al., Assimilation of GIRO data into a real-time IRI, *Radio Sci.*, 2012, 47, RS0L07.

13. S. M. Radicella and R. Leitinger, The evolution of the DGR approach to model electron density profiles, *Adv. Space Res*., 2001, 27(1), 35—40.

14. B. Nava, P. Coisson, and S. M. Radicella, A new version of the NeQuick ionosphere electron density model, *J. Atmos. Solar-Terr. Phys.*, 2008, 70(15), pp. 1856—1862.

Simulation of Vertical Propagation of Acoustic Gravity Waves in the Atmosphere Based on Variations of Atmospheric Pressure and Research of Heating of the Upper Atmosphere by Dissipated Waves

Sergey P. Kshevetskii[1], Yuliya A. Kurdyaeva[1], Nikolay M. Gavrilov[2], and Ivan V. Karpov[1,3]

[1]Physics Department, Immanuel Kant Baltic Federal University, 236004, Nevskogo 14, Kaliningrad, Russia
[2]Atmospheric Physics Department, Saint-Petersburg State University, 198504,Ulyanovskaya 1, Saint-Petersburg, Russia
[3]Institute of Terrestrial Magnetism, Ionosphere, and Radiowave Propagation, Western Division, Russian Academy of Sciences, 236017, pr. Pobedy 41, Kaliningrad, Russia

On modern representations, the acoustic-gravity waves vertically propagating from the troposphere heights and dissipating in the upper atmosphere can bring essential contribution to the upper atmosphere energy balance. The effect of the atmosphere heating by dissipated waves is insufficiently studied now. In the given research, the problem of vertical propagation of waves generated by meteorological phenomena is stated, and the effects of heating up the atmosphere by these waves is studied.

Now it is supposed that the majority of AGWs propagating in the atmosphere arise at tropospheric heights.

They are obliged by their origin to meteorological phenomena. Detailed modeling of meteorological processes is inconveniently in view of their complexity and

variety. The waves propagating from meteorological sources lead to variations of atmospheric pressure, which are well registered now. Therefore, we hope to study many parameters of these waves, being based on the information on variations of the atmospheric pressure. We hope to restore the parameters of waves propagated upward from tropospheric sources with use data on variations of atmospheric pressure.

These ideas force us to state and study the problem of vertical propagation of AGWs in the atmosphere and of the influence of these waves on atmosphere parameters. We will apply the source of waves utilizing observable variations of atmospheric pressure.

As the problem of wave propagation from a boundary pressure source is only a little studied mathematically now, we start our consideration with the simplified problem of wave generation and propagation in two-dimensional model of the atmosphere.

The model equations are:

$$\begin{gathered}
\frac{\partial \rho}{\partial t}+\frac{\partial \rho u}{\partial x}+\frac{\partial \rho w}{\partial z}=0, \\
\frac{\partial \rho u}{\partial t}+\frac{\partial \rho u^2}{\partial x}+\frac{\partial \rho u w}{\partial z}=-\frac{\partial P}{\partial x}+\frac{\partial}{\partial x_i}\xi(z)\frac{\partial u}{\partial x_i}, \\
\frac{\partial \rho w}{\partial t}+\frac{\partial \rho u w}{\partial x}+\frac{\partial \rho w^2}{\partial z}=-\frac{\partial P}{\partial z}+\frac{\partial}{\partial x_i}\xi(z)\frac{\partial w}{\partial x_i}, \qquad (1) \\
\frac{1}{\gamma-1}\left(\frac{\partial P}{\partial t}+\frac{\partial P u}{\partial x}+\frac{\partial P w}{\partial z}\right)=-P(\nabla\vec{v})+\frac{\partial}{\partial x_i}\kappa(z)\frac{\partial T}{\partial x_i}+\xi(z)\frac{\partial v_k}{\partial x_i}\frac{\partial v_k}{\partial x_i}+Q(z), \\
Q(z)=-\frac{\partial}{\partial z}\kappa(z)\frac{\partial}{\partial z}T_0(z)
\end{gathered}$$

In the equations, ρ is density, u, w are horizontal and vertical velocity components $\vec{v}=(u,w)$; P is pressure; g is the acceleration of gravity, γ is an adiabatic index; $\xi(z)$, $\kappa(z)$ are coefficients of viscosity and thermal conductivity; $T_0(z)$is a background temperature. Here x and y axis are horizontal. The axis z is directed upward. In index labels: $i,k=1,2$; $(x_1,x_2)=(x,z)$; $(v_1,v_2)=(u,w)$. The symbol t designates time and $P=\frac{\rho RT}{\mu(z)}$, where $\mu(z)$ is a gas molecular weight.

A background state of the atmosphere and dependence of equations coefficients on z has been taken from the empirical MSIS2000 model of the atmosphere. The source $Q(z)$ is introduced into the model to make a background state be stable.

The boundary conditions at the altitude h=5000 km are standard:

$$\left(\frac{\partial T}{\partial z}\right)_{z=h}=0,\left(\frac{\partial u}{\partial z}\right)_{z=h}=0,(w)_{z=h}=0$$

At research of the problem of a vertical propagation of waves, it is convenient to take boundary conditions along horizontal borders of the simulated field to be periodic:

$$u(x+L,z,t)=u(x,z,t),,v(x+L,z,t)=v(x,z,t),w(x+L,z,t)=w(x,z,t),$$
$$\rho(x+L,z,t)=\rho(x,z,t),T(x+L,z,t)=T(x,z,t)$$

Here L is a period.

The two-dimensional hydrodynamic equations considering viscosity and heat conductivity usually demand of three boundary conditions at the border. For example, from a mathematical point of view, the following boundary conditions are admissible:

$$(T)_{z=0}=0,(u)_{z=0}=0,(w)_{z=0}=0$$

However, we intend to assimilate experimental data of variation of pressure at the Earth surfaces in our statement of the problem of vertical propagation of acoustic-gravity waves. That is, we wish to solve the problem in which the condition $(P)_{z=0}=f(x,t)$ instead of the condition $(w)_{z=0}=0$ is used. It is unusual, non-standard statement of a hydrodynamic problem. Use of this condition can entail changes of other standard conditions on the bottom border, because if we refuse from on the bottom border needs to be set also the density. Thus, the question of admissible conditions on the bottom border demands special mathematical research and the question of correctness of the problem that we desire to state and to solve is worthy.

We solve equations (1) with finite-difference methods with using of explicit-implicit schemes. The algorithm of numerical integration of the equations is described in papers [1], [2], [3].

The equation system (1) is nonlinear and therefore is difficult for strict analysis of correctness of the statement of the problem. Therefore, at the analysis we use admissible simplifications of the equation system. The amplitude of acoustic-gravity waves near the Earth surface is usually very small. Therefore, at research of correctness of the problem, we linearize the equation system (1). It is known, that viscosity and heat conductivity below 100 km weakly influence waves, therefore, we will neglect of dissipative terms too.

The linearized system of equations is derived from (1) standardly. Neglecting also of dissipative terms, we obtain the system of equations

$$\begin{gathered}
\frac{\partial\rho_0(z)\psi}{\partial t}+\frac{\partial\rho_0(z)u}{\partial x}+\frac{\partial\rho_0(z)w}{\partial z}=0,\\
\frac{\partial\rho_0(z)u}{\partial t}=-\frac{\partial\rho_0(z)gH(z)(\psi+\phi)}{\partial x},\\
\frac{\partial\rho_0(z)w}{\partial t}=-\frac{\partial\rho_0(z)gH(z)(\psi+\phi)}{\partial z},\\
\frac{\partial\rho_0(z)\phi}{\partial t}+(\gamma-1)\left[\frac{\partial\rho_0(z)u}{\partial x}+\frac{\partial\rho_0(z)w}{\partial z}\right]+\frac{\alpha(z)}{H(z)}\rho_0(z)w=0,
\end{gathered}\qquad(2)$$

Here $\rho_0(z)$ is a background density of the atmosphere; $\alpha(z) = \gamma - 1 + \gamma \frac{dH(z)}{H(z)}$, $\psi = \frac{\rho - \rho_0(z)}{\rho_0(z)}$, $\phi = \frac{T - T_0(z)}{T_0(z)}$, $H(z) = \frac{RT_0(z)}{g\mu}$. The horizontal boundary conditions are periodic, with the period L. The upper boundary condition

$$(w)_{z=h} = 0 \tag{3}$$

We put the lower boundary condition for the pressure:

$$\left(\rho_0(z) g H(z)(\psi + \phi)\right)_{z=0} = f(x,t), \tag{4}$$

where f (x, t) is a function defined from experimental data.

As we solve the problem of propagation of a boundary regime, the initial conditions correspond to absence of waves are used:

$$u(x,z,0) = w(x,z,0) = \phi(x,z,0) = \psi(x,z,0) = 0. \tag{5}$$

The following statement is proved: the system of the equations (2) with initial conditions (5), and boundary conditions (3), (4) is correct.

Thus, the boundary conditions for the equations (1), including the boundary condition for pressure, look as follows:

$$(T)_{z=0} = T_0(0), (\rho)_z = 0 = \rho_0(0), (u)_{z=0} = 0, \quad (P)_{z=0} = f(x,t)$$

Thus, boundary conditions for temperature and density essentially affects only in a thin layer near the Earth surface, while the boundary condition for pressure defines the solution globally, at all heights.

The authors have experimental data on the surface pressure variations during thunderstorm phenomena 10—11 April 2006. The data were obtained in observations at the infrasound station IS17 [4]. These variations of pressure are used in calculations of a wave propagation and atmosphere heating.

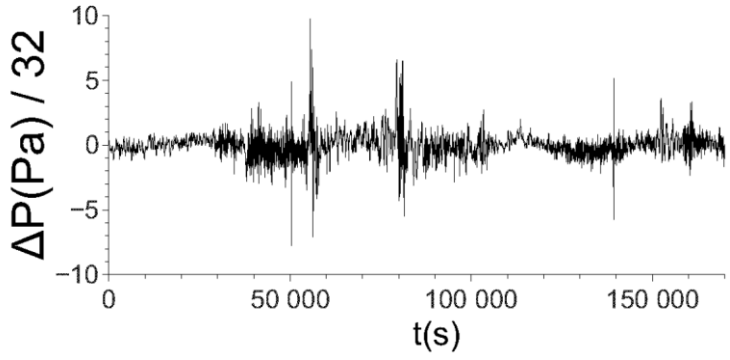

FIGURE 1. Experimental data on Δp(x0; t) variations for April 10—11, 2006, which were obtained at the IS17 infrasonic station (6:70N; 4:90W).

Within the framework of two-dimensional nonlinear hydrodynamic model of atmospheric processes, the additive to the temperature caused by heating of the atmosphere by the waves going from below from variations of atmospheric pressure is simulated. In the simulations, the source with pressure variations is set on the bottom border.

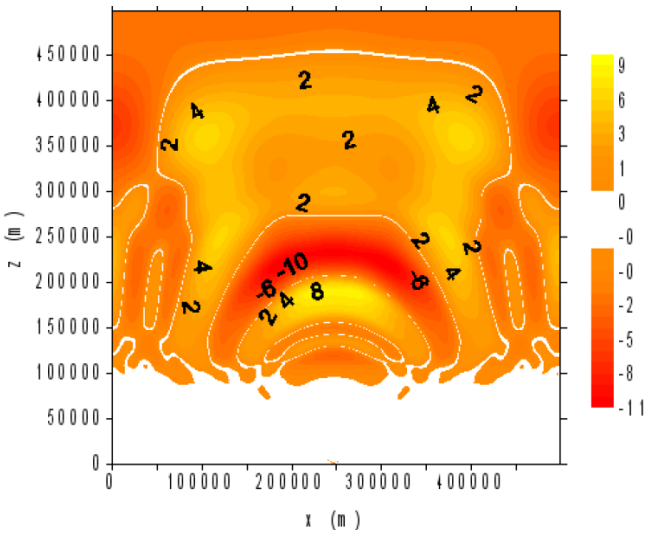

FIGURE 2. Wave perturbation of temperature from the local source of pressure variations at t = 21 minutes.

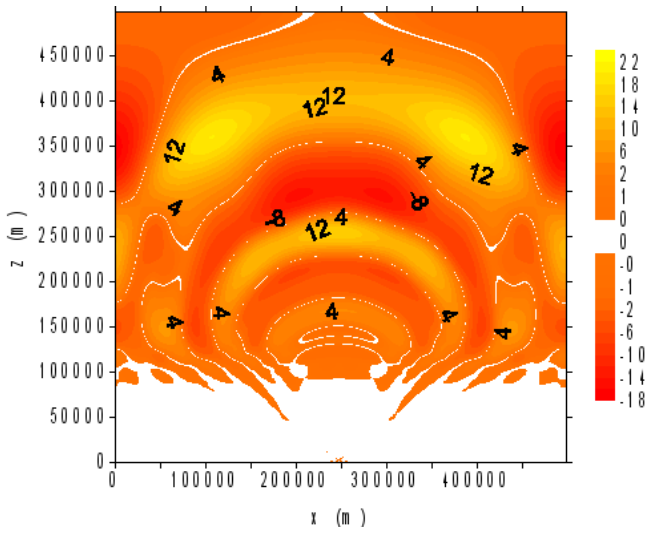

FIGURE 3. Wave perturbation of temperature from the local source of pressure variations at t = 39 minutes.

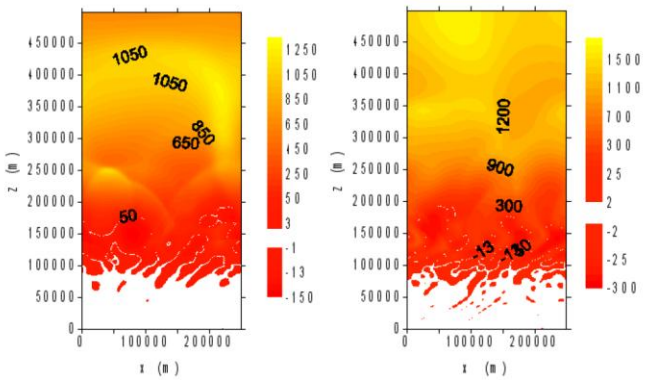

FIGURE 4. The addition to the temperature caused by the heating of the upper atmosphere by the source of pressure variations distributed along the bottom border, at t = 28 min (left) and t = 45 min (right). The temperature is stabilized.

In Fig. 2, 3, the wave propagation from the localized source of the pressure variations upon the bottom borders is shown.

In Fig. 4, the simulated heating of the atmosphere by the test source distributed along the bottom border is shown.

We see that 30 minutes are enough for atmosphere heating by the acoustic-gravity waves going from the tropospheric heights. That is, link of processes in the troposphere and the upper atmosphere is fast enough. Despite the heating of atmosphere by the waves going from below, the temperature is stabilized in time less than 1 hour. That is, in time less than 1 hour after source inclusion, balance between the inflows of heat at the expense of dissipation of waves, and energy drains has come. As to amplitude of the heating, the two-dimensional model gives a little overestimated heating owing to a two-dimensional geometry, and the surface source certainly needs to be calibrated.

Thus, the numerical model allowing simulation of vertical propagation of acoustic-gravity waves and of the heating of the upper atmosphere by waves from the fluctuations of atmospheric pressure is developed.

The work was supported by the Ministry of Education of the Russian Federation grant №3.1127.2014 / K and RFBR 13-05-0043, grants 15-05-01665. The numerical simulations were performed with supercomputers of I. Kant BFU and "Lomonosov" of Moscow State University.

1. S. P. Kshevetskii, Analytical and numerical investigation of nonlinear internal gravity waves, *Nonlinear Proc. Geoph*., 2001a, 8, pp. 37—53.

2. S. P. Kshevetskii, Numerical simulation of nonlinear internal gravity waves, *Comp. Math. Math.Phys.*, 2001b, 12, pp. 1777—1791.

3. I. V. Karpov and S. P. Kshevetskii, Formation of large-scale disturbances in the upper atmosphere caused by acoustic gravity wave sources on the Earth's surface, *Geomagn. Aeronomy*, 2014, 54, pp. 553—562.

4. E. Blanc, T. Farges, and A. Le Pichon, Gravity waves driven by thunderstorms, *in Proc. of the First ARISE Workshop*, 2012, 16 p.

The Supercomputer Model of Atmospheric Processes of Common Access Shared via the Internet

Sergey P. Kshevetskii[1], Nikolay M. Gavrilov[2], and Yuliya A. Kurdyaeva[1]

[1]Physics Department, Immanuel Kant Baltic Federal University,
236004, Nevskogo 14, Kaliningrad, Russia
[2]Atmospheric Physics Department, Saint-Petersburg State University,
198504, Ulyanovskaya 1, Saint-Petersburg, Russia

Lately, the problems of propagation of acoustic-gravity waves in the atmosphere and of influence of these waves on the atmosphere call significant interest. It is, for example, the problems of generation of waves by an auroral electrojet. These are also the problems of generation of waves by diverse meteorological phenomena and of influence of these waves on the upper atmosphere and ionosphere. These are the problems of origin and evolution of tornadoes and the problems of waves generated by tornadoes. These are the problems of atmospheric convection, storms and squalls and of influence of these phenomena on the upper atmosphere. These are also the problems of wave propagation from earthquakes, or of wave propagation from micro-oscillations of the Earth surface before earthquakes. Saying about influence of waves on the atmosphere, we first mean the heating the atmosphere by waves. On the modern representations, the heating of the upper atmosphere by propagated upward waves is significant; this heating is comparable to heating by the solar radiation. The waves can influence essentially on atmospheric flows; that is, they influence on the general atmospheric circulation. At last, breaking waves can create turbulence in the atmosphere; the investigation of formation and evolution of turbulence presents doubtless interest.

For modeling and examination of these diverse phenomena, the authors in the beginning of 2000's have developed a supercomputer numerical model based on numerical integration of non-linear complete three-dimensional system of hydrodynamic equations:

$$\frac{\partial \rho}{\partial t}+\frac{\partial \rho u}{\partial x}+\frac{\partial \rho v}{\partial y}+\frac{\partial \rho w}{\partial z}=0,$$

$$\frac{\partial \rho u}{\partial t}+\frac{\partial \rho u^2}{\partial x}+\frac{\partial \rho uv}{\partial y}+\frac{\partial \rho uw}{\partial z}=-\frac{\partial P}{\partial x}+\frac{\partial}{\partial x_i}\xi(z)\frac{\partial u}{\partial x_i}+2\rho\omega_z v,$$

$$\frac{\partial \rho v}{\partial t}+\frac{\partial \rho uv}{\partial x}+\frac{\partial \rho v^2}{\partial y}+\frac{\partial \rho vw}{\partial z}=-\frac{\partial P}{\partial y}+\frac{\partial}{\partial x_i}\xi(z)\frac{\partial u}{\partial x_i}+2\rho\omega_z u,$$

$$\frac{\partial \rho w}{\partial t}+\frac{\partial \rho uw}{\partial x}+\frac{\partial \rho vw}{\partial y}+\frac{\partial \rho w^2}{\partial z}=-\frac{\partial P}{\partial z}+\frac{\partial}{\partial x_i}\xi(z)\frac{\partial w}{\partial x_i},$$

$$\frac{1}{\gamma-1}\left(\frac{\partial P}{\partial t}+\frac{\partial Pu}{\partial x}+\frac{\partial Pv}{\partial y}+\frac{\partial Pw}{\partial z}\right)=-P(\nabla\vec{v})+\frac{\partial}{\partial x_i}\kappa(z)\frac{\partial T}{\partial x_i}+\xi(z)\frac{\partial v_k}{\partial x_i}\frac{\partial v_k}{\partial x_i}+Q(z),$$

$$Q(z)=-\frac{\partial}{\partial z}\kappa(z)\frac{\partial}{\partial z}T_0(z)$$

In the equations, ρ is density, u, v, w are horizontal and vertical velocity components $\vec{v} = (u,v,w)$; P is pressure; g is the acceleration of gravity, γ is an adiabatic index; $\xi(z)$, $\kappa(z)$ are coefficients of viscosity and thermal conductivity; $T_0(z)$ is a background temperature. Here x and y axis are horizontal. The axis z is directed upward. In index labels; $i,k = 1,2,3$; $(x_1,x_2,x_3) = (x,y,z)$; $(v_1,v_2,v_3) = (u,v,w)$. The symbol t designates time and $P = \frac{\rho RT}{\mu(z)}$, where $\mu(z)$ is a gas molecular weight. ω_z represents local vertical component of the Earth's angular velocity. The equation system can include external sources of momentum or heat.

A background state of the atmosphere and dependence of equations coefficients on z has been taken from the empirical MSIS200 model of the atmosphere. The source $Q(z)$ is introduced into the model to make a background state be stable.

The considered model is a regional one. It allows modeling the behavior of the atmospheric gas in a field with a horizontal scale of several thousand kilometers and with a vertical size of from the Earth surface up to the altitude of 500 km. The boundary conditions at the altitude h=5000 km are standard:

$$\left(\frac{\partial T}{\partial z}\right)_{z=h}=0,\ \left(\frac{\partial u}{\partial z}\right)_{z=h}=0,\left(\frac{\partial v}{\partial z}\right)_{z=h}=0,(w)_{z=h}=0$$

The conservative numerical method is applied for solving the equation system. In a pattern, the numerical method scheme is similar to the known Lax-Wendroff method. Lax and Wendroff has considered hydrodynamic equations written in the form of conservation laws

$$r_t + (q(r))_x + (q(r))_y + (q(r))_z = 0$$

Here r is a column consisting of density, momentum density and energy density. Accordingly, $q(r)$-is a column-function of fluxes of the enumerated values. Lax and Wendroff has approximated these conservation laws as follows:

$$\frac{r_{ijk}^{j+1} - r_{ijk}^{j}}{\tau} + \frac{q_{i+1/2,j,k}^{j+1/2}(r) - q_{i-1/2,j,k}^{j+1/32}(r)}{h_1} + \frac{q_{i,j+1/2k}^{j+1/2}(r) - q_{i,j-1/2,k}^{j+1/2}(r)}{h_2} + \frac{q_{i,j,k+1/2}^{j+1/2}(r) - q_{i,j,k-1/2}^{j+1/2}(r)}{h_3} = 0$$

For evaluation of $r_{ijk}^{j+1/2}$, Lax and Wendroff used explicit methods. However, we use for evaluation of $r_{ijk}^{j+1/2}$ only implicit approximati

$$2 * \frac{r_{ijk}^{j+1/2} - r_{ijk}^{j}}{\tau} + \frac{q_{i+1/2,j,k}^{j+1/2}(r) - q_{i-1/2,j,k}^{j+1/2}(r)}{h_1} + \frac{q_{i,j+1/2k}^{j+1/2}(r) - q_{i,j-1/2,k}^{j+1/2}(r)}{h_2} + \frac{q_{i,j,k+1/2}^{j+1/2}(r) - q_{i,j,k-1/2}^{j+1/2}(r)}{h_3} = 0$$

It does simulations essentially more difficult, than within the limits of standard Lax-Wendroff method. Nevertheless, these complications caused by necessity. We need counteract against accumulation of the errors evoked by discretization of equations. It is well known, that the discretization errors of equations are accumulated.

After a while, a numerical solution, as a rule, considerably differs from the exact solution. The rate of accumulation of these discretization errors essentially depends on structure of the used numerical scheme. The carried out mathematical investigations have shown the discretization errors from acoustic waves give a potential greatest contribution to the common computation error. For numerical methods of the suggested structure, these computation errors are not accumulated, but mutually canceled; it is confirmed by proven theorems and by test calculations. The analysis of accumulation of commutation errors is studied in details in [1—3]. In these papers and in [4], the outcomes of test simulations are given also; the test simulations have demonstrated the numerical solution gives three correct digits during several hours of real time simulation.

Therefore, the developed numerical method allows calculating correctly behavior of acoustic-gravity waves up to significant times, till several tens of hours. The horizontal scales of the simulated field can be of several thousand kilometers. The vertical size of the simulated field is from the Earth surface up to thermosphere altitudes. The simulations are performed without significant contortion of waves and allow us to calculate the influence of waves on the atmosphere with well accuracy.

High accuracy simulation is important at calculation of the influence of waves on the atmosphere parameters, because the influence of waves on the atmosphere is a final stage of wave evolution and takes place at major times. Besides, the separate wave often gives weak effect on the atmosphere, but this effect should be calculated correctly because the weak effects of influence on the atmosphere are accumulated. As a result, we can have a vital modification of the atmosphere parameters caused by influences of many waves during significant time.

All computations are performed a supercomputer in parallel at 3 levels. The calculations are in parallel within each processor kernel; the calculations are scheduled between node kernels at each node of a cluster, and computations are proportioned between the nodes of a computing cluster. Therefore, the supercomputer program is very productive and is one of the fastest.

The development of supercomputer programs demands a lot of special knowledge far from problematic of physics of atmosphere and ionosphere and belonging to both the mathematical field and the field of parallel supercomputer computations. A specialist in the field of physics of the atmosphere and ionosphere is not supposed to be a major specialist in mathematical and computer sciences. Taking this cicumstance in view, some special computer program with GUI that allows utilizing the supercomputer program without any skills in supercomputer computations and numerical methods is developed.

On the Internet, some special server is placed, and any scientist can work with the atmosphere simulation program. The program disposed on the server, after user registration, starts a dialogue with the scientist, and the program ask some questions about the problem interesting to the scientist.

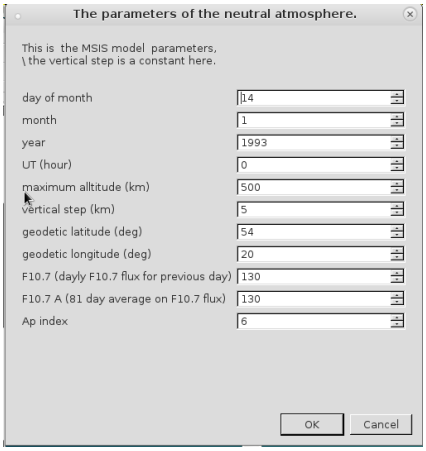

FIGURE 1. The questions about geographical location and time.

For example, the program ask the geographical place under consideration, date, time. These answers are necessary to use a built-in empirical model of the atmosphere to determine a background state of the atmosphere and the behavior of equations coefficients. Further, the user chooses dimensionality of a commutative grid, and decides, whether he will allow for a wind or not. At the next step, the user answers whether he considers an initial-value problem, or a boundary problem, or an initial-boundary-value one. The program asks also about presence of sources (heating, momentum transfer to gas from other processes).

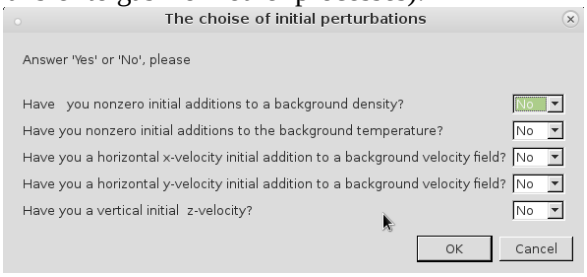

FIGURE 2. Some questions concerning of initial conditions.

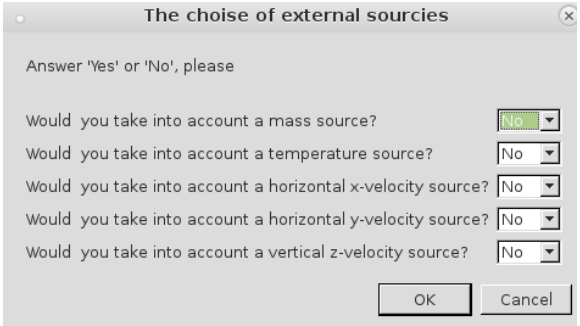

FIGURE 3. Some questions concerning sources.

The statement of initial and boundary conditions, also the statement of sources can demand inputting the complementary information. Namely, inputting of functions describing sources in field and on the boundary, or inputting the functions describing the initial conditions may be necessary. Taking in view this necessaty, some little possibility of programming and inputting the demanded data is represented to the user.

In the course of data input, the server inspects the information inputted by the user concerning syntactic errors; if the inputted data is correct, then the server makes tentative compilation of the program. If no errors are discovered, then, if the user considers the inputted data to be correct, then the server makes a contact with a supercomputer. It configures the program to a supercomputer, and sends the problem to a supercomputer. Since this step, the interaction of the user with the process is restricted. The problem is anew compiled and checked up by a supercomputer, and the task is putt to a sequential queue on fulfillment on a supercomputer. In the course of calculations, the supercomputer and the server regularly come into contact and are synchronized: outcomes of computations are systematically sent to the server.

The user can inspect the course of computations and can take the outcomes of simulations from the server. Thus, direct contact of the user to a supercomputer is absent. The developed complex of programs fulfills the parallel computations automatically. Knowledge of the mathematical theory of a solution of equation is not required, it is necessary only to answer questions asked by the program.

The program also allows the simulation of transfer of impurities.

In Fig. 4 an example of the supercomputer simulation of wave propagation from a small hot field localized near 100 km in the altitude is shown.

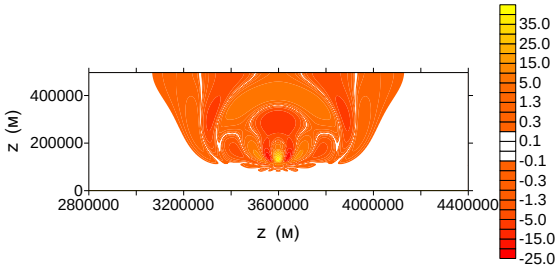

FIGURE 4. Temperature perturbation at t = 553 sec.

The authors hope that the developed complex of supercomputer programs will progress.

The work was supported by the Ministry of Education of the Russian Federation grant №3.1127.2014 / K and RFBR 13-05-0043, grants 15-05-01665. The numerical simulations were performed with supercomputers of I. Kant BFU and "Lomonosov" of Moscow State University.

1 S. P. Kshevetskii, Analytycal and numerical investigation of nonlinear internal gravity waves, *Nonlinear processess in geophysics*, 2001, 8, pp. 37—51.

2. S. P. Kshevetskii, Numerical symulation of nonlinear internal gravity waves, *Computational Mathematics and Mathematical Physics*, 2001, 41(12). pp. 1777—1791.

3. S. P. Kshevetskii, Modeling of propagation of internal gravity waves in gases, *Computational Mathematics and Mathematical Physics*, 2001, 41(2), pp. 273—288.

4. N. M. Gavrilov, S. P. Kshevetskii, and A. V. Koval, Verifications of the high-resolution numerical model and polarization relations of atmospheric acoustic-gravity waves, *Geosci. Model Dev.*, 2015, 8, pp. 1831—1838.

On Analysis of N-wave Coseismic Ionospheric Response in Estimation of The Seismic Energy for Submarine Earthquakes

Ekaterina V. Ol'shanskaya

Schmidt Institute of Physics of the Earth, Russian Academy of Sciences, ul. Bol'shaya Gruzinskaya 10, Moscow, 123995 Russia

N-wave type variations of Total Electron Content (TEC), registered via GPS during the first 15 minutes after the seismic event, are observed as the ionospheric response to the transition of acoustic waves, generated during the strong ($M_w \geq 8.2$) submarine earthquakes. The coseismic variations of TEC are filtered in acoustic diapason of 120—720 s and the means of the duration of the positive phase of the shock wave pulse $\mathbf{t}_+$ are calculated for the set of the strongest tsunamigenic earthquakes, occurred between the years 2003—2015.

The particular features of the N-wave shape ionosperic response depend on 1) the seismic moment M_0 and hence the radiated seismic energy $\mathbf{E}_s$ of the event, — the stronger earthquakes have bigger amplitude and shorter duration of the compression phase; 2) the angle of the incidence of acoustic rays, coming from the source of perturbations, with the geomagnetic field at ionospheric heights, — the maximum amplitude is observed where the vectors of the acoustic ray and geomagnetic field have the same direction; 3) geomagnetic impact on the propagation of the signal in the ionosphere, — signal propagation toward the geomagnetic equator is amplified and toward the geomagnetic pole is suppressed [1]; 4) distance of the subionosperic point, where the maximum of perturbations in TEC variations is registered, from the epicenter of the seismic event [2] and relative position of the ray of acoustic perturbations and the line-of-sight between the GPS-receiver and the satellite.

We used the least squares (LS) approximation for calculation of the regression of the average duration of the positive phase $\mathbf{t}_+$ on the seismic energy of the submarine earthquakes $\mathbf{E}_s$. Information on $\mathbf{E}_s$ was taken from USGS catalogue of the earthquakes and from estimation in [2], inferred from the duration of the compression phase of the shock wave in TEC variations. LS-estimates of the RMS deviation indi-

cate the fair accuracy of the approximation, which allow to consider the inverse problem of determination of the radiated seismic energy of the tsunamigenic earthquake from the measures of the positive phase duration of the N-wave TEC-response, thus provide the additional information for Tsunami Early Warning System.

1. M. Gokhberg, E. Ol'shanskaya, G. Steblov, and S. Shalimov, The ionospheric response to the acoustic signal from submarine earthquakes according to the GPS data, *Izv., Phys. Solid Earth*, 2014, 50(1), pp. 1—8.

2. E. Ol'shanskaya and S. Shalimov, On Estimating the Seismic Energy of Tsunamigenic Earthquakes from the Ionospheric Response Observed by GPS, *Fizika Zemli*, 2015, 6, pp. 16—23.

Comparison of Height-Diurnal Electron Density Variations between Irkutsk Incoherent Scatter Radar and GSM TIP and IRI Models

Konstantin G. Ratovsky[1], Maxim V. Klimenko[2,3], Vladimir V. Klimenko[3], Andrey V. Medvedev[1], Sergey S. Alsatkin[1], and Alexey V. Oinats[1]

[1]Institute of Solar-Terrestrial Physics SB RAS, Irkutsk 664033, Russia
[2]West Department of Pushkov Institute of Terrestrial Magnetism, Ionosphere and Radio Wave Propagation, RAS, Kaliningrad 236017, Russia
[3]Immanuel Kant Baltic Federal University, Department of Radiophysics and Information Safety, Kaliningrad 236000, Russia

The long-duration Irkutsk incoherent scatter radar (ISR) (52.9N, 103.3E) [1] measurements allowed us to obtain monthly averaged patterns of diurnal electron density (Ne) variations in the 180—600 km height range for different seasons and solar activity levels. Table 1 shows the periods of the long-duration measurements.

TABLE 1. Periods of the long-duration measurements.

Low solar activity				Moderate solar activity			
Season	Period	Mean F10.7	Mean Ap	Season	Period	Mean F10.7	Mean Ap
Winter	2011 Jan. 16 — Feb 02	87	5.9	Winter	2014 Jan 01—12	152	7.2
Summer	2007 Jun 05—24	75	6.5	Summer	2013 Jun 22 — Jul 01 2014 Jul 28 — Aug 01	117	12.5
Spring	2009 Apr 01—12	70	5.2	Spring	2012 Apr 05—22	118	8.1
Autumn	2008 Sep 22—30	70	7.5	Autumn	2014 Oct 15—30	152	11

For each period we averaged Ne profiles and obtained Ne height-diurnal variations for 4 seasons and 2 solar activity levels. These variations were compared with the Global Self-consistent Model of the Thermosphere, Ionosphere and Protonosphere (GSM TIP) [2, 3] simulations and the International Reference Ionosphere (IRI) [4] predictions to test how these models reproduces the features revealed from the ISR measurements. For comparison we used the height-diurnal variations of Ne normalized to the height-diurnal maximum.

Figure 1 shows the height-diurnal structures of normalized Ne obtained with ISR and calculated with the GSM TIP and IRI models for winter and summer under low solar activity (SA). Both for winter and summer, both for ISR and the models, at heights lower than ~ 230 km, the Ne diurnal behavior follows solar zenith angle showing the maximum in the daytime and the minimum in the nighttime. The most interesting features are seen at ~ 300 km and above.

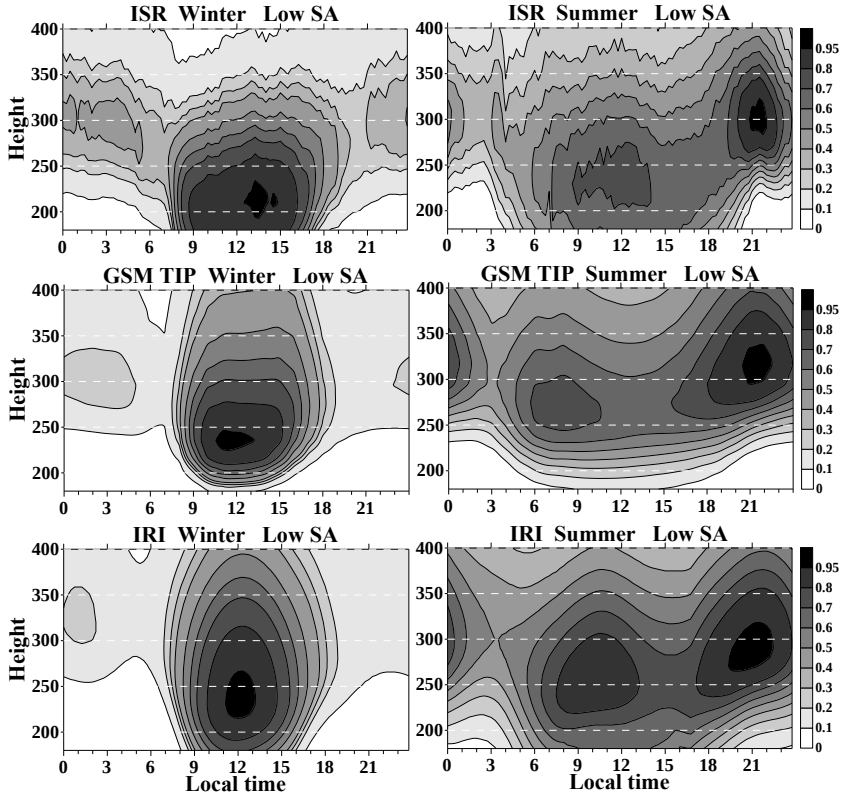

FIGURE 1. Height-diurnal structures of normalized Ne obtained with ISR (upper panel) and calculated with GSM TIP (middle panel) and IRI (low panel) for winter (left) and summer (right) under low solar activity (SA).

In winter the ISR measurements show an additional peak (~ 0.3 of the daytime peak) in the postmidnight time at ~300 км. Both the models reproduce this feature but with somewhat lower peak values (~0.2 of the daytime peak). The ISR height-

diurnal behavior shows that the daytime electron density is close to the nighttime one at~ 350 km and above, and this feature is not reproduced by the models (the daytime Ne is at least 2 times larger than the nighttime one).

In summer both for ISR and the models the main height-diurnal peak is seen in the evening (21:15—22 LT) at 290—300 km, and this is the manifestation of the so-called mid-latitude summer evening anomaly. The differences are seen in the amplitude and LT of an additional summer peak: ~0.7 of the eveningpeak at ~ 12 LT from ISR, ~0.8 at ~ 8 LT from GSM TIP, and ~0.9 at ~ 10 LT from IRI.

Figure 2 shows the height-diurnal structures of normalized Ne obtained with ISR and calculated with the GSM TIP and IRI models for spring and autumn under low SA. As well as for winter and summer, at heights lower than ~ 230 km the Ne diurnal behavior follows solar zenith angle both for ISR and the models.

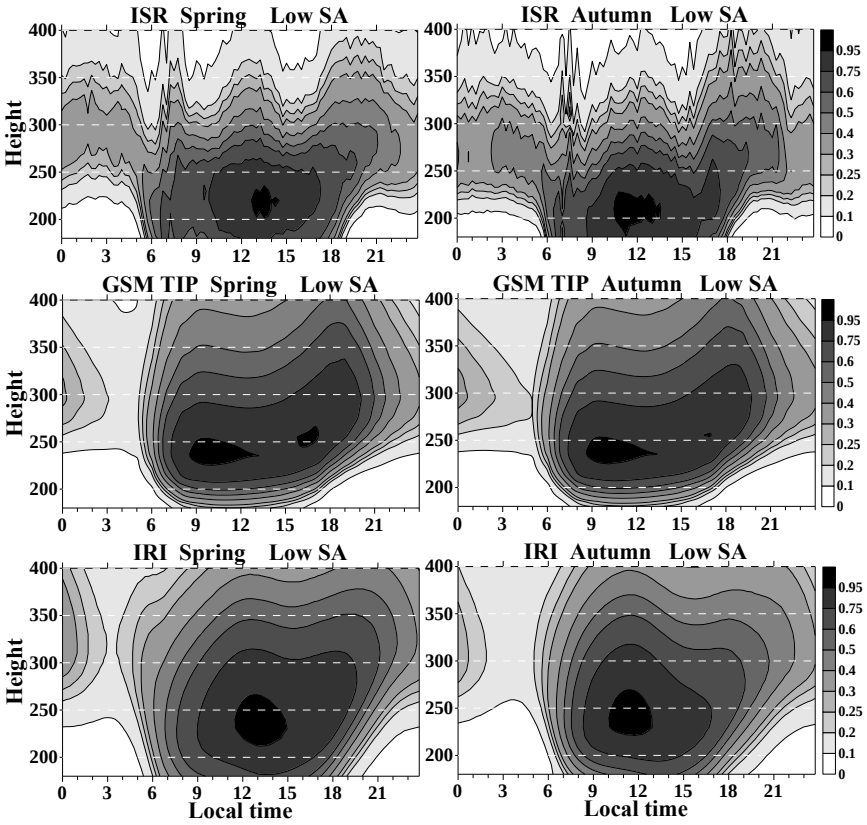

FIGURE 2. Height-diurnal structures of normalized Ne obtained with ISR (upper panel) and calculated with GSM TIP (middle panel) and IRI (low panel) for spring (left) and autumn (right) under low solar activity (SA).

In spring the most interesting features of the Ne pattern from ISR is a multi-peak behavior with the evening (main), daytime, morning and weakly pronounced nighttime peaks at ~ 300 km and above. This feature is not reproduced by the mod-

els. At ~ 300 km and above, GSM TIP shows a summer-like behavior with the main peak in the evening (~ 18 LT), whereas IRI gives close values for all the 12—18 LT period. The autumn pattern is basically close to the spring one. The difference is in the fact that IRI gives higher values in the daytime and ISR gives higher values in the evening in autumn compared to spring.

The main differences in the height-diurnal structures of normalized Ne under moderate and low SA are the follows.

In winter the nighttime peak is weaker in terms of normalized Ne (common feature of ISR and both the models). ISR shows that the daytime Ne is at least 1.5 times larger than the nighttime one, and therefore, close day- and nighttime winter Ne values is the feature of the only low solar activity. Both ISR and GSM TIP show appearance of an evening peak at heights > ~ 450 km. In summer ISR shows that the evening appears earlier at higher heights and this feature is not reproduced by the models. Both the models show an enhancement of the peak seen before noon (mentioned above as an additional summer peak), while ISR does not show such an enhancement. At the same time, ISR shows appearance of an morning peak at heights > ~ 450 km, and this is a common feature of ISR and GSM TIP. In spring and autumn ISR does not show a multi-peak behavior, and therefore, such a behavior is the feature of the only low solar activity.

Finally, the comparison of height-diurnal electron density variations between Irkutsk incoherent scatter radar and GSM TIP and IRI models gave the following results.

The common features of ISR and both the models are the following: (1) at heights < ~ 230 km the Ne diurnal behavior follows solar zenith angle; (2) in winter there is a postmidnight peak, whose ratio to the daytime peak reduces with increasing solar activity; and (3) in summer the main height-diurnal peak is seen in the evening, and this is the manifestation of the so-called mid-latitude summer evening anomaly.

The features revealed from the ISR measurements but not reproduced by both the models are the following: (1) in winter under low solar activity at heights > ~ 350 km the nighttime electron density is close to the daytime one; (2) in spring and autumn under low solar activity at heights > ~ 300 km the diurnal electron density behavior has multi-peak structure.

The closest agreement between ISR and both the models is seen in Summer excluding the features of morning-prenoon peak. Under moderate solar activity both ISR and GSM TIP shows appearance of the evening peak in winter and the morning peak in summer at topside heights.

Acknowledgments.*This investigations were performed with financial support of the Russian Foundation for Basic Research Grants 14-05-92002-HHC_a. This work was partially carried out with-in the project "Physical mechanisms of the reaction of the upper atmosphere and ionosphere on the processes in the lower atmosphere and on the Earth surface" (State task Education and Science Ministry of the Russian Federation, the competitive part of the task No 3.1127.2014/K).*

1. A. P. Potekhin, A. V. Medvedev, A. V. Zavorin et al., Development of diagnostic capabilities of the Irkutsk incoherent scattering radar, *Cosmic Research*, 2008, 46(4), pp. 347—353.

2. A. A. Namgaladze, Yu. N. Koren'kov, V. V. Klimenko et al., Global model of the thermosphere-ionosphere-protonosphere system, *Pure Appl. Geophys*. (*PAGEOPH*), 1988, 127(2/3), pp. 219—254.

3. M. V. Klimenko, V. V. Klimenko, and V. V. Bruykhanov, Numerical simulation of the electric field and zonal current in the Earth's ionosphere: the dynamo field and equatorial electrojet, *Geomagn. Aeron.*, 2006, 46(4), pp. 457—466.

4. D. Bilitza, D. Altadill, Y. Zhang et al., The International Reference Ionosphere 2012 — a model of international collaboration, *J. Space Weather Space Clim*., 2014, 4(A07), pp. 1—12.

Upper Atmosphere Conductivity Model and Conductivities Effects on Modeling of Atmospheric Tides

Nikita O. Shevchuk[1], Alexander I. Pogoreltsev[2]

[1]Department of Atmospheric physics, St Petersburg University,
St. Petersburg-Petrodvorets, 198904, Russia
[2]Department of Meteorological Forecasting, Russian State Hydrometeorological University,
St. Petersburg, 195196, Russia

Original version of the Middle and Upper Atmosphere Model (MUAM) includes very rough parameterization of charged particles influence on the dynamic of neutral gas. Only globally and daily averaged vertical profiles of ionospheric Pedersen and Hall conductivities are considered. To more accurately reproduce the electro-magnetic effects the space and temporal variations of ionospheric conductivities have to be taken into account. The semi-empirical model of ionospheric conductivities based on neutral atmosphere model NRLMSISE-00 [1] and ionospheric model IRI_Plas [2] has been developed.

Momentum equations for horizontal wind components with the contribution of the Lorenz force could be written as follows [3, 4]:

$$\frac{du}{dt} - \left(2\Omega \sin\varphi + \frac{u \tan\varphi}{a}\right) v = -\frac{1}{a\rho \cos\varphi}\frac{\partial p}{\partial \lambda} + \frac{1}{\rho}\frac{\partial}{\partial z}\mu_1 \frac{\partial u}{\partial z} + \frac{1}{c\rho}\left[\vec{j} \times \vec{H}\right]_\lambda, \qquad (1)$$

$$\frac{dv}{dt} + \left(2\Omega \sin\varphi + \frac{u \tan\varphi}{a}\right) u = -\frac{1}{a\rho}\frac{\partial p}{\partial \varphi} + \frac{1}{\rho}\frac{\partial}{\partial z}\mu_1 \frac{\partial v}{\partial z} + \frac{1}{c\rho}\left[\vec{j} \times \vec{H}\right]_\varphi.$$

One can obtain Ohm's law for the ionospheric plasma:

$$\vec{j} = \sigma_0\left(\vec{E}' \cdot \vec{H}\right)\vec{H}/H_0^2 + \sigma_1 \vec{H} \times \vec{E}' \times \vec{H}/H_0^2 + \sigma_2 \vec{H} \times \vec{E}'/H_0, \qquad (2)$$

where$\sigma_0, \sigma_1, \sigma_2$are the parallel conductivity, Pedersen and Hall conductivities, respectively.

Below are the components of the Lorenz force:

$$\frac{1}{c}\left[\vec{j} \times \vec{H}\right]_\lambda = -\frac{\sigma_1 u H_0^2}{c^2} + \frac{\sigma_2 v H_z H_0}{c^2}, \quad (3)$$
$$\frac{1}{c}\left[\vec{j} \times \vec{H}\right]_\varphi = -\frac{\sigma_1 v H_z^2}{c^2} - \frac{\sigma_2 u H_z H_0}{c^2}.$$

Using the expressions (3) let us to rewrite momentum equations in terms of atmospheric conductivities:

$$\frac{du}{dt} - \left(2\Omega \sin\varphi + \frac{u \tan\varphi}{a} + \frac{\sigma_2 H_z H_0}{c^2}\right) v == -\frac{1}{a\rho \cos\varphi}\frac{\partial p}{\partial \lambda} + \frac{1}{\rho}\frac{\partial}{\partial z}\mu_1 \frac{\partial u}{\partial z} - \frac{\sigma_1 u H_0^2}{\rho c^2}, \quad (4)$$
$$\frac{dv}{dt} + \left(2\Omega \sin\varphi + \frac{u \tan\varphi}{a} + \frac{\sigma_2 H_z H_0}{c^2}\right) u = -\frac{1}{a\rho}\frac{\partial p}{\partial \varphi} + \frac{1}{\rho}\frac{\partial}{\partial z}\mu_1 \frac{\partial v}{\partial z} - \frac{\sigma_1 v H_z^2}{\rho c^2}.$$

Evidently the terms containing Hall conductivity (σ_2) act as the Coriolis force (so-called geomagnetic torque) but have an opposite sign, i. e. geomagnetic torque tends to compensate the Coriolis force and to reduce the geostrophic balance in the dinamo region [4]. Terms containing the Pedersen conductivity (σ_1) behave like additional Rayleigh friction (proportional to the wind velocity with the negative sign). This dissipative effect is also called ion drag.

The ionospheric Pedersen and Hall conductivities have been calculated using empirical electron and ion densities and neutral atmosphere:

$$\sigma_1 = eN(\mu_1^e + \mu_1^i), \quad (5)$$
$$\sigma_2 = eN(\mu_2^e - \mu_2^i).$$

The electron and ion mobilities could be expressed as follow [5]:

$$\mu_1^e = \frac{e}{m_e A \nu_{in}^2}(\omega_i^2 \nu_{en} + \nu_e \nu_{in}^2),$$
$$\mu_1^i = \frac{e}{m_i A \nu_{in}}(\omega_e^2 + \nu_e \nu_{en}),$$
$$\mu_2^e = \frac{e\omega_e}{m_e A \nu_{in}^2}\left(\omega_i^2 + \nu_{in}^2 + \frac{m_e}{m_i}\nu_{ei}\nu_{in}\right), \quad (6)$$
$$\mu_2^i = \frac{e\omega_e}{m_e A \nu_{in}^2}\left(\omega_i^2 + \frac{m_e}{m_i}\nu_{ei}\nu_{in}\right),$$
$$\nu_e = \nu_{ei} + \nu_{en},$$
$$A = A_1 + A_2 = \frac{\omega_e^2}{\nu_{in}^2}\left(\omega_i^2 + \nu_{in}^2 + 2\frac{m_e}{m_i}\nu_{ei}\nu_{in}\right),$$

wherem_e, m_i are the electron and ion masses; ω_e, ω_i are cyclotron frequencies for electron and ions, respectively; $\nu_{ei}, \nu_{en}, \nu_{in}$ are the electron-ion, electron-neutral, and ion-neutral collision frequencies.

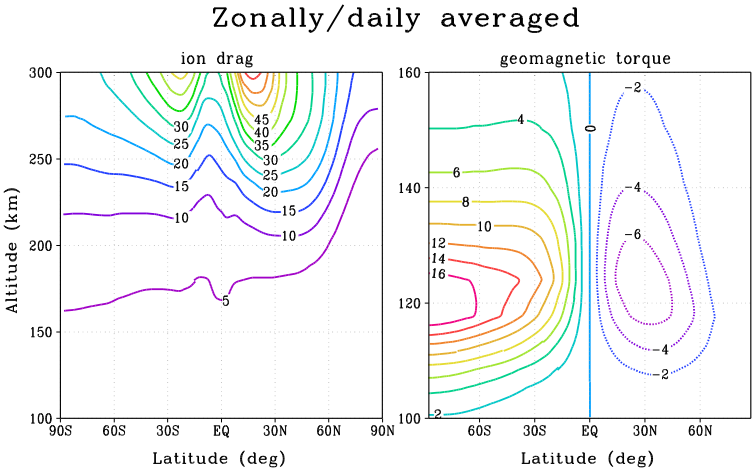

FIGURE 1. Latitude — altitude cross sections of daily and zonally averaged geomagnetic torque (right panel) and ion drag (left panel) distributions.

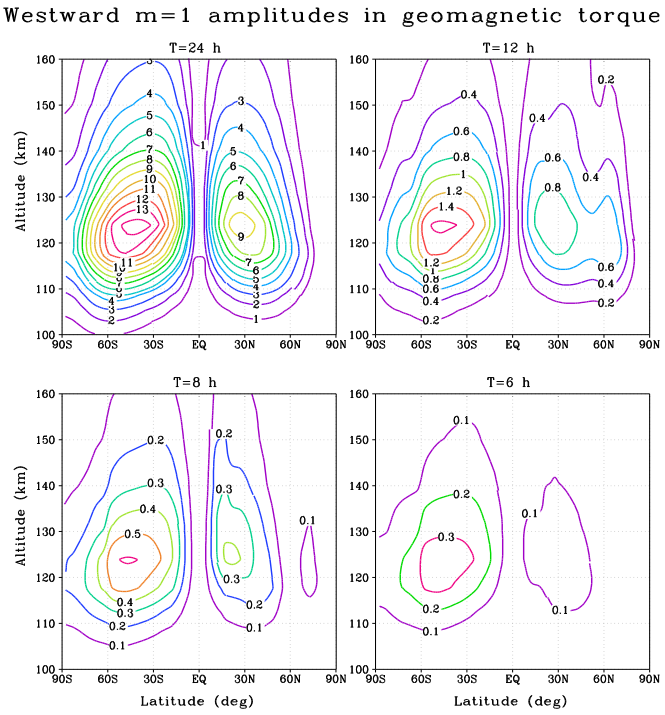

FIGURE 2. Latitude — altitude cross sections daily and zonally averaged geomagnetic torque (right panel) and ion drag (left panel) distribution.

The set of equations (5) and (6) is the basis of ionospheric conductivities model. Geomagnetic torque and ion drag have been calculated for all latitudes and longi-

tudes at 23 levels (from 100 to 380 km). Daily and zonally averaged geomagnetic torque and ion drag for mid-January conditions and moderate solar activity are shown in Figure 1. In all Figures the geomagnetic torque and ion drag are shown with the factors of $10^6$and 10^5, respectively.

The figure shows, that under these conditions maximum values of ion drag are observed at altitude of about 300 km at low latitudes regions ($6 \cdot 10^{-4}$ s^{-1} for Northern and $45 \cdot 10^{-5}$ s^{-1} for Southern hemispheres, respectively). Geomag netic torque is equal to zero at the equator, has the positive values in Southern hemisphere with the maximum of $16 \cdot 10^{-6}$ s^{-1} at the heights of 116—125 km at South Pole and negative values in North hemisphere with minimum of $-6 \cdot 10^{6}$ s^{-1} at low and mid latitudes and the heights of 116—130 km.

The next step was to decompose the obtained geomagnetic torque and ion drag into zonal and temporal harmonics. Consequently the amplitudes and phases of calculated harmonics in MUAM have been used. As a result the geomagnetic torque and ion drag can be determined at any time step. In the Fig. 2 the example of harmonic decomposition is shown. There are westward amplitudes of geomagnetic torque with zonal number 1 and periods of 24, 12, 8 and 6 hours.

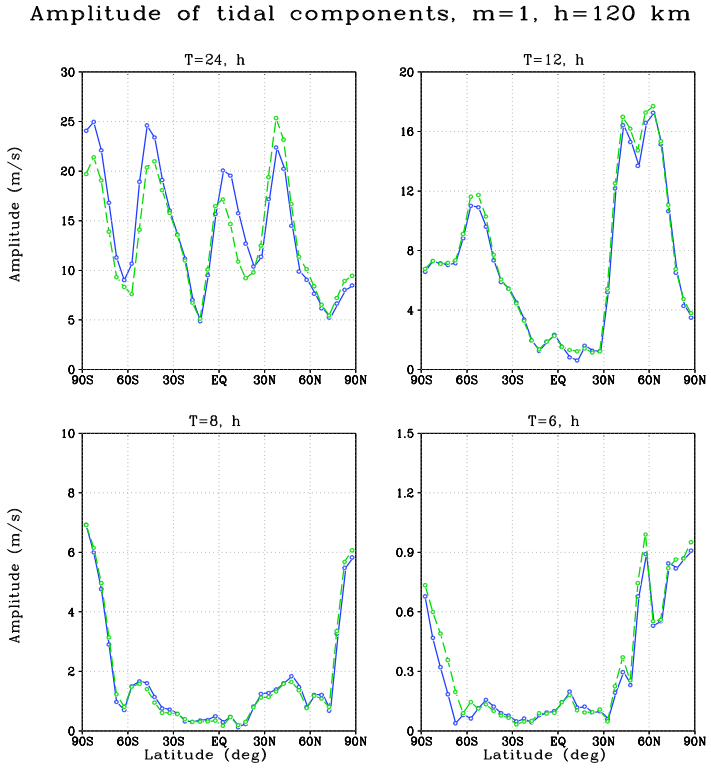

FIGURE 3. Zonal wind tide amplitude, m = 1, altitude is 120 km. Dashed line — without diurnal variations of ionosperic conductivities, solid line — with diurnal variations of ionosperic conductivities.

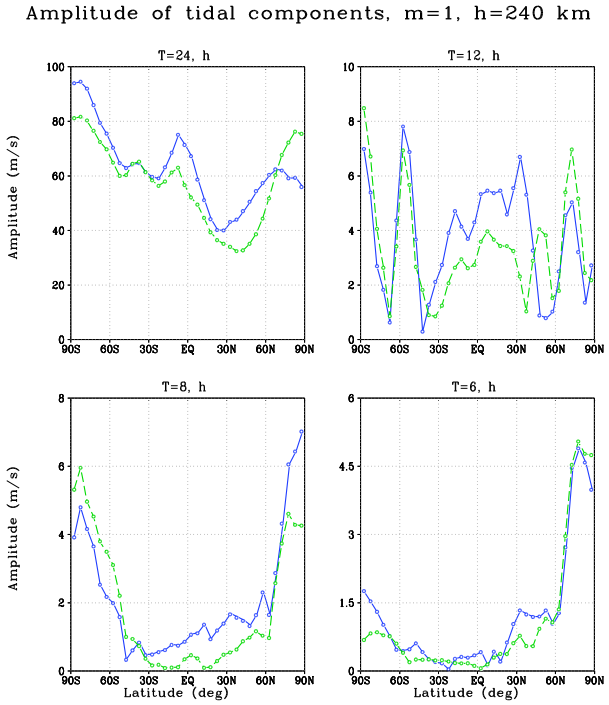

FIGURE 4. Zonal wind tide amplitude, m = 1, altitude is 240 km. Dashed line — without diurnal variations of ionosperic conductivities, solid line — with diurnal variations of ionosperic conductivities.

Tide amplitude with m = 1 and T = 24 h has two maxima at the height of 120—130 km: $14 \cdot 10^{-6}$ s^{-1} at Southern hemisphere middle latitudes and $9 \cdot 10^{-6}$ s^{-1} at Northern hemisphere low latitudes. There are two maxima for tides with m = 1 and T = 12 h ($1.6 \cdot 10^{-6}$ s^{-1} in Southern hemisphere and $0.8 \cdot 10^{-6}$ s^{-1} in Northern hemisphere) and m = 1 and T = 8 h ($0.6 \cdot 10^{-6}$ s^{-1} in Southern hemisphere and $0.4 \cdot 10^{6}$ s^{-1} in Northern hemisphere). Tide amplitude with m = 1 and T = 6 h has only one maximum in Southern hemisphere at mid latitudes ($0.3 \cdot 10^{-6}$ s^{-1}).

The last step is the inclusion of ionospheric conductivity effect in the MUAM. Amplitudes of tidal component for atmospheric dynamo-region (120 km) and for upper thermosphere (240 km) are shown in Figures 3 and 4. It is evident that diurnal variations of geomagnetic torque and ion drag lead to significant changes in characteristics of migrating as well as non-migrating tides. It should be noted that diurnal variations of geomagnetic torque have been calculated for quiet geomagnetic conditions. If there are other geomagnetic conditions the additional discussion is needed and could be the aim of the following work.

As a result of current work the ionospheric conductivity model has been developed and a significant role of geomagnetic torque and ion drag in upper atmospheric dynamicshas been demonstrated.

1. J. M. Picone, A. E. Hedin, D. P. Drob, and A. C. Aikin, *J. Geophys. Res.*, 2002, 107(A12), pp. 1221—1231.
2. T. L. Gulyaeva, X. Huang, and B. W. Reinich, *Act Geod. Geophys.Hu*, 2002, 37(3), pp. 25—30.
3. B. N. Gershman, *The Dynamic of Ionospheric Plasma*, Nauka, Moskow (in Russian).
4. M. L. Glushakov, V. N. Dulkin, and A. I. Ivanovskiy, *Geomagn.Aeron.*, 1979, 19(4), pp. 663—670.
5. A. I. Pogoreltsev, *J. Atmos. Terr. Phys.*, 1996, 58(10), pp. 1125—1141.

Improving Space Weather Prediction using IRTAM and GSM TIP

Artem M. Vesnin[1], Maxim V. Klimenko[2,3]

[1]Institute of Solar-Terrestrial Physics of Siberian Branch of Russian Academy of Sciences, Irkutsk, Russia.
[2]West Department of the Institute of Terrestrial Magnetism, the Ionosphere, and Radiowave Propagation,Russian Academy of Sciences, West Department, Kaliningrad, Russia
[3]Kant Baltic Federal University, Kaliningrad, Russia

We present a procedure to improve IRI-based Real-Time Assimilative Mapping (IRTAM) [1] model where no observation are available. IRTAM uses the advantages of the empirical IRI model and improves the climatology presentation of ionospheric parameters using the data of the vertical sounding ionosondes network presented by the Global Ionospheric Radio Observatory (GIRO) [2]. It is widely known that IRI describes the climatology behavior of the ionosphere [3] and has a history of successful use over more than 40 years. Recent studies have shown that IRI on the average provides good results on predicting ionospheric parameters in various conditions [4]. The IRTAM model uses the IRI formalism [5] for the description of ionospheric parameters and inputs corrections in such a way that the resulting presentation corresponds better to observational data. The IRTAM model uses separate set of expansion coefficients for each ionospheric parameter. This expansion is performed in terms of modified spherical harmonics in which the asymmetry of Earth's magnetic field is taken into account. The IRTAM model, in the same way as IRI, uses the empirical model of the Earth's magnetic field IGRF (International Geomagnetic Reference Field) for the correct allowance for the geomagnetic field, which has a more complicated structure than the magnetic dipole field [6]. The latter is especially important for the exact description of the global distribution of ionospheric parameters

IRTAM is known to be accurate in a vicinity observational sites locations [7], but it's simulation qulaity falls to IRI's quality far from a site. It can cause artificial artifacts in simulations. One example of such artifacts is patchy structure occurring

during recovery phase of intense geomagnetic storm 7—8 November 2004. Figure 1 shows this effect as depicted by critical frequency of F2 layer, *foF2*.

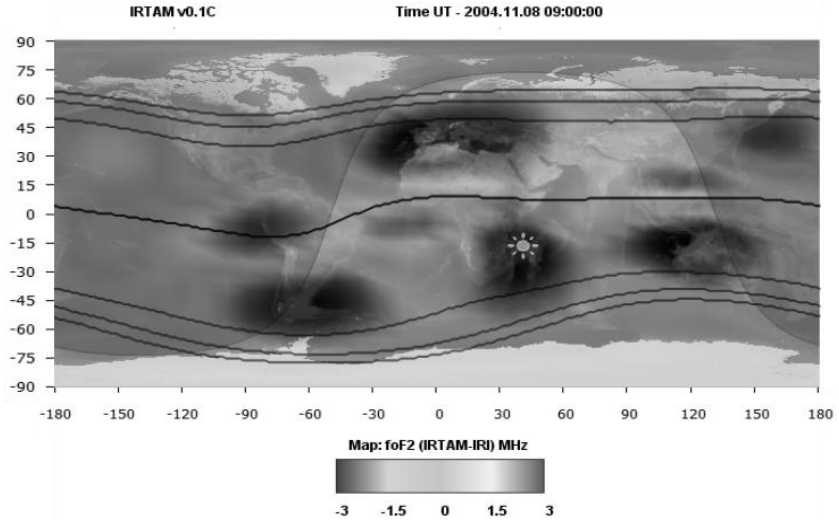

FIGURE 1.Cell structure during recovery phase of 7—8 November 2004 geomagnetic storm as shown by IRTAM *foF2* simulations. Lines represent magnetic equator and 3 first L-shells. Subsolar point and solar terminator locations are shown.

Figure 1 shows difference between disturbed and quite time maps of *foF2*. We see decreased *foF2* compared to quite time in mid-latitude of both south and north hemispheres. As a reference we consider IRI simulation for the same time epoch. The *foF2* depletion is referred to plasmasphere refilling during recovery phase of the geomagnetic storm. The cell structure is artificial. The cells coincide with observation sites located in Europe, South Africa, South America and Asia. US stations do not shown the effect in absolute *foF2* difference since they are located at the night side at the time. When it is day at US sector *foF2* depletion is clearly seen. However cell structure similar to the presented one can be real and governed by processes going on in the atmosphere. Here comes an issue with IRTAM data interpretation: when do we say effects are real and when they are artificial and caused by non uniform spatial coverage of the data. There is no doubt in simulation result validity near observation site, but far from those they are not so clear.

Our proposal is to use Global Self-consistent Model of Termosphere Ionosphere Plasmasphere outputs to extend IRTAM results further from the locations where no observations are available. It has been shown [7], that IRTAM simulations is reliable as far as 1500 km from a site. We employ this fact and GSP TIP data to see whether effect shown by IRTAM is really and extends further from sites. We stress that effects depicted by IRTAM near sites should be taken as real, since they based on observations. The questions is only about locations where no observations are

presented.

IRTAM uses artificial neural network (ANN) approach to extrapolate observations data beyond sites locations. This is done in order to get data for even grid. In the case of IRTAM neurons of ANN are the grid nodes. We propose to use GSM TIP simulations on this step of the assimilation procedure to get more "physics-based extrapolation" of the data. When we deal with ANN the concept of weight pops up. The weight defines strength with which neurons and connections between them affect the state of a system represented by ANN. It is natural to link GSM TIP data into IRTAM via weights. Procedure is as follows:

- data at certain grid node show similar effect both in IRTAM and GSM TIP models;
- we define the entire region (grid nodes) of effect by means of GSM TIP;
- links between neurons those represent grid nodes found on previous step and the neuron of the first step have larger weights.

The region of effect can be defined using different algorithms. The simplest one is just when difference between quite and disturbed time representation of a parameter exceeds some threshold. The approach that defines definition of linked regions is not novel and has been used in ionospheric studies [8].

If we consider case presented on Fig. 1, we expect to see decreased *foF2* is continuous in zonal direction and repeat magnetic equator geometry. Although absolute values of *foF2* depletion is less on the night side the relative depletion is almost as large as on the day side. Relative means we take difference between IRTAM and IRI and divide on IRI. Increased weights between neurons inside "affected" region will cause the effect shown by IRTAM will extend to the entire region effect takes place. GSM TIP predicts ionosphere dynamics better than IRI, especially during disturbed time, and hence it seems promising to use it's data to improve IRTAM. GSM TIP models well longitudinal and latitudinal variations of the ionospheric parameters [6], which can improve IRTAM reperesentaions of space weather.

1. I. A. Galkin, B. W. Reinisch, X. Huang, and D. Bilitza, Assimilation of GIRO data into a real-time IRI, *Radio Sci.*, 2012, 47, RS0L07, doi: 10.1029/2011RS004952.

2. B. W. Reinisch and I. A. Galkin, Global ionospheric radio observatory, *Earth, Planets Space*, 2011, 63(4), pp. 377—381.

3. T. Damboldt and P. Suessmann, Information document on the analysis and validity of present ITU foF2 and M(3000)F2 maps, *International Telecommunication Union*, 2011, http://www.itu.int/md/R07-WP3L-C-0086/en.

4. D. Bilitza, D. Altadill, Y. Zhang et al., The International Reference Ionosphere 2012—a model of international collaboration, *J. Space Weather Space Clim*., 2014, 4, A07, doi: 10.1051/swsc/201400 4.

5. W. B. Jones, R. P. Graham, and M. Leftin, Advances in ionospheric mapping by numerical methods, ESSA Technical Report ERL, ERL 107-ITS 70 1969, Washington DC: US Government Printing Office, 1969.

6. M. V. Klimenko, V. V. Klimenko, F. S. Bessarab et al., Diurnal and longitudinal varia-

tions in the earth's ionosphere in the period of solstice in conditions of a deep minimum of solar activity.*Cosmic Research*, 2016, 54(1), pp. 8—19.

7. A. M. Vesnin, I. A. Galkin, and P. Song, Validation of F2 layer peak height and density by Real-Time IRI, *Radio Science Conference (URSI AT-RASC), 2015 1st URSI Atlantic* (pp. 1—1), IEEE, 2015.

8. Yu. V. Yasyukevich and I. V. Zhivetiev, Using network technology for studying the ionosphere, *Sol.—Terr. Phys*., 2015, 1(3), pp. 21—27, doi: 10.12737/10545.

Generating Ionospheric Irregularities During the 2015 June 22 Magnetic Storm

Yury V. Yasyukevich, Roman V. Vasilyev, Artem M. Vesnin, Mariia V. Globa, and Konstantin G. Ratovsky

Institute of Solar-Terrestrial Physics of Siberian Branch of Russian Academy of Sciences, Irkutsk, Russia

Introduction. Magnetic storm is a global phenomenon which results in different effects on Earth's magnetosphere and underlying regions. It is well known that during a magnetic storm ionospheric irregularities of different scales can be generated. Such irregularities affect radio wave propagation and thus services provided with use of radio wave telecommunication. That's why theory of such irregularities generation is of special interest.

We have studied irregular ionosphere dynamic during the 2015 June 22 magnetic storm and present result in this paper. Although we investigated irregularities of different scales, the primary attention is devoted to small-scale irregularities.

Experimental facilities. Intensive small scale ionospheric irregularities cause scattering of radio signal and hence distort it [1]. The most significant scattering occurs when irregularity size is of the order of the first Fresnel zone. To study small-scale irregularities one can analyze the radio signal amplitude scintillations [2].

For studying small scale irregularities used data from ISTP SB RAS experimental facilities located next to Irkutsk, Russia (~ 52°N, 104°E). We used:

1) Ionosonde DPS-4. It allows us to record F-spread appearance and its quantitative characteristics.

2) Irkutsk Incoherent Scatter Radar (IISR). IISR records amplitude scintillations of intensive radio wave source given source passes through radar's directional diagram.

3) GPS/GLONASS signal receiver NovAtel GPStation-6. It records navigation signal amplitude scintillations S4 and phase fluctuations $\sigma\varphi$ [3].

To study large-scale irregularities we used data from regional and worldwide GPS/GLONASS receiver networks. We used classical techniques of total electron content (TEC) mapping [4] to obtain global scale view.

Experimental results. The 2015 June 22 magnetic storm began at 18:36 UT caused by shock wave hit the magnetosphere. It was revealed in storm sudden commencement (Fig. 1). Fig. 2 shows F-spread, "Sygnus-A" radio signal amplitude scintillations and GPS L1 phase fluctuations σφ from all satellites during 15:00—24:00 UT June 22, 2015.

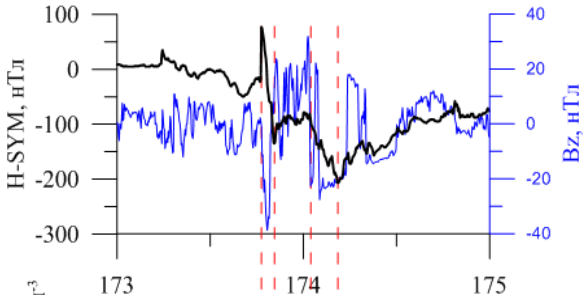

FIGURE 1. H-SYM index and z-component of interplanetary magnetic filed (Bz) during June 22—23, 2015.

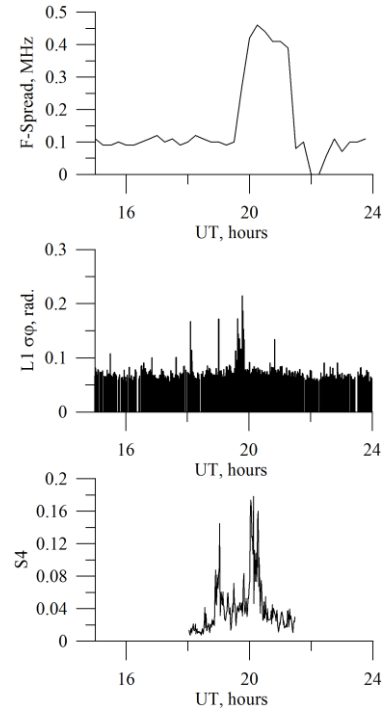

FIGURE 2. F-spread (upper panel), L1 phase fluctuations σφ (middle panel) and "Sygnus-A" radio signal amplitude scintillations S4 (bottom panel).

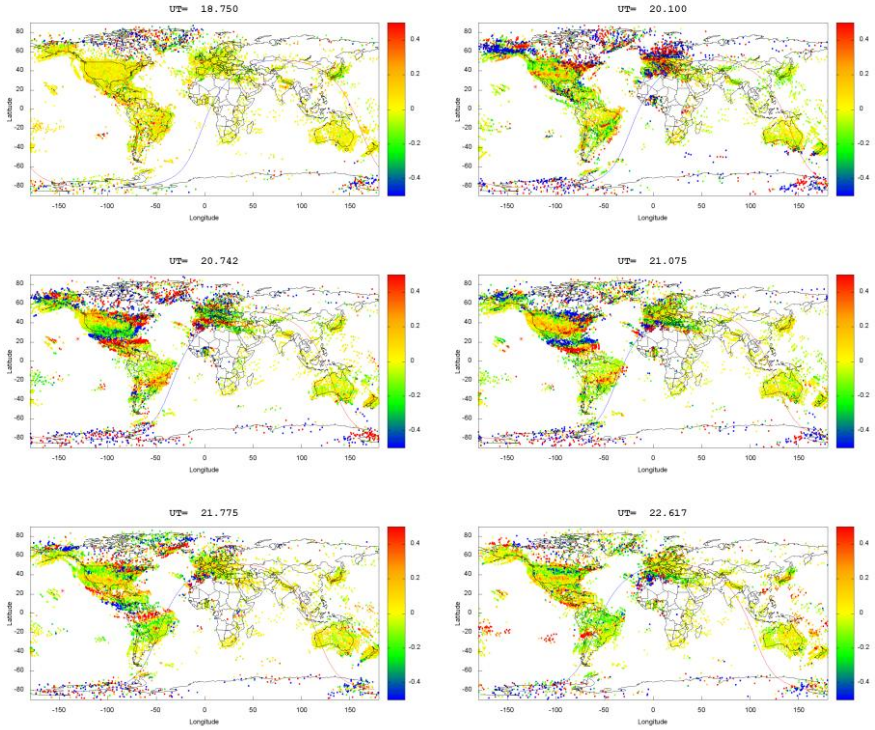

FIGURE 3. Maps TEC showing large scale ionospheric irregularities.

We see F-spread increases during 19:45—21:15 UT with maximum at 20:15 UT. We recorded short-term increasing in GPS L1 phase fluctuations at 19:30 UT. It was not accompanied by GPS/GLONASS amplitude scintillations (not shown on Fig. 2, since there was no visible effect). "Sygnus-A" amplitude scintillations increase around ~20 UT, which corresponds to the time of the F-spread maximum.

Figure 3 shows TEC variations maps deduced from global and regional GPS/GLONASS networks. At 18.875 UT we can see simultaneous generation of negative disturbance in the auroral oval regions of both south and north hemispheres. These disturbances are global and forming belt can be recorded worldwide where there are GPS/GLONASS stations.

At 20:06 (20.1) UT we see that negative disturbance reach midlatitudes in Asian longitude sector. At this time we see effects of small-scale irregularities (see Fig. 2).

It is clearly seen that disturbances generated at the auroral oval boundary move equatorward. Amplitude of disturbance in northern hemisphere is higher than those in southern. This disturbance generated in auroral area cross the equator and reach 35—40°S. At 22.617 UT we see intensive disturbance prolonged from 120° E up to ~ – 30°E. It is very probable that the belt covers all sectors but is not detected inAfrica and ocean regions due to small number of GPS/GLONASS stations in those

regions. We see uniform structure in North America and Europe with gap in the ocean region where there are not the stations at least for 20.742 and 21.075 UT.

Conclusions. During the 2015 June 22 magnetic storm we recorded small-scale irregularities effects and large-scale irregularities. There are strong evidence that those are connected. We argue that small-scale irregularities appear when large-scale ones came across observation sites. The large-scale irregularities are generated at the auroral oval boundaries in the northern and southern hemispheres. Large-scale irregularities generated in North region were found to propagate across equator and reach 35—40°S. So overall travel distance is ~10 000 km, which is unexpectedly large distance for acoustic-gravity waves.

Acknowledgements.*The study was supported by the Russian Foundation for Basic Research, project no. 15-05-03946_a.*

1. K. C. Yeh and C. H. Liu, Radio wave scintillation in the ionosphere, *Proc. IEEE*, 1982, 704, pp. 324—360.

2. P. M. Jr. Kintner, T. E. Humphreys and J. Hinks, GNSS and Ionospheric Scintillation How to Survive the Next Solar Maximum, *InsideGNSS*, 2009, pp. 22—30.

3. S. Shanmugam, J. Jones, A. MacAulay, and A. J. Van Dierendonck, Evolution to Moder-nized GNSS Ionoshperic Scintillation and TEC Monitoring, *IEEE/ION PLANS 2012 — April 24—26*, Myrtle Beach, SC, Session B2A, 2012.

4. E. L. Afraimovich, E. I. Astafyeva, V. V. Demyanov et al., A review of GPS/GLONASS studies of the ionospheric response to natural and anthropogenic processes and phenomena, *J. Space Weather Space Clim.*, 2013, 3, A27, 2013.

Comparison Calculation Results by the Homing and Optimization Methods Using IRI Model with Traveling Ionospheric Disturbances

Oleg S. Rubcov[1], Igor A. Nosikov[1,2], Maxim V. Klimenko[1,2], Pavel F. Bessarab[3], and Gennady A. Zhbankov[4]

[1]Immanuel Kant Baltic Federal University, 236041, Kaliningrad, Russia,
[2]West Department of Pushkov Institute of Terrestrial Magnetism, Ionosphere and Radio Wave Propagation of the Russian Academy of Sciences, 236017, Kaliningrad, Russia
[3]Royal Institute of Technology KTH, SE-16440, Stockholm, Sweden
[4]Southern Federal University, 344006, Rostov-on-Don, Russia

Introduction. Nowadays the most popular approach for point-to-point ionosheric ray tracing problem is homing method [1, 2]. In that approach the first part is ray tracing procedure, the second is finding of direction of emission radio waves and the third is construction of radio path. Another approach is direct minimization

of the optical path (Fermat's principle) [3, 4].The main idea is transforming initial trajectory in optimal form, while its end-points are secure in accordance with limiting condition. The most important aim of this report is to compare results obtained using these two approaches and defined problem of its implementing.

Optimization method. In terms of variational theory the functional of the ray path in isotropic medium is defined by

$$S[\gamma] = \int_A^B n(\bar{r})dl\,. \tag{1}$$

Integration is performed along the curve γ, which joins boundary points *A*и*B*; $n(\bar{r})$ — refractive indexes in each point of curve γ with $\bar{r} = (x, y, z)$; *dl*— the length of the element along γ. According with Fermat's principle the functional of the ray path must satisfies to the expression

$$\delta S = 0\,. \tag{2}$$

Simplify curve γ can be represented as a polygonal line joining *N* points in chosen space. Consequently we have a discrete representation of curve $\bar{r} = [\bar{r}_1, \bar{r}_2, .. \bar{r}_N]$ while the end points *A* and *B* are keep fixed according with boundary condition. Thus the problem adduct to the problem of finding minimum of the functional. For compute calculation the integral (1) can be rewritten using trapezoidal or Simpson rule. The most of computational methods based on antigradient of objective function:

$$\bar{F} = -\nabla S = (\bar{F}^2, \bar{F}^3, ..., \bar{F}^{N-1}) \tag{3}$$

However the optimization methods can be improved by two procedures: force projection and elastic forces. The first one is described in detail in [5] and solve the problem of points down-sliding near the minimum of refraction index. This approach is the base of method of transvers displacement (MTD) performed for ionospheric ray tracing by Nosikov et al. [6]. The second one is implementing of points interaction which extremely important for control of points distribution along the ray-path and described in [5]. These two approaches are the base of nudged elastic band (NEB) method. According with NEB method the full force acting on each point *i* of the curve can be defined as

$$\bar{F}^i = \bar{F}_{\perp}^{\ i} + \bar{F}_{spring}^i \tag{4}$$

Thus the force on each point contains only the parallel component of the spring force, and perpendicular component of the true force.

Calculation results. Two-dimensional isotropic model of the ionosphere, where the electron density was obtained by the international reference model (IRI) was chosen as a medium for the point-to-point ray tracing problem. According with the boundary condition the transmitter was positioned in Kaliningrad, Russia (54.57º N; 20º E) and reviewer was positioned in Tromso (65.65º N; 18.57º E). Verifica-

tion of our results was carried out by comparison with calculation results, obtained by the standard ray tracing method (Zhbankov's model).

Figure 1 shows the calculation results of Kaliningrad — Tromso radio paths by using NEB method with frequency of 9 MHz. The calculation results by the NEB method have a good agreement with the calculations of the homing method. In this case all high rays were found by changing the initial approximations of the ray. Low rays were obtained by fixing the position of the top of the path, with a priori information about the ray paths (Fig. 1b).

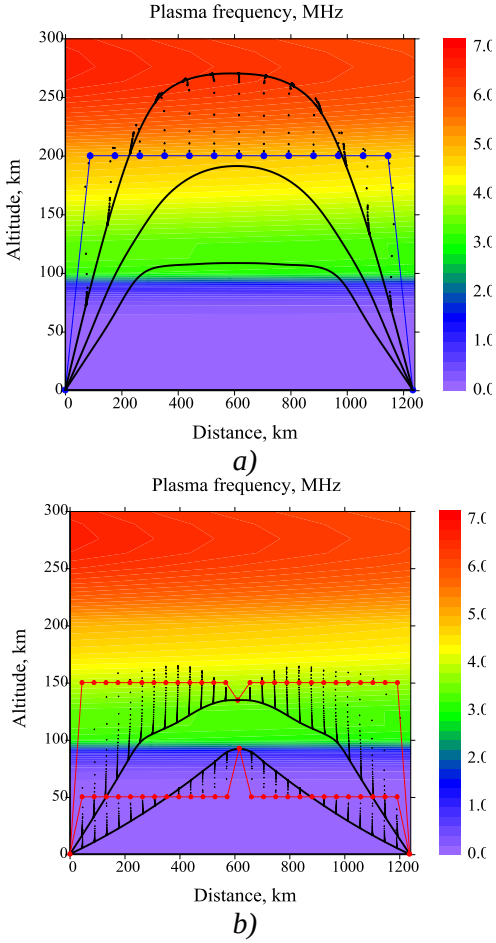

FIGURE 1. Calculation results for the high *a)* and low *b)* rays with frequency of 9 MHz by NEB method between Kaliningrad, Russia (54.57º N; 20º E) and Tromso, Norway (65.65º N; 18.57º E) for IRI modeled ionosphere (13:00 UT 22.06.2014). Black dots represent initial approximation and their position during optimization procedure; solid black lines — found solutions.

Figure 2 shows the calculation results of radio paths Kaliningrad — Tromso for modeled ionosphere with traveling ionospheric disturbances by the NEB (Fig. 2a.) and homing methods (Fig. 2b.). Both methods produce an identical result which shows that the direct variational approach can provide effective point-to-point ray tracing in ionosphere with the heterogeneous distribution of the electron density.

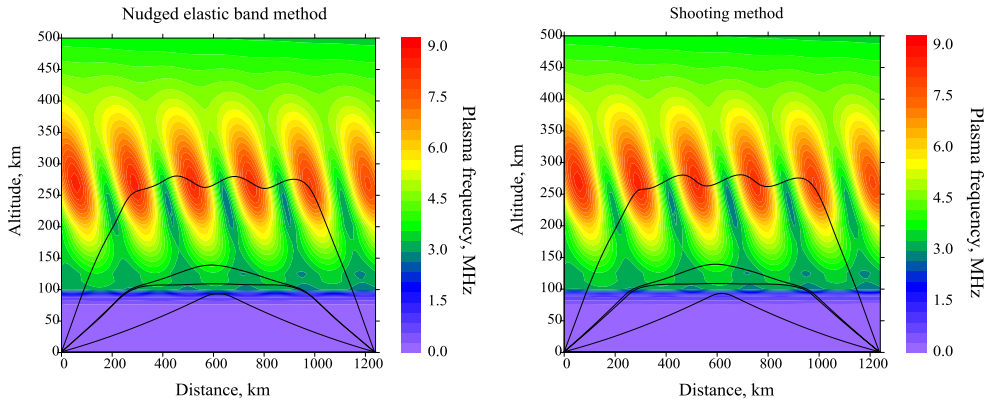

a) *b)*

FIGURE2. Calculation results for the ray paths with frequency of 9 MHz by NEB method *a)* and homing method *b)* between Kaliningrad, Russia (54.57º N; 20º E) and Tromso, Norway (65.65º N; 18.57º E) for IRI modeled ionosphere with traveling ionospheric disturbances (13:00 UT 22.06.2014).

Summary. Point-to-point ionospheric ray tracing problem is solved for two-dimensional isotropic ionosphere, where the electron density was obtained by IRI model. The NEB method was chosen as a optimization method which allows to find all high rays by choosing of initial approximations.

Comparison calculation results obtained by NEB method for modeled ionosphere including traveling ionospheric disturbances with results obtained by homing method show a good agreement.

Acknowledgments. *This investigations were performed with financial support of the Russian Foundation for Basic Research Grants No. 16-35-00590 and № 15-35-20364. This work was partially carried out within the project "Physical mechanisms of the reaction of the upper atmosphere and ionosphere on the processes in the lower atmosphere and on the Earth surface" (State task Education and Science Ministry of the Russian Federation, the competitive part of the task No 3.1127. 2014/K).*

1. N. Y. Zaalov, E. M. Warrington, and A. J. Stocker, *Radio Sci.*, 2003, 38(3), pp. 1052—1058.

2. D. V. Blagoveshchensky, M. Yu. Andreyev, V. S. Mingalev et al., *Adv. Space Res.*, 2009, 43(12), pp. 1974—1985.

3. Y. A. Kravtsov and Y. I. Orlov, *Science*, Moscow, 1980, 304 p.
4. C. J. Coleman, *Radio Sci.*, 2011, 46, RS5016.
5. G. Mills and H. Jónsson, *Phys. Rev. Lett.*, 1994, 72, pp. 1124.
6. I. A. Nosikov, P. F. Bessarab, and M. V. Klimenko, *Radiophysics and Quantum Electronics*, 2016, 59(1).

TEC Variations over Mexico under Disturbed Conditions

Maria A. Sergeeva [1], Olga A. Maltseva [2], and J.-A. Gonzalez-Esparza[1]

[1]SCiESMEX, Instituto de Geofisica, Unidad Michoacan, Universidad Nacional Autonoma de Mexico, Antigua Carretera a Pátzcuaro 8701,Morelia, Mexico
[2]Institute of Physics, Southern Federal University, Stachki, 194, Rostov-on-Don, Russia

In 2014 the Mexican Space Weather Service (Sciesmex) was created. It is operated by the Geophysics Institute, National Autonomous University of Mexico (UNAM). To monitor Space Weather conditions, Sciesmex combines open access satellite data with a local network of different ground instruments covering solar, interplanetary, geomagnetic and ionospheric observations. The present study focuses on one of the tasks of the service — monitoring of ionosphere state over the Mexican region. As there is no ionosonde in operation in Mexico, it was chosen to estimate the state of the ionosphere with use of total electron content (TEC) data reconstructed using data extracted from global positioning system (GPS) signals. TEC values can differ enough depending on the method of their calculation [1]. Two options were considered for the present analysis. First, the vertical total electron content (vTEC) obtained from global ionospheric maps (GIM) technology was used. Second, the data obtained from local networks of GPS signal receivers were used to calculate vTEC. This calculation was performed on the base of the software complex provided by the Institute of Solar-Terrestrial Physics, Siberian Branch, Russian Academy of Sciences [2].

For the present study the data for the last five years was studied. Diurnal and seasonal trends in TEC behaviour were revealed in base of GIM TEC data.

It is known that geomagnetic disturbances are the principal cause of the irregular state of near-Earth Space Weather [3]. Therefore, the cases of different geomagnetic storm events and their impact on the ionospheric conditions were considered. The additional data was involved for the analysis: geomagnetic indexes, local magnetometer data, satellite data (DSMP and CHAMP), data of critical frequencies foF2 measured by ionosondes from the regions close to Mexico. The impact of geomagnetic disturbances over the considered region was reported in some previous works [4, 5, 6], proving the fact that understanding of the ionospheric processes during storms of different intensity is of paramount importance for the region.

First series of results show that GIM TEC and TEC calculated from local GPS receivers show rather good consistency of data for the Mexican region. Example is

given in Fig. 1. Panel "a" illustrates TEC variations under quiet conditions during September 26—27, 2015 (Dst = – 6nT, Kp = 2), panel "b" — during moderate disturbance of September 9—11, 2015 (Dst = – 97nT, Kp = 6). Here, the curves for local stations calculated on the base of the program complex [1] are a little bit higher (MCIG) and lower (UCOE) than the TEC curve based on GIM technology (INEG). This can be probably explained by the fact that the chosen GPS receivers are located at different latitudes (Table 1). The higher the latitude the less the magnitude of TEC curve [7]. This similarity of results proves the following. First, the algorithm applied for calculation of local vertical TEC values in the used software complex provides a reasonable result.

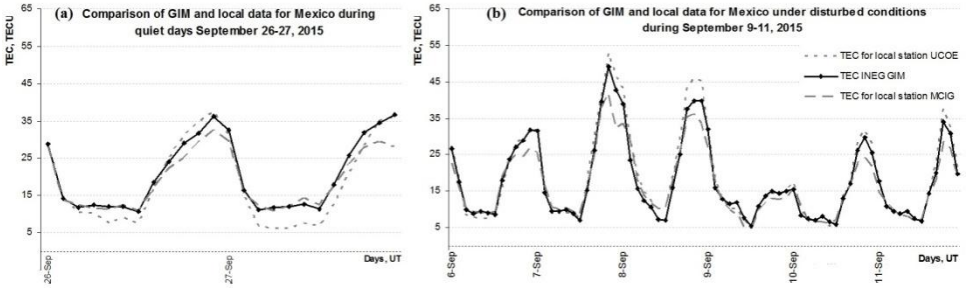

FIGURE 1.Comparison of GIM TEC and TEC from local receivers.

Second, the global maps reflect the ionosphere state over the region rather well. However, GIM TEC data are available in the Internet with a certain delay, but local TEC data can be used for real-time monitoring of the ionosphere. Another benefit is that local TEC calculations are based on a rather dense network of stations if compare to global maps. There is only one station (INEG) that is included in the International GNSS Service (IGS) network of receivers used for global maps production. This means that interpolation has more impact in this case. From the other hand, there is not always the local data available for past periods because the receiver network was developed during the last years.

The second series of results concerned TEC behaviour itself. It was of interest to understand how TEC values can change during the disturbed periods. Various recent events were chosen for the analysis. Figure 2 represents the results for two disturbances which took place in April, 2014 and in March, 2015. The disturbance in March was twice stronger. Here, median and observed GIM TEC values (middle panels) and TEC deviations (lower panels) are illustrared as well as the calculated deviations of TEC from its median value for these periods. The TEC values in general were lower in March 2015 than in April 2014 which can be explained by the seasonal trend of parameter. TEC behaviour during these disturbances was almost of its "classical" nature: the positive phase was followed by the negative phase. The TEC responses to both disturbances were similar, although the intensities (see Dst in Fig. 2) of these the disturbances differed twice.

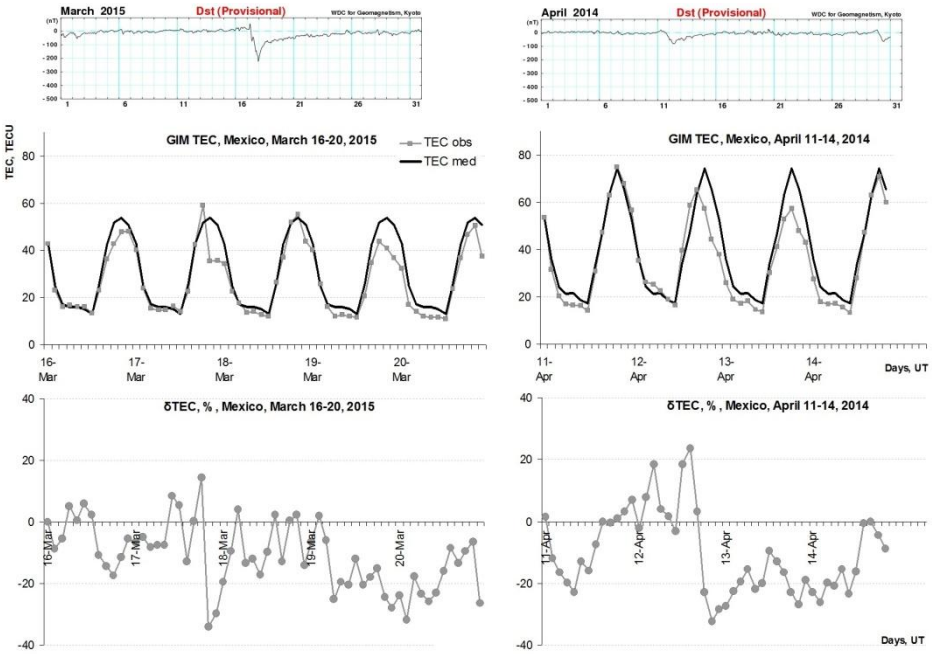

FIGURE 2.Dst-index values (upper panels), median and observed TEC values (middle panels) and TEC deviations (lower panels).

TABLE 1.Coordinates of GPS receivers.

GPS receiver station	Geographic latitude	Geographic longitude	Geomagnetic latitude	Gemagnetic longitude
UCOE (local)	19.48 N	101.41 W	27.77 N	30.89 W
MCIG (local)	27.88 N	101.48 W	36.09 N	31.91 W
INEG (GIM)	21.85 N	102.28 W	30.04 N	32.07 W

It was also of interest to compare TEC results for Mexico with other stations located in the adjacent regions having ionosondes. The comparison was made with stations in Jicamarca (Peru), Fortaleza (Brazil), Ramey (Puerto-Rico), Eglin (USA). In this case the character of ionospheric disturbance was proved by δfoF2 behaviour. It was revealed that in the majority of cases the character of TEC variations in Mexico was close to the variations over Puerto Rico. Figure 3 shows the example of such a comparison during the recent intense storm of June 22—25, 2015 (Kp = 8.3, Dst = – 204nT). It could be expected that for Mexico station δfoF2 variations would be identical to δTECin a similar way like in Puerto-Rico. However, even the first comparisons of results reveal the complicity of interpretation of disturbances without involving additional data (solar and geophysical indexes).

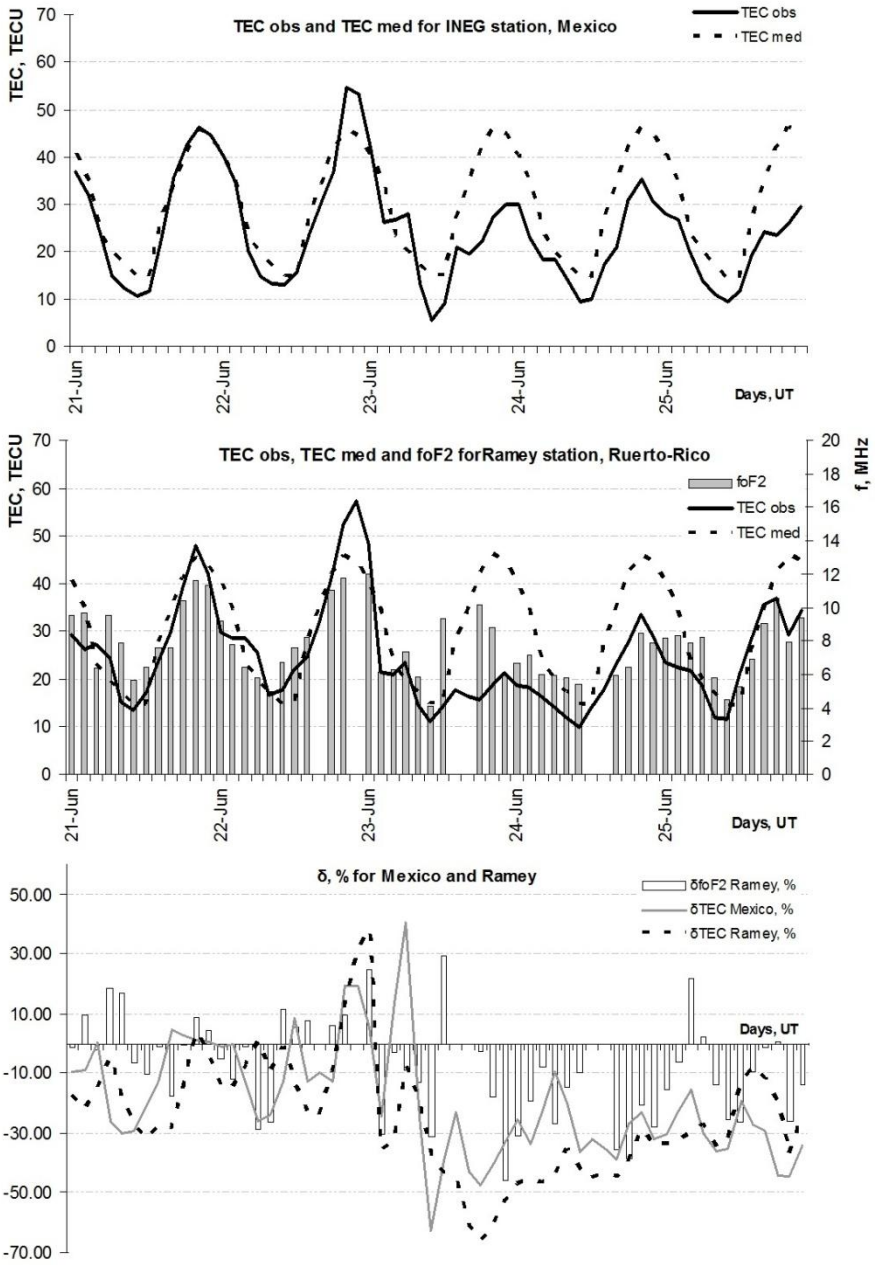

FIGURE 3. Comparison of TEC values for Mexico and Puerto-Rico during the storm of June 22—25, 2015. foF2 variations in general prove the curve of TEC in Puerto-Rico.

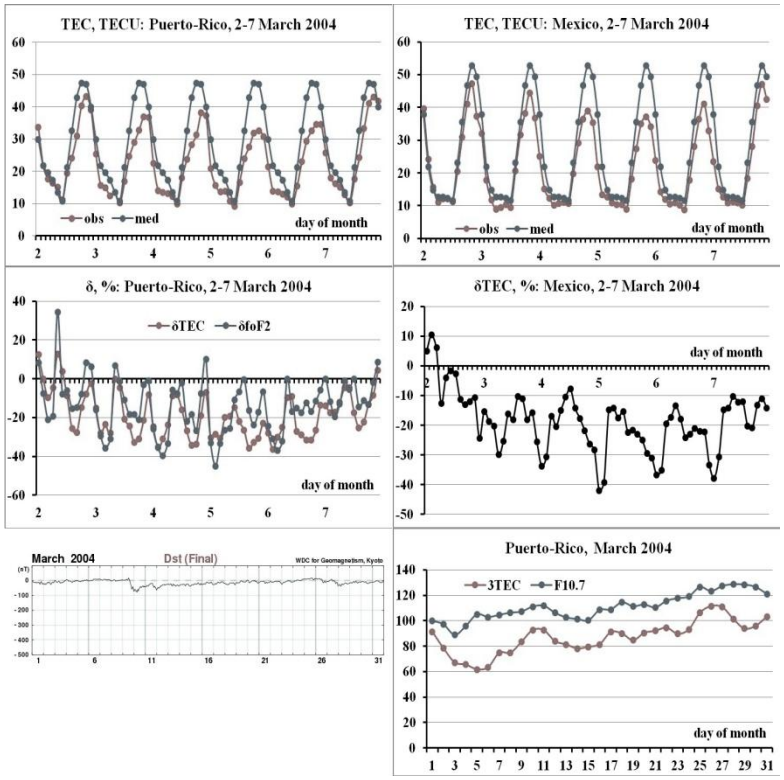

FIGURE 4.Illustration of disturbed state of ionosphere over Puerto-Rico and Mexico during the quiet Dst-index and with no correlation to F10.7.

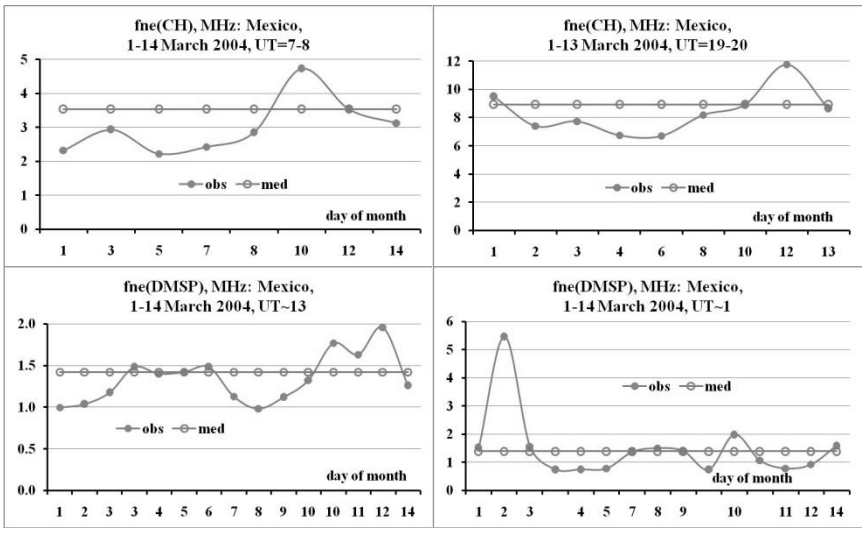

FIGURE 5. Plasma frequencies measured by CHAMP and DSMP satellites over Puerto Rico and over Mexico during different hours (UT) of the day.

Third series of results touch on the comparison of TEC behaviour with Dst-index of geomagnetic activity as well as with plasma frequency values fne from DSMP and CHAMP satellites and F10,7 index of solar activity. It was revealed that sometimes TEC manifests the disturbed state of the ionosphere over Mexico while Dst does not reveal the disturbance. Example is given in Fig. 4. for March 2—7, 2004: the Dst-index behaviour was quiet, but the variations of ionospheric characteristics (foF2, TEC) revealed the negative disturbances. Such a behaviour can not be explained by the relationship between the ionospheric parameters andthe index of solar activity F10.7 as it can be seen from the lower right panel of Fig. 4. But at the same time the fne variations prove the character of TEC behaviour in both cases: for the disturbance identified with Dst index and for the period of quiet Dst. fne deviation from its median value for different hours of a day (UT) is shown in Fig. 5. Thus, TEC proved to be a good indicator of changes in the Mexican ionosphere. Even when F10.7 and Dst indexes do not show any disturbance, TEC can manifest its strong variations of ionospheric conditions as its correlation with fne(sat) exists.

To conclude, the main results of the study are as follows. (1) It was confirmed the opportunity of monitoring of the Space Weather effects in Mexican region with the use TEC data: both global ionospheric maps and calculations based on the software complex [1] reveal the disturbed state of the ionosphere. The second option has an advantage of rapid access for data including the real-time measurements from local GPS receivers. (2) It was revealed that in the majority of cases the character of TEC variations in Mexico was close to the variations in Puerto-Rico and it is of "classical" nature. (3) The relationship between the ionospheric response and the Dst-index in the Mexican region was studied. It was found that ionospheric characteristics can manifest the disturbance when sometimes the Dst is quiet. This was confirmed by fne values. It goes to prove that TEC is a good indicator of the state of the ionosphere: when F10.7 and Dst indexes do not show any disturbance, TEC can manifest its strong variations of ionospheric conditions.

Acknowledgments. *The SCIESMEX operation is partially funded by CONACYT grant AEM-2014-C01-247722 and PAPIIT grant IN106916. The work of Maltseva O.A. was supported by Southern Federal University Grant № 213.01-11/2014-22.*

1. O. Maltseva and G. Zhbankov, Total Electron Content of ionosphere: Conditions of wave propagation, LAP Lambert Academic Publishing, ISBN: 978-3-659-48571-8, Saarbrücken, Germany, 2013, 153 p.

2. Yu. V. Yasyukevich, A. A. Mylnikova, V. E. Kunitsyn, and A. M. Padokhin, GIM Influence of GPS/GLONASS Differential Code biases on the Determination of the Absolute Accuracy Total Electron Content in the Ionosphere, Geomagn. Aeron., 2015, 55(6), pp. 763—769.

3. D. V. Blagoveshchensky, Short waves in the anomalous radio channels, LAP Lam-

bert Academic Publishing, ISBN: 978-3-8454-2535-1, Saarbrücken, Germany, 2011, 422 p.

4. A. Carrillo-Vargas, H. R. Pérez-Enríquez, M. Rodríguez-Martínez et al., Ionospheric disturbances detected by MEXART, Adv. Space Res., 2012, 49(11), pp. 1570—1580.

5. R. López-Montes, R. Pérez-Enríquez, and E. A. Araujo-Pradere, The impact of large solar events on the total electron content of the ionosphere at mid latitudes,*Adv. Space Res*., 2012, 49(7), pp. 1167—1179.

6. M. Rodríguez-Martínez, H. R. Pérez-Enríquez, A. Carrillo-Vargas et al., Ionospheric disturbances and their impact on IPS using MEXART observations, *Solar Physics*, 2014, 289(7), pp. 2677—2695.

7. E. L. Afraimovich and N. P. Perevalova, GPS-monitoring of the Earth's upper atmosphere, Irkutsk: SC RRS SB RAMS, IBSN: 5-98277-033-7, Irkutsk, 2006, 480 p.

Using GPS Datasets for Monitoring Integrated Water Vapor Content

Nikita A. Tereshin, Ivan A. Nesterov

Department of Atmospheric Physics, Lomonosov Moscow State University, Faculty of Physics, Leninskiye Gory 1—2, Moscow, 119991, Russia

Water vapor is a key driving factor behind many extreme weather events like typhoons, floods and draughts. Due to its high variability and lack of proper global data coverage, prediction of those events remains a difficult task. Currently, satellite microwave radiometry applications allow robust measurements of integrated water vapor (IWV) content over sea surface, but its retrieval over land is complicated, and there's a dependence on weather conditions (clear-sky bias). This article presents another approach for estimating integrated water vapor content in the atmospheric column using networks of land-based dual-frequency GPS receivers.

THE TECHNIQUE: Dual-frequency GPS receivers simultaneously measure signal phase delay (pseudorange) for multiple satellites on two frequencies: L1 (1575,42 MHz) and L2 (1227,60 MHz). Signal delay depends on the distance traveled by the signal, but is affected by the atmospheric refraction as well. Additionally, errors are introduced by imprecise time synchronization between satellites and receivers, uncertainties in their positions, relativistic effects, as well as signal processing-related noises.

To provide satellite-independent observations, range-dependent delay is eliminated, along with relativity-induced range error. Atmospheric optical depth has to be normalized for each observation, and any satellite-related clock errors need to be corrected. The former is achieved by using Niell mapping functions [1], providing zenith delay values. To achieve the latter, single differences technique is used [2].

Due to uncertainty in the positioning of GPS receivers the actual position has to be determined to provide a correct estimation of tropospheric delay. One approach is to estimate it beforehand, but in this technique a correction vector **δρ** (the difference between actual position and approximate position of the receiver) is introduced as an unknown variable, producing a following correction to satellite-receiver range (**n** is the normal vector between receiver and satellite):

$$\Delta\rho = (\vec{n}, \delta\vec{\rho}) \quad (1)$$

To account for water vapor-induced refraction, the next step is to eliminate ionospheric and dry air effects. Using dual-frequency receivers allows a simple ionosphere-free combination to be constructed from both L1 and L2 observations by noting the strong dependence of ionosphere-induced delay on signal frequency. The resulting quantity is called zenith tropospheric delay (ZTD).

Dry air, however, does not possess such properties to distinguish it from water vapor, so it has to be estimated *a priori*. To estimate dry air delay, Saastamoinen tropospheric model is used [3]. Weather parameters required for model calculations are obtained by interpolating relevant reanalysis data.

By eliminating all aforementioned factors, zenith wet delay (ZWD) is obtained. One can show that it is directly related to total precipitable water amount and, for most cases, they are proportional to each other [4].

Due to unusual frequency band for water remote sensing (1—2 GHz, no nearby absorption lines), combined with a range of unaccounted-for GPS errors, signal-to-noise ratio is low for recovered IWV data. To counteract that, Tikhonov-regularized B-splines are used to set up an inverse problem linear system.

RESULTS: The described technique was applied to data collected from Scripps Orbit and Permanent Array Center (SOPAC) archive.

To estimate the accuracy of calculated tropospheric delay values, Saastamoinen tropospheric delay model was applied to existing surface pressure, temperature and humidity data extracted from the NCEP NCAR reanalysis (Fig. 1). Correlation coefficient was calculated (R-values > 80 %), with average RMS error reaching 3 cm.

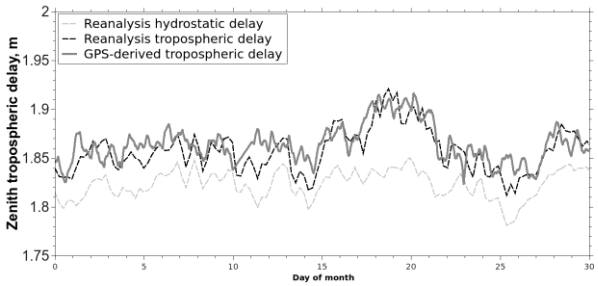

FIGURE 1. Comparison of reanalysis-derived and GPS-derived tropospheric delay (Station AMC2, Colorado Springs, May 2014).

For selected stations in immediate proximity to AERONET photometers (example on Fig. 2), calculated IWV data was compared to photometry measurements. For those, correlation coefficient was calculated (R-values > 70 %), demonstrating that the designed technique is a good fit for existing water vapor data.

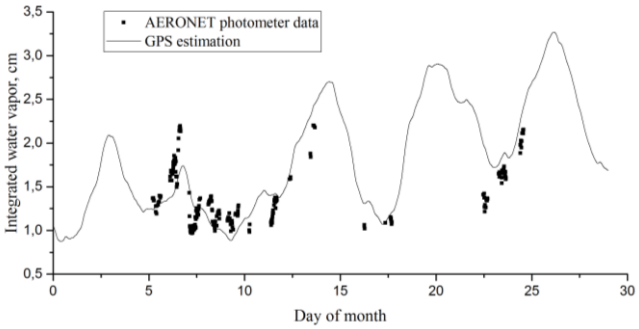

FIGURE 2. Comparison of photometer data and GPS-based estimation of water vapor content (Station ZWE2, Zvenigorod, June 2015).

To provide a sense of spatial accuracy of the technique, a network of receiver stations located on the western coast of North America (with average density of 1 station per 100 km^2) was chosen. For each, the IWV data series was calculated, providing a map of integrated water vapor amount, which was later compared to NCEP NARR reanalysis values. Comparison revealed that the relative RMS error for IWV values reaches around 30 % for dry seasons, and improves up to 15 % in summer.

This technique allows for robust retrieval of integrated water vapor content in the atmospheric column. While the data collected is imprecise when compared to other techniques for water vapor sensing like radiometry, this technique allows for uninterrupted collection of data over long periods of time that isn't dependent on cloud coverage, in contrast to satellite measurements. Due to land-based measurements, the technique doesn't rely on surface parameters such as emissivity, which makes it a good complementary instrument for monitoring water vapor transfer over land, considering the existence of numerous networks of GPS receivers.

Acknowledgements*: The processing software used in this work includes modified GPSTk library code (https://github. com/rumkex/GPSTk), originally developed by the Space and Geophysics Laboratory of the University of Texas, USA.*

This work has been financially supported by Russian Foundation for Basic Research grant № 16-35-00607.

1. A. E. Niell, Global mapping functions for the atmosphere delay at radio wavelengths. *J. Geophys. Res.: Solid Earth*, 1996,101(B2), pp. 3227—3246.

2. C. Alber, et al. Obtaining single path phase delays from GPS double differences. *Geophys. Res. Lett.*, 2000, 27(17), pp. 2661—2664.

3. J. Saastamoinen, Atmospheric correction for the troposphere and stratosphere in radio ranging satellites, *The use of artificial satellites for geodesy*, 1972, pp. 247—251.

4. F. S. Solheim, et al. Propagation delays induced in GPS signals by dry air, water vapor, hydrometeors, and other particulates, *J. Geophys. Res. Atmos.*, 1999, 104(D8), pp. 9663—9670.

On the Temperature Effects of the Seismogenic Electric Current

Mikhail I. Karpov, Alexandr A. Namgaladze, and Maria A. Knyazeva

Research and International Cooperation Department, Murmansk Arctic State University, Kapitan Egorov Str., 15, Murmansk, 183720, Russia

The ionosphere electric field variations observed by the Intercosmos Bulgaria 1300 and DEMETER satellites [1—2] over seismic active regions are considered as a primary cause of the ionosphere total electron content (TEC) positive and/or negative disturbances several days before the strong earthquakes. Via the electromagnetic plasma drift the seismogenic electric field drives F2-layer plasma upwards or downwards (depending on direction of the zonal electric field) in the areas with the lower or, respectively, higher loss rates of ions O^+ in the ion-molecular reactions, enhancing or decreasing the NmF2 and TEC [3].

The origin of seismogenic electric field is explained by the generation of the vertical electric current flowing between the tectonic fault and ionosphere [4]. It appears due to the vertical separation and transport by gravity force and pressure gradients of the oppositely charged particles, which are created as a result of air ionization, attachments of electrons to heavy neutral particles, condensation of water vapors with subsequent coagulation of water drops [5]. These currents have the same nature as the thunderstorm currents do. The ionization sources (radioactive soil gases emanating from the fault and cosmic rays) and fluxes of warm humid air with high concentration of water and dust particles (aerosols) facilitate their generation.

Using the vertical electric currents as the source of the seismogenic electric field, the TEC disturbances were calculated numerically, and a good agreement was found with the typical relative TEC disturbances observed prior to the strong earthquakes [6]. Numerical calculations also revealed dependence of the relative TEC variations' features on the direction, intensity and spatial distribution of the vertical electric currents. It was also shown that meridional components of the seismogenic electric field redistribute plasma in the horizontal plane, thus, the joint action of the zonal and meridional electric fields creates complicated three-dimensional electron density disturbances.

It was proposed that an increase of electric field causes related increase of the electron temperature in the E-region due to the Joule heating, and these electron temperature enhancements influence on the F-region and TEC disturbances [7]. But due to the low electron heating in the E-region [8] its influence on the ionosphere electron density above it seems to be doubtful. In order to check this, the series of numerical calculations were performed using the Upper Atmosphere Model (UAM).

The UAM is the modified version of the global self-consistent model of the thermosphere, ionosphere and protonosphere (GSM TIP) developed in the Western Department of the IZMIRAN [9]. It calculates the global three-dimensional distribution of the neutral and charged particles' concentrations, temperatures and velocities at the height range of 80—100 000 km as well as the electric potential by numerical integration of the continuity, motion, heat balance and electric potential equations [10]. The background parameters distribution was calculated for the conditions corresponding to the Haiti 2010 earthquake, and for disturbed conditions the vertical electric currents j_s = 10—^{9} A/m^2 were added in the equation for the electric potential (1) to generate the local seismogenic electric field in addition to the regular global electric field of dynamo and magnetospheric origins.

$$\nabla[\hat{\sigma}(\nabla\phi - [\vec{V}\times\vec{B}]) - \vec{j}_m - \vec{j}_s] = 0\,. \qquad (1)$$

The vertical electric currents were switched on at the limited area of 250 by 4500 km with the center located at the earthquake epicenter (0º geom. long., 30º geom. lat.).

Firstly, the self-consistent solution of the continuity, motion and heat balance equations for both neutral and charges particles was obtained. Secondly, the NLRMSISE-00 empirical model for the neutral particles was used, similarly to the calculations performed in [6]. New approach allowed to investigate the effects of the electron temperature possibly occurring in the ionosphere. The third variant of calculations was carried out with both the electron and ion temperatures setup as equal to each other as well as to the neutral temperature, which was obtained from NLRMSISE-00, both for background and disturbed values. Thus, only impact of the plasma drift under the action of seismogenic electric field was taken into account.

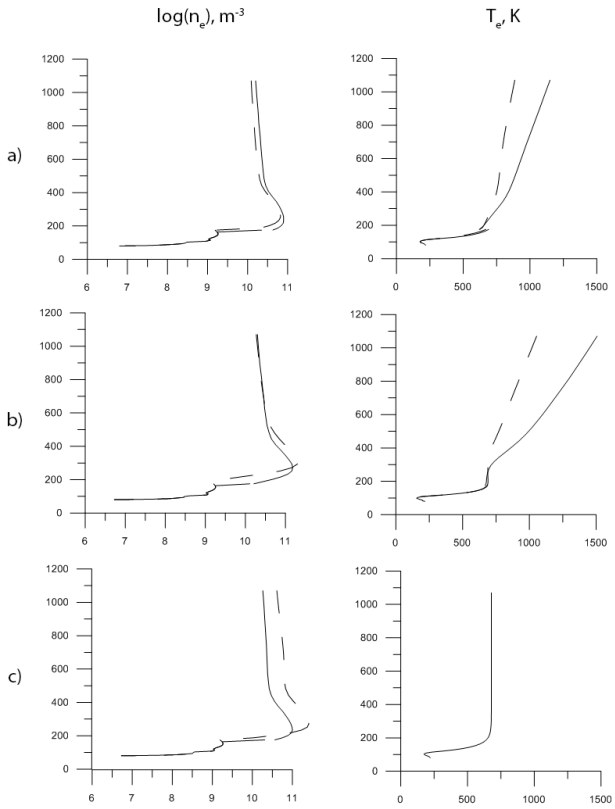

FIGURE 1. The UAM calculated electron number density (left) and electron temperature (right) profiles at 335º geom. long. 30º geom. lat. Dashed and solid lines correspond to the background and disturbed values, respectively: a) the neutral gas parameters obtained from the NLRMSISE-00, b) self-consitent calculation, c) $T_i = T_e = T_{nNLRMSISE-00}$.

Figures 1 and 2 show vertical profiles of electron number density (left panels) and electron temperatures (right panels) at 335º geom. long.30º geom. lat. and 25º geom. long.30º geom. lat. for three calculation variants at 04:00 LT. These coordinates were considered, since as it has been shown in [6] the zonal electric field has its maximums to the West and to the East from epicenter. Calculation results show that maximum changes of the electron concentration relative to the background values occur at the height range of 200—450 km. The shape of vertical profiles for three different modeling variants stay pretty much the same, and any differences are negligible at the whole range up to 1000 km.

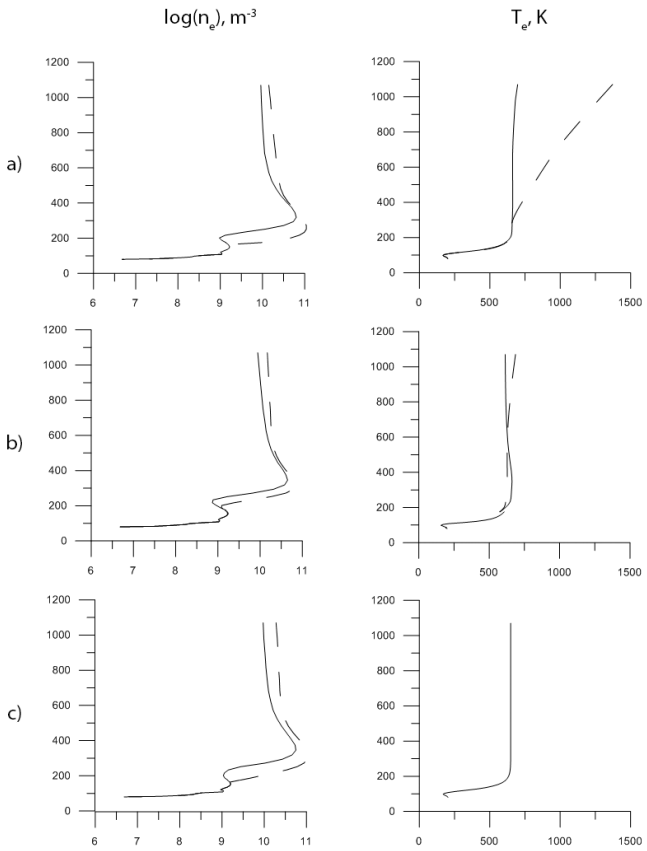

FIGURE 2. The UAMcalculated electron number density (left) and electron temperature (right) profiles at 25º geom. long. 30º geom. lat. Dashed and solid lines correspond to the background and disturbed values, respectively: a) the neutral gas parameters obtained from the NLRMSISE-00, b) self-consitent calculation, c) $T_i = T_e = T_{nNLRMSISE-00}$.

The electron temperature at the heights of 200—300 km do not change significantly, no matter whether the self-consistent solution or empirical data for the neutral gas was used. Therefore, the main physical mechanism responsible for the electron number density disturbances in the F2-layer is the electromagnetic plasma drift under the action of seismogenic electric field generated as a result of the vertical electric current. As calculation results clearly show, the impact of electron temperature increase in the E-region has no significant effect in the F2-layer. This is due to the fact, that they practically absent, since the lifetime of the electrons at the heights below 250 km is short relatively to the characteristic time of the transport.

More pronounced changes of calculated electron temperature were obtained at the height of about 400 km and above. Differences relative to the background values were about 100—250 K (15—30 %), growing with the altitude and in a good agreement with the measured data. For example, the electron temperature was enhanced by 1.2—1.5 times than the average normal values according to the meas-

urements by the Indian SROSS-C2 satellite (altitude range 430—630 km) during the earthquakes in 1995—1998 [11]. Significant decreases of the electron temperature were found by the Hinotori satellite before and after the three earthquakes in 1981—1982 [12], and decrease to a value above 20 % was detected in the 4 and 5 days prior to the Wenchuan earthquake on May 12, 2008 by DEMETER at 660—710 km altitude [13]. Most often positive and less often negative correlations between the electron concentration and temperature were found by DEMETER for thousands of earthquakes with $M \geq 5.0$ during 2005—2010 [14]. It is worth noting that disturbed area extended to 80—120 degrees for Hinotori measurements, which was twice as big than in our calculations, and 1000 km from epicenter for DEMETER.

Thus, our calculation results showed no influence of the E-region electron temperature disturbances on the electron number density.

Acknowledgments. *The reported study was funded by RFBR according to the research project No. 16-35-00397 мол_а.*

1. M. Gousheva, D. Danov, P. Hristov, and M. Matova, Ionospheric quasi-static electric field anomalies dusring seismic activity in August-September 1981, *Natural Hazards and Earth System Sciences*, 2009, 9, pp. 3—15.

2. X. Zhang, X. Shen, S. Zhao et al., The characteristics of quasistatic electric field perturbations observed by DEMETER satellite before large earthquakes, *Journal of Asian Earth Sciences*, 2014, 79, pp. 42—52.

3. A. Namgaladze, M. Klimenko, V. Klimenko, and I. Zakharenkova, Physical Mechanism and Mathematical Modeling of Earthquake Ionospheric Precursors Registered in Total Electron Content, *Geomagn. Aeron.*, 2009, 49(2), pp. 252—262.

4. V. Sorokin and Yu. Ruzhin, Electrodynamic Model of Atmospheric and Ionospheric Processes on the Eve of an Earthquake, *Geomagn. Aeron.*, 2015, 55(5), pp. 626—642.

5. A. Namgaladze and M. Karpov, Conductivity and external electric currents in the global electric circuit, *Russ.J. Phys. Chem. B*, 2015, 9(4), pp. 754—757.

6. M. Karpov, A. Namgaladze, and O. Zolotov, Modeling of Total Electron Content Disturbances Caused by Electric Currents between the Earth and the Ionosphere, *Russ.J. Phys. Chem. B*, 2013, 7(5), pp. 594—598.

7. Yu. Ruzhin, V. Sorokin, and A. Yashchenko, Physical Mechanism of Ionospheric Total Electron Content Perturbations over a Seismoacive Region, *Geomag.Aeron.*, 2014, 54(3,) pp. 337—346.

8. E. Brunelli and A. Namgaladze, Fizika ionosfery (Physics of the Ionosphere), Moscow, 1988, 528 p. (in Russian).

9. A. Namgaladze, Yu. Korenkov, V. Klimenko et al., Numerical modeling of the thermosphere-ionosphere-protonosphere system, *J. Atmos. Sol.—Terr. Phys*., 1991, 53(11/12), pp. 1113—1124.

10. A. A. Namgaladze, O. Martynenko, M. Volko et al., High-latitude version of the global numeric model of the Earth's upper atmosphere, *Proceedings of the MSTU*, 1998, 1(2), pp. 23—84.

11. D. Sharma, A. Bardhan, and J. Rai, Ionospheric electron and ion temperatures response to seismic activity, *Indian Journal of Radio & Space Physics*, 2013, 42, pp. 18—26.

12. K. Oyama, Y. Kakinami, J. Liu et al., Season, local time, and longitude variations of electron temperature at the height of ~600km in the low latitude region, *Adv. Space Res.*, 2008, 113, pp. 269—278.

13. Z. Zeng, B. Zhang, G. Fang et al., The analysis of ionospheric variations before Wenchuan earthquake with DEMETER data, *Chinese Journal of Geophysics*, 2009, 52, pp. 13—22 (in Chinese).

14. X. Shen, X. Zhang, J. Liu et al., Analysis of the enhanced negative correlation between electron density and electron temperature related to earthquakes, *Ann. Geophys*., 2015, 33, pp. 471—479.

Calculation of Meridional Neutral Winds With Irkutsk Incoherent Scatter Radar (IISR)

Alexander A. Shcherbakov, Andrey V. Medvedev, Dmitry S. Kushnarev, Maxim V. Tolstikov, and Sergey S. Alsatkin

Institute of Solar-Terrestrial Physics, 664033, Lermontova 126a, Irkutsk, Russia

This paper presents a technique for velocity determination of meridional neutral winds from the Irkutsk Incoherent Scatter Radar (IISR). We calculated plasma drift velocity based on phase analysis of an autocorrelation function of an incoherent scatter signal. Mid-latitude meridional neutral winds were calculated using a "three-beam" technique from the IISR velocity with taking into account motions due to electric fields across magnetic field lines in both meridional and zonal direction. The results obtained were compared with the modeled wind values.

All kinds of ionospheric motions can be roughly divided into two classes, namely, winds and drifts. When we talk about the thermospheric winds, we usually mean the motions in the neutral atmosphere, global and slowly changing over time. The main controlling process for it is the effect of pressure gradients due to uneven heating and cooling of Earth atmosphere. When we talk about the ionospheric velocities, we mean drift of an ionized in general, or motion of ionospheric inhomogeneities embedded in the ambient plasma under the dynamic action of external forces.

In general, an ionized component is affected by three categories of forces, which can be conceived as $V_i = V_d + V_n + V_e$, where V_d is diffusion processes associated with a gravity gradient and electron density; V_n is the motions of neutral particles associated with spatio-temporal variations of parameters of the neutral atmosphere; V_e is the motions caused by electric fields generated in the dynamo region and magnetosphere and coming into the F-region along the geomagnetic field lines. The ultimate goal of this paper is to separate these three forces and to assess their

contribution to plasma-drift velocity along the incoherent scatter radar line-of-sight, which we get in our regular experiments.

In its regular experiments, the IISR can simultaneously emit at two different frequencies, as shown in Fig.1. Because of the frequency scanning principle, each beam will have its inclination, which means its own angle between the radar line-of-sight and a magnetic field. Plasma drift velocity in this case can be represented as two components parallel and perpendicular to the field. The first one is contributed by neutral wind and diffusion; the second and third, by electric fields both in zonal and in meridional planes:

$$V_{ll} = U_{wind} \cdot CosY + U_{dif} \tag{1}$$

$$V_{p} = U_{E\times B} \tag{2}$$

$$V_{pe} = U^{'}_{E\times B} \tag{3}$$

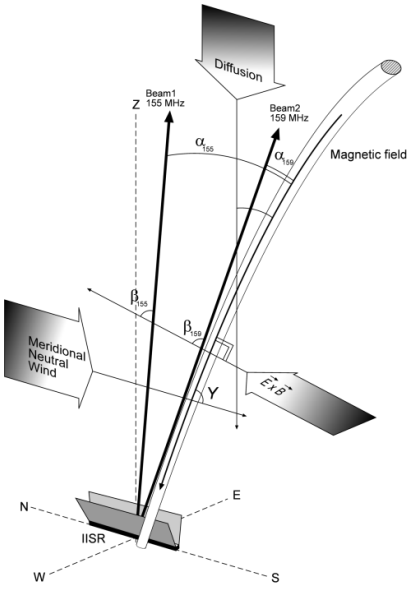

FIGURE 1. Diagram of geometry of the three-beam experiment. Here thin black line shows the magnetic field along which the charged particles move under ambipolar diffusion (V_d)and ion transfer($Vn_.$) The bold black lines show the incoherent scatter radar beams, 159 MHz beam have a smaller angle with the magnetic field, 155 MHz beam have lager angle.

All if this components in their turn make different contributions to determined radial velocities at different frequencies, as the beams have different position relative to the Earth's magnetic field:

$$V_{159} = V_{ll} \cdot Cos\alpha_{159} + V_{p} \cdot Cos\beta_{159} + V_{pe} \cdot Cos\gamma_{159} \tag{4}$$

$$V_{155} = V_{ll} \cdot Cos\alpha_{155} + V_{p} \cdot Cos\beta_{155} + V_{pe} \cdot Cos\gamma_{155} \tag{5}$$

where: α,$\beta$and γ are the angles between the radar line-of-sight and velocity component.

We don't have a third beam to create third equation, so we can solve this system of equations (4)—(5), only by entering an extra regularizing component. That is why we call this technique a "three-beams". As such a regularizing component, we used the criterion of a minimum plasma velocity module:

$$V^2 = V_{ll}^2 + V_p^2 + V_{pe}^2 \to \min \tag{6}$$

The wind obtained by "three-beams" technique as shown in Fig.2 for the summer 2013 experiment is greatly consistent with the estimation of the HWM07, a new theoretical model. It can be seen that with took into accounts perpendicular field motions, the amplitude of meridional wind is in good consistent with the modelled values.

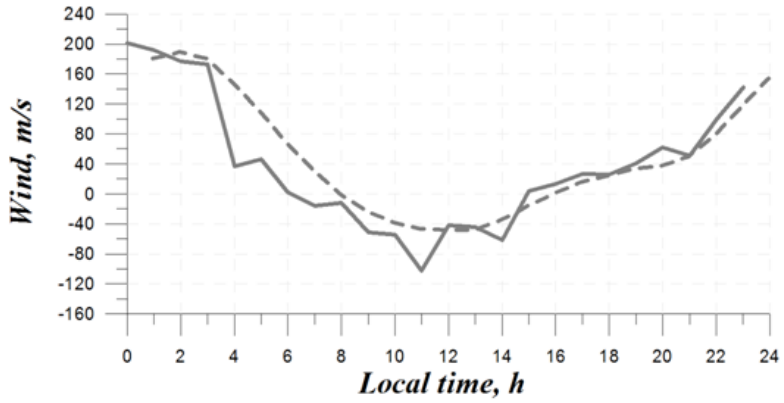

FIGURE 2. Neutral wind velocity averaged up to diurnal variations in June 2013 at the height of 270 km (solid gray line), as well as diurnal variations of wind velocity as per the HWM07 model (dotted grey line.), obtained by "three-beams" technique.

This study was supported by the Russian Foundation for Basic Research, project No. 15-05-02313.

CONTENTS

Plenary sessions (PL)

Young Scientist Oral Reports

MAGNETOSPHERE-IONOSPHERE-ATMOSPHERE COUPLING

Proceedings
Of First Baltic School

Компьютерная верстка *Г. И. Винокуровой*

Подписано в печать 03.06.2016 г.
Формат 70×100 $^{1}/_{16}$. Усл. печ. л. 44,7
Тираж 500 экз. (1-й завод 50 экз.). Заказ 105

Издательство Балтийского федерального университета им. И. Канта
236022, г. Калининград, ул. Гайдара, 6